eman ta zabal zazu

Universidad del País Vasco

Euskal Herriko Unibertsitatea

Theoretical studies on molecular adsorption and the effect of strain on core-level spectroscopy in different metal surfaces

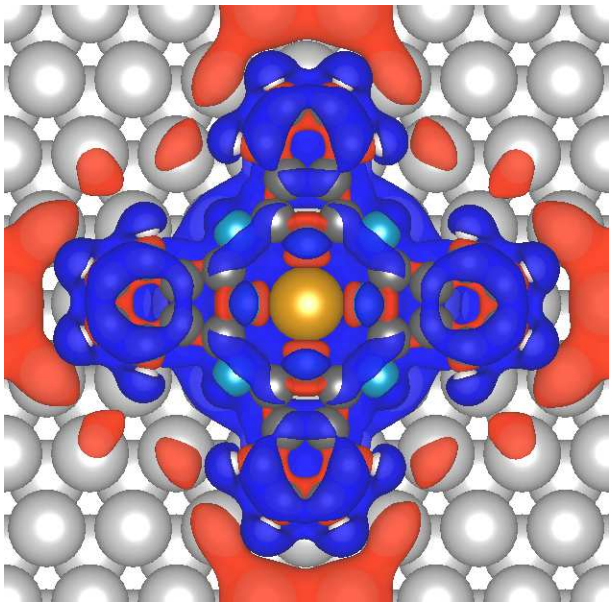

Thesis submitted to the
University of the Basque Country
for the degree of Doctor in Physics by

Antón X. Bríon-Ríos

Donostia-San Sebastián, 2018

Universidad del País Vasco
Euskal Herriko Unibertsitatea
Facultad de Química
Departamento de Física de materiales

PhD Thesis

Theoretical studies on molecular adsorption and the effect of strain on core-level spectroscopy in different metal surfaces

Thesis submitted to the University of the Basque Country for the degree of Doctor in Physics

Author:
Antón Xosé Brión Ríos

Supervised by:
Dr. Daniel Sánchez Portal and Dr. María José Cabrera Sanfelix

Donostia-San Sebastián, 2018

Pentru Sânziana şi Artai, familia şi lumina din viaţa mea.

Acknowledgements

Homo sum, humani nihil a me alienum puto.

Publius Terentius Afer, Heauton Timorumenos

Esta tese de doutoramento é o resultado do apoio e colaboración de moitas persoas. Sirvan estas liñas como máxima expresión do meu máis profundo agradecemento a tódalas xentes e institucións que dunha ou outra forma son parte dela.

Primeiramente nomear ás persoas encargadas de levar a cabo a dirección deste proxecto. A miña directora no Donostia International Physics Center (DIPC), a Dra. María José Cabrera Sanfelix pola axuda e dirección prestada. O meu director de tese e mentor na Euskal Herriko Unibertsitatea (UPV/EHU) e o Centro de Física de Materiales (CFM) do CSIC-UPV/EHU, o Dr. Daniel Sánchez Portal pola súa inestimábel axuda, guía e apoio na consecución deste traballo que doutro xeito non tería sido posíbel.

Dar as grazas a tódolos grupos experimentais que colaboraron neste traballo e que foron un aporte fundamental para as investigacións discutidas nos distintos capítulos. O grupo do NanoPhysics Lab dirixido polo Prof. Enrique Ortega no CFM (CSIC-UPV/EHU) e o grupo de Nanoimaging liderado polo Prof. José Ignacio Pascual no nanoGUNE, ámbolos dous en Donostia-San Sebastián. Tamén quero citar a nosa conexión internacional, Laura Fernández, e o grupo de Surface Physics dirixido polo Prof. Peter Jakob da Philipps-Universtät en Marburg (Alemaña) por tódalas discusións, aclaracións e aportaces feitos a este documento.

Quixera destacar como lles correspondente a todo o Persoal de Administración e Servizos (PAS) do DIPC, o CFM e a UPV/EHU que tanto nos facilitan as cousas. Aínda que nun segundo plano son parte esencial dos éxitos acadados, sen eles o noso traballo sería inmensamente máis complicado. No tocante a parte institucional debo recoñecer o soporte financieiro e os recursos facilitados para o desenrolo desta tese dende UPV/EHU e o DIPC . Na miña etapa inicial como bolseiro predoutoural do programa ZabaldUz e posteriormente co apoio do centro de investigación. Así mesmo agradecer ó Ministerio de Economía, Industria y

Competitividad (MINECO) no tocante ós proxectos MAT2013-46593-C6-2-P e MAT2016-78293-C6-4-R, ó Departamento de Educación do Goberno Vasco polo proxecto IT-756-13 e ó centro de investigación colaborativa "Structure and Dynamics of Internal Interfaces" (SFB 1083) financiado pola axencia alemana de investigación (DFG).

Nun plano máis persoal non quixera esquecerme da Dra. Olalla Nieto Faza e o Dr. Carlos Silva López da Universidade de Vigo que foron os que dalgún xeito iniciaron esta aventura, animándome a vir ate tan lonxanas terras e facer realidade este proxecto. Grazas tamén a Euskadi e as súas xentes, en particular os veciños e veciñas de Igeldo e Andoain polo seu trato agarimoso e cordial e por deixarnos participar na cultura e tradicións que aquí se atesouran.

Un lugar aparte está reservado para a Casa de Galicia en Gipuzkoa por abrirme as súas portas, ás persoas que a fan posíbel e os seus mestres de infinda paciencia. A tódolos compañeiros e compañeiras de Trisquele, xa sempre seredes parte de min. Un recordo especial para tódolos que xa se foron, os que aínda están e ós que quedan por vir. Mil grazas e mil primaveras máis.

Finalmente a miña inconmensurábel gratitude para a familia e amigos que teño tan lonxe pero sinto tan preto. A todos vós, que me arroupades nas horas baixas e compartimos a ledicia das boas tempadas. Por ensinarme a gozar do sol, bailar debaixo da chuvia e camiñar ergueito no temporal. Especialmente os meus pais polo incondicional apoio ó longo dos anos. E a ti, Sânziana, compañeira de viaxe por compartir os meus soños e axudarme a acadalos.

En Donostia-San Sebastián, outono do 2018.

Antón X. Brión-Ríos.

Motivation

O verdadeiro heroísmo consiste en trocar os anceios en realidades, as ideias en feitos.

Alfonso Daniel Rodríguez Castelao,
Sempre en Galiza

The interaction between molecules and matter has important technological and industrial implications that make it a really interesting field [1–6]. Molecular adsorption is a fundamental issue due to its practical applications, as for example in catalytic reactions [7–9].

The aim of this Thesis is the study of molecular adsorption on different surfaces. The fact that a molecule is adsorbed on a surface can modify its electronic structure. The molecule can be chemically bond to the surface, the electronic charge be displaced, relocated or transferred between the adsorbate and adsorbent and the hybridization with the surface electronic states would rearrange the molecular density of states. Every single change would modify the properties of the studied system. Furthermore, the interaction between neighbours and the modifications in the electronic density on the substrate can affect to the self-assembly process on the surface.

The adsorption process is ruled by various aspects like van der Waals (vdW) forces, ionic or electrostatic interactions or geometrical factors to name but a few. The molecule adsorbed on the substrate could be strongly modified during the process, changing its electronic properties and creating a chemical bond with the surface (chemisorption). On the other hand, it could have a weaker interaction with a minimum distortion of the molecule (physisorption).

From the theoretical point of view the description of the many-body system could be done using the Schrödinger equation. Nevertheless, the main problem arises in the complexity of the many-body system that, if there are more than a few particles involved, cannot be solved exactly. For a system containing N electrons, any of them depending on 3 spatial coordinates and the spin coordinate, and N being from a few tens up to $\sim 10^{23}$ electrons, the Schrödinger

equation is impossible to solve. Therefore, it is necessary to find a practical approximation that would make the solution of the system feasible.

An alternative route was developed in the 60's based on the Hohenberg-Kohn theorems [10] and the Kohn-Sham [11] equations. The basic assumption consisted on using the electronic density distribution to describe the system instead of the many-electron wave function. In this approach lays the foundations of the density functional theory (DFT). The ground state density of the system is obtained and the physical properties of the system derived from it. DFT calculations were used to study solid state systems since the 70's. However, it was not until the 90's when the computational resources and the improvement in the approximations converted the DFT calculations in a versatile tool in condensed-matter physics. The increment in its accuracy permitted a correct description of the physical systems. This fact converted DFT in a popular methodology and the combination of first-principles calculations and experimental observation achieved excellent results.

Based on DFT and using the Vienna *ab initio* simulation package (VASP) developed by Kresse *et al.* [12] we have studied the adsorption of different molecules on metal surfaces, as well as the electronic and structural properties of several stepped surfaces. The research described in this Thesis is divided in the following chapters.

In **Chapter 1** we describe the theoretical foundations of our methodology. Starting from Schrödinger equation, the Born-Oppenheimer approximation is introduced. The next section contains the main principles of DFT and a description of the exchange-correlation functional approximations used in our research. The last part is dedicated to the periodic crystal theory, the pseudopotential approximation and the projected augmented wave methodology.

Our group studied the carbon monoxide (CO) adsorption on O(2x1)/Cu[110] in a previous research, finding the formation of long rows of CO molecules distributed evenly on this anisotropic substrate [13, 14]. Therefore, the starting point in **Chapter 2** was the theoretical study of nitrogen monoxide (NO) adsorption on Cu surfaces in order to explore the character of the interaction between NO molecules and the possibility to form extended structures also in the case of NO on O(2x1)/Cu[110] [15].

A large part of the Thesis was the result of a collaboration with different experimental groups. Therefore, our research intended to help in the interpretation of the results obtained by our collaborators. During these years we developed a fruitful collaboration with the group of Prof. P. Jakob at Philipps-Universtät in Marburg (Germany) [16] and the group of Prof. José Ignacio Pascual in nanoGUNE in Donostia-San Sebastián (Spain) [17] on several topics related to the adsorption of phthalocyanine molecules on Ag[111]. Thus, in **Chapter 3** an exhaustive investigation is presented on the adsorption of metal phthalocyanines (MePc, with Me=Cu, Ti-O, Mn and Mn-Cl) on Ag[111] [16, 17]. We find that the metal core of the MePc

affects to the properties of the molecule and also modifies the interaction with the surface. We investigate the molecular adsorption and the geometrical variations suffered by the molecule, the electronic density of states and the charge transfer in the system. The induced electronic density and dipole moments were also calculated. Using all the data we describe the main aspects of the MePc adsorption and the interaction with the metal substrate. As a continuation of this research, and with a view to comparing with our experimental observations [18], we studied the adsorption of carbon dioxide (CO_2) molecules on titanium phthalocyanine (TiOPc). The results shown in **Chapter 4** reveal the most plausible adsorption geometry. In addition, the theoretical results support the possibility of a multiple CO_2 molecular adsorption on TiOPc, as well as its fingerprint in the vibrational spectra as indicated by experiments, and disclose the bonding mechanism for the system.

The work described in **Chapter 5** focuses on the characterization of the electronic and structural properties of stepped surfaces of transition metals. In collaboration with the group of Prof. Enrique Ortega from the NanoPhysics Lab in the Centro de Física de Materiales (CFM) in Donostia-San Sebastián (Spain) and BihurCrystal company, which is dedicated to the production of curved crystals, we performed a systematic study of the surface core-level energy shift (CLS) in x-ray photoelectron spectroscopy (XPS) in [111] vicinal surfaces. The experimental measurements show a variation in the binding energies for the Pt 4f and Rh 3d levels on curved crystals which is related with the terrace size [19]. Trying to elucidate this behaviour we have run different calculations on stepped surfaces (Pt and Rh). Although the calculations reproduce the observed behaviours, the results overestimate the CLS. The calculations indicate that the main mechanism to explain the observed binding energy shift is the increase of the average surface strain with the miscut angle. In order to distangle this effect from others and to highlight the importance of strain, we explored the dependence of the CLS separately on the in-plane and on the out-of-plane strain of the surface layer using model systems. The results obtained with this so-called Terrace Compression Model (TCM) are able to account for the experimental results.

Building on this information, **Chapter 6** presents a theoretical and experimental study of the CO adsorption and XPS on a Pt[111] curved crystal. It was a daunting challenge due to the known difficulties of DFT to properly describe the most stable adsorption site of CO on flat Pt[111]. However, we succeeded to describe and understand the relative stability of adsorption at the step egdes and on the terraces of the vicinal surfaces, as well as its dependence on the step orientation. We also simulated the high CO coverage regime and our results allowed interpreting the experimental information. Finally, the CLS for the C 1s was investigated after adsorption on the stepped surfaces. Interestingly, our interpretation of the observed systematic variation of the C 1s binding energy as function of the miscut angle

for CO molecules adsorbed on the terrace indicates that this can be associated with a larger relief of the compression surface strain when CO molecules adsorb in smaller terraces.

Table of Contents

Chapter 1

Theory of Electronic Structure Calculations

Physics is like sex. Sure, it may give some practical results, but that's not why we do it.

Richard P. Feynman

1.1 Schrödinger equation

Matter is composed of atoms, which are formed by an ionic nucleus and electrons moving around it. Quantum chemistry tries to explain and predict the behaviour of atoms and molecules using the principles of the quantum mechanics. This is the basis of *ab initio* calculations. Any non-relativistic atomic system can be described by the time-dependent Schrödinger equation [20].

$$\hat{H}\psi(\mathbf{r_i},t) = i\hbar\frac{\mathrm{d}\psi(\mathbf{r_i},t)}{\mathrm{d}t} \tag{1.1}$$

However, in most of the cases related to atoms and molecules, we focus our attention on time-independent interactions. In this case we can define a time-conserved quantity, the energy E, such that the equation transforms into the time-independent Schrödinger equation. Thus, for an atomic system formed by $\mathbf{N}_e$ electrons, and $\mathbf{N}_n$ nucleus, the equation is:

$$\hat{H}\Phi = E\Phi \tag{1.2}$$

where $\hat{\mathrm{H}}$ is the non-relativistic hamiltonian operator of the system that can be written as:

$$\begin{aligned}\hat{H} =& -\sum_{i=1}^{N_e}\frac{1}{2}\nabla_i^2 - \sum_{A=1}^{N_n}\frac{1}{2M_A}\nabla_A^2 \\ &+\frac{1}{2}\sum_{i=1}^{N_e}\sum_{j\neq i}^{N_e}\frac{1}{|\mathbf{r_i}-\mathbf{r_j}|} - \sum_{i=1}^{N_e}\sum_{A=1}^{N_n}\frac{Z_A}{|\mathbf{r_i}-\mathbf{R_A}|} + \frac{1}{2}\sum_{A=1}^{N_n}\sum_{B\neq A}^{N_n}\frac{Z_A Z_B}{|\mathbf{R_A}-\mathbf{R_B}|} \\ =&\hat{T}_e + \hat{T}_n + \hat{V}_{ee} + \hat{V}_{en} + \hat{V}_{nn}\end{aligned} \tag{1.3}$$

We are assuming atomic units ($\hbar$ = m_e = e = $1/4\pi\varepsilon_0$ = 1), which permits to simplify the notation. $\mathbf{N}_e$ electrons with coordinate $\mathbf{r}_i$, $\mathbf{r}_j$ for the i-th and j-th electron respectively. $\mathbf{N}_n$ nucleus where the A-th (B-th) posses mass M_A, atomic charge Z_A and $\mathbf{R}_A$ coordinate. In **Eq. 1.3** $\hat{T}_e$ and $\hat{T}_n$ are the electron kinetic energy and the nuclear kinetic energy operators respectively, as well as, $\hat{V}_{ee}$, $\hat{V}_{en}$ and $\hat{V}_{nn}$ are the electron-electron, electron-nucleus and nucleus-nucleus Coulombic potentials.

For a system with a large number of electrons N_e and nuclei N_n, the Schrödinger equation can not be solved exactly. In order to tackle the problem, it is needed to simplify the system, so we can obtain an approximate solution that is sufficiently accurate but, simultaneously, numerically tractable.

1.2 Born-Oppenheimer approximation

The Born-Oppenheimer (BO) or adiabatic approximation [21] is a powerful tool to study accurately the electronic structure of a system composed of sufficiently heavy atoms. The BO approximation [21, 22] consists in assuming that the nucleus is infinitely heavier than the electrons (a proton is $\sim$ 1800 heavier than an electron). Thus, it can be considered that the electrons move around fixed nuclei. This permits to neglect the kinetic energy of the nuclei in **Eq. 1.3** and consider the repulsion between them constant. The electronic hamiltonian describing the $\mathbf{N}_e$ electrons in a fixed field created by $\mathbf{N}_n$ nuclei is :

$$\hat{H}_{elec} = -\sum_{i=1}^{N_e}\frac{1}{2}\nabla_i^2 + \frac{1}{2}\sum_{i=1}^{N_e}\sum_{j\neq i}^{N_e}\frac{1}{|\mathbf{r_i}-\mathbf{r_j}|} - \sum_{i=1}^{N_e}\sum_{A=1}^{N_n}\frac{Z_A}{|\mathbf{r_i}-\mathbf{R_A}|} \tag{1.4}$$

Solving the Schrödinger equation for the electronic hamiltonian,

$$\hat{H}_{elec}\Phi_{elec} = \varepsilon_{elec}\Phi_{elec} \tag{1.5}$$

we obtain the electronic wave function which describes the motion of the electrons for a fixed atomic system.

$$\Phi^n_{elec} = \Phi^n_{elec}(r_i, \{R_A\}) \tag{1.6}$$

The superscript n is a reminder of the multiple solutions to the Schrödinger equation. This electronic wavefunction not only depends on the electronic coordinates explicitly, but also parametrically on the nuclear coordinates, as does the electronic energy.

$$\varepsilon^n_{elec} = \varepsilon^n_{elec}(\{R_A\}) \tag{1.7}$$

Then, for any fixed nuclear arrangement, Φ^n_{elec} is a different function of the electrons' coordinates. The total energy must include the nuclear repulsion between the nuclei.

$$\varepsilon^n_{tot} = \varepsilon^n_{elec}(R_A) + \frac{1}{2}\sum_{A=1}^{N_n}\sum_{B\neq A}^{N_n}\frac{Z_A Z_B}{|\mathbf{R_A} - \mathbf{R_B}|} \tag{1.8}$$

Similarly, we can solve the Schrödinger equation for the nuclei. As the nuclei are much slower than electrons, in this case we can substitute the functions that depend on the electron coordinates by their expected value in the electronic state described by the solutions of **Eq. 1.7**. Then, the nuclear hamiltonian for the system in the average electronic field is :

$$\begin{aligned}
\hat{H} =& -\sum_{A=1}^{N_n}\frac{1}{2M_A}\nabla^2_A + \frac{1}{2}\sum_{A=1}^{N_n}\sum_{B\neq A}^{N_n}\frac{Z_A Z_B}{|\mathbf{R_A} - \mathbf{R_B}|} \\
&\left\langle -\sum_{i=1}^{N_e}\frac{1}{2}\nabla^2_i + \frac{1}{2}\sum_{i=1}^{N_e}\sum_{j\neq i}^{N_e}\frac{1}{|\mathbf{r_i} - \mathbf{r_j}|} - \sum_{i=1}^{N_e}\sum_{A=1}^{N_n}\frac{Z_A}{|\mathbf{r_i} - \mathbf{R_A}|}\right\rangle_n \\
=& -\sum_{A=1}^{N_n}\frac{1}{2M_A}\nabla^2_A + \frac{1}{2}\sum_{A=1}^{N_n}\sum_{B\neq A}^{N_n}\frac{Z_A Z_B}{|\mathbf{R_A} - \mathbf{R_B}|} + \varepsilon^n_{elec}(\{R_A\}) \\
=& -\sum_{A=1}^{N_n}\frac{1}{2M_A}\nabla^2_A + \varepsilon^n_{tot}(\{R_A\})
\end{aligned} \tag{1.9}$$

Thereby, the nuclei move on an effective potential energy surface defined by the energy of a given electronic state n, most frequently taken as the ground state. The solution to the nuclear Schrödinger equation

$$\hat{H}_{nucl}\Phi_{nucl} = \varepsilon_{nucl}\Phi_{nucl} \tag{1.10}$$

describes the vibration, rotation and translation of a system.

$$\Phi^n_{nucl} = \Phi^n_{nucl}(R_A) \tag{1.11}$$

Thus, within the BO approximation we can describe the solutions of the full Schrödinger equation as:

$$\Phi^n(r_i, R_A) = \Phi^n_{elec}(r_i, R_A) \times \Phi^n_{nucl}(R_A) \tag{1.12}$$

This permits to estimate the total energy of the complete system, including electronic, vibrational, rotational and translational energies. The initial unsolvable Schrödinger equation was changed into an electronic system moving on a potential created by the frozen nuclei. Providing an affordable approximation to solve the system by decoupling the movements of electrons and nuclei.

In this Thesis we did not only use the BO approximation, but we took an additional drastic approximation that, however, it is known to provide good results for sufficiently heavy atoms. We have considered all nuclei as classical particles with well-defined positions and velocities, and treated them like that to perform relaxations to find the equilibrium configuration of adsorbed molecules on metal surfaces and other related systems. This approximation is once more justified by the large mass of the nuclei and it is a standard approximation in quantum chemistry and solid state physics.

1.3 Density Functional Theory

The Density Functional Theory (DFT) is an alternative method to calculate the ground state energy for many-electron systems. It differs from the conventional *ab initio* methods due to its use of the electronic density as the central quantity that completely determines the ground state of the system [23, 24]. This is contrast to quantum chemistry methods that use the many-electron wavefunction as the central quantity. Thus, DFT constitutes a drastic simplification from a computational point of view.

The solutions of the many-body Schrödinger equation depend on $3N_e$ degrees of freedom for N_e electrons. However, in DFT any property depends on the ground state density $n_0(\mathbf{r})$. This simplifies the N_e electrons problem into a one-particle equation describing the motion of individual electrons on an effective external potential. Thus, the initial problem of $3N_e$ degrees of freedom has changed to solve a system which depends only on three spatial coordinates plus an additional degree of freedom to describe the electron spin [25–29].

The original idea came from Thomas-Fermi theory [30, 31]. These authors proposed a simple functional to compute the ground state energy using solely the density $n(\mathbf{r})$ as an input.

In order to do so, it is necessary to have functionals to compute each energy component. They proposed to use a simple approximation for the kinetic energy using the result for the homogeneous electron gas to express the kinetic energy density in each point. Nevertheless, they did not consider the exchange and correlation contribution to the energy among electrons that was introduced later by Dirac [32–34]. The Thomas-Fermi-Dirac theory is a rough approximation that provides general qualitative trends but fails in describing the atomic systems or molecular interactions [35].

1.3.1 The Hohenberg-Kohn theorems

It was not until 1964 that density functional theory acquired a formal basis with the publication of Hohenberg-Kohn (HK) theorems [10]. They probed that the exact solution for the ground state of a many-body interacting system can be achieved using the electronic density, rather than the many-electron wavefunction, as the only variable. This paved the way for the initial steps of the DFT, providing a powerful tool to obtain the atomic or molecular properties and describe the atomic interactions.

For a system of N_e electrons interacting in an external potential $V_{ext}(\mathbf{r})$, with fixed nuclei, the hamiltonian can be written as :

$$\begin{aligned}\hat{H} &= -\sum_{i=1}^{N_e}\frac{1}{2}\nabla_i^2 + \frac{1}{2}\sum_{i=1}^{N_e}\sum_{j\neq i}^{N_e}\frac{1}{|\mathbf{r_i}-\mathbf{r_j}|} + \sum_{i=1}^{N_e}V_{ext}(\mathbf{r_i}) \\ &= \hat{T} + \hat{V}_{ee} + \sum_{i=1}^{N_e}V_{ext}(\mathbf{r_i})\end{aligned} \tag{1.13}$$

where $\hat{T}$ and $\hat{V}_{ee}$ are the kinetic and Coulomb repulsion operators respectively.

The HK theorems can be summarized as:

Theorem I: For a system of interacting particles in an external potential $V_{ext}(\mathbf{r})$, the potential $V_{ext}(\mathbf{r})$ is determined uniquely, except for a constant, by the ground state particle density $n_0(\mathbf{r})$ [25].

Theorem II: For a given external potential $V_{ext}(\mathbf{r})$, the non-degenerate ground state density can be found exactly from a variational principle which involves only the density. The ground state energy can be written as a functional of the density as:

$$E_0 \leq E_{v_{ext}}[n] = F^{HK}[n] + \int V_{ext}(\mathbf{r})n(\mathbf{r})d\mathbf{r} \tag{1.14}$$

where the HK functional $F^{HK}[n]$ is an universal functional in the sense that it is the same functional for any number of particles and any external potential $V_{ext}(\mathbf{r})$.

$$F^{HK}[n] = \hat{T}[n] + \hat{V}_{ee} = \hat{T}[n] + \hat{J}[n] + nonclassical\ terms \tag{1.15}$$

where $\hat{T}[n]$ is the kinetic energy, and $\hat{J}[n]$ is the classical electron electron repulsion both expressed as a function of the density. These theorems were extended by Levy and Lieb for the degenerate ground state case [36, 37].

1.3.2 The Kohn-Sham equations

Kohn and Sham (KS) [11] proposed an approach to obtain the ground state density of the system. Applying the HK formalism, they obtained a set of self-consistent equations which permits to compute the ground state density. These set of equations are analogous to the conventional Hartree-Fock equations.

Their assumption is based on the idea that the ground state density of the many-body interacting system can be represented by an auxiliary system of non-interacting particles [23, 25, 26], *i. e.*:

$$n(\mathbf{r}) = \sum_{i=1}^{N_e} |\psi_i(\mathbf{r})|^2 \tag{1.16}$$

where $\psi_i(\mathbf{r})$ are one-electron wavefunctions usually called Kohn-Sham orbitals. These independent particles move in an effective local potential $V_{eff}(\mathbf{r})$ that differs from the original external potential.

We can rewrite the energy of the system as:

$$E_{KS}[n] = \hat{T}_s[n] + \int V_{ext}(\mathbf{r}) n(\mathbf{r}) d\mathbf{r} + \frac{1}{2} \int\int \frac{n(\mathbf{r}) n(\mathbf{r}')}{|\mathbf{r} - \mathbf{r}'|} d\mathbf{r} d\mathbf{r}' + E_{xc}[n] \tag{1.17}$$

Where $\hat{T}_s[n]$ is the kinetic energy of a non-interacting electron system, $V_{ext}(\mathbf{r})$ is the external potential. The next term is $\hat{J}[n]$, the classical Coulomb interaction energy of the electron density (Hartree energy) interacting with itself and $E_{xc}[n]$ is the exchange-correlation (XC) energy. It contains the difference between $\hat{T}[n]$ and $\hat{T}_s[n]$ and the non classical part of $\hat{V}_{ee}[n]$.

Minimising the energy functional in **Eq. 1.17** with respect to the density $n(\mathbf{r})$, the Euler-Lagrange equation is:

$$\delta E_{KS}[n] = \int \delta n(\mathbf{r}) \{ V_{eff}(\mathbf{r}) + \frac{\delta \hat{T}_s[n]}{\delta n(\mathbf{r})} - \mu \} d\mathbf{r} = 0 \tag{1.18}$$

μ is the Lagrange multiplier associated with the constrain that the orbitals must be orthonormal $\langle\psi_i|\psi_j\rangle = \delta_{i,j}$ which implies that n[r] stays normalized $\int n(\mathbf{r})d\mathbf{r} = N$.

Eq. 1.18 leads to a Schrödinger-like equation, usually called Kohn-Sham equation:

$$\hat{H}_{eff}\psi_i(\mathbf{r}) = [-\frac{1}{2}\nabla^2 + V_{eff}(\mathbf{r})]\psi_i(\mathbf{r}) = \varepsilon_i\psi_i(\mathbf{r}) \tag{1.19}$$

Thus, we describe the system of particles moving in a effective external potential, this potential $V_{eff}(\mathbf{r})$ is defined as :

$$V_{eff}(\mathbf{r}) = V_{ext}(\mathbf{r}) + \frac{\delta\hat{J}[n]}{\delta n(\mathbf{r})} + \frac{\delta E_{xc}[n]}{\delta n(\mathbf{r})} = V_{ext}(\mathbf{r}) + \int\frac{n(\mathbf{r}')}{|\mathbf{r}-\mathbf{r}'|}d\mathbf{r}' + V_{xc}(\mathbf{r}) \tag{1.20}$$

where $V_{xc}(\mathbf{r})$ is the local exchange-correlation potential, which depends on the electronic density. From **Eq. 1.19** a set of energies ε_i and orbitals ψ_i are obtained, we can calculate the ground state electronic density using the lowest energy KS orbitals.

The total energy of the system is determined with:

$$\begin{aligned} E &= \sum_i^N \varepsilon_i - \frac{1}{2}\int\int\frac{n(\mathbf{r})n(\mathbf{r}')}{|\mathbf{r}-\mathbf{r}'|}d\mathbf{r}d\mathbf{r}' + E_{xc}[n] - \int V_{xc}(\mathbf{r})n(\mathbf{r})dr \\ \sum_i^N \varepsilon_i &= \sum_i^N \langle\psi_i| - \frac{1}{2}\nabla^2 + V_{eff}(\mathbf{r})|\psi_i\rangle \end{aligned} \tag{1.21}$$

The KS equations simplify the many-body system to a set of equations for each electron interacting with an external effective potential $V_{eff}(\mathbf{r})$. Since the effective potential depends on the density the solution must be obtained self-consistently and we have a set of N_e coupled equations. The procedure is schematically explained on **Figure 1.1**.

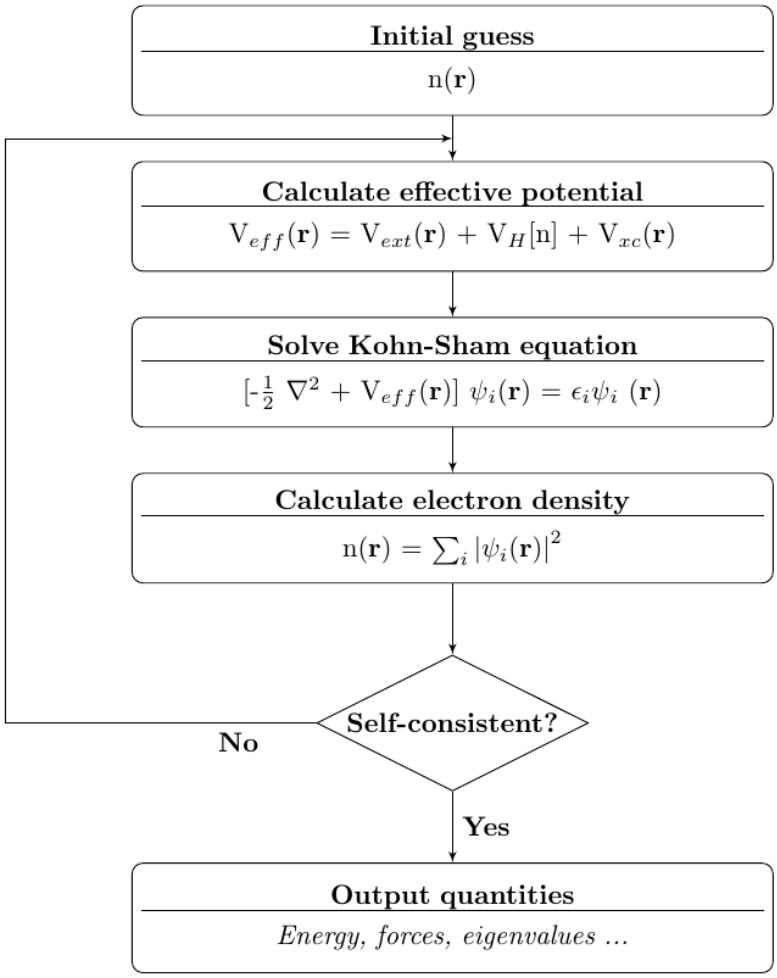

Fig. 1.1 Schematic representation of the self-consistent loop for solution of Kohn-Sham equations [25].

The KS theory, which in principle is exact, depends on the XC term that is only approximately known. Therefore, the precision of the result depends on the $V_{xc}(\mathbf{r})$ approximation that is employed in the calculation.

1.3.3 Exchange-Correlation approximations

The discussion above shows that a suitable approximation to the E_{xc}[n] functional is the key ingredient for an accurate description of the ground state on an arbitrary system. The E_{xc}[n] functional and the $V_{xc}(\mathbf{r})$ potential are unknown. It is necessary an approximation in order to obtain the electronic density. We focus our attention on the Local Density Approximation (LDA) and the Generalized Gradient Approximations (GGA) which are the most relevant for our purposes.

1.3.3.a Local Density Approximation

The Local Density Approximation (LDA) was proposed by Kohn and Sham [11]. It is the simplest approximation for the exchange-correlation energy. This approximation uses the results of the exchange-correlation energy from the uniform electron gas. The exchange-correlation effects are assumed to be local and depend only on the value of the electronic density at each point. If n($\mathbf{r}$) is sufficiently slowly varying this should be a reasonable approximation. The XC energy is defined as:

$$E_{xc}^{LDA}[n] = \int n(\mathbf{r})\varepsilon_{xc}^{hom}(n(\mathbf{r}))d\mathbf{r} \tag{1.22}$$

where the $\varepsilon_{xc}^{hom}(n)$ is the XC energy per particle of a uniform electron gas density n. The function $\varepsilon_{xc}^{hom}(n)$ can be separated in two different parts, the exchange and the correlation contributions.

$$\varepsilon_{xc}^{hom}(n) = \varepsilon_x(n) + \varepsilon_c(n) \tag{1.23}$$

The exchange part, that was derived by Dirac and Bloch [38, 39] originally, could be expressed in atomic units as [40]:

$$\varepsilon_x(n) = -\frac{0.458}{r_s} \tag{1.24}$$

where r_s is the radius of a sphere containing one electron given by

$$r_s = \left(\frac{3}{4\pi n}\right)^{\frac{1}{3}} \tag{1.25}$$

On the other hand, it does not exist any simple prescription for the correlation contribution, it can not be calculated in an analytic form. It was estimated by Wigner[41] for the first time. Highly accurate quantum Monte-Carlo calculations for the correlation energies were done by

Ceperley and Alder [42, 43]. Since then, different interpolation schemes have been proposed to date in order to obtain an analytical expression of the correlation energy. This is the case of the widely used functionals of Perdew *et al.* [44] and Vosko *et al.* [45].

The LDA approach works relatively well if the electronic density presents a slow variation. For this reason, it describes better solids and condensed systems rather than isolated atoms or small molecules. Although it does not give accurate energy results, however, the bond lengths of molecules and solids are usually surprisingly well described, with an accuracy of ~ 1 % [46].

1.3.3.b Local Spin Density Approximation

An extension of LDA is necessary to calculate spin-polarised electronic systems. In the Local Spin Density Approximation (LSDA), the electronic density n($\mathbf{r}$) is considered as the sum of spin up (α) and spin down (β) densities[47]:

$$n(\mathbf{r}) = n^{\alpha}(\mathbf{r}) + n^{\beta}(\mathbf{r}) \tag{1.26}$$

Thus, the exchange-correlation energy is the integral over all space of the XC energy (per particle) of a homogeneous electron gas with a spin-polarised density [25, 23].

$$E_{xc}^{LSDA}[n^{\alpha}, n^{\beta}] = \int n(\mathbf{r})[\varepsilon_x^{hom}(n^{\alpha}(\mathbf{r}), n^{\beta}(\mathbf{r})) + \varepsilon_c^{hom}(n^{\alpha}(\mathbf{r}), n^{\beta}(\mathbf{r}))]d\mathbf{r} \tag{1.27}$$

LSDA can be defined using $n^{\alpha}(\mathbf{r})$ and $n^{\beta}(\mathbf{r})$ spin densities or with the total density n($\mathbf{r}$) and fractional spin polarisation, defined as:

$$\zeta(\mathbf{r}) = \frac{n^{\alpha}(\mathbf{r}) - n^{\beta}(\mathbf{r})}{n(\mathbf{r})} \tag{1.28}$$

where $\zeta(\mathbf{r})$ vary from 0 (spin compensated) to 1 (fully spin polarised).

In a closed-shell system, $n^{\alpha}(\mathbf{r})$ coincide with $n^{\beta}(\mathbf{r})$. So, in this system the LDA density can be found easily by setting $n^{\alpha}(\mathbf{r}) = n^{\beta}(\mathbf{r}) = \frac{1}{2}n(\mathbf{r})$. In the case of a spin-polarised system, where there is nonvanishing spin polarization, the correct method consist in solving the coupled equations for α and β.

1.3.3.c Generalized Gradient Approximation

The next step consists in introducing the dependence on the density gradient in the exchange correlation energy [11]. With the inclusion of the density gradient in the XC term,

in addition to use the density value, it is possible to include the description of the density change around each point. It was in the early eighties when the first successful extensions of the local approximation were developed. Until that moment, the DFT was mostly employed in solid-state physics and it had smaller impact in computational chemistry. The initial versions of the gradient expansion presented some issues since they violated several sum rules and other relevant conditions [48, 49]. The reason is that the gradient expansion for the correlated hole is only a truncated expansion. These issues were solved including some constraints, modifying the functional behaviour at large gradients in order to preserve the desired properties. The functionals that respect these conditions are known as generalized gradient approximations (GGA). Thus, the GGA XC energy is a semi-local functional that takes into account the non-homogeneity of the electron density in an approximate way [50, 47].

$$E_{xc}^{GGA}[n^{\alpha},n^{\beta}] = \int f(n^{\alpha},n^{\beta},\nabla n^{\alpha},\nabla n^{\beta})d\mathbf{r} \tag{1.29}$$

It is necessary to obtain an analytic expresion for the $f(n^{\alpha},n^{\beta},\nabla n^{\alpha},\nabla n^{\beta})$ function and different approximations had been proposed [51–55]. Most of these functionals include empirical parameters, which are calibrated against reference values rather than being derived from first principles [47]. As in LDA, the E_{xc} functional is usually separated in two terms $E_{xc}^{GGA} = E_{x}^{GGA} + E_{c}^{GGA}$ and approximantions are sought independently.

We will focus our attention on the functionals that we used in our research. They are the Perdew-Burke-Erzenhof (PBE) [55] and the Becke 86 (B86b) [51].

In the widely used functional PBE [55] the correlation term is defined as :

$$E_{c}^{GGA}[n^{\alpha},n^{\beta}] = \int n[\varepsilon_{c}^{hom}(r_s,\zeta) + H(r_s,\zeta,t)]d\mathbf{r} \tag{1.30}$$

where r_s is the local Seitz radius define in **Eq. 1.25**, $\zeta(\mathbf{r})$ the relative spin polarization and $t = \frac{|\nabla n|}{2\phi k_s n}$ is a dimensionless density gradient. Here, $\phi(\zeta) = [(1+\zeta)^{2/3} + (1-\zeta)^{2/3}]/2$ is a spin factor and $k_s = \sqrt{4K_F/\pi}$ is the Thomas-Fermi screening wave number. Thus, the gradient contribution H(r_s, ζ,t) is:

$$H(r_s,\zeta,t) = \gamma\phi^3 ln\left\{1 + \frac{\beta}{\gamma}t^2\left[\frac{1+At^2}{1+At^2+A^2t^4}\right]\right\} \tag{1.31}$$

where

$$A = \frac{\beta}{\gamma}\left[exp\left\{\frac{-\varepsilon_{c}^{hom}}{\gamma\phi^3}\right\} - 1\right]^{-1} \tag{1.32}$$

with $\beta = 0.66725$ and $\gamma = 0.031091$.

The exchange energy is calculated as :

$$E_x^{GGA}[n_\alpha, n_\beta] = \int n(\mathbf{r})\varepsilon_x^{hom}(n)F_x(r_s,\zeta,s)]d\mathbf{r} \tag{1.33}$$

where $\varepsilon_x^{hom}(n)$ is the exchange energy defined in **Eq. 1.24** and $F_x(r_s,\zeta,s)$ is the spin-polarised enhancement factor.

$$F_x(r_s,\zeta,s) = 1 + \kappa - \frac{\kappa}{1+\mu s^2+\kappa} \tag{1.34}$$

with $\kappa = 0.804$ and $\mu = 0.21915$. The factor s is a measure of inhomogeneity [50], another dimensionless gradient defined as:

$$s = \frac{|\nabla n|}{2k_F n} \tag{1.35}$$

On the other hand, the functional B86b developed by Becke [51] fitted the exchange energies of the atoms using a few parameters. So, the exchange term is defined as:

$$\begin{aligned} E_x^{GGA}[n] = E_x^{LDA} & \\ & -\beta \int \frac{(\nabla n^\alpha)^2}{(n^\alpha)^{4/3}} \left[1+\gamma\frac{(\nabla n^\alpha)^2}{(n^\alpha)^{8/3}}\right]^{-4/5} d\mathbf{r} \\ & -\beta \int \frac{(\nabla n^\beta)^2}{(n^\beta)^{4/3}} \left[1+\gamma\frac{(\nabla n^\beta)^2}{(n^\beta)^{8/3}}\right]^{-4/5} d\mathbf{r} \end{aligned} \tag{1.36}$$

where the parameters $\beta = 0.00375$ and $\gamma = 0.007$

GGA functionals represents an improvement in most of the cases with respect to the previous method. Reasonable geometries and energies are obtained in general, however, they still fail to describe van der Waals interactions.

1.3.4 van der Waals approximations

In the study of the interaction between molecules or molecules with surfaces, the inclusion of van der Waals (vdW) forces is a fundamental ingredient. The vdW interactions act at long range and they are mostly attractive. They play an important role in some phenomena such as physisorption, adhesion or surface tension.

In order to obtain a correct description of the interaction between atoms it is necessary to take into account the fluctuating dipolar interaction between them. Strictly speaking they cannot be represented as a sum of pair interactions, as they are affected by the presence of other bodies nearby. Still, they have been frequently approximated by additive pair contributions. This is partially justified by its very rapid decay with distance ($\sim \frac{1}{r^6}$). Although vdW forces are extremely weak, they are important to obtain an accurate description of solid systems [56, 57]. With a view to addressing this issue, corrections to simulate these forces and describe the correct behaviour of the systems are added to the method. The most direct way to deal with the vdW forces in DFT is introducing a dispersion correction in the usual KS energy.

$$E_{DFT} = E_{KS} + E_D \tag{1.37}$$

In our research we used two different approximations. The first method is the non-local van der Waals density functional (vdW-DF) approximation [58–61]. It was applied using the optimized Becke 86 functional (OptB86b-vdW) where exchange-correlation energy is corrected by adding the vdW-DF non-local correlation.

$$E_{xc} = E_x^{GGA} + E_c^{LDA} + E_c^{nl} \tag{1.38}$$

E_x^{GGA} is the exchange energy, E_c^{LDA} is the local energy correlation obtained with the LDA method and E_c^{nl} is the non-local correlation energy. The exchange energy is defined generally in **Eq. 1.33**. In this case, the enhancement factor is:

$$F_x^{OptB86b} = 1 + \frac{\mu s^2}{(1+\mu s^2)^{4/5}} \tag{1.39}$$

Where s is the reduced density gradient (**Eq. 1.35**) and $\mu = 0.1234$.

The E_c^{nl} is obtained from the electron densities interacting via a model response function proposed by Vydrov *et. al.* [62]. In the limit of large distances, for two interacting molecules A and B at a distance R_{AB} this interaction behaves as:

$$E_c^{nl} = -\sum_{A,B} \frac{C_6^{AB}}{R_{AB}^6} \tag{1.40}$$

where C_6^{AB} is the dispersion coefficient.

The second method applied was the van der Waals D3 (vdW-D3) method developed by Grimme *et. al.* [63, 64]. This procedure leads to good results in large systems with a low-cost computational effort. In this case, the dispersion correction is defined as a sum of two- and

three-body energies.

$$E_D = E^{(2)} + E^{(3)} \tag{1.41}$$

$E^{(2)}$ is the two-body contribution to the dispersion energy and it adds the major contribution ($\sim$ 90-95 %). It is expressed as:

$$E^{(2)} = -\sum_{A,B}\sum_{n=6,8,10,\ldots} s_n \frac{C_n^{AB}}{R_{AB}^n} f_{d,n}(R_{AB}) \tag{1.42}$$

where C_n^{AB} is the averaged nth-order dispersion coefficient for an atomic pair AB, R_{AB} is their internuclear distance and s_n is scaling factor. The other term, $f_{d,n}$, is the damping function which determines the range of the dispersion correction.

$$f_{d,n}(R_{AB}) = \frac{1}{1+6(R_{AB}/(s_{R,n}R_0^{AB}))^{-\alpha_n}} \tag{1.43}$$

$s_{R,n}$ is the n-th order-dependent scaling factor of the cutoff radii R_0^{AB} and α_n are the steepness parameters.

The third-body dispersion term E^{ABC} is derived from third-order perturbation theory for three atoms A B C as :

$$E^{ABC} = \frac{C_9^{ABC}(3cos\theta_a cos\theta_b cos\theta_c + 1)}{(R_{AB}R_{BC}R_{CA})^3} \tag{1.44}$$

where $cos\theta_a$,$cos\theta_b$ and $cos\theta_c$ are the internal angles of the triangle formed by R_{AB}, R_{BC} and R_{CA} and C_9^{ABC} is the triple-dipole constant, which can be reasonably approximated to $C_9^{ABC} \sim \sqrt{C_6^{AB}C_6^{BC}C_6^{CA}}$. Using this simplifications finally we can obtain the nonadditive energy contribution for the third-body dispersion part.

$$E^{(3)} = \sum_{ABC} f_{d,(3)}(\bar{r}_{ABC})E^{ABC} \tag{1.45}$$

where the damping function was defined in **Eq. 1.43** with α=16, s_r=4/3 and $\bar{r}_{ABC}$ is the geometrically averaged radii.

Calculations using ab initio DFT-vdW functionals like the OptB86b-vdW were computationally very demanding until recently. However, applying the numerical approximation described in Ref. [59] the overhead paid to include the highly non-local vdW interactions is marginal and it has become the standard algorithm.

Both methods, vdW-DF and vdW-D3, permit to take in account the contribution of the van der Waals forces between the atoms in the systems. They showed accurate results [61, 63] with a reasonable computational cost on large systems.

1.3.5 Core-Level Energy Shift

X-ray photoelectron spectroscopy (XPS) is an experimental technique widely used in the study of solid surfaces since its introduction in the 50's [65]. It has been extensively applied for surface characterization in heterogeneous catalysis [66, 67] or determining the electronic, chemical and geometrical properties of adsorbed molecules on surfaces [68–73]. XPS is usually applied in ultra high vacuum. High-energy photons excite inner electrons from the core that are ejected towards vacuum. The kinetic energy of those electrons is measured, from which their binding energies (BEs) can be deduced. The BE is the energy needed to pull out the electron from the atom. For a given chemical species and a given electronic shell, the BE depends on the chemical environment of the atom and the screening properties of its surroundings. Therefore, *e.g.*, between an atom in the topmost surface layer and other in the bulk there is a variation of the BE. Such variation is known as the core-level energy shift (CLS).

DFT permits to simulate the process and obtain the CLS. These calculations are a valuable method with a view to interpreting the experimental observations. There are different approximations in order to simulate the CLS [74–81].

In the initial state approximation (IS) the variation of the CLS is associated with the variation of the electrostatic potential that atoms with different local environment are subject to. The core electron is removed without changing the potential, *i.e.*, maintaining the rest of the electrons frozen Thus, the electronic screening of the core hole is neglected [78, 81, 82].

In the IS the CLS is obtained as the variation on the orbital eigenenergies for a particular Khon-Sham core state.

$$CLS_{IS} = -[\varepsilon_c^a(n_c) - \varepsilon_c^b(n_c)] \tag{1.46}$$

where $\varepsilon_c^i(n_c)$ is the eigenvalue for the core state c in the atom i = a, b.

In the transition state approximation (TS) the screening effects due to the core hole created in the atom are considered. Slater-Janak transition state model [83, 84] introduces an extension in the standard DFT redefining the charge density.

$$n(\mathbf{r}) = \sum_{i=1}^{N_e} \eta_i \, |\psi_i(\mathbf{r})|^2 \tag{1.47}$$

where η_i is an occupation number for the state i ($0 < \eta_i < 1$). It would permit to solve the Kohn-Sham equation self-consistently for a non-integral occupation. The modification in the occupation number produces a different total energy functional $\tilde{E}$. In general $\tilde{E} \neq E$, however, if the η_i follows a Fermi-Dirac distribution $\tilde{E}$ will be equal to E [74, 76, 77].

The Janak's theorem [84] states that:

$$\frac{\partial \tilde{E}}{\partial \eta_i} = \varepsilon_i \tag{1.48}$$

independently of the detailed form of the exchange-correlation functional.

Thus, integrating the **Eq. 1.48** it is possible to connect the ground state of a N electron system with the N+1 electron system by inserting η_i electrons in the valence level i.

$$E_{N+1} - E_N = \int_0^1 \varepsilon_i(\eta_i) d\eta_i \tag{1.49}$$

Assuming that the eigenvalue ε is a linear function of the occupation number η_i, the BE can be obtained as:

$$BE_{TS} = \int_0^1 \varepsilon_i(\eta_i) d\eta_i \sim \varepsilon_i(1/2) \sim \varepsilon_i(0) + \frac{1}{2}[\varepsilon_i(1) - \varepsilon_i(0)] \tag{1.50}$$

which contains the inital and final state contributions to the BE.

Thus, the CLS can be determined as:

$$CLS_{TS} = -[\varepsilon_c^a(n_c - 1/2) - \varepsilon_c^b(n_c - 1/2)] \tag{1.51}$$

where $\varepsilon_c^i(n_c - 1/2)$ are the Kohn-Sham eigenvalues of a particular core state of the *i* atom with half electron promoted to the valence band.

The final state approximation (FS) takes into consideration both contributions, the initial state part before the excitation of the core electron and final state part due to the screening of the core hole created in the atom after removing the core electron [76, 78, 79, 82, 85, 86].

The BE is obtained from the total energy variation in two different calculations. The first one is a standard calculation where the system is in the ground state (E(n_c,n_v)). In the second calculation a core electron is removed from a particular atom. The electron is added to the lowest unoccupied valence state creating an excited system (E($n_c - 1$, $n_v + 1$)) but keeping the charge neutrality. In principle, this procedure should work better for metals, where the screening guarantees a rapid convergence of the calculation with the supercell size. The BE is calculated as:

$$BE_{FS} = E(n_c - 1, n_v + 1) - E(n_c, n_v) \tag{1.52}$$

where E($n_c - 1$,$n_v + 1$) and E(n_c, n_v) are the total energies for the excited and ground state calculations respectively.

We are assuming that the core hole is always localized at the excited atom. The valence electrons are allowed to relax after the core electron excitation, however, the core electrons are kept frozen in the Vienna *ab initio* simulation package (VASP) implementation that we have used in this Thesis [12, 87–89]. Thus, when the projected augmented wave potential is generated, only the valence electrons contribute to the screening effect and the core electrons are not taken into consideration.

Therefore, the CLS can be obtained as the difference in the BE.

$$CLS_{FS} = \Delta BE = [E_a(n_c - 1, n_v + 1) - E_a(n_c, n_v)] - [E_b(n_c - 1, n_v + 1) - E_b(n_c, n_v)] \quad (1.53)$$

where a and b represent two atoms of the same species with different local environments.

1.4 Periodic crystal

The main characteristic in a solid crystal is the ordered position of the atoms in any direction. This permits to describe a crystal as a periodic repetition of an atomic cell in space. This periodicity is described by the Bravais lattice and a basis (single atoms, groups of atoms, molecules, etc.). The Bravais lattice defines the geometry of the periodic structure.

$$\mathbf{R} = n_1\mathbf{a_1} + n_2\mathbf{a_2} + n_3\mathbf{a_3} \quad (1.54)$$

where $\mathbf{a}_i$ i = 1, 3 are the primitive vectors in the Bravais lattice and define the Wigner-Seitz cell of the crystal and n_i are integral values. From the primitive vectors in real space one can obtain the reciprocal lattice that satisfied $\mathbf{b}_i \cdot \mathbf{a}_j = 2\,\pi\delta_{ij}$. The Bravais lattice in the reciprocal space is :

$$\mathbf{G} = m_1\mathbf{b_1} + m_2\mathbf{b_2} + m_3\mathbf{b_3} \quad (1.55)$$

where m_i are integers and the $\mathbf{b}_i$ i=1,3 are the primitive vectors in the reciprocal space. They define the first Brillouin zone (FBZ) which is equivalent to the Wigner-Seitz primitive cell but in reciprocal space.

Bloch's theorem established that the eigenstates of one electron moving in a periodic potential can be described as the product of plane waves and a function with the periodicity of the Bravais lattice.

$$\psi_{n\mathbf{k}}(\mathbf{r}) = u_{n\mathbf{k}}(\mathbf{r})exp[i\mathbf{k}\cdot\mathbf{r}] \quad (1.56)$$

where $u_{n\mathbf{k}}(\mathbf{r}) = u_{n\mathbf{k}}\ (\mathbf{r} + \mathbf{R})$ is the periodic part of the function. Applying the Born-Von Karman boundary conditions to the $\psi_{n\mathbf{k}}(\mathbf{r})$ function implies that the wave vector $\mathbf{k}$ can

always be chosen within the FBZ. The number of wave vectors in a primitive cell of the reciprocal lattice is limited by the total number (N) of unit cells in the crystal [57].

Due to the crystal structure, we can expand the periodic function in the reciprocal space as a Fourier series:

$$u_{n,\mathbf{k}} = \frac{1}{\sqrt{\Omega_{cell}}} \sum_m C_{n,m}(\mathbf{k}) exp[i\mathbf{G_m} \cdot \mathbf{r}] \tag{1.57}$$

Ω_{cell} is the crystal cell volume, $C_{n,m}$ are the expansion coefficients of the wavefunctions in the orthonormal plane waves basis for each n band at k-point **k**.

Thus, it is possible to define the Kohn-Sham eigenfunctions as:

$$|\psi_{n\mathbf{k}}(\mathbf{r})\rangle = \frac{1}{\sqrt{\Omega}} \sum_m C_{n,m}(\mathbf{k}) exp[(i(\mathbf{k}+\mathbf{G_m}) \cdot \mathbf{r}] \equiv \sum_{\mathbf{q}} C_{n,\mathbf{q}}(\mathbf{k}) |\mathbf{q}\rangle \tag{1.58}$$

Where $\mathbf{q} = \mathbf{k}+\mathbf{G}_m$ and $\frac{1}{\sqrt{\Omega}}$ is a normalization constant. The Kohn-Sham eigenfuction is represented by an infinite expansion in the orthonormal plane basis set $|\mathbf{q}\rangle$. Of course, it is not possible to manage the infinite summation in the reciprocal space in practice. In order to avoid the problem, it is necessary a truncation in the summation fixing a energy cutoff which satisfies:

$$\frac{1}{2}|\mathbf{k}+\mathbf{G_m}|^2 \leq E_{cut} \tag{1.59}$$

It is important to bear in mind that the E_{cut} value will define the precision of the calculation. The minimum value of E_{cut} such that a reasonably accurate description is achieved depends strongly on the type of system (*e.g.*, chemical composition). It is always possible to increase the accuracy of the computation by increasing the value of E_{cut}, unfortunately this comes at the price of a larger computational cost.

Using the expansion defined in **Eq. 1.58** it is possible to solve the Kohn-Sham equation directly in reciprocal space. The equation now reads as:

$$\sum_{\mathbf{q}} \langle \mathbf{q}'|\hat{H}_{eff}|\mathbf{q}\rangle C_{n,\mathbf{q}} = \varepsilon_n \sum_{\mathbf{q}} \langle \mathbf{q}'|\mathbf{q}\rangle C_{n,\mathbf{q}} = \varepsilon_n C_{n,\mathbf{q}'} \tag{1.60}$$

The kinetic energy operator in the matrix is :

$$\langle \mathbf{q}'| -\frac{1}{2}\nabla^2 |\mathbf{q}\rangle = \frac{1}{2}|\mathbf{q}|^2 \delta_{\mathbf{q},\mathbf{q}'} \tag{1.61}$$

Meanwhile, the $V_{eff}(\mathbf{r})$ potential in the reciprocal space is :

$$V_{eff}(\mathbf{r}) = \sum_{m} V_{eff}(\mathbf{G_m}) exp[(i\mathbf{G_m} \cdot \mathbf{r}] \tag{1.62}$$

where

$$V_{eff}(\mathbf{G}) = \frac{1}{\Omega_{cell}} \int_{\Omega_{cell}} V_{eff}(\mathbf{r}) exp[(-i\mathbf{G_m} \cdot \mathbf{r}] d\mathbf{r} \tag{1.63}$$

After that, the potential could be wrote in matrix notation as:

$$\langle \mathbf{q}' | V_{eff} | \mathbf{q} \rangle = \sum_{m} V_{eff}(\mathbf{G_m}) \delta_{\mathbf{q}-\mathbf{q}',\mathbf{G_m}} \tag{1.64}$$

and only the terms which **q** and **q'** differ by some reciprocal lattice vector $\mathbf{G}_m$ are non-zero.

We have used that **q= k+** $\mathbf{G}_m$ and **q'= k+** $\mathbf{G}_{m'}$. This permits to write the Schrödinger equation in a matrix notation for any **k** value as :

$$\sum_{m'} H_{m,m'}(\mathbf{k}) C_{n,m'}(\mathbf{k}) = \varepsilon_n(\mathbf{k}) C_{n,m}(\mathbf{k}) \tag{1.65}$$

where

$$H_{m,m'}(\mathbf{k}) = \frac{1}{2} |\mathbf{k} + \mathbf{G_m}|^2 \delta_{\mathbf{m},\mathbf{m}'} + V_{eff}(\mathbf{G_m} - \mathbf{G_{m'}}) \tag{1.66}$$

Thus, a discrete set of solutions could be obtained for the different eigenfuctions and eigenvalues n=1, 2, ... solving the matrix equation for a given **k**. It is important to note that, given the large number of plane-waves usually necessary to describe the system, the Hamiltonian matrix in **Eq. 1.66** is very large. For this reason, in most implementations the Hamiltonian matrix is never explicitly constructed and the solutions are found using efficient iterative methods [12, 90, 87–89], rather than explicit diagonalisation. In the calculations presented in this Thesis we have used the efficient implementation provided by the VASP code [12, 87–89].

Knowing the Kohn-Sham orbitals the electronic density function can be obtained as :

$$n(\mathbf{r}) = \frac{1}{N_k} \sum_{\mathbf{k},n} f(\varepsilon_{n,\mathbf{k}}) n_{n,\mathbf{k}}(\mathbf{r}) = \frac{1}{N_k} \sum_{\mathbf{k},n} f(\varepsilon_{n,\mathbf{k}}) |\psi_{n,\mathbf{k}}(\mathbf{r})|^2 \tag{1.67}$$

which is an average over the **k** points in the FBZ obtained for any n band and the function $f(\varepsilon_{i,\mathbf{k}})$ is the Fermi-Dirac distribution.

An usual election for the K-mesh is the Monkhorst-Pack sampling [91], which is composed by a grid of suitably chosen equally spaced k-points. In our case we usually choose k-point grids that are centered around Γ. The calculation can be simplified taking in con-

sideration the symmetries in the crystal using the irreducible Brillouin zone (IBZ) which contains all the symmetry group operations in the FBZ. It reduces the computational cost of the calculations.

The use of plane-waves basis sets offers some advantages with respect to other methods. The change from the real space to the reciprocal space is easy via fast Fourier transformation. The convergence can be increased in order to obtain a more accurate solution just increasing the E_{cut} values. Furthermore, the basis set is independent of the atomic position and the Hellmann-Feynman forces acting on the atoms can be calculated directly using the expected values of the derivatives of the Hamiltonian operator with respect to the ionic coordinates [92] without the need of adding any Pulay correction terms [25].

1.5 The pseudopotential approximation

Many properties in solids are mostly determined by valence electrons. The core electrons are strongly bonded to the nucleus and, for instance, chemically inert. Including core electrons explicitly, the so-called all-electron calculations, increases considerably the computational cost. The reason is two-fold: on the one hand, one needs to determine and explicitly handle the Kohn-Sham orbitals that describe such internal electrons. On the other hand, the energy cut-off of the plane-wave basis has to be increased to be able to describe the rapid oscillations of the wave-functions nearby the nuclei.

The pseudopotential approximation consist on replacing the core electrons and the strong ionic potential by a weaker pseudopotential acting on a set of pseudo wave functions to describe the valence electrons, rather than using the true wave functions [90]. Thus, it simplifies the electronic structure calculations and permits to reduce drastically the number of plane waves required in the basis set.

1.5.1 Norm-conserving pseudopotentials

The first family of *ab initio* pseudopotentials that was proposed was that of the norm-conserving pseudopotentials [93]. Norm-conserving pseudofunctions are normalized solutions of a model potential which reproduce the valence properties of an all-electron calculation. Norm conservation condition produces simple, accurate and transferable pseudopotentials [25]. In a norm-conserving pseudopotential the following characteristics are desired [93]:

1. All-electron and pseudo valence eigenvalues agree for a chosen atomic configuration.

2. All-electron and pseudo atomic wave functions agree beyond a chosen core radius (R_c).

3. The charge integration for the real and pseudo charge densities agree for r>R_c (norm conservation).

4. The logarithmic derivatives of the real and pseudo wave functions and the first energy derivatives agree for r>R_c.

Points 1. and 2. guarantee that the atomic potential outside the core region (r>R_c) is equal to the norm-conserving pseudopotential (except for a constant) and it is exclusively determined by the wavefunction and its energy. Point 3. means that the electronic charge inside R_c

$$\int_0^{R_c} r^2 |\psi^{PS}(\mathbf{r})|^2 dr = \int_0^{R_c} r^2 |\Phi_l(\mathbf{r})|^2 dr \tag{1.68}$$

is identical for the pseudo wave fuction $\psi^{PS}(\mathbf{r})$ and the all-electron radial orbital $\Phi_l(\mathbf{r})$ for each valence state. Point 4. guarantees the scattering properties of the real ion cores are reproduced with minimum errors.

In order to describe an ionic pseudopotential it is useful to separate the pseudopotential operator in two different parts containing the local part (l-independent) of the potential and the nonlocal terms.

$$\hat{V}(\mathbf{r}) = V_{local}(\mathbf{r}) + V_{NL}(\mathbf{r}) \tag{1.69}$$

where $V_{local}(\mathbf{r})$ is the local part that contains the long-range Coulombic effects and $V_{NL}(\mathbf{r})$ the nonlocal part. Thus, in general, the semilocal pseudopotential operator could be written as :

$$\hat{V}_{SL}(\mathbf{r}) = V_{local}(r) + \sum_{lm} |Y_{lm}\rangle V_{NL}(r) \langle Y_{lm}| \tag{1.70}$$

where Y_{lm} are the spherical harmonic functions.

Several norm-conserving pseudopotentials were developed [93–97] in order to accurately describe the behaviour of valence electrons outside the core region, being computationally efficient and applicable to any element.

1.6 Projected Augmented Wave method

In spite of the requirement of producing a smoother electron-ion effective interaction, norm-conserving pseudopotentials usually require relatively large plane-wave expansions. This is a problem particularly when dealing with large system sizes. For this reason, other alternatives have been envision. One of the most popular nowadays is the so-called projected augmented wave (PAW) method, originally developed by Blöchl [98].

PAW method combines the pseudopotential method and the linear augmented plane wave method with excellent results. It permits to obtain simultaneously computational efficiency and accuracy in the electronic density calculations of materials in the DFT approach. In the PAW method the all-electron valence wave functions are obtained based on a linear transformation of the pseudo wave functions [92, 99, 100] and applying the frozen-core approximation [101]. The augmented wave method strategy consists on separating the wave function in two parts. A partial wave expansion within the augmentation region, which corresponds with the core region, and plane wave functions in the interstitial areas.

Thus, the all electron wave function $|\psi>$ could be written as a sum of pseudo wave functions:

$$|\psi\rangle = |\tilde{\psi}\rangle + \sum_i (|\phi_i\rangle - |\tilde{\phi}_i\rangle)\langle\tilde{p}_i|\tilde{\psi}\rangle \tag{1.71}$$

$|\tilde{\psi}>$ is a smooth plane wave function. The index i refers to the atomic site **R**, the angular momentum numbers L=l,m for the n band and **k** wave vector. The all electron partial waves ϕ_i are calculated for a reference atom. The pseudo wave function $\tilde{\phi}_i$ are equal to the all electron outside the core radius and match continuously onto $\tilde{\phi}_i$ inside the augmentation region. The projector function $\tilde{p}_i$ obeys the relation $<\tilde{p}_i|\tilde{\phi}_j> = \delta_{i,j}$.

In the PAW method the all electron charge density is obtained with the addition of three contributions:

$$n(\mathbf{r}) = \tilde{n}(\mathbf{r}) + n^1(\mathbf{r}) - \tilde{n}^1(\mathbf{r}) \tag{1.72}$$

where $\tilde{n}(\mathbf{r})$ is the pseudo charge density calculated from the pseudo wave functions on a plane wave grid. $\tilde{n}^l$ and n^l are the pseudo and all electron on-site charge densities obtained on a radial support grid in an angular momentum representation.

This method ensures the orthogonality between the valence and core wave functions and is able to describe the nodal behaviour of the valence orbitals. Thus, the PAW method joins together the computational efficiency of the pseudopotential methods and the precision of the augmented wave methods. The calculations presented in this Thesis, using the VASP code, utilise the PAW method.

Chapter 2

NO adsorption on Cu[110] and O(2x1)/Cu[110]

Fomos ficando sós
o Mar o barco e mais nós.

Manuel Antonio, De catro a catro

2.1 Introduction

Nitric oxide (NO) is a common gas present in industrial processes, product of engine combustion (cars, power plants) and present in air pollution. Chemical interactions between NO and metal surfaces have been extensively studied, experimentally and theoretically, in the last twenty years. This diatomic molecule posses a free unpaired electron in the $2\pi^*$ antibonding orbital that renders NO be very reactive. Thus, NO is a free radical that can donate or receive an electron in the interaction with the surface.

In the early eighties it was already demonstrated that adsorption and dissociation of NO on copper depends strongly on the temperature and coverage [102]. Brown *et al.* [103] using Reflection Absorption Infra-Red Spectroscopy (RAIRS) showed the different behaviour of the NO molecule as a function of temperature and exposure in Cu[110]. At low coverage the monomer is the favoured specie, however, when coverage is increased the dimer $(NO)_2$ is more stable.

Gajdoš *et al.*, using DFT calculations, studied the energetics, geometry and vibrational properties of adsorbed NO and the dissociation process of NO on the [111] surfaces of transition metals (Co, Ni, Ru, Rh, Pd, Ir, Pt) and noble metals (Cu, Ag, Au) [104, 105]. In most cases, adsorption was predicted to be more favourable in the hollow site with triple

coordination. However, the adsorption energy differences were sufficiently small to allow for the simultaneous occupation of different adsorption sites on Ir, Co, Ru, Rh and Pt.

The adsorption and dissociation process of $(NO)_2$ on Cu[110] was studied by García and Arnolds [106] using RAIRS. They observed the photodissociation of $(NO)_2$ due to the break of the weak N-N bond, obtaining one NO in the gas phase and one NO that remains adsorbed. Recent Scanning Tunnelling Microscopy (STM) experiments [107] on the same substrate showed that the preferred adsorption site of NO is the short bridge between two copper atoms. They found two possible configurations, an upright position perpendicular to the surface at T<40 K and a tilted geometry when T $\geq$ 40 K. In the present work we have investigated the interaction of NO molecules with the clean Cu[110] surface using DFT calculations. We focus on the change of the structural, electronic and magnetic properties occurring during adsorption, comparing our results with experimental observations available for Cu[110] [102, 103, 107].

Here we also investigate the interaction of NO with the reconstructed O(2×1)/Cu[110] surface [15]. It is well known that, when the Cu[110] surface is exposed to oxygen dosage, the surface suffers a reconstruction and Cu-O rows appear along the $\langle 001 \rangle$ direction, rearranging the surface to O(2×1)/Cu[110] [108–111]. Previous work by some of the present authors analysed the interaction of carbon monoxide (CO) molecule over O(2×1)/Cu[110] by a combination of low-temperature STM and DFT calculations. It was demonstrated that CO adsorbs in a tilted configuration, forming extended rows over the surface [13, 14]. The CO molecules strongly deform the configuration of the Cu-O rows in the surface by pulling the bonding Cu atoms. In addition, the tilted adsorption configuration of the CO on this surface favours an attractive dipole-dipole interaction between CO molecules. Thus, rows of tilted molecules appear along the $\langle 1\bar{1}0 \rangle$ direction, whereas a long range surface mediated repulsion keeps the CO rows well-separated along $\langle 001 \rangle$ direction. This lead us the question of whether this intriguing behaviour found for CO could also appear for other small molecules on O(2×1)/Cu[110]. NO, being a similar diatomic molecule that differs from CO in the presence of an unpaired electron in the $2\pi^*$ orbital, seems a reasonable first choice for such an investigation.

As discussed below in the Results section, while NO molecules on Cu[110] tend to form dimers along the $\langle 1\bar{1}0 \rangle$, such tendency is not observed on O(2×1)/Cu[110] along any direction. Furthermore, our calculations do not predict the formation of extended NO molecular rows for any of the surfaces, in clear contrast to the case of CO for O(2×1)/Cu[110].

2.2 Methodology

Our DFT calculations were performed using VASP [12] and the optB86b-vdW density functional, based on a functional originally developed by Becke [51] and recently modified by Klimeš *et al.* [60, 61] to account for van der Waals interactions. This functional is part of the recent efforts to develop non-local density functionals capable of describing vdW interactions with sufficient accuracy [58, 112]. The optB86b-vdW functional has been shown to provide good results for a large variety of solids [61], as well as for the description of water interactions and dissociation [60]. We used a plane-wave cutoff of 400 eV, as well as the PAW method to describe the atomic cores. All calculations were spin-polarised.

Our calculated lattice parameter for bulk Cu is a_0= 3.599 Å, in good agreement with the experimental value 3.595 Å [61]. A 25×25×25 k-point sampling of the Brillouin-zone was used in this bulk calculation. Using this calculated bulk lattice parameter we constructed a slab containing 5 Cu layers, relaxing the two topmost surface layers in our studies of the clean and decorated surface. Relaxations were pursued until forces acting on all the atoms were smaller than 0.03 eV/Å. We kept a large vacuum distance ($\sim$ 25 Å) to avoid interaction between periodic replicas of the slab along the z-direction.

We first studied the clean Cu[110] surface, which was relaxed using a 15×15×1 k-sampling Monkhorst-Pack in the 1×1 unit cell. To study the adsorption of the NO molecules on this substrate we used both 4×2 and 2×4 lateral supercells utilising, respectively, 7×9×1 and 9×7×1 k-samplings.

The O(2x1)/Cu[110] surface is obtained by placing a Cu-O row, oriented along the $\langle 001 \rangle$ direction, on top of the Cu[110] surface and doubling the size of the cell along the $\langle 1\bar{1}0 \rangle$ direction. The study of the NO adsorption on this substrate was performed using a 4×2 supercell of the 1×2 cell of the O(2×1)/Cu[110] reconstruction. A 7×9×1 k-sampling was used in these calculations.

The adsorption energy (E_{ads}) is defined as:

$$E_{ads} = \frac{n \times E_{mol} + E_{surf} - E_{total}}{n} \tag{2.1}$$

where E_{total} is the total energy of the surface decorated with n molecules in the simulation cell, E_{surf} is the corresponding energy of the clean surface and E_{mol} is the total energy per molecule in the gas phase.

Population analysis was performed using the Bader charge analysis [113] as implemented in the program developed by G. Henkelman *et al.* [114–116]. STM simulations were performed using the Tersoff-Hamann [117, 118] approximation, *i.e.*, they correspond to maps

of the local density of states integrated in an energy window $[\varepsilon_F, \varepsilon_F + V]$ where V is the applied bias and ε_F is the Fermi level.

2.3 Results

2.3.1 NO adsorption on Cu[110]

Figure 2.1 shows the possible adsorption sites of the NO molecule on Cu[110] that we have explored here: (**T**) Cu top site, (**H**) 2-fold hollow site, (**LB**) long bridge between two Cu rows and (**SB**) short bridge along the same Cu row. We have checked both the possibility of the nitrogen atom or the oxygen atom targeting the surface. Positions with the nitrogen atoms bonded to the surface are always more favourable.

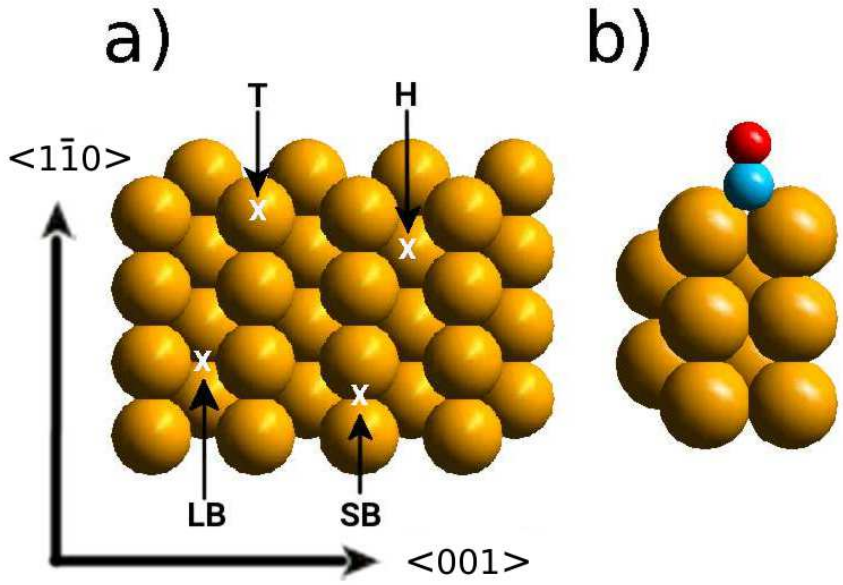

Fig. 2.1 a) Possible adsorption sites for NO monomers on Cu[110] explored here. (**T**) stands for top site, (**H**) for a 2-fold hollow site, (**LB**) for long bridge and (**SB**) for short bridge. b) Front view of most stable NO adsorption, with the nitrogen atom (blue) pointing towards the surface in a (**SB**) configuration.

As it is shown in **Table 2.1**, the most stable monomer adsorption occurs on the **SB** site with an upright orientation of the molecule. The N atom is pointing towards the surface and bonded to two of the Cu atoms in the rows running along the $\langle 1\bar{1}0 \rangle$ direction. This site is $\sim$300 meV more stable than the **LB** site, that follows in stability. The adsorption energy

Table 2.1 Relative adsorption energies (Δ E_{ads}) for NO monomers in the different adsorption sites on Cu[110] shown in **Figure 2.1**. The N atoms are always pointing towards the surface. The Cu-N bond length (l) is also given.

site	Δ E_{ads} (eV)	l (Å)
T	-0.355	1.78
H	-0.484	2.31
LB	-0.304	2.02
SB	0.000	1.90

in the **SB**-upright configuration is 1.522 eV (see **Table 2.2**) and the N-Cu bond length is 1.90 Å. The surface does not present any significant distortion after adsorption, and the intermolecular (N-O) bond length increases up to 1.207Å, i.e., $\sim$3 % longer than the calculated equilibrium bond length (1.171 Å) for the free-standing molecule. The magnetisation (1 μ_B) of the gas-phase NO molecule is lost upon adsorption due to the strong interaction with the Cu[110] surface. This calculated adsorption configuration is in good agreement with STM data at temperatures below 40 K [107].

Shiotari *et al.* interpreted their STM images for temperatures above 40K in terms of a tilted adsorption configuration [107]. However, in spite of our efforts, we could not stabilise any such tilted configuration. We tried multiple calculations varying the initial tilt angle (60°, 45°, 30°), and even placing the molecule parallel to the surface along both the $\langle 001 \rangle$ and $\langle 1\bar{1}0 \rangle$ directions. All these calculations either converged directly to the upright configuration, or to configurations significantly less stable than the **SB**-upright. Thus, at least within our computational scheme, the observation by Shiotari *et al.* cannot be explained by the population (as temperature increases) of energetically less-stable, tilted adsorption configurations.

We performed an analysis of the Projected Density of States (PDOS) onto the molecule in order to understand the molecule-surface interaction. It is instructive to compare the PDOS of the gas-phase molecule (**Figure 2.2**) with that of the monomer adsorbed on Cu[110] (**Figure 2.3**). The strong interaction of the $2\pi^*$ molecular orbitals (MOs) with the surface can be easily appreciated: upon adsorption the $2\pi^*$ MOs develop a considerable width (see peak 1 in **Figure 2.3**). As a consequence of this hybridisation the NO molecule loses its magnetisation after adsorption. The appearance of peak 2 in the molecular PDOS provides another signature of the strong interaction with the 3d orbitals of the Cu atoms in the surface. As it is shown in one of the insets in **Figure 2.3**, peak 2 has a strong contribution from the $2\pi^*$ MO formed by the p orbitals of the molecule pointing along the $\langle 1\bar{1}0 \rangle$ direction (p_y according to the notation used in the following). This is another clear signature of the strong interaction with the anisotropic Cu[110] surface. We can also find indications of such

interaction in the lower lying MOs. Similar to the case of CO adsorption on close-packed transition and noble metal surfaces [119, 120], we observe that the 5σ MO shifts downwards during the adsorption and changes its relative position with respect to the 1π MOs (the 5σ becomes now the lowest MO). We can also observe the splitting of the 1π levels due to the interaction with the surface.

The population analysis presented in **Table 2.3** indicates that there is a charge transfer of approximately half an electron from the surface to the NO monomer. This charge transfer is accompanied by an internal rearrangement of the charge. The charge of the O atom decreases by approximately half an electron and the net charge of the N atom increases by one electron. A similar behaviour was observed by Valmoria *et al.* [121] for NO on CuO(110).

Once the most stable adsorption configuration of the single monomer was determined, we considered the interaction between two and more adsorbed molecules. In **Table 2.2** we compare the adsorption energies of NO monomers, dimers and extended rows of molecules on Cu[110]. A 4×2 supercell was used to study the dimer and rows oriented along the $\langle 001 \rangle$ direction, whereas a 2×4 supercell was used to calculate the dimer and rows along the $\langle 1\bar{1}0 \rangle$ direction. The monomer adsorption energy is the same using both supercells within 6 meV. As one can see only the formation of dimers along the $\langle 1\bar{1}0 \rangle$ direction is stable as compared to the monomer adsorption.

Table 2.2 Adsorption energy per NO molecule on Cu[110] in different configurations (single monomer, dimers and extended rows of molecules). The angle of the molecular axis with respect to the surface normal is also reported.

molecule/s	$\mathbf{E_{ads}}$ **(eV)**	**angle** (°)
monomer	1.522	0.0
dimer $\langle \mathbf{001} \rangle$	1.510	15.2
dimer $\langle \mathbf{1\bar{1}0} \rangle$	1.569	7.2
row $\langle \mathbf{001} \rangle$	1.476	14.6
row $\langle \mathbf{1\bar{1}0} \rangle$	1.307	0.0

We discuss first the dimer formed along $\langle 001 \rangle$ direction (see **Figure 2.4 a**). This dimer is only 12 meV per molecule less stable than the monomer adsorption. The NO molecules change from the upright to a slightly tilted configuration in which both molecules keep a N-N distance of 3.23 Å and tilt towards each other with an $\sim$15.2° angle, as it is shown in **Figure 2.4 a**. Other configurations have also been investigated by forcing both molecules to remain in an upright position, to have a parallel tilt (i.e., both molecules tilted towards the same direction) and to have a repulsive tilt, i.e. increasing the separation between both O atoms. In all those cases E_{ads} decreases by 30-60 meV per molecule. Therefore, and in

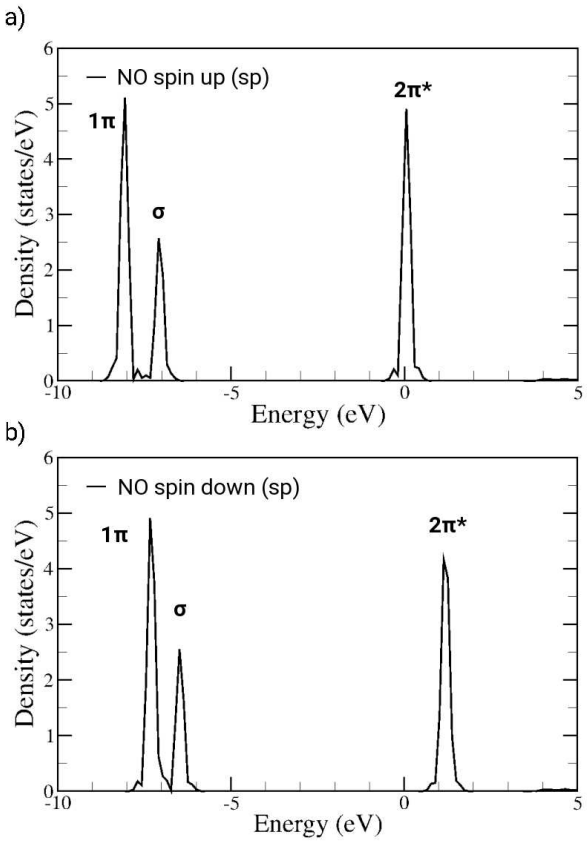

Fig. 2.2 PDOS of a single NO molecule in a supercell of the same size as the 4×2 supercell used in the NO/Cu[110] calculations. a) spin up and b) spin down. Energies are referred to the Fermi energy.

spite of the electron accumulation on the O atoms, there seems to be an attractive interaction mediated by the O atoms when the NO dimer is formed along the $\langle 001 \rangle$ direction.

The PDOS analysis in **Figure 2.5** reveals the mechanism behind the inter-molecular interaction responsible of the favourable tilting. The splitting of the $2\pi^*$ peak, absent in the case of the adsorbed monomer, reveals the covalent interaction among the MOs of the neighbouring molecules, as well as the influence of the molecular tilt in the hybridisation of the $2\pi^*$ with the surface. In the insets of **Figure 2.5** we can see the distinct character of the charge distribution associated with peak 1 and 2, respectively, with dominant $2\pi_x^*$ and 2 π_y^* (x-axis along the $\langle 001 \rangle$ and y-axis along the $\langle 1\bar{1}0 \rangle$ direction as it is shown in **Figure 2.4 a**).

The Bader population analysis presented in **Table 2.3** shows a situation clearly different to that of the adsorbed monomer. The O atoms almost keep the same charge as in the gas phase, whereas each N atom takes half an electron from the copper substrate. Thus, although the total charge of each individual NO molecule is very similar to that of the adsorbed monomer,

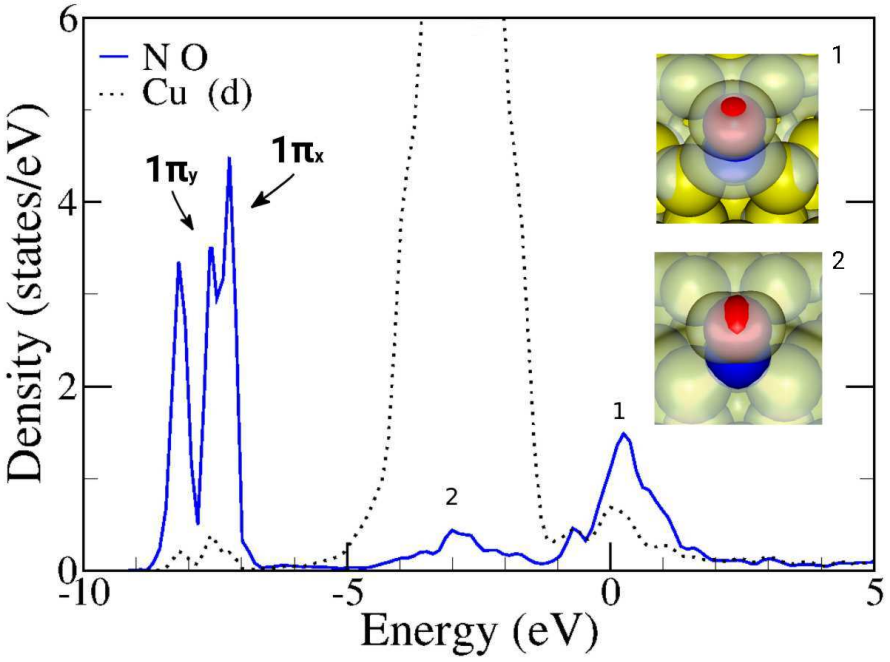

Fig. 2.3 PDOS of the NO monomer adsorbed on Cu[110]. The Local Density of States (LDOS) corresponding to peaks 1 and 2 are depicted in the insets, showing the interaction between $2\pi^*$ MOs and Cu *d* orbitals. Energies are referred to the Fermi energy.

the distribution of this charge is different: the oxygen atoms are more negatively charged in the case of the dimer. This would be counter-intuitive, particularly in view of the tilted geometry, if one would assume that the interaction between molecules is purely Coulombic. Thus, the population analysis and the PDOS indicates that the covalent interaction between molecules must be an important ingredient for the formation of NO dimers on Cu[110].

As it is shown in **Table 2.2** the formation of NO dimers along the $\langle 1\bar{1}0\rangle$ direction becomes favourable. Those dimers are 47 meV per molecule more stable than the monomer adsorption on clean Cu[110], and 59 meV per molecule than the dimer in the $\langle 001\rangle$ direction. In this case, the molecules keep a N-N distance of 2.76 Å and also tilt towards each other with an angle $\sim$7.2° (see **Figure 2.4 b**), smaller than the tilt angle of the NO molecules in the $\langle 001\rangle$ dimers. This is due to the smaller distance between molecules along the $\langle 1\bar{1}0\rangle$ direction. The PDOS in **Figure 2.6** reflects the increased interaction among molecules for the $\langle 1\bar{1}0\rangle$ dimer. The splitting of the $2\pi^*$ MOs around the Fermi level becomes larger, with the highest peak (peak 1) developing a clear $2\pi_x^*$ antibonding character (see the inset in **Figure 2.6** and the simulated STM images for occupied and unoccupied states in **Figure 2.7**). Peak 2 at lower energies has a clear bonding character (see **Figure 2.7**) with somewhat mixed $2\pi_y^*$ and $2\pi_x^*$ symmetry. Interestingly, peak 2 is now clearly below the Fermi level, reinforcing the idea

Table 2.3 Bader analysis of the valence-electron population. Charge in the NO molecule and the N and O atoms when the molecule is adsorbed on Cu[110] in different configurations.

molecule/s	NO (e)	N (e)	O (e)
gas phase	11.000	3.862	7.138
monomer	11.486	4.867	6.619
dimer $\langle$**001**$\rangle$	11.461	4.439	7.022
dimer $\langle$**1$\bar{1}$0**$\rangle$	11.444	4.392	7.052
row $\langle$**001**$\rangle$	11.460	4.433	7.027
row $\langle$**1$\bar{1}$0**$\rangle$	11.419	4.368	7.051

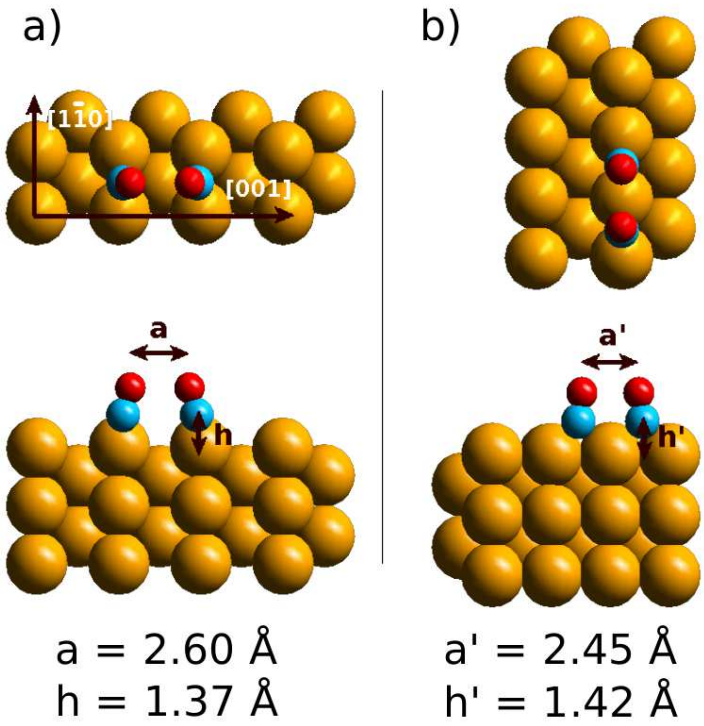

Fig. 2.4 a) Top and side view of an NO dimer along the $\langle 001 \rangle$ direction in a 4×2 supercell b) Top and front view of an NO dimer along the $\langle 1\bar{1}0 \rangle$ direction in a 2×4 supercell. Here h is the distance between the N atom and the Cu top most layer, and a stands for the distance between O atoms in neighbouring NO molecules.

of the stabilisation of the $\langle 1\bar{1}0 \rangle$ dimers due to the covalent interaction among the $2\pi^*$ MOs in neighbouring molecules. The population analysis shows a situation similar to that of the $\langle 001 \rangle$ NO dimer. The population of the O atoms is similar to the gas phase molecule (and $\sim$0.4 electrons larger than for the single monomer), while there is a charge transfer of half an electron to the N atoms coming from the metallic surface.

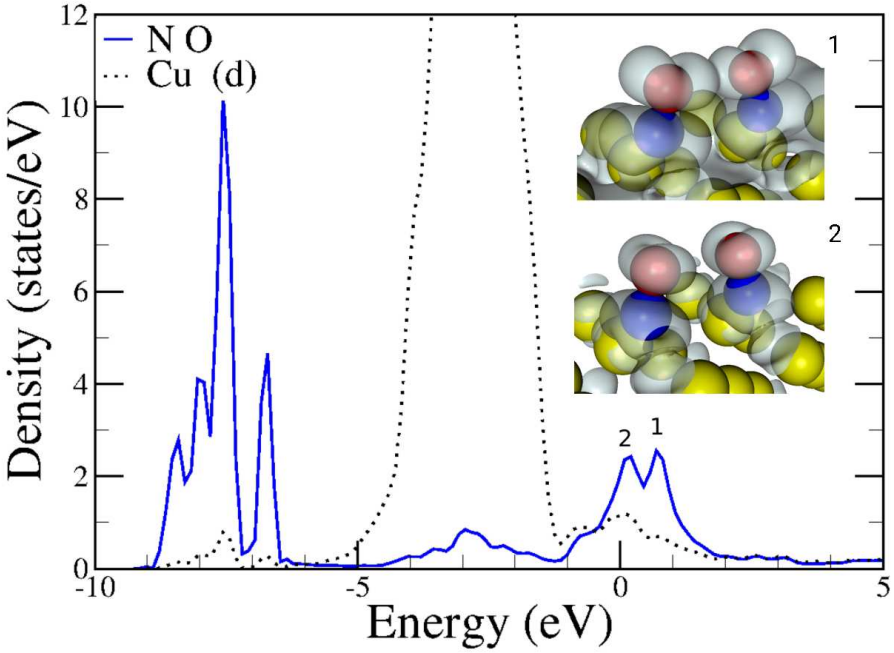

Fig. 2.5 PDOS of the NO dimer along the $\langle 001 \rangle$ direction on Cu[110]. The splitting of the $2\pi^*$ peak, absent in the case of the monomer, is a signature of the inter-molecular interaction. The insets show the LDOS at the energies corresponding to peak 1 and 2, respectively. Energies are referred to the Fermi energy.

Comparing NO dimers along both surface directions, dimer adsorption along the $\langle 1\bar{1}0 \rangle$ direction is energetically favoured over dimer formation along $\langle 001 \rangle$ direction. While for the monomer adsorption our calculations predict an upright adsorption configuration, for the dimers the overlap between molecular orbitals in neighbouring molecules induces the attractive tilting of the molecules. The smaller distance between molecules along the $\langle 1\bar{1}0 \rangle$ direction increases the interaction between them at a lower tilting angle (i.e., with a smaller distortion of the preferred NO adsorption configuration). This might be one of the factors behind the larger stability of this dimer with respect to the $\langle 001 \rangle$ dimer. Given their stability ($\sim$40 meV) with respect to the single monomers, the formation of NO pairs along the $\langle 1\bar{1}0 \rangle$ direction should be experimentally detected at low temperature. Indeed, this is in good agreement with the experimental STM observations by Shiotari *et al.* [107].

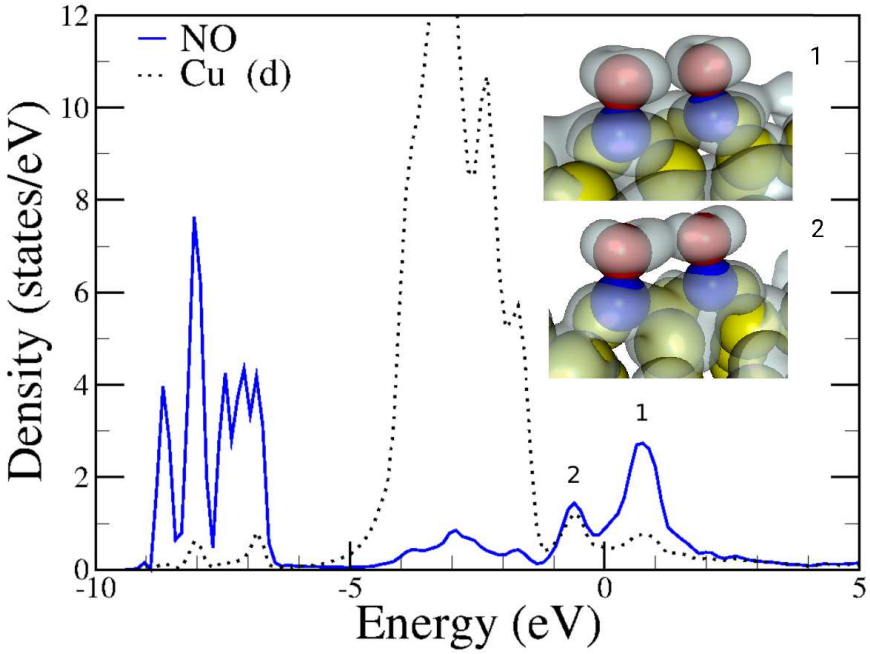

Fig. 2.6 PDOS of the NO dimer along the $\langle 1\bar{1}0 \rangle$ direction on Cu[110]. The insets show the LDOS at the energies corresponding to peak 1 and 2, respectively. Notice the increased splitting of the $2\pi^*$ peak as compared to the $\langle 001 \rangle$ dimer. Energies are referred to the Fermi energy.

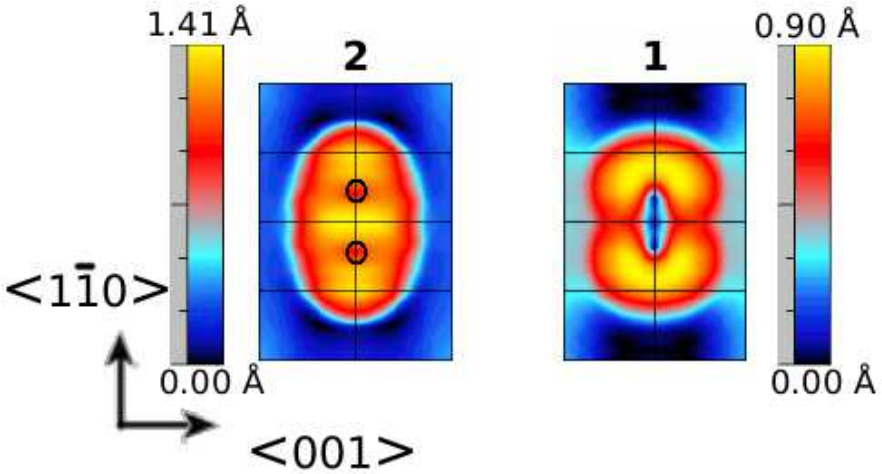

Fig. 2.7 Constant current simulated STM images [117, 118, 122] of the $\langle 1\bar{1}0 \rangle$ NO dimer on Cu[110]. A +730 meV bias is used in image (1), while a -600 meV is used in image (2). They correspond to peaks 1 and 2 in the PDOS showed in **Figure 2.6** . The dominant bonding character of the peak below E_F (2) and the antibonding character of that above E_F (1) are evident, as well as the $2\pi_x^*$ character of peak 1. The network created by the thick black lines indicates the position of the top most Cu atoms. We also indicate in 2 the positions of the oxygen atoms of the molecules.

We next investigate the possible formation of NO rows along both $\langle 001 \rangle$ and $\langle 1\bar{1}0 \rangle$ directions on the Cu[110] surface (see **Figure 2.8**) . The formation of such one-dimensional molecular assemblies turns out to be always unfavourable with respect to monomer and dimer adsorption. For rows along the $\langle 001 \rangle$ direction the adsorption energy per molecule is 46 meV lower than for the NO monomer and 34 meV smaller than for the corresponding $\langle 001 \rangle$ NO dimer. Interestingly, in the most stable structure for the $\langle 001 \rangle$ row, the NO molecules tilt towards each other in pairs, forming an $\sim 14.6^{\circ}$ angle with respect to the surface normal. Rows along the $\langle 1\bar{1}0 \rangle$ direction are significantly more unstable, respectively, 260 meV and 312 meV with respect to the dimer and monomer adsorption. In this case the molecules keep an upright position. We attribute the lower stability of the $\langle 1\bar{1}0 \rangle$ row to the increased coordination of the surface Cu atoms in this case. Since NO molecules adsorb on **SB** sites, all the bonding Cu atoms in the substrate are now shared by two NO molecules, decreasing the stability of each N-Cu bond. These results indicate that, in spite of the stability of the dimers, the formation of longer NO aggregates along the $\langle 1\bar{1}0 \rangle$ direction is very unlikely.

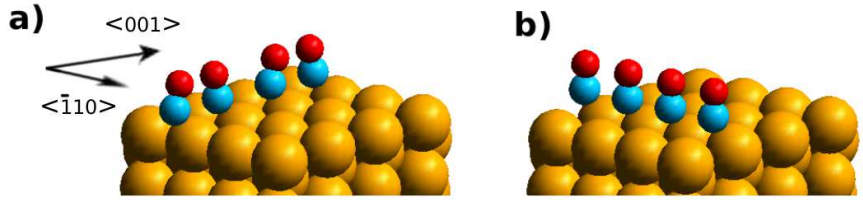

Fig. 2.8 Relaxed structures of NO rows on Cu[110] along the $\langle 001 \rangle$ and $\langle 1\bar{1}0 \rangle$ directions.

2.3.2 NO adsorption on O(2X1)/Cu[110]

DFT calculations have been also performed to investigate the adsorption of NO on the O(2×1)/Cu[110] surface. We have considered different adsorption sites and orientations of the NO molecule. **Figure 2.9** shows the investigated sites: on top over a Cu row atom (**TCu**), on top over an O row atom (**TO**), a bridge site between two Cu atoms of the Cu-O rows (**BCu**), and a bridge site between two O atoms of the Cu-O rows (**BO**). The molecule was approached perpendicularly to the surface with either the N or the O atom facing towards the surface. We found that it is always more stable for the molecules to bind to the substrate through the N atoms. As it is shown in **Table 2.4**, the most stable adsorption, by at least 50 meV, corresponds to the **BCu** site.

Thus, NO on O(2x1)/Cu[110] is predicted to form a bridge between Cu atoms in two neighbouring Cu-O rows as illustrated in **Figure 2.10 (a)** and **(b)**. The NO pulls the Cu atoms

Table 2.4 Relative adsorption energies (ΔE_{ads}) for NO monomers on O(2×1)/Cu[110] on the different adsorption sites showed in **Figure 2.9**. The N atoms are assumed to point towards the surface in all cases. The bond distances (l) between the N atom and the closest atoms in the surface are also given.

site	Δ **E**$_{ads}$ **(eV)**	l **(Å)**
TCu	-0.283	1.93
TO	-0.630	2.07
BO	-0.051	2.05
BCu	0.000	1.90

from the Cu-O rows to keep a Cu-N bond distance similar to that found on the clean Cu[110] surface, i.e., ∼1.90 Å. The Cu atoms directly bonded to the monomer are spontaneously shifted ∼0.87Å along the $\langle 1\bar{1}0\rangle$ direction and ∼ 0.35 Å perpendicularly to the surface. A similarly large substrate distortion is caused by the adsorption of CO on O(2×1)/Cu[110], as it is shown in Ref. [13]. However, in that case the CO molecule chemisorbs on a top Cu site of the Cu-O rows, pulling that Cu atom upwards about 1 Å.

Table 2.5 Adsorption energies, tilt angles, and spin polarisations per NO molecule adsorbed in different configurations on the O(2×1)/Cu[110] surface. The tilt angle is referred to the surface normal.

molecule/s	**E**$_{ads}$ **(eV)**	**angle** (°)	**S** (μ_B)
monomer	0.976	0.0	0.58
monomer tilt	0.964	34.7	0.64
dimer $\langle$**001**$\rangle$	0.800	12.3	0.67

Table 2.6 Bader analysis of the valence-electron population. Charge in the NO molecule and the N and O atoms when the molecule is adsorbed on O(2×1)/Cu[110] in different configurations.

molecule/s	**NO (e)**	**N (e)**	**O (e)**
gas phase	11.000	3.862	7.138
monomer	11.476	4.901	6.575
monomer tilt	11.471	4.968	6.505
dimer $\langle$**001**$\rangle$	11.404	4.365	7.038

The adsorption energies are presented in **Table 2.5**. The vertical adsorption configuration described above, has an adsorption energy of 976 meV. Notice the much smaller stability as compared to the adsorption on clean Cu[110]. Based on the information available for the CO molecule in this substrate [13], and given the bridge adsorption configuration that adopts, we

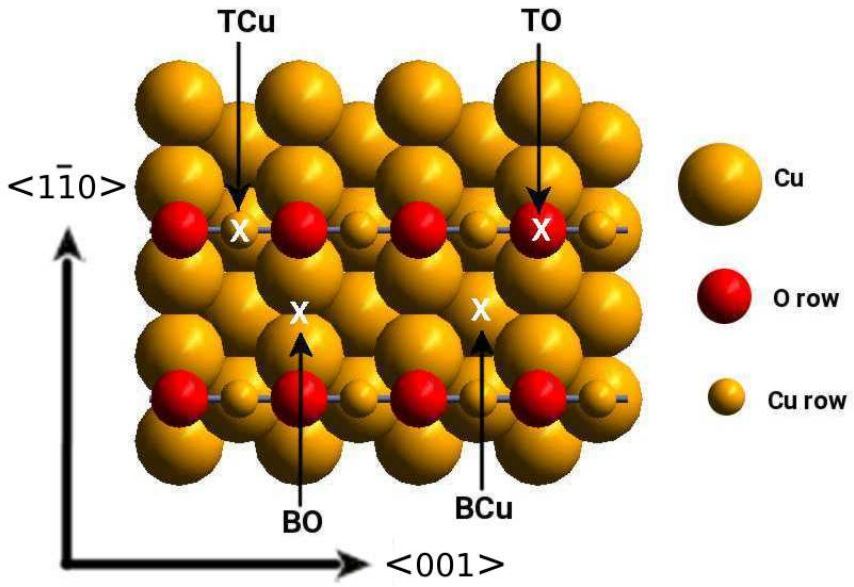

Fig. 2.9 Investigated adsorption sites for a NO monomer on the O(2×1)/Cu[110] surface: top sites above Cu atoms on the Cu-O rows (**TCu**), top sites on the corresponding O atoms (**TO**), bridge site between Cu atoms (**BCu**), and bridge site between O atoms (**BO**).

have explored the possibility to stabilize a configuration where the molecule tilts towards the $\langle 001 \rangle$ direction. **Figure 2.10(c)** and **(d)** depict the geometry obtained starting from an initial tilt angle of 45°. The geometry optimization stopped, when forces became smaller than our threshold value 0.03 eV/Å, at an angle of ∼35° with respect to the surface normal. However, this tilted geometry is 12 meV less stable than the vertical adsorption. This indicates that the energy landscape is extremely flat with respect to the tilt angle and, as a consequence, we can expect strong fluctuations of the NO adsorption angle with temperature.

Figure 2.11 shows the PDOS on the NO molecule and the 3*d* orbitals of the Cu atoms in the Cu-O rows for the vertically adsorbed molecule. In general, the peaks associated with the $2\pi^*$ MO present a smaller width as compared to the adsorption on clean Cu[110] surface (see **Figure 2.3**), indicating a somewhat smaller interaction with the substrate. This is particularly clear for the main $2\pi^*$ resonance at the Fermi level (peak 1), with a clear Cu-NO antibonding interaction (see in the corresponding inset the nodal planes appearing between the Cu atoms in the substrate and the N atom in the molecule). As a consequence of the partial occupation and small width of this peak, both vertical and tilted adsorbed molecules present a ~ 0.6 μ_B spin moment. Still, the relatively strong interaction with the substrate is reflected in the peaks appearing at lower energies with a clear Cu-$2\pi^*$ bonding character (e.g., see the charge distribution associated with peak 2 in the inset).

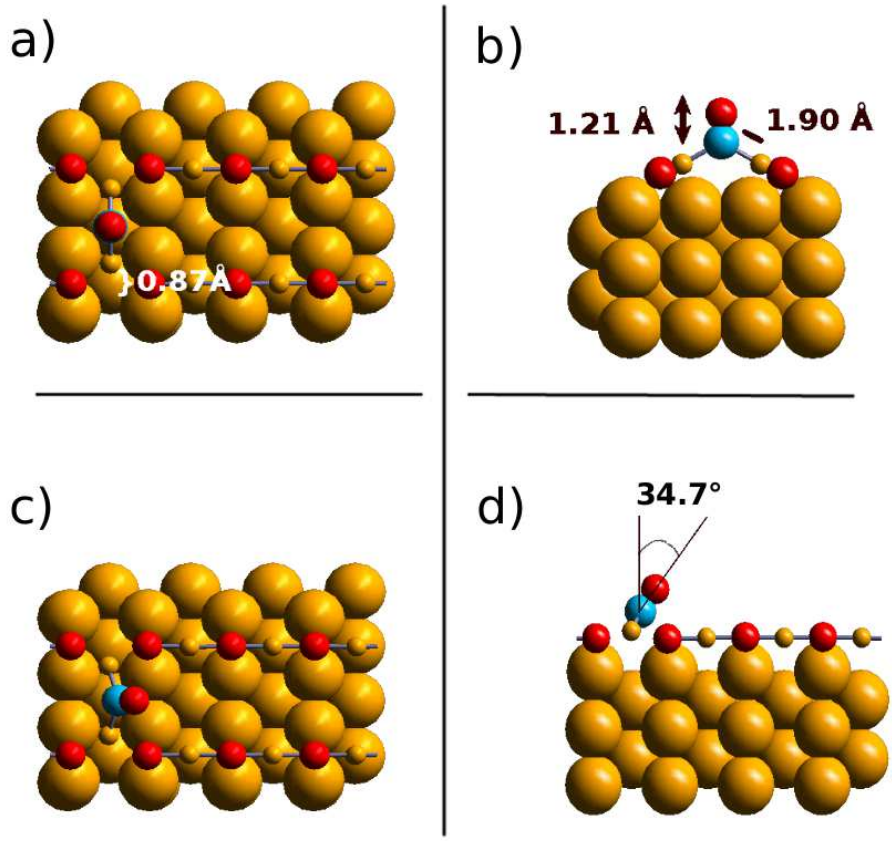

Fig. 2.10 The most stable NO adsorption on O(2×1)/Cu[110] takes place in between two Cu atoms of adjacent Cu-O rows. The upright NO monomer is depicted in panels a) (top view) and b) (front view). A tilted configuration only 12 meV less stable is shown in panels c) (top view) and d) (side view).

In spite of these differences in the strength of the interaction with the substrate, the populations obtained from a Bader population analysis in **Table 2.6** are very similar to those found on clean Cu[110]. Again the NO monomer adsorbed on O(2×1)/Cu[110] takes half an electron from the surface. The charge is rearranged inside the molecule, with the O atom losing half an electron and the N atom gaining one electron with respect to the free-standing molecule.

We now analyse the possible formation of NO dimers in this substrate. In particular, given the low energy cost for tilting the molecule along the $\langle 001 \rangle$ direction and the indications of covalent interaction among neighbouring molecules on clean Cu[110], we expected that the formation of dimers along this direction could be favourable. However, we find that the formation of NO dimers on O(2×1)/Cu[110] is not favourable along any direction. For dimers

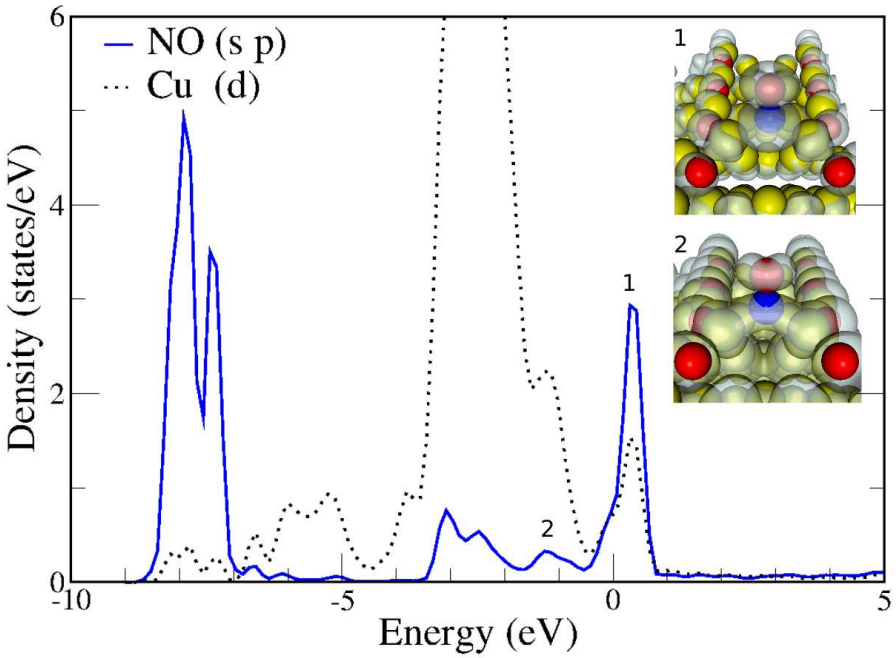

Fig. 2.11 PDOS on the molecule and the 3d orbitals of the Cu atoms in the Cu-O rows for a NO monomer adsorbed on O(2×1)/Cu[110] surface. The insets depict the LDOS associated with peaks 1 and 2. Energies are referred to the Fermi level.

along the $\langle 001 \rangle$ direction the adsorption energy decreases $\sim$ 175 meV per molecule compared to the monomer. The molecules forming the dimer tilt towards each other with an angle about 12° and keep a N-N distance of 5.49 Å. This is a signature of a short-range attractive interaction between molecules that, however, is not able to overcome the overall effective repulsion among adsorbed monomers. Interestingly, the dimer keeps a spin polarisation almost identical to that of the adsorbed monomers ($\sim$0.67 μ_B per molecule). The Bader population analysis shows a rearrangement of charge very similar to that found for the NO dimers on clean Cu[110]. While the total amount of charge ($\sim$0.5 e per molecule) transferred from the substrate to each molecule is the same as for the monomer, the population of the O atoms increase by approximately half an electron with respect to the monomer. This can be interpreted as an effect of the covalent interaction among the neighbouring molecules that tends to stabilise the oxygen sites. The PDOS in **Figure 2.12** shows the interaction between molecular orbitals from the NO molecules and with the 3*d* orbitals of the bonding Cu atoms in the Cu-O rows. The interaction between MOs of both molecules is reflected in the splitting of the peaks nearby the Fermi energy. However, it is interesting to compare this plot with that reported in **Figure 2.6** for the NO dimer along the $\langle 1\bar{1}0 \rangle$ direction on the clean Cu[110] surface. In the later case, due to the NO-ON interaction the $2\pi^*$ MOs basically split into a

fully occupied and a fully unoccupied main peaks, with an energy difference of more than 1 eV around the Fermi level. In the present case, however, the splitting is much smaller and a large density of states is found at the Fermi level, consistent with the persistent magnetisation in the dimer. All this indicates a much smaller covalent interaction between the molecules that, as mentioned above, is not able to stabilise the NO dimer with respect to the monomer adsorption.

Along the $\langle 1\bar{1}0 \rangle$ direction the need to share Cu atoms and the difficulty of the molecules to tilt towards each other lead to a further reduction of the adsorption energy. The adsorption energy diminishes by 250 meV with respect to the monomer while keeping a N-N distance of 3.14 Å. Thus, contrary to the behaviour observed on clean Cu[110], we conclude that NO dimer formation is not expected along any direction on O(2×1)/Cu[110]. Furthermore, in contrast to the case of CO molecules [13], we also found that the formation of NO rows is unfavourable along any direction. Thus, we cannot expect the formation of extended rows of NO molecules on this substrate.

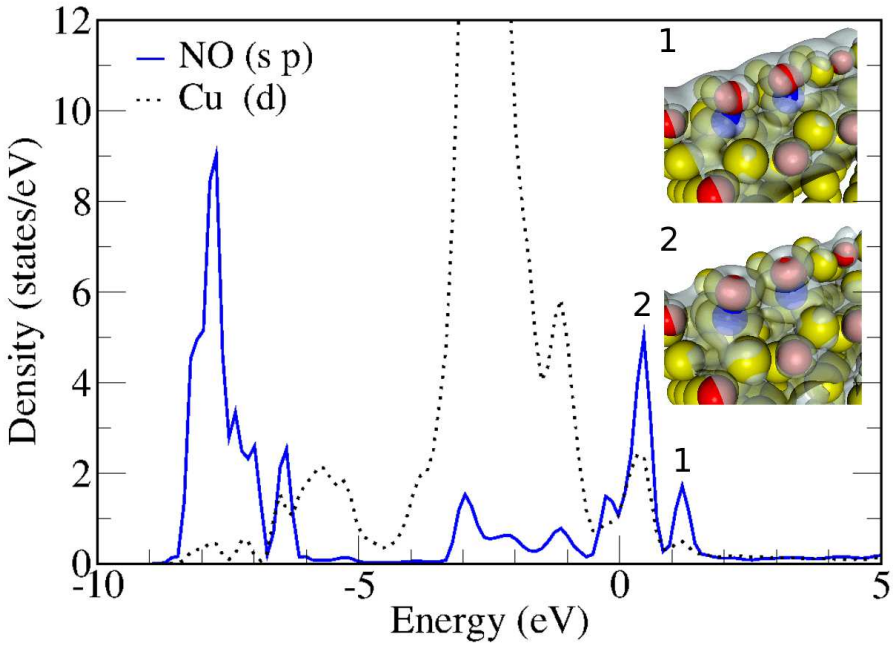

Fig. 2.12 PDOS on the molecules and the 3d orbitals of the Cu atoms in the Cu-O rows for a NO dimer oriented along the $\langle 001 \rangle$ direction on O(2×1)/Cu[110] along. The insets depict the LDOS associated with peaks 1 and 2. Energies are referred to the Fermi level

2.4 Conclusions

In this chapter we have studied NO adsorption on Cu[110] and on O(2×1)/Cu[110] surfaces. On the clean Cu[110] surface, monomer adsorption takes place vertically on short bridge sites with the N atoms directly attached to the surface. The strong hybridisation of the frontier molecular orbitals with the metal states can be read in the width of the peaks in the PDOS on the molecule. Consequently, the NO monomer loses the spin polarisation of the gas-phase molecule. Population analysis also indicates a substantial charge transfer from the metal surface, ∼0.5 e per molecule. The formation of NO dimers is found to be favourable (by ∼47 meV/molecule with respect to the adsorbed monomers) only along along the $\langle 1\bar{1}0\rangle$ direction, in good agreement with available experimental information [107]. The overlap between the $2\pi^*$ MOs of the NO molecules in the dimer gives rise to a splitting of the dimer levels around the Fermi level, again clearly visible in the PDOS. This covalent interaction is responsible for the stabilisation of the dimer geometry with tilted monomers. The covalent intermolecular interaction also causes a rearrangement of charge inside the molecules, increasing the population of the O atoms. In spite of the stability of $\langle 1\bar{1}0\rangle$ dimers, the formation of longer rows is not favourable along any surface direction.

The NO monomer on O(2×1)/Cu[110] attaches to two Cu atoms on two neighbouring Cu-O rows, causing a strong distortion of the CuO rows. For the monomer, vertical adsorption is found to be only marginally more stable than configurations tilted along $\langle 001\rangle$ direction, parallel to the Cu-O rows. The lower energy adsorption as compared to Cu[110], the smaller width of the molecular peaks in the PDOS analysis, and the presence of a magnetic moment ∼0.6 μ_B, clearly indicate the smaller interaction of the NO molecules with the substrate in this case. In spite of the easiness to tilt the NO molecules, which could favour both attractive covalent and dipolar interactions among the NO molecules, dimers are substantially less stable than NO monomers. Thus, in striking contrast to the case of CO on O(2×1)/Cu[110], from the present simulations we can conclude that NO molecules would not form extended molecular rows in this substrate.

Chapter 3

Adsorption of metal phthalocyanines on Ag[111]

Ever tried. Ever failed. No matter. Try Again. Fail again. Fail better.

Samuel Beckett

3.1 Introduction

Metal phthalocyanines (MePc) are well-known organic semiconducting molecules. MePc's are flat molecules with a four-leaf clover shape, formed from four benzene rings bonding to a central frame that contains a metallic atom at the centre. An example can be found in **Figure 3.1**, where we show the relaxed structure for an isolated titanyl phthalocyanine (TiOPc) molecule. Phthalocyanines are extensively used due to their interesting properties and possible applications as key component in organic field-effect transistors [123], light-emitting diodes [124–126], gas sensors [127, 128] organic photovoltaic cells [129, 130] or even spintronic devices [131–135].

Adsorption of MePc molecules on different substrates may lead to important changes in their electronic structure. For instance, Yamane *et al.* studied the Zinc phthalocyanine (ZnPc) and F_{16}ZnPc on Cu[111] [136]. Using x-ray standing wave (XSW) and angle-resolved photoemission spectroscopy (ARPES) they showed how geometric and electronic properties are related. The ZnPc molecule presents a distortion of the planar gas-phase geometry upon adsorption. This change produces a variation on the Zn-N bond distance, increasing its ionic character. Ren *et al.* using the same molecules showed that molecular adsorption

also modifies the electronic structure of the underlying substrate. By STM, DFT and time-dependent DFT (TD-DFT), they found that the competition between molecule-substrate and intermolecular van der Waals interactions plays a crucial role in establishing the molecular patterns and strongly modifies the electronic structure of the graphene substrate [137].

The electronic and magnetic properties of MePc's can be tuned depending on the way they assemble on different substrates. For example, Heutz *et al.* [134] observed different inter-molecular magnetic couplings (including the quenching of the coupling) in thin films of copper phthalocyanine (CuPc) and manganese phthalocyanine (MnPc) molecules depending on the detailed structure of the film. Molecules are adsorbed on thermally stable polyimide substrates (Kapton) forming flexible films on the surface. MePc changes from a magnetically ordered state to a non-magnetic one just by changing the crystal structure in the MePc films.

Nevertheless, the most extended approach with a view to controlling the MePc properties is changing the metallic ion. There are plenty of studies exploring the effect of different metal centres in the MePc properties [138, 139]. Sun *et al.* [140] studied MePc (Me = Mn, Fe, Cu) adsorption on Fe[110] surface using first-principles calculations. Their results showed an almost planar molecular geometry after adsorption. MePc preferred the top site adsorption in all cases on this surface. The spin-polarized states of the central Mn and Fe atoms changed because of the strong interaction with the iron surface. In a similar way but with a different surface, Hu *et al.* [141] theoretically investigated MePc (Me = Mn, Fe, Ni, Cu) adsorption on Au [111]. The preferred adsorption site was at hcp site for all molecules with the exception of MnPc that preferred the top site. Charge transfers between metallic ions and the surface at the molecule-surface interface accompanied the adsorption. In addition, they predicted that Kondo effect could be observed for the MnPc and FePc molecules on this surface because of the magnetic moments remaining after adsorption.

A purely experimental work was done by Grobosch *et al.* [142]. They studied the influence of transition metals (TM) ($\mathbf{d}^5$-$\mathbf{d}^{10}$) in the electronic properties of MePc films formed on KBr and Au substrates. Using electron energy-loss spectroscopy (EELS) and x-ray (XPS) and ultra-violet (UPS) photoelectron spectroscopy they showed the increasing impact of the **3d** metal states on the electronic properties. They probed that the electronic states close to the Fermi level are formed with the contribution of the **3d** shell of the metal in the FePc and MnPc cases. Bathon *et al.* [143] presented an attractive approach to the issue. They studied self-assembled networks of MePc (Me = Mn, Co, Cu) in a chalcogenide topological insulator Bi_2Te_3. STM observations permitted to explain the self-assembly process. Whereas most MnPc molecules do not showed any tendency to self-assemble due to the intermolecular repulsive interaction and the strong adsorption in the substrate, CoPc and CuPc molecules form self-assembled molecular film. These authors claimed that this

difference is produced by the presence of $\mathbf{d}_{z^2}$ orbitals near the Fermi level. As the number of electrons on the metal core increases, these orbitals are more populated and the interaction with the surface is reduced leading to better conditions for the self-assembly.

The codeposition of CuPc as a donor and perfluoropentacene (PFP) as an acceptor was explored on silver and copper surfaces [144]. STM and XSW results showed a variation in the adsorption height of the PFP (increased by ~ 0.3 Å) upon mixing, while CuPc remains the same in both substrates. The interaction between molecules is dominated by hydrogen-bond interactions. The authors could measure the effective PFP dipole variation leading to a variation of the surface work function.

Many studies of the interaction between the MePc and surfaces combine experimental and theoretical investigations. This allows comparing and contrasting the results to account for the experimental observations. For example, the coadsorption of the 3,4,9,10-perylene tetracarboxylic dianhydride (PTCDA) and CuPc on Ag[111] was investigated using scanning tunneling spectroscopy (STS), XPS, ARPES, normal incidence X-ray standing wave (NIXSW) and first-principles calculations [145]. Both molecules present a weak chemisorption on the silver substrate. In addition, the results showed that when both molecules are simultaneously adsorbed, the Ag[111] surface transfers charge to the PTCDA molecule, filling its lowest unoccupied molecular orbital (LUMO) while the CuPc LUMO remains empty. Thus, PTCDA is a stronger acceptor and CuPc turns into a donor.

Mugarza *et al.* studied extensively MePc molecules adsorbed on Ag[100]. Using STM and *ab initio* calculations they investigated the effect of dopants within CuPc and NiPc deposited on the surface [146]. They probed the electronic properties of the molecules co-adsorbed with Li atoms. They showed that each molecules could host up to six dopant atoms, occupying three different doping sites. The amount of charge transfer to the molecule was controlled by the number of dopants embeded in the molecule, while the molecular band gap depends on distance between the MePc and the Li dopants. Moreover, in a previous work these authors were able to control the spin degeneracy by artificially fabricating molecular clusters of different size and shape [147]. In addition, in a complete study of MePc (Me= Fe, Co, Ni, Cu) adsorption on Ag[110] using STS, STM and DFT they proved that the amount of charge transfer from the substrate to the MePc is similar in all cases [148]. For the FePc and CoPc molecules the hybridization of the metal core orbitals with the surface reduces the magnetic moment. However, in the case of NiPc and CuPc phthalocyanines an additional magnetic moment is induced on the aromatic Pc ligand, leaving the metal core spin unperturbed. This behaviour is due to the small hybridization of the planar $\mathbf{d}_{x^2-y^2}$ orbital with the metallic surface.

Petraki *et al.* centred their attention in the charge transfer between metal phthalocyanines and the substrate. The experimental observations were done with XPS, UPS, x-ray absorption spectroscopy (XAS) and x-ray resonant photoemission spectroscopy (ResPES) techniques. They studied the electronic structure and the interface properties of FePc adsorbed on Ag[111] and Au[100]. The **3d** states in the metal core are involved in the interface interaction through the charge transfer with the Ag[111] surface. In contrast, on Au[100], the Fe molecular orbitals do not show significant changes. Thus, FePc interaction with the surface depends strongly on the metal substrate [149]. In the case of MnPc adsorbed on Au[100], the **3d** metal orbitals contribute to the highest occupied molecular orbital (HOMO) and there exists a clear MnPc/Au interface interaction due to charge transfer between the substrate and the manganese atom. In addition, they observed that the N-atoms exhibit a strong interaction with the metal centre. A clear signature of this was observed in the hybridization between unoccupied N p-states with the $\mathbf{d}_{zx}$ and $\mathbf{d}_{zy}$ electronic states of the Mn-central atom [150]. In the case of the adsorption of CoPc and MnPc on Ag[111] a significant charge transfer was expected in analogy to previously explored cases. In fact, for the CoPc a significant charge transfer from the substrate to the central metal Co atom was observed. This produced a **3d** electron redistribution inducing changes in the Co-related absorption spectra. The same behaviour was observed in the MnPc spectra, but it was less pronounced because of a weaker change of the electronic configuration on the metallic ion [151].

Thus, it is clear that phthalocyanines are interesting molecules, whose adsorption on metal substrates has attracted a large amount of experimental and theoretical work in recent years. To compare with our own results, they are specially relevant the works for MePc molecules adsorbed on Ag[111]. For example, Huang *et al.* studied, theoretically (DFT) and experimentally (UPS), the adsorption of CuPc and ZnPc on Ag[111] [152]. Their results indicated that the charge transfer from the silver substrate to the molecule is a key ingredient to understand the strong interaction with this substrate. This was reflected in the partial filling of the LUMO orbital, as well as in the reduction of the adsorption height and the work function. Continuing with CuPc on Ag(111), the experimental work by Kröger *et al.* [153] is also very relevant. They measured the distance between the molecule and the substrate using spot profile analysis low-energy electron diffraction (SPA-LEED), NIXSW and UPS techniques, as well as DFT calculations. The weak intermolecular attractive force permitted the molecules to move freely at low coverages, avoiding the formation of islands. As the coverage increases, they form a commensurate superstructure that derives into a point-on-line (POL) phase. They proved that there is a competition between the charge transfer with the substrate and the intermolecular interaction with the nearest neighbours. As the coverage increases, molecules tend to separate from the surface in order to compensate the increment

in the Pauli repulsion due to the overlapping of their the electronic states and the cost of being forced to stay in an unfavourable adsorption site. They also studied TiOPc adsorption on Ag[111] using the same methodology plus STM and high resolution electron energy loss spectroscopy (HREELS) techniques [154]. Their results showed a similar behaviour than for CuPc, finding three different adsorption phases depending on the coverage on the surface as in the previous case. Their NIXSW data, together with the work function variation, indicated that the TiOPc adsorption happens with the Ti-O group pointing towards vacuum. Increasing the coverage, they studied multilayer adsorption, where the second layer presents a Ti-O down orientation. This neutralizes the dipole moment of the first layer stabilizing the bilayer structure.

In the present chapter we present our own results for the low coverage adsorption of TiOPc on Ag(111). Our work is motivated by a collaboration with the group of Prof. P. Jakob at Philipps-Universtät in Marburg (Germany). The focus of this work was to clarify the structure of the commensurate phase. Our results for the TiOPc adsorption on Ag[111] revealed a flat-lying geometry when the molecule is adsorbed [16]. In accordance with the previously discussed results, we observed three different adsorption phases, a 2D-gas phase at low coverage, changing into a well ordered commensurate phase (c-phase) and as the coverage increases a POL phase. The combination of STM, SPA-LEED, infrared absorption spectroscopy (IRAS) and DFT calculations permitted to understand the molecular arrangement in the commensurate phase. It was found that this phase is constituted by molecules adsorbed on bridge positions with two different orientations over the substrate. As described in more detailed below, our theoretical results indeed showed a small preference of the TiOPc molecule for adsorption on bridge sites. Still, most of the properties, at least in the low/medium coverage regime, were rather insensitive to the adsorption site. This includes the electronic structure of the molecules, that we found to be similar for the different adsorption sites. In particular, in spite of the calculated position of the LUMO close to the Fermi level of the system, our calculations did not find a large charge transfer to the molecule. This is in contrast to the experimental result that found, even if small, a partial population of the LUMO. Furthermore, in the commensurate phase, the different STM contrast of molecules showing the two different orientations seems consistent with a slightly different charging of these two species. Finally, IRAS measurements of the Ti-O stretching band showed a stable intensity increment with coverage, indicating that the molecular adsorption takes place with the Ti-O group pointing towards vacuum.

In spite of the many experimental and theoretical studies developed until now, a perfect understanding on the interaction between MePc and surfaces has not been achieved yet. In addition to the extensively investigated TiOPc we also study MePc (Me = Cu, Mn) adsorption

on the Ag[111] surface. Our purpose in choosing these particular MePc molecules is two fold. On the one hand, it is driven by the collaboration with different experimental group. CuPc and TiOPc has been studied in collaboration with the group of Prof. Peter Jakob in Germany as mentioned above, while MnPc was explored together with the group of Prof. José Ignacio Pascual in nanoGUNE in Donostia-San Sebastián (Spain) [17]. On the other hand, these molecules are expected to present clear differences in the way they interact with the silver substrate. We want to explore to what extent our theoretical tools can successfully predict the different behaviours. Furthermore, experimental results from nanoGUNE's group indicates that the inter-molecular interactions are very different for MnPc and the chlorinated manganese phthalocyanine (Cl-MnPc). This is an interesting opportunity to explore how the bonding ligand can change the way the molecules adsorb and assemble on the substrate. Thus, we also included Cl-MnPc to our pool of theoretically studied systems. We investigate the adsorption energies, geometries, charge transfer and magnetic moments after adsorption on the substrate. We analyse different adsorption sites and starting configurations. Thus, our calculations predict the most plausible adsorption geometries. We investigate the changes in the electronic structure of the molecule upon adsorption, in order to try to identify how they correlate with the adsorption site, the charge transfer and different metal-surface interaction. However, in most cases we found that the interaction between the MePc and the substrate is weak and not strongly influenced by the adsorption site. Our results are consistent with the experimental observation of charge transfer into the LUMO orbital in the MnPc and Cl-MnPc molecules. Finally, we study the induced electron density and the dipole moment of all the systems. All these analysis give us a global view of the MePc interaction on this coinage metal substrate. Moreover, we are able to identify the main characteristics of the MePc-surface interface. Thus, our calculations provide insight that will help to understand how the metal centre controls the interaction between the molecule and the surface.

3.2 Methodology

Our theoretical approach to MePc was performed using VASP (version 5.3.5) [12] and the PBE functional [55]. The D3 Grimme approximation [63] was included in the calculations with a view to incorporating the long-range van der Waals interactions. We used a 400 eV plane-wave cutoff as well as the PAW method [99] to describe the atomic cores.

The lattice constant obtained for Ag bulk is 4.073 Å, in good agreement with the experimental value 4.056 Å [60]. We employed a k-sampling of 25x25x25 Monkhorst-Pack grid [91] in the bulk calculation to sample the Brillouin zone. After that, using this lattice parameter, an Ag[111] slab was created. It contained 3 layers and only the topmost surface

layer was relaxed. The relaxation of the system was performed until the forces acting on all the atoms were smaller than 0.03 eV/Å. We kept a large vacuum distance ($\sim$ 20 Å) to avoid interaction between periodic replicas of the slab along the z-direction.

To study the interaction of the molecule with the surface in the low coverage regime we used a (7x4$\sqrt{3}$) lateral supercell and a 3x3x1 k-point sampling. Thus, these calculation aim to explore mostly the effects of the molecule-substrate interaction. In this system, MePc on Ag [111], we explored different adsorption configurations that will be described extensively below. Figures representing the MePc adsorption configurations, as well as the corresponding induced electron density were created using the VESTA software [155]. The adsorption energy (E_{ads}) is obtained using **Eq. 2.1** and the population analysis was performed with the same methodology than in **Chapter 2**. Molecular heights reported along the chapter were obtained using the topmost surface layer average height as a reference.

The induced electron density for the system was calculated as:

$$\Delta n = n_{system} - n_{adsorbate} - n_{adsorbent} \tag{3.1}$$

where n_{system} is the total electron density obtained in our system. $n_{adsorbate}$ is the electron density calculated for the MePc molecule on gas phase with the frozen atoms in the adsorption geometry in the same supercell. $n_{adsorbent}$ is the electron density obtained for the substrate with the frozen atoms in the adsorption geometry and in the same supercell.

The dipole moment for the molecule in the gas phase was calculated as:

$$\vec{\mu}_j = \sum_i^N Q_i R_i - \int n_{molecule}(\vec{r}) r_j d\vec{r} \tag{3.2}$$

the induced dipole moment is obtained as:

$$\vec{\mu}_{j_{induced}} = \int \Delta n(\vec{r}) r_j d\vec{r} \tag{3.3}$$

where, $\vec{\mu}_j$ is the dipole moment in the j direction, N is the number of atoms in the system, Q_i is the atomic valence charge and R_i the atom position. Δn(**r**) is the induced charge defined above and r_j the position vector in the j direction.

3.3 Results

3.3.1 Adsorption energy and geometry

MePc are formed by a central frame whose carbon atoms bond to four benzene rings. Additionally, MePc possesses metallic centre. This metal centre is usually a transition metal, and can be used to control the electronic and optical properties of the molecule and the way it interacts with the substrate.

3.3.1.a *TiOPc/Ag[111]*

We have deeply studied the interaction between the TiOPc and the Ag[111] surface. TiOPc is a non planar π-conjugated molecule due to the oxygen atom bonding the central metal ion. It produces a pyramidal structure (see **Figure 3.1**).

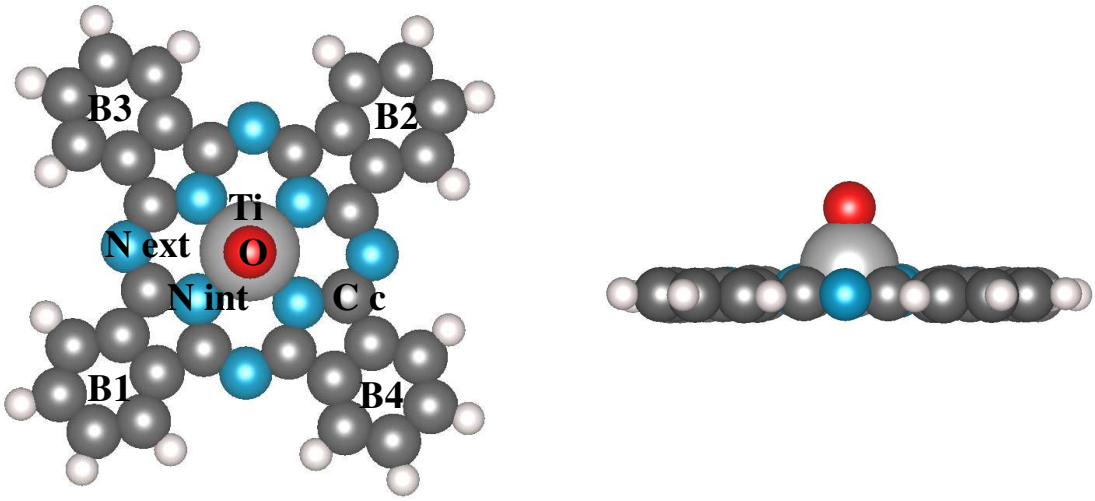

Fig. 3.1 Relaxed structure of TiOPc in the gas phase, top and side view. N int are the nitrogen atoms bonding the metallic core, N ext correspond to exterior nitrogen atoms in the central ring. C c are carbon atoms in the central frame and B1, B2, B3, B4 the different benzene rings.

Our simulations have contemplated two possible geometries with the Ti-O group pointing towards vacuum (**O-up**) or the other way round, with the oxygen interacting with the surface (**O-down**). We have investigated three possible adsorption sites where the metal core is at fcc, top or bridge sites on the surface. In addition, the azimuthal angle on the surface plane was also taken into account. We have considered two different geometries as a function of the azimuthal angle: (i) with two of the inner-ring N atoms aligned along the $\langle \bar{1}10 \rangle$ high

symmetry direction of Ag[111], in the following referred to as **top**$_+$ and **bridge**$_+$ and (ii) a 45° rotated geometry of the TiOPc molecule with respect to the $\langle\bar{1}10\rangle$ high symmetry direction of the surface. These last configuration are designated as **fcc**$_\times$, **top**$_\times$ and **bridge**$_\times$. All relaxed adsorption geometries are plotted in **Figure 3.2** for the Ti-O pointing towards vacuum.

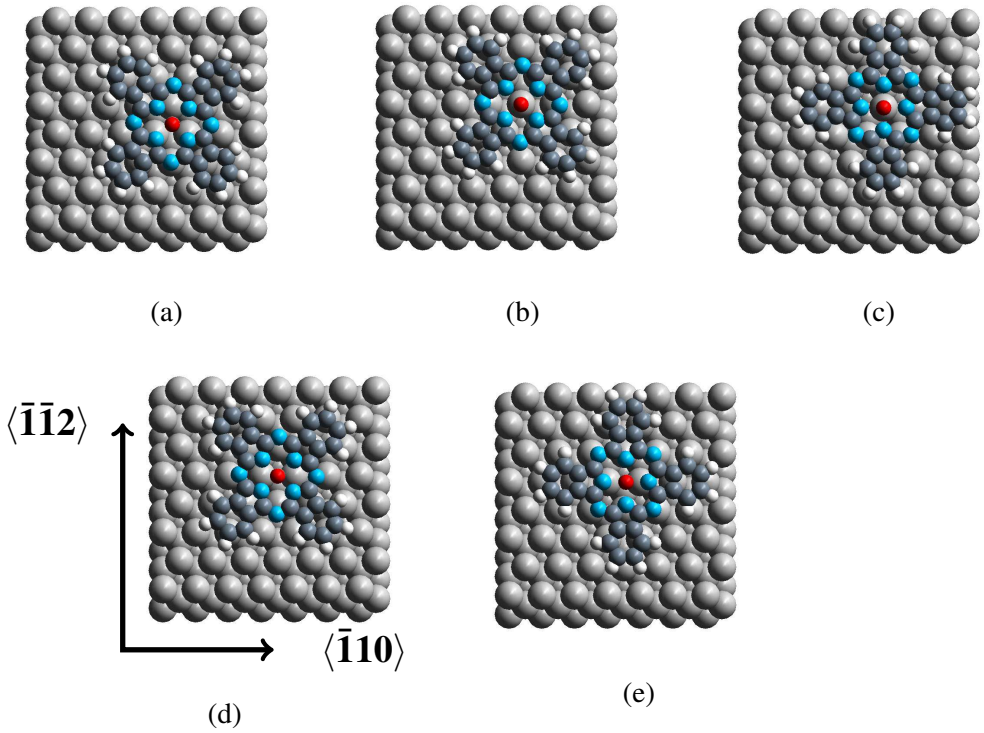

Fig. 3.2 TiOPc adsorption sites on Ag[111]. The adsorption site is defined by the metal core site on the surface and the azimuthal angle of the MePc on the substrate. The molecules are oriented either so that two of the inner-ring N atoms are aligned along the $\langle\bar{1}10\rangle$ high symmetry direction of the Ag[111] (X) or rotating 45° the molecule with respect to the $\langle\bar{1}10\rangle$ (+). Thus, the adsorption sites are: a) fcc$_\times$, b) top$_\times$, c) top$_+$, d) bridge$_\times$ and e) bridge$_+$.

We have used a 7x4$\sqrt{3}$ supercell, in this way, the distance between periodic TiOPc molecules is considered to be large enough to avoid significant interactions between periodic images (see **Figure 3.3**). Table **Table 3.1** shows the distances between adjacent molecules along both $\langle\bar{1}10\rangle$ and $\langle\bar{1}\bar{1}2\rangle$ surface directions. The distance is defined as the minimum distance between the atoms belonging to neighbouring molecules. We can see that the lowest distance corresponds to the **+** configurations, but it is still close to 7 Å. Thus, these calculations represent a relatively dilute system, where we can expect a dominant role of the molecule-surface interactions. We have also measured the molecular separation for the other MePc's, obtaining similar distances (see the tables in **Appendix A**).

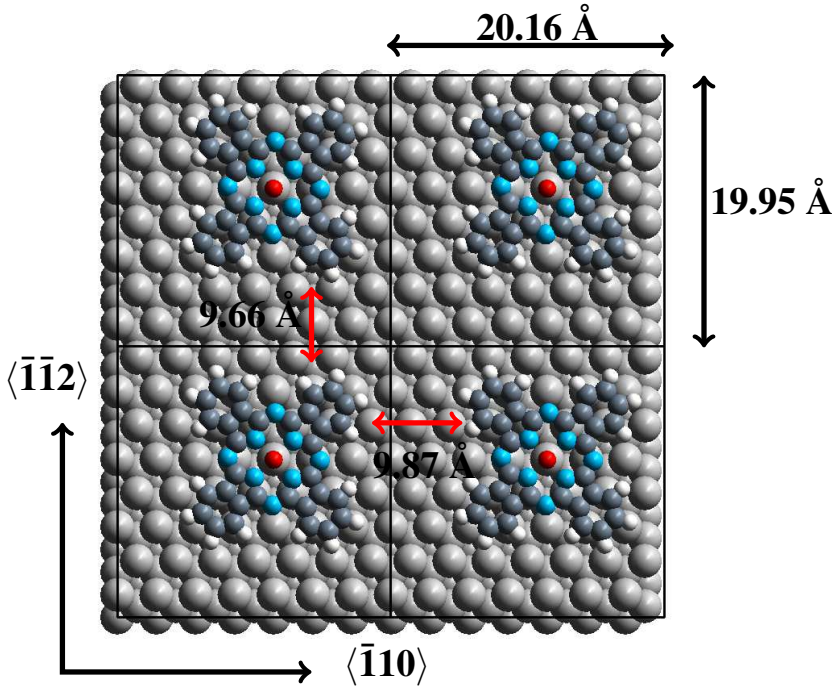

Fig. 3.3 TiOPc adsorption on Ag[111] at top$_\times$ site.

We have calculated the adsorption's height of the MePc molecules over the surface. The surface topmost layer was taken as reference, however, distances have been referred to the molecular plane. The molecular plane is define as the average of the vertical positions of all the atoms in the molecule with the exception of the metal centre and the hydrogen atoms. Therefore, $h1$ is the distance between the metal core and the molecular plane (positive when the metal core is above the molecular plane or negative if it is under the plane) and $h2$ is the height from the surface topmost layer to the molecular plane (see **Figure 3.4**).

The TiOPc adsorption energies are presented in **Table 3.2**. When the titanyl group is pointing towards vacuum, the preferred adsorption site on the Ag[111] is at **bridge**$_+$ (E$_{ads}$ = 3.741 eV) which is $\sim$ 54 meV more stable than **bridge**$_\times$ and **top**$_\times$. The **fcc**$_\times$ adsorption energy is $\sim$ 78 meV less stable, while the **top**$_+$ site is $\sim$ 200 meV less stable than the **bridge**$_+$. The adsorption heights are very similar ($h2 \sim 3.29$ Å) for all adsorption sites, showing only small differences. The variation on the Ti-O bond length is extremely small, less than 0.003 Å, pointing out the absence of a direct interaction between the substrate and the metallic atom in the molecule. Nonetheless, after adsorption the distance between the molecular plane and the metallic ion $h1$ is reduced from the original 0.70 Å to the final $\sim$ 0.64 Å. The heights of different types of atoms at different adsorption sites are presented in **Table 3.3** and depicted in **Figure 3.5**. In general we only observe a minimal molecular

Table 3.1 Distance between adjacent TiOPc molecules (C-C) along the high symmetry direction of the Ag[111] (see **Figure 3.3**).

	$\langle\bar{1}10\rangle$ (Å)	$\langle\bar{1}\bar{1}2\rangle$ (Å)
TiOPc fcc$_\times$	9.88	9.66
TiOPc top$_\times$	9.87	9.66
TiOPc top$_+$	7.00	6.79
TiOPc bridge$_\times$	9.87	9.66
TiOPc bridge$_+$	7.00	6.79
TiOPc fcc$_\times$ (O-down)	9.88	9.67
TiOPc top$_\times$ (O-down)	9.91	9.69
TiOPc top$_+$ (O-down)	7.06	6.82
TiOPc bridge$_\times$ (O-down)	9.90	9.68
TiOPc bridge$_+$ (O-down)	7.02	6.84

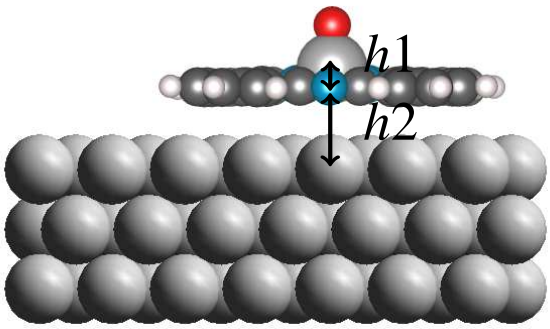

Fig. 3.4 TiOPc adsorption on Ag[111] at fcc$_\times$ hollow site (side view). h_1 is the distance between the molecular plane and the Ti atom (0.643 $\pm$ 0.012 Å) and h_2 is the distance from the surface topmost layer to the TiOPc molecular plane (3.294 $\pm$ 0.023 Å).

deformation after adsorption on Ag[111]. The molecular adsorption barely reduces the height difference between the benzene-rings and the inner ring of the molecule in comparison to the gas-phase geometry. Furthermore, the bending in the molecule with the benzene rings closer to the Ag[111] surface, indicates that the main interaction with the substrate is mediated, through van der Waals interactions, by the molecular framework and not by the metal ion.

We now will make connection with the experimental work performed by our collaborators in Philipps Universität at Marburg. From their measurements and previous data in the literature it is known that, as the coverage increases, an ordered c-phase appears on Ag[111]. However, the exact structure and the details of the molecular adsorption in this configuration were not known previous to our work. **Figure 3.6**, taken from Fernández *et al.* [16], shows an STM image and SPA-LEED data for this phase appearing at intermediate coverage above 0.6 ML. In this experimental data we can clearly identify two inequivalent molecules, with

Table 3.2 E_{ads} per molecule, Ti-O bond length, $h1$ distance between Ti atom and the TiOPc molecular plane, and $h2$ distance between the Ag [111] surface and the TiOPc molecular plane (see **Fig 3.4**).

	E_{ads} **(eV)**	**Ti-O (Å)**	$h1$ **(Å)**	$h2$ **(Å)**
TiOPc gas phase		1.686	0.707	
TiOPc fcc$_\times$	3.663	1.685	0.643	3.294
TiOPc top$_\times$	3.687	1.685	0.656	3.292
TiOPc top$_+$	3.538	1.684	0.643	3.299
TiOPc bridge$_\times$	3.688	1.684	0.653	3.292
TiOPc bridge$_+$	3.741	1.685	0.645	3.289

Table 3.3 Heights $\pm$ standard deviation in (Å) for the TiOPc in the gas phase and after adsorption on Ag[111]. The TiOPc molecular plane is used as reference.

	gas phase	**fcc$_\times$**	**top$_\times$**	**top$_+$**	**bridge$_\times$**	**bridge$_+$**
Ag[111] (h2)		-3.294 $\pm$ 0.023	-3.292 $\pm$ 0.022	-3.299 $\pm$ 0.025	-3.292 $\pm$ 0.022	-3.289 $\pm$ 0.020
Ti (h1)	0.707 $\pm$ 0.009	0.643 $\pm$ 0.011	0.656 $\pm$ 0.009	0.643 $\pm$ 0.009	0.653 $\pm$ 0.009	0.645 $\pm$ 0.009
N int	0.078 $\pm$ 0.035	0.064 $\pm$ 0.042	0.073 $\pm$ 0.031	0.065 $\pm$ 0.029	0.075 $\pm$ 0.030	0.066 $\pm$ 0.029
N ext	0.015 $\pm$ 0.044	0.016 $\pm$ 0.052	0.017 $\pm$ 0.039	0.018 $\pm$ 0.036	0.016 $\pm$ 0.038	0.015 $\pm$ 0.036
C c	0.029 $\pm$ 0.036	0.031 $\pm$ 0.042	0.033 $\pm$ 0.032	0.031 $\pm$ 0.030	0.034 $\pm$ 0.031	0.032 $\pm$ 0.030
B1	-0.039 $\pm$ 0.024	-0.036 $\pm$ 0.028	-0.038 $\pm$ 0.024	-0.036 $\pm$ 0.025	-0.038 $\pm$ 0.025	-0.036 $\pm$ 0.025
B2	-0.009 $\pm$ 0.027	-0.004 $\pm$ 0.037	-0.011 $\pm$ 0.031	-0.011 $\pm$ 0.032	-0.012 $\pm$ 0.032	-0.010 $\pm$ 0.032
B3	-0.031 $\pm$ 0.036	-0.028 $\pm$ 0.046	-0.031 $\pm$ 0.040	-0.028 $\pm$ 0.043	-0.032 $\pm$ 0.040	-0.028 $\pm$ 0.037
B4	-0.042 $\pm$ 0.024	-0.042 $\pm$ 0.029	-0.043 $\pm$ 0.027	-0.039 $\pm$ 0.029	-0.044 $\pm$ 0.026	-0.039 $\pm$ 0.025
Oxygen	2.393 $\pm$ 0.009	2.328 $\pm$ 0.011	2.341 $\pm$ 0.009	2.327 $\pm$ 0.009	2.337 $\pm$ 0.009	2.330 $\pm$ 0.009
central ring	0.041 $\pm$ 0.026	0.037 $\pm$ 0.031	0.041 $\pm$ 0.024	0.038 $\pm$ 0.022	0.042 $\pm$ 0.023	0.038 $\pm$ 0.022
Benzene	-0.030 $\pm$ 0.019	-0.028 $\pm$ 0.024	-0.031 $\pm$ 0.020	-0.028 $\pm$ 0.021	-0.031 $\pm$ 0.020	-0.028 $\pm$ 0.019
Molecular plane	0.000 $\pm$ 0.018	0.000 $\pm$ 0.022	0.000 $\pm$ 0.018	0.000 $\pm$ 0.018	0.000 $\pm$ 0.018	0.000 $\pm$ 0.017

different orientations, in the rectangular unit cell of the c-phase. A close inspection of the STM images indicates that the molecular diagonals (lines joining to benzene rings and passing through the center) of the two molecular species form azimuthal angles of approximately 4° and 27°, respectively, with respect to the $\langle \bar{1}10 \rangle$ direction.

In order to find these adsorption sites various possible geometries compatible with the experimental information (*e.g.*, size of the unit cell and shape of the cell from EELS and STM information) have been considered. In **Figure 3.7**, four different geometries have been proposed. The TiOPc molecule is adsorbed in the corners of the unit cells at (a) hcp hollow site, (b) fcc hollow site, (c) top site and (d) where the TiOPc is adsorbed at bridge site. Constraining the adsorption site in the corners determines the site of the second TiOPc molecule in the center of the box. To begin with, we can exclude the (a) and (b) adsorption arrangements in the substrate due to the associated unfavorable off-site adsorption geometry of the central molecule. For the (c) and (d) proposed configurations, in order to clarify which geometry is preferred by the system, we have studied the dependence of the adsorption energy with the azimuthal angle. Performing fully relaxed calculations for many different azimuthal angles is an extraordinarily demanding task from a computational point of view

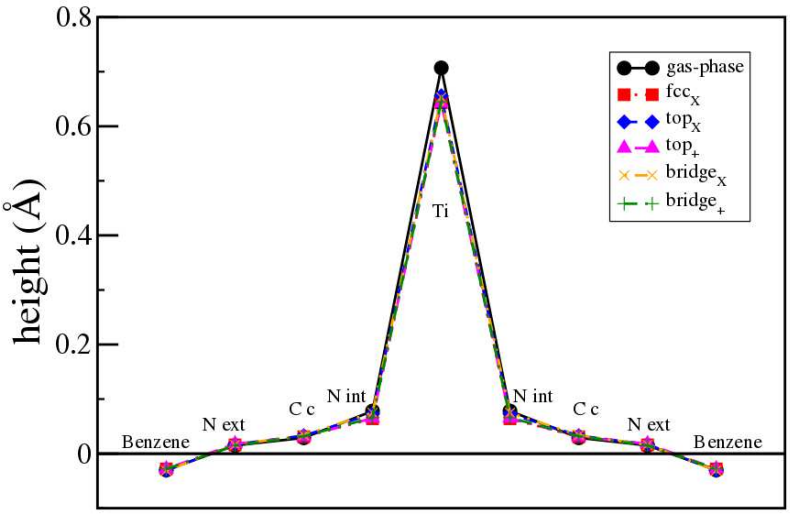

Fig. 3.5 Molecular height profile for the TiOPc in the gas phase (black) and after adsorption on Ag[111] at fcc$_\times$ (red), top$_\times$ (blue), top$_+$ (magenta), bridge$_\times$ (orange) and bridge$_+$ (green) adsorption sites. TiOPc molecular plane is used as reference.

given the size of our simulation cell (even that containing just one molecule). Therefore, it was necessary to adopt some simplifications. In this case we used fixed geometries taken, respectively, from the molecular gas-phase calculation and from the clean Ag[111] surface, and performed single-point total energy calculations as a function of the azimuthal angle. Results are plotted in **Figure 3.8**. In spite of this approximation, the computed adsorption energies are in good agreement with those obtained in the fully relaxed calculations. This is also consistent with our previous observation that geometrical changes are rather small upon adsorption. This indicates that the used approximation permits to extract meaningful conclusions about the most stable azimuthal angle. In the case of bridge adsorption, **bridge**$_+$ is the most stable geometry while for the top site, orientation **top**$_\times$ is preferred. Due to the fourfold symmetry of the TiOPc parallel adsorption on the substrate, same geometries are obtained after rotations of 90°. In the case of on-top adsorption the sixfold symmetry of the Ag[111] surface layer additionally leads to equivalent configurations for rotation angles with respect to the $\langle\bar{1}10\rangle$ azimuth of the substrate of Θ = 0°, ± 30° (**top**$_+$), as well as for Θ = 15°, ± 45° (**top**$_\times$). Examples thereof with the blue lines denoting the directions of the benzene 'wings' of TiOPc have been included in **Figure 3.8**.

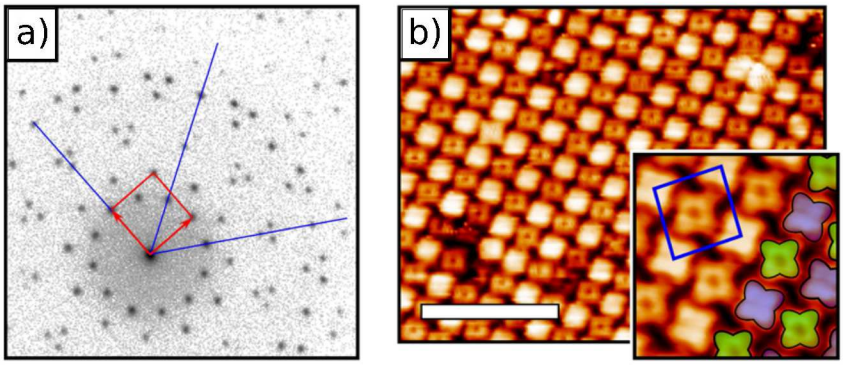

Fig. 3.6 a) SPA-LEED image and corresponding b) STM micrographs of the TiOPc monolayer c-phase on Ag[111]. In the SPA-LEED measurement the close-to-square surface unit cell and Ag[111] high symmetry directions are highlighted in red and blue, respectively. The STM micrograph reveals the presence of two molecules within the unit cell. The unit cell orientation and molecular schemes are superimosed to the image (U_{Bias} = 0.39 V, I_t = 150 pA). The scale bar in b) corresponds to 10 nm.

Combining the experimental results with the present calculations, we are able to determine precisely the TiOPc adsorption sites on Ag[111] in the c-phase. On the one hand, if the c-phase geometry takes the form suggested in **Figure 3.7 c**, one of the molecules should occupy the unfavorable **top**$_+$ site (with slight extra zimuthal rotations of either 3° or 4°). On the other hand, if the **Figure 3.7 d** configuration, two possible geometries should be considered, depending on which of the two molecules within the unit cell is rotated by either 4° or by 27° in correspondence with the STM images. The derived azimuthal rotations for the two TiOPc molecules from the analysis of the experimental data are indicated by the green (A) and the red (B) horizontal lines on **Figure 3.8**, where option A is energetically preferred arrangement.

Thus, based on our theoretical results and the STM measurements, we have proposed a model for the c-phase. As it is shown on **Figure 3.9**, there are two TiOPc molecules on the unit cell, one is at **bridge**$_+$ adsorption site and other is at **bridge**$_\times$ adsorption site. We assume that the Ti atoms are located on well-defined adsorption sites. However, the azimuthal angles of the molecules are slightly rotated in order to reduce the repulsive intermolecular interactions among adjacent molecules when their electron clouds overlap, this is also in better correspondence with the STM observation.

We have also investigated the possibility of the TiOPc inverted adsorption on the silver substrate. In this case the Ti-O group is pointing towards the Ag[111] substrate and the oxygen atom is directly interacting with the surface (**O-down**). The final geometries are

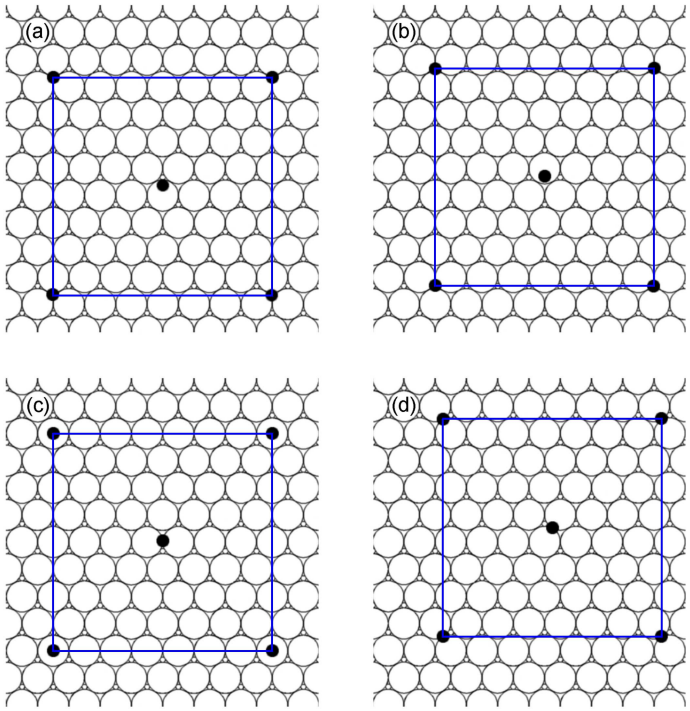

Fig. 3.7 Possible adsorption site combinations for the adsorption of two TiOPc within the rectangular unit cell in the commensurate phase. We label these arrangements according to the position of the molecule in the corner of the rectangular unit cell: (a) hcp site, (b) fcc site, (c) on-top site and (d) bridge site.

plotted in **Figures 3.10**. Adsorption energies in **Table 3.4** reveal that the **fcc**$_\times$ adsorption site is preferred (3.791 eV) in this case, nearby followed by **bridge**$_\times$ and **bridge**$_+$, which are just 10 meV and 25 meV less stable respectively. TiOPc top sites are less favourable for adsorption. According to the energy results, **top**$_+$ is 98 meV less stable than **fcc**$_\times$, while for **top**$_\times$ the energy difference increases up to 200 meV. Comparing with **O-up** configuration, **fcc**$_\times$ is more stable (40 meV) as compared to the preferred **bridge**$_+$ **O-up** adsorption site. Here it is interesting to point out that our terminology is somewhat misleading in this **O-down** case for the top and bridge configurations. These names make a clear reference to the position of the oxygen atom over the silver surface in the starting configuration. However, during relaxation, in those cases the oxygen moves from those high symmetry positions. This is in contrast to the fcc position, which is kept during relaxation. The oxygen predilection for the fcc hollow site adsorption on this substrate [156–158] is straightforwardly visible at top sites adsorption in the **Figure 3.10** . Although the molecule is well centered on a top site the position of the oxygen atom is moved off-centered from a perfect on-top position. A similar distortion, although somewhat less evident, also happens for the bridge configurations. The

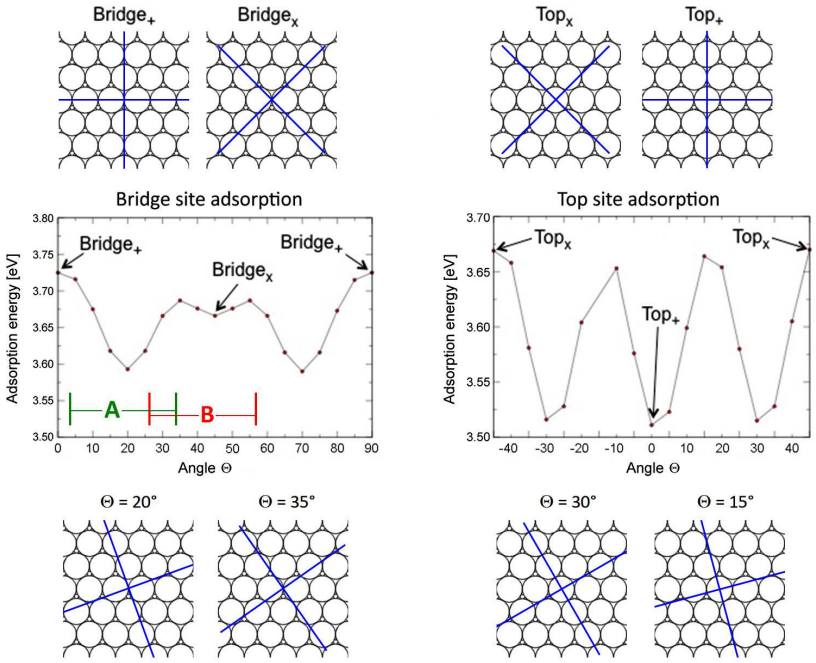

Fig. 3.8 TiOPc adsorption energy (eV) versus the azimuthal angle Θ when the molecule is adsorbed on Ag[111] at bridge and top sites.

strong interaction between the oxygen atom and the surface is clearly reflected in the Ti-O bond length. The titanium-oxygen bond-length increases by ~ 3.5 % , so it changes from the original 1.69 Å in the gas phase to ~ 1.75 Å after adsorption.

Table 3.4 E_{ads} per molecule, Ti-O bond length, $h1$ distance between Ti atom and the TiOPc molecular plane. $h2$ distance between the Ag [111] surface and the TiOPc molecular plane (see **Fig 3.4**).

	E_{ads} **(eV)**	**Ti-O (Å)**	$h1$ **(Å)**	$h2$ **(Å)**
TiOPc gas phase		1.686	-0.707	
TiOPc fcc$_\times$ (O-down)	3.791	1.748	-0.357	3.442
TiOPc top$_\times$ (O-down)	3.555	1.755	-0.409	3.479
TiOPc top$_+$ (O-down)	3.693	1.753	-0.366	3.468
TiOPc bridge$_\times$ (O-down)	3.781	1.763	-0.312	3.466
TiOPc bridge$_+$ (O-down)	3.766	1.746	-0.314	3.469

In addition, the distance between the molecular plane and the metal core $h1$ is reduced $\sim$ 0.35 Å with respect to the gas phase. This means a reduction of about 50% in the height of the metal core over the molecular plane. Thus, the interaction between the oxygen and the substrate weakens the bonding with the metallic centre, permitting the Ti atom to get closer

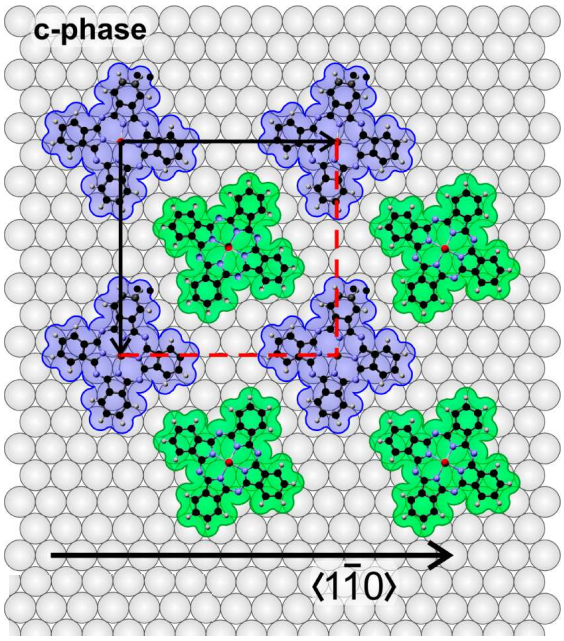

Fig. 3.9 TiOPc structure model of the molecular rearrangement in the c-phase.

to the N int atoms in the central frame Moreover, the distance between the molecular plane and the surface $h2$ increased to 3.44-3.48 Å. Therefore, $h2$ is $\sim$ 0.17 - 0.26 Å bigger than for the **O-up** adsorption configurations, leading to a weaker interaction between the molecular framework and the surface. All of that leads to a bigger distortion from the original geometry which is showed in **Figure 3.11**.

TiOPc **O-down** adsorption sites are barely more stable than those with **O-up** configuration. Therefore, it would be plausible to observe a competition between both **O-up** and **O-down** configurations. However, the experimental results [16, 153] reveals that the **O-down** geometry is not observed in the first wetting layer on Ag[111] at low temperature. This conclusion is mainly derived from the analysis of the vibrational spectrum using infrared spectroscopy [16]. There it is seen that the energy of the Ti-O stretching mode is only slightly modified upon adsorption and only weakly depends on coverage. This seems only compatible with **O-up** adsorption all the way up to 1 ML coverage. The reason why **O-down** configurations do not appear is not completely clear to us. It could be due to a larger energy barrier to access the most stable adsorption configuration that involves the formation of a Ag-O bond. However, we failed to find a theoretical evidence of such barrier. In our calculations the final **O-down** adsorption structures were found even starting from initial configurations with the TiOPc molecule at a considerable height over the substrate. In any case, experimental evidence seems to rule out the **O-down** adsoprtion of TiOPc below the 1

ML coverage. On the other hand, once a wetting layer of **O-up** molecules is formed, it has been suggested that the second layer has a tendency to arrange with **O-down** molecules in order to cancel the molecular dipoles.

Table 3.5 Heights ± standard deviation in (Å) for the TiOPc in the gas phase and after inverted (**O-down**) adsorption on Ag[111]. The TiOPc molecular plane is used as reference.

	gas phase	**fcc$_\times$**	**top$_\times$**	**top$_+$**	**bridge$_\times$**	**bridge$_+$**
Ag[111] (h2)		-3.442 ± 0.038	-3.479 ± 0.092	-3.468 ± 0.075	-3.466 ± 0.060	-3.469 ± 0.060
Ti (h1)	-0.707 ± 0.009	-0.357 ± 0.016	-0.409 ± 0.069	-0.366 ± 0.054	-0.312 ± 0.039	-0.314 ± 0.039
N int	-0.078 ± 0.035	0.102 ± 0.035	0.115 ± 0.345	0.136 ± 0.250	0.171 ± 0.153	0.167 ± 0.163
N ext	-0.015 ± 0.044	0.037 ± 0.039	0.071 ± 0.307	0.072 ± 0.234	0.090 ± 0.123	0.083 ± 0.128
C c	-0.029 ± 0.036	0.061 ± 0.033	0.086 ± 0.288	0.095 ± 0.217	0.115 ± 0.122	0.111 ± 0.129
B1	0.039 ± 0.024	-0.045 ± 0.073	-0.226 ± 0.094	-0.124 ± 0.128	-0.122 ± 0.124	-0.147 ± 0.110
B2	0.009 ± 0.027	-0.028 ± 0.060	0.070 ± 0.240	-0.001 ± 0.181	-0.058 ± 0.172	-0.043 ± 0.183
B3	0.031 ± 0.036	-0.045 ± 0.077	-0.049 ± 0.167	0.031 ± 0.192	-0.059 ± 0.175	-0.075 ± 0.132
B4	0.042 ± 0.024	-0.082 ± 0.064	-0.068 ± 0.179	-0.209 ± 0.126	-0.137 ± 0.117	-0.096 ± 0.133
Oxygen	-2.393 ± 0.009	-2.104 ± 0.016	-1.953 ± 0.069	-2.019 ± 0.054	-2.011 ± 0.039	-2.011 ± 0.039
central ring	-0.041 ± 0.026	0.067 ± 0.027	0.091 ± 0.211	0.101 ± 0.158	0.125 ± 0.094	0.120 ± 0.098
Benzene	0.030 ± 0.019	-0.050 ± 0.043	-0.068 ± 0.126	-0.076 ± 0.107	-0.094 ± 0.095	-0.090 ± 0.091
Molecular plane	0.000 ± 0.018	0.000 ± 0.032	0.000 ± 0.138	0.000 ± 0.108	0.000 ± 0.079	0.000 ± 0.078

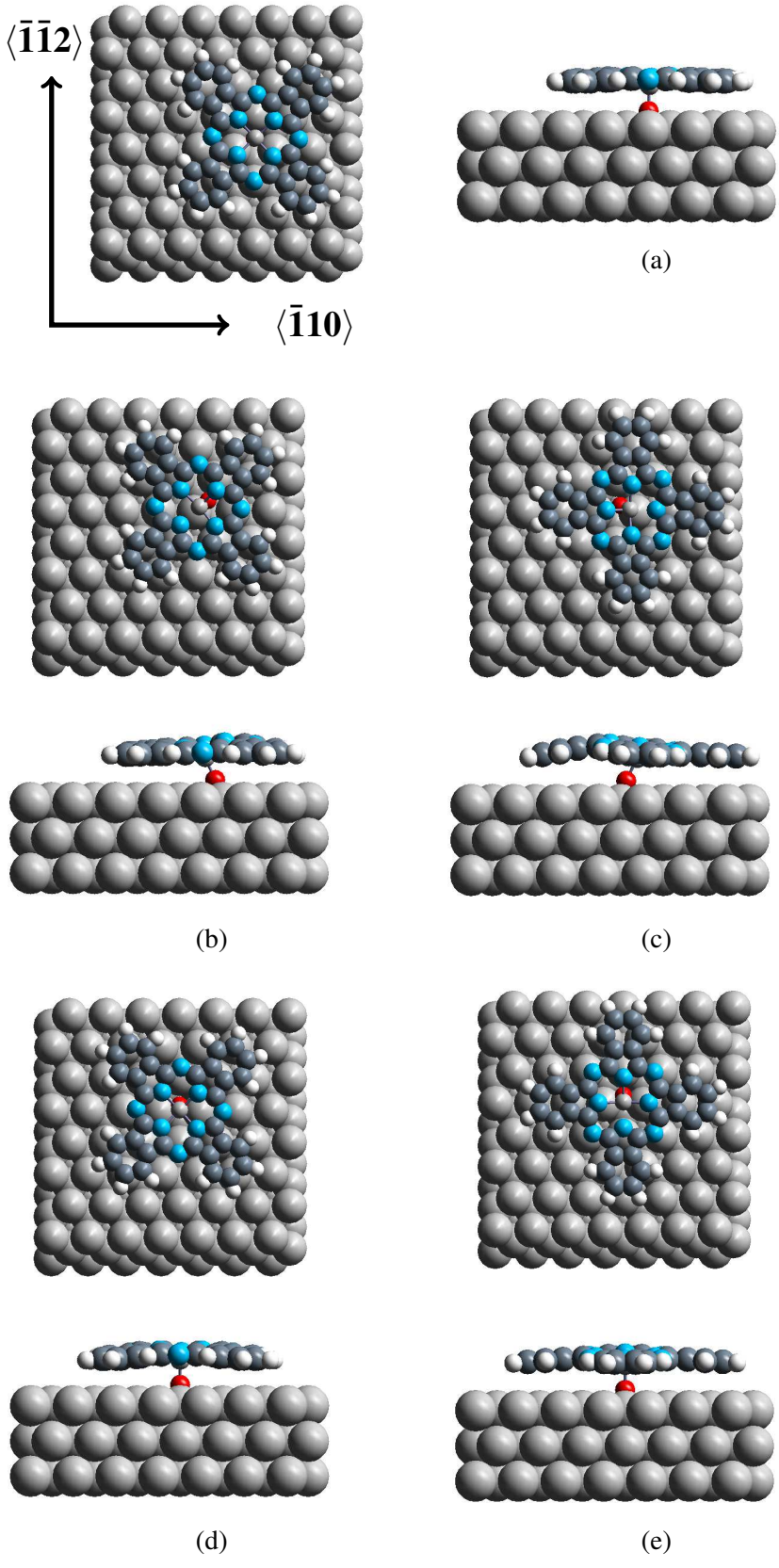

Fig. 3.10 **O-down** geometries for the TiOPc adsorption on Ag[111] at a) $fcc_{\times}$, b) $top_{\times}$, c) top_{+} d) $bridge_{\times}$ and e) $bridge_{+}$ sites. Top and side view.

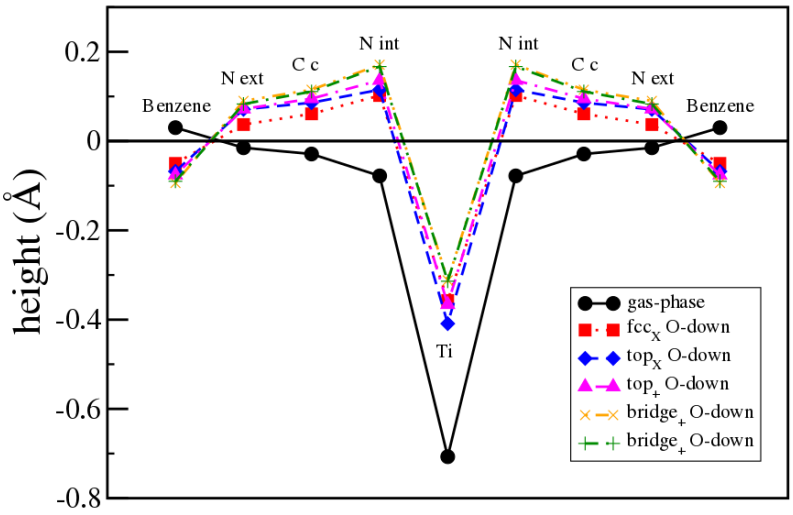

Fig. 3.11 Molecular height profile for the TiOPc in the gas phase and after (O-down) adsorption on Ag[111] at fcc$_\times$ (red), top$_\times$ (blue), top$_+$ (magenta), bridge$_\times$ (orange) and bridge$_+$ (green) adsorption sites. TiOPc molecular plane is used as reference.

3.3.1.b *CuPc/Ag[111]*

Continuing with the analysis of the metal phthalocyanines, we have studied the adsorption of CuPc on Ag[111]. We studied the same adsorption sites than for the TiOPc, specified on **Figure 3.2**. The addition of the copper atom to the phthalocyanine frame gives a magnetic moment to the molecule. The adsorption energies are presented in **Table 3.6** as well as its magnetization. Although after adsorption the molecule keeps its spin polarization it is slightly reduced due to the interaction with the surface.

Table 3.6 E_{ads} per molecule, magnetization per molecule (S), $h1$ distance between Cu atom and the CuPc molecular plane, and $h2$ distance between the Ag [111] surface and the CuPc molecular plane (see **Fig 3.4**).

	E_{ads} **(eV)**	**S** (μ_B)	$h1$ **(Å)**	$h2$ **(Å)**
CuPc gas phase		0.94	0.000	
CuPc fcc$_\times$	3.863	0.83	-0.161	3.224
CuPc top$_\times$	3.836	0.85	-0.105	3.218
CuPc top$_+$	3.705	0.87	-0.120	3.304
CuPc bridge$_\times$	3.874	0.87	-0.076	3.287
CuPc bridge$_+$	3.946	0.84	-0.160	3.200

As far as adsorption energies are concerned, the **bridge**$_+$ adsorption site is preferred. E_{ads} is 72 meV larger than form the **bridge**$_\times$ adsorption site, which is close in energy to the **fcc**$_\times$site. The **top**$_\times$ adsorption site is preferred over the **top**$_+$, however, it is still $\sim$ 109 meV less stable than the **bridge**$_+$. The $h1$ height changed due to the interaction with the substrate so the Cu metal core gets closer to the surface. Thus, from the original flat geometry, the metal core moves under the molecular plane. The molecular distance to the surface $h2$ is 3.20 Å at the most stable adsorption site, increasing up to 3.30 Å for the less favoured adsorption site (**top**$_+$). This seems to indicate that as the CuPc gets closer to the substrate the interaction increases. Nevertheless, the adsorption process does not affect strongly to the molecular geometry. As it is shown in **Figure 3.12**, the distortion in the CuPc molecule upon adsorption is small. A complete table with the atom heights is in **Appendix A**. Thus, after adsorption CuPc slightly vary its geometry, keeping a mostly flat molecular geometry. This fact together with its spin polarization is a clear signature that the metal core does not possesses a strong interaction with the silver substrate.

3.3.1.c *MnPc/Ag[111] and Cl-MnPc/Ag[111]*

We have also carried out research into the phthalocyanine adsorption using a Mn atom as metal centre on the same surface. Adsorption energies, heights and polarization moments

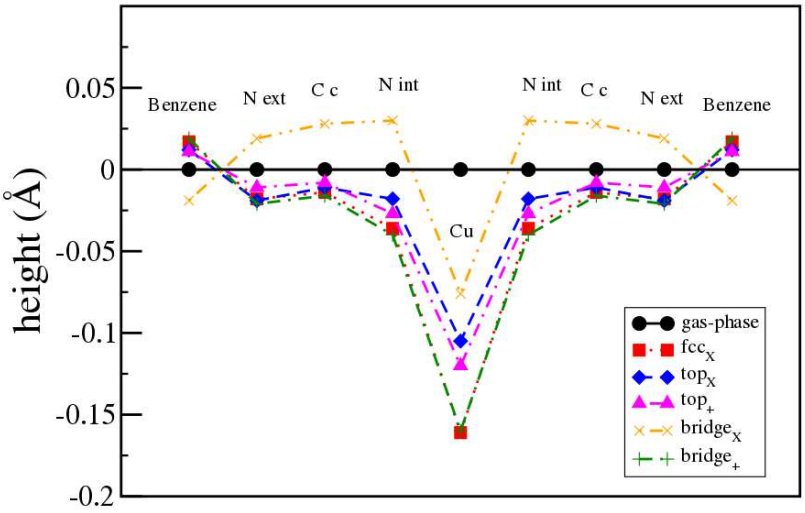

Fig. 3.12 Molecular height profile for the CuPc in the gas phase (black) and after adsorption on Ag[111] at fcc$_\times$ (red), top$_\times$ (blue), top$_+$ (magenta), bridge$_\times$ (orange) and bridge$_+$ (green) adsorption sites. CuPc molecular plane is used as reference.

are shown on **Table 3.7**. When the manganese is used as metal core the adsorption energy is slightly reduced in comparison with the previous cases. MnPc posses a strong magnetic moment ($\sim$ 3.00 μ_B) in the gas phase. However, MnPc's spin polarization disappears after adsorption because of the interaction with the surface. MnPc adsorption energy reveals that the **bridge**$_+$ site is preferred (3.578 eV) when the molecule is on the surface. The **fcc**$_\times$ and **bridge**$_\times$ sites showed a similar adsorption energy, which is $\sim$ 125 meV less stable than the **bridge**$_+$ adsorption site. Top sites are the less favourable sites. At **top**$_\times$ site its adsorption energy is reduced by 180 meV meanwhile the **top**$_+$ presents the smallest adsorption energy (3.199 eV) for this molecule.

The interaction between MnPc and the surface produces a strong variation in its geometry as it is shown in **Figure 3.13**. The TM directly interacts with the substrate so that $h1$ changes to $\sim$ -0.300 Å after the adsorption, moving closer to the topmost surface layer of silver. The adsorption height of the molecular frame, $h2$, is smaller than for the TiOPc and the CuPc molecules, being $h2$ at **bridge**$_+$ site 3.08 Å and increasing up to 3.20 Å for the less stable adsorption **top**$_+$ site. Because of metal-substrate interaction, there is a competition between the benzene rings that prefer a longer distance to the surface and the manganese atom which wants to be closer to the substrate. This produces a deformation of the molecule, passing

Table 3.7 E_{ads} per molecule, magnetization per molecule (S), $h1$ distance between Mn atom and the MnPc molecular plane, and $h2$ distance between the Ag [111] surface and the MnPc molecular plane (see **Fig 3.4**).

	E_{ads} **(eV)**	**S** (μ_B)	$h1$ **(Å)**	$h2$ **(Å)**
MnPc gas phase		3.00	0.000	
MnPc fcc$_\times$	3.456	0.12	-0.304	3.130
MnPc top$_\times$	3.398	0.12	-0.306	3.132
MnPc top$_+$	3.199	0.10	-0.363	3.200
MnPc bridge$_\times$	3.439	0.12	-0.251	3.150
MnPc bridge$_+$	3.578	0.01	-0.344	3.084

from a flat geometry to a inverse pyramidal-like structure. Thus, despite that the TM atom has a strong interaction with the surface and the molecule is globally closer to the substrate the adsorption energy has decreased in comparison to TiOPc and CuPc.

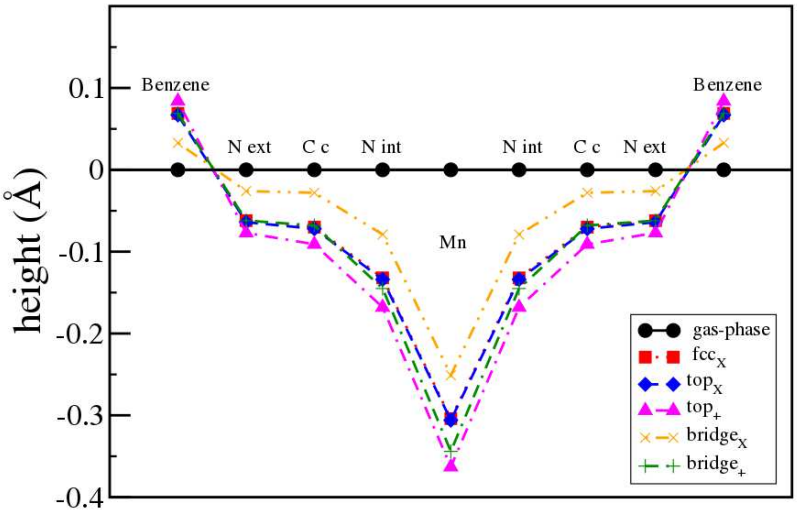

Fig. 3.13 Molecular height profile for the MnPc in the gas phase (black) and after adsorption on Ag[111] at fcc$_\times$ (red), top$_\times$ (blue), top$_+$ (magenta), bridge$_\times$ (orange) and bridge$_+$ (green) adsorption sites. MnPc molecular plane is used as reference.

The addition of a ligand (chlorine atom) to the manganese phthalocyanine was an interesting idea in order to compare how it affects to the molecular adsorption. This was also motivated by our collaboration with the group of Pr. J. I. Pascual at nanoGUNE [17], since in their work they initially sublimated chlorinated MnPc molecules over the surface. Upon

deposition on Ag[111] at room temperature most of the Cl-MnPc molecules lose their Cl ligand spontaneously. However, a few molecules maintain it. Therefore, it was instrumental to characterize the properties of both species on the Ag[111] surface to support the work of our experimental colleagues. Similar to the case of oxygen in TiOPc, here the Cl ligand binds to the Mn centre. This increases the spin polarization of the molecule up to 4.00 μ_B in the gas phase. Nevertheless, similar to the MnPc adsorption, after the Cl-MnPc is adsorbed on the substrate the molecule loses its magnetization. Adsorption energies, spin moments, Cl-Mn bond lengths are presented in **Table 3.8**. The **bridge**$_+$ is once again preferred over the other adsorption sites. Cl-MnPc adsorption energy at **bridge**$_+$ is 89 meV and 103 meV more stable than **bridge**$_\times$ and **fcc**$_\times$ adsorption sites, respectively. The adsorption at top site is less favoured, by 141 meV at **top**$_\times$ and 350 meV **top**$_+$ compared with the most stable adsorption at **bridge**$_+$ site.

Table 3.8 E_{ads} per molecule, magnetization per molecule (S), Mn-Cl bond distance, $h1$ distance between Mn atom and the Cl-MnPc molecular plane, and $h2$ distance between the Ag [111] surface and the Cl-MnPc molecular plane (see **Fig 3.4**).

	E_{ads} **(eV)**	**S** (μ_B)	**Mn-Cl (Å)**	$h1$ **(Å)**	$h2$ **(Å)**
Cl-MnPc gas phase		4.00	2.296	0.349	
Cl-MnPc fcc$_\times$	3.274	0.11	2.231	-0.004	3.156
Cl-MnPc top$_\times$	3.236	0.08	2.223	0.101	3.166
Cl-MnPc top$_+$	3.027	0.07	2.219	0.088	3.176
Cl-MnPc bridge$_\times$	3.288	0.13	2.222	0.039	3.143
Cl-MnPc bridge$_+$	3.377	0.05	2.238	-0.072	3.122

In the gas phase the Cl atom pulls the metal core out from its original equilibrium position, so $h1$ becomes 0.349 Å. After adsorption the Mn-Cl bond distance is shortened by $\sim$ 0.06 Å. This implies that the interaction with the surface reinforces the Mn-Cl bond. In addition, $h1$ is reduced when the molecule is on the substrate. At same time, the distance between the surface and the molecular plane $h2$ is slightly increased compared with the MnPc, and the distortion in the geometry is smaller (see **Figure 3.14**). In summary, the addition of the Cl ligand produces a less stable adsorption.

3.3.1.d *Summary of energetics and geometrical results*

We have discussed the energetics and geometrical results for MePc adsorption on Ag[111]. Adsorption energies, magnetic moments and heights for the most stable adsorption sites (**bridge**$_+$ in all cases) are shown in **Table 3.9**.

Regarding adsorption energies, CuPc is the most stable followed by the TiOPc molecule, which is 205 meV per molecule less stable. The oxygen atom bonding the Ti atom prevents

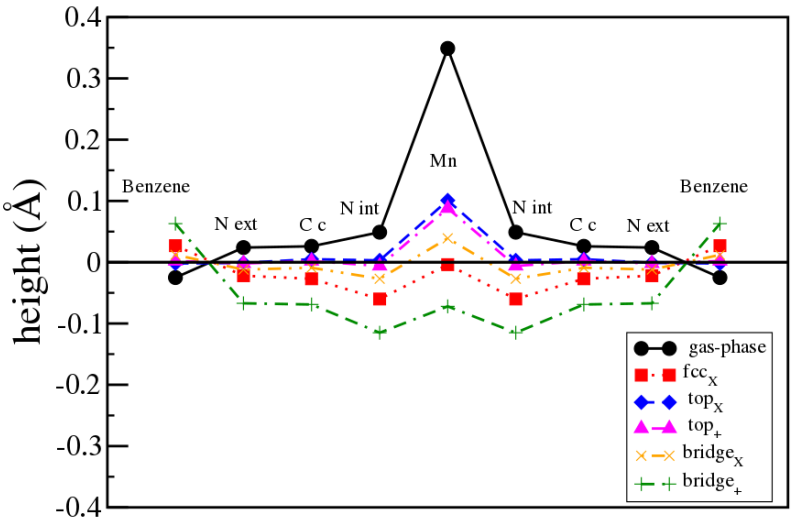

Fig. 3.14 Molecular height profile for the Cl-MnPc gas-phase (black) and after adsorption on Ag[111] at fcc$_\times$ (red), top$_\times$ (blue), top$_+$ (magenta), bridge$_\times$ (orange) and bridge$_+$ (green) adsorption sites. Cl-MnPc molecular plane is used as reference.

a strong Ti-surface interaction and increases the distance with the topmost layer. Despite the fact that CuPc keeps part of its magnetic moment after adsorption and is more distant to the surface ($\sim$ 3.20 Å) than MnPc or Cl-MnPc, it is energetically more stable. This is due to a smaller interaction between the metal ion and the surface. On the contrary, MnPc and Cl-MnPc lost their spin polarization when they are adsorbed on the surface. As happened with the TiOPc, the addition of the chlorine atom to the MnPc causes a less stable adsorption. Cl atom bonding pulls the metal centre out of the molecular plane, reducing the hybridization with the surface. Thus, ligands adsorbed on the TM reduce the interaction with the surface and tend to reduce the adsorption energies.

Nevertheless, the main result from adsorption energy and the geometries obtained is the adsorption site. As it was showed , in all cases studied the **bridge**$_+$ site was preferred whereas the **top**$_+$ was the less stable. It is a significant result, which stands out the importance of the stacking with respect to the surface atoms. Despite the different metal cores and ligands that we used in this theoretical study, the principal factor for the adsorption site selection is the relative molecular disposition above the surface and not the metallic centre. Of course, the ionic centre controls many important phenomena, such as the magnetic moment, the distance

to the substrate or the molecular distortion. However, the adsorption configuration selection does not strongly depend on it but involves all the atoms in the molecule.

Table 3.9 E_{ads} per molecule, magnetization per molecule (S), $h1$ distance between metallic centre and the molecular plane, and $h2$ distance between the Ag [111] surface and the MePc molecular plane (see **Fig 3.4**).

Adsorption site	E_{ads} **(eV)**	**S** (μ_B)	$h1$ **(Å)**	$h2$ **(Å)**
TiOPc bridge$_+$	3.741		0.645	3.289
CuPc bridge$_+$	3.946	0.84	-0.160	3.200
MnPc bridge$_+$	3.578	0.01	-0.344	3.084
Cl-MnPc bridge$_+$	3.377	0.05	-0.072	3.122

3.3.2 Bader charges and density of states

In an attempt to explain the nature of the metal-substrate interaction, we present now the Bader charges and the density of states within the molecule (DOS).

3.3.2.a *TiOPc/Ag[111]*

Valence Bader charges for TiOPc are presented in **Table 3.10** for the free-standing and the molecule adsorbed on Ag[111] both in the **O-up** and **O-down** configurations. It shows the titanium and oxygen atoms, as well as the molecular total charge. In the **O-up** configuration the molecule get slightly charged, taking ~ 0.2 e from the surface. However, the charge of the metal ion does not present a significant variation with respect to the gas phase. When the molecule is adsorbed in an inverted configuration (**O-down** geometry) the oxygen atom interacts directly with the surface. Correspondingly, the charge transfer between the surface and the molecule increases. Thus, TiOPc takes ~ 0.5 e from the surface, however, neither the Ti nor the O atoms show significant variations of their charges.

Figure 3.15 shows the charge variation on the TiOPc molecule by subtracting the atomic valence charge from the Bader atomic charge for all atoms in the molecule. While this plot clearly characterizes the strong ionic character of some of the bonds within the molecule, we do not find any significant or systematic variation in the atom's charge after adsorption. The same analysis was developed for all MePc molecules (see **Appendix A**).

The molecular PDOS (M-DOS) for the MePc systems adsorbed on the Ag[111] surface were calculated in all the proposed adsorption sites. TiOPc M-DOS is plotted in **Figure 3.16** for the **O-up** adsorption on the substrate. The molecule does not present significant variations in the electronic distribution related to the adsorption site. Thus, the electronic structure for the different adsorption sites is almost identical, which is completely consistent with the

Table 3.10 Valence Bader charges for the titanium atom, oxygen atom and the TiOPc molecule.

	Ti (e)	**O (e)**	**total charge (e)**
TiOPc gas phase	1.482	7.118	194.000
TiOPc fcc$_\times$	1.490	7.196	194.208
TiOPc top$_\times$	1.483	7.104	194.201
TiOPc top$_+$	1.489	7.096	194.216
TiOPc bridge$_\times$	1.485	7.100	194.204
TiOPc bridge$_+$	1.494	7.093	194.218
TiOPc fcc$_\times$ (O-down)	1.475	7.189	194.539
TiOPc top$_\times$ (O-down)	1.495	7.185	194.461
TiOPc top$_+$ (O-down)	1.488	7.184	194.419
TiOPc bridge$_\times$ (O-down)	1.470	7.192	194.544
TiOPc bridge$_+$ (O-down)	1.480	7.195	194.526

weak dependence of the adsorption energy on the molecular position above the substrate observed in the previous section. Moreover, the M-DOS presents a partial occupation in the LUMO at the Fermi level, although it is smaller ($\sim$ 0.2 e) in comparison with other metal phthalocyanines. This is consistent with experimental observations, nevertheless the LUMO occupation seems to be somewhat larger in the photoemission results [159].

It is obvious that there are minimum differences between adsorption sites as shows the M-DOS plotted for two different adsorption sites on **Figure 3.17** (**top**$_\times$ and **bridge**$+$). In addition, we have analysed the atomic contributions to the density of states. In order to get further understanding on the character of the different molecular states, we have plotted in the inset of **Figure 3.17** the PDOS onto the titanyl group and the molecular frame in the **bridge**$_+$ adsorption site. The LUMO corresponds with the molecular frame contribution. The central frame and the benzene rings participate in this molecular orbital. Thus, the small charge transfer upon adsorption takes place from the substrate onto the TiOPc backbone, while the population of the titanyl group remains unchanged as was shown in **Table 3.10**. The Ti atom contributes to the LUMO+1 orbitals (with $\mathbf{d}_{xy}$ character), however, with a negligible hybridization with the substrate due to the small geometrical distortion of the molecule after adsorption that keeps the Ti atoms far from the substrate. These facts support the notion that the TiOPc chemisorption is due to the aromatic body of the molecule instead of the metal core. This result was demonstrated experimentally by Koger *et al.* [154]. The charge transfer is distributed among the atoms in the molecular frame and the titanyl group does not show any clear signature of exchanging charge with the metal substrate.

A similar behaviour was found for the TiOPc adsorbed in the inverted geometry (**O-down**). The M-DOS showed in **Figure 3.18** does not present a clear difference between the

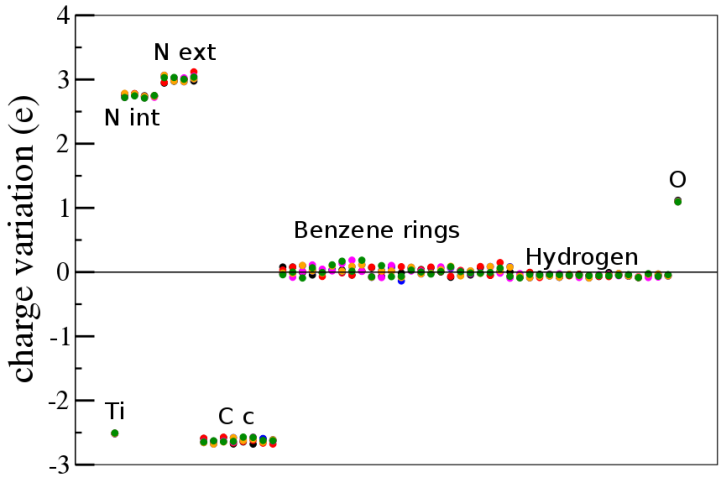

Fig. 3.15 Charge variation (Bader charge - atom valence charge) for all atoms in the TiOPc molecule in the gas phase (black) and after (**O-up**) adsorption on Ag[111] at $fcc_{\times}$ (red), $top_{\times}$ (blue), top_{+} (magenta), $bridge_{\times}$ (orange) and $bridge_{+}$ (green) sites.

possible adsorption sites around the Fermi level. Despite the fact that the TiOPc adsorption with the titanyl group pointing towards the surface produces a strong molecular deformation, the molecular electronic structure does not present a clear variation on the adsorption site. The increase of the charge transfer into the molecule from the surface indicated by the data in **Table 3.10** can be clearly seen in the larger partial occupation of the LUMO.

The molecular frame and Ti contributions are depicted on **Figure 3.19**. Contrary to the **O-up** case, the interaction between the surface and the oxygen leads to a small increment of the oxygen charge of ~ 0.1 electrons. The interaction between the titanyl group and the substrate lowers the energy position of the LUMO+1 with a large Ti content. This level now becomes almost resonant with the LUMO state, with delocalized character in the molecular frame, allowing the partial population of both molecular orbitals and explaining the larger charge transfer in this case. Thus, when the TiOPc adsorption takes place with the inverted configuration, the interaction between the surface and the TiOPc is due to the molecular backbone and the titanyl group.

3.3.2.b *CuPc/Ag[111]*

In the CuPc case, there is also a rather small charge transfer between the metallic substrate and the molecule. As it is shown in **Table 3.11**, the CuPc takes 0.195 e from the surface

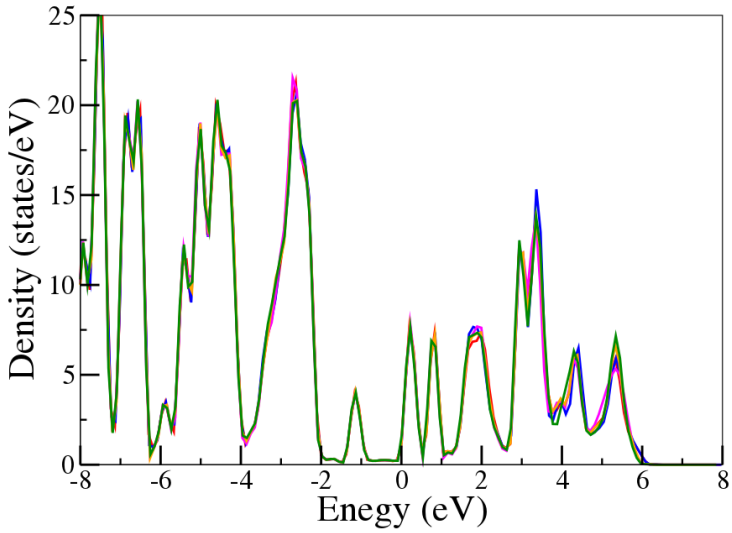

Fig. 3.16 M-DOS TiOPc comparison between adsorption sites. TiOPc (**O-up**) adsorption on Ag[111] at fcc$_\times$ (red), top$_\times$ (blue), top$_+$ (magenta), bridge$_\times$ (orange) and bridge$_+$ (green) sites. Energies are referred to the Fermi level.

in the most stable adsorption site (**bridge**$_+$). Nevertheless, just a 20 % of this charge is transferred to the metal core. The same behaviour is observed for the different adsorption sites, however, the charge taken by the metal core vary between 12% - 30% depending on the adsorption site selected. In spite of the fact that the molecule gets some charge from the surface, just a small fraction of it goes to the metal centre and the molecule keeps most of its initial magnetic moment after adsorption.

Table 3.11 Valence Bader charges for the cooper atom and the CuPc molecule.

	Cu (e)	**total charge (e)**
CuPc gas phase	9.905	195.000
CuPc fcc$_\times$	9.960	195.181
CuPc top$_\times$	9.961	195.174
CuPc top$_+$	9.927	195.177
CuPc bridge$_\times$	9.949	195.154
CuPc bridge$_+$	9.941	195.195

In **Figure 3.20** we have plotted the M-DOS for the different adsorption sites close to the Fermi level. Similar to the TiOPc case, the variation with the adsorption site is rather small. The LUMO is partially charged due to the interaction with the surface. **Figure 3.21** shows the PDOS molecular contributions for the **bridge**$_+$ adsorption site close to the Fermi level.

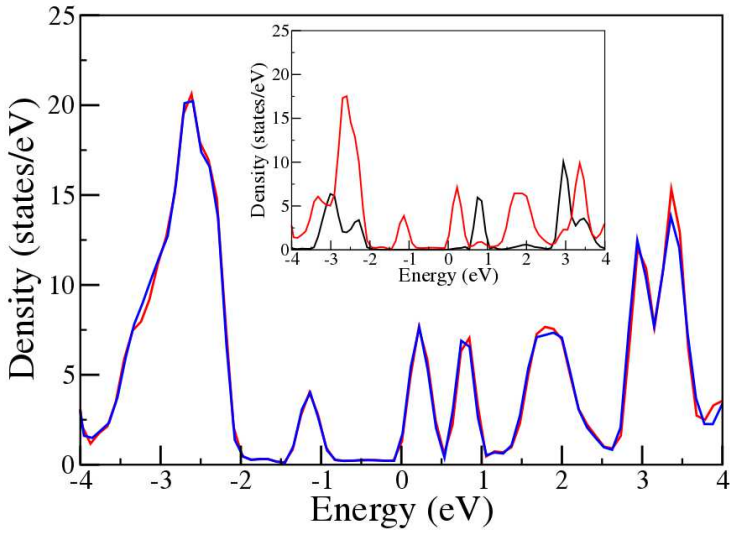

Fig. 3.17 M-DOS projected onto the molecule calculated for TiOPc on Ag[111] at top$_\times$ (red) and bridge$_+$ (blue) adsorption sites (**O-up**). The inset shows the M-DOS projected onto the titanyl group (black) and the molecular backbone (red) at bridge$_+$ site. Energies are referred to the Fermi level.

When the copper is acting as metal core, the LUMO is formed by an hybridization of the molecular frame with the $\mathbf{d}_{x^2-y^2}$ metal core orbital. The Cu atom gives to the molecule a magnetic moment ($\sim 1\ \mu_B$) in the gas phase. Our results show that the CuPc loses part of the magnetization after adsorption due to the charge transfer towards the molecule. Nevertheless, the molecule is still magnetic when it is adsorbed on the surface The inset of **Figure 3.21** contains the α spin and β spin contributions to the density of states for the metal centre. Nonetheless, the charge transfer is not enough to fully charge the metal orbital. This explains the fact that despite the interaction with the surface, the molecule keeps part of its original magnetic moment. In agreement with Mugarza's group conclusions [147], the hybridization between the $\mathbf{d}_{x^2-y^2}$ metal orbital and the surface is not significant. This explains why the CuPc molecule can retain its magnetization when adsorbed on Ag[111]. If the molecular orbitals would be substantially broaden by the interacion with the surface, most likely the spin polarization will be lost. Thus, we only find a small reduction due to the small charging.

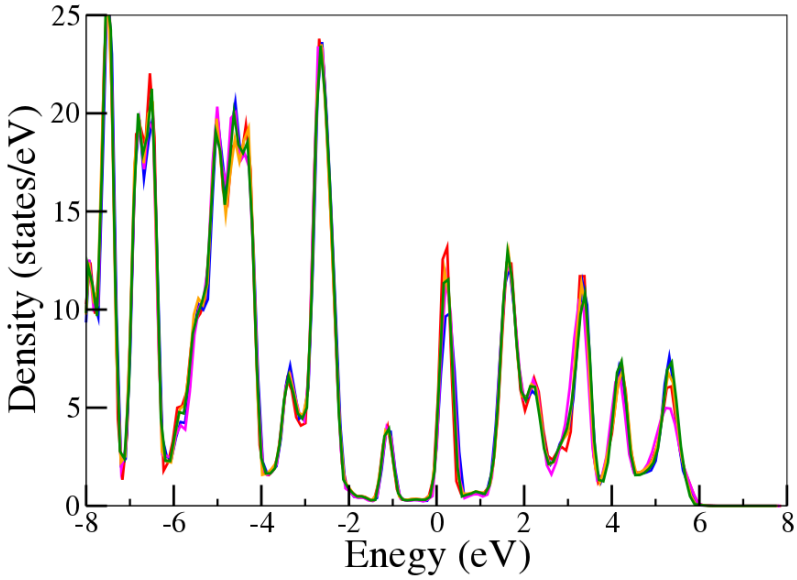

Fig. 3.18 M-DOS TiOPc comparison between adsorption sites. TiOPc (**O-down**) adsorption on Ag[111] at $fcc_{\times}$ (red), $top_{\times}$ (blue), top_{+} (magenta), $bridge_{\times}$ (orange) and $bridge_{+}$ (green) sites. Energies are referred to the Fermi level.

3.3.2.c *MnPc/Ag[111] and Cl-MnPc/Ag[111]*

For MePc formed by a manganese atom as metal centre the interaction with the surface is mediated by the aromatic system and the metal core. The MnPc has also a magnetic moment in the gas phase, although much larger than in the case of CuPc ($\sim 3\ \mu_B$). However, after adsorption it loses its magnetization. This is a clear indication of the increased interaction with the substrate. The charge transfer between the surface and the molecule increases in comparison with the TiOPc and the CuPc cases. **Table 3.12** contains the Bader charges for the Mn atom and the molecule. MnPc takes $\sim$ 0.7 e from the surface in the **bridge**$_{+}$ configuration. This amount is reduced until 0.608 e for the top adsorption site. The Mn atom keeps $\sim$ 1/3 of this extra charge. The charge transferred to the metal core is reflected in **Figure 3.22** where it is perceptible the charge variation in the Mn atom after adsorption. The remaining charge is divided among the atoms in the molecule and they do not show any clear variation in their charge.

The M-DOS is plotted in **Figure 3.23**. Similar to the other molecules presented so far, the M-DOS is very weakly dependent on the adsorption site. The HOMO and LUMO orbitals have a subtle variation for the **bridge**$_{+}$ adsorption site, however, we do not think

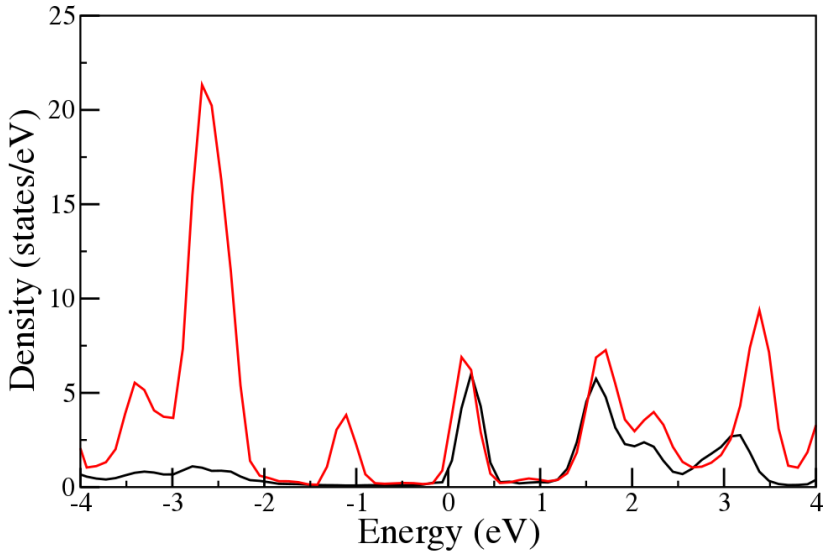

Fig. 3.19 PDOS TiOPc projected onto the titanyl group (black) and the molecular backbone (red) for the case of TiOPc adsorption in the bridge$_+$ (**O-down**) configuration. Energies are referred to the Fermi level.

Table 3.12 Valence Bader charges for the manganese atom and the MnPc molecule.

	Mn (e)	**total charge (e)**
MnPc gas phase	5.345	191.000
MnPc fcc$_\times$	5.546	191.672
MnPc top$_\times$	5.530	191.608
MnPc top$_+$	5.537	191.608
MnPc bridge$_\times$	5.530	191.646
MnPc bridge$_+$	5.547	191.713

it is really significant. The LUMO is not totally occupied. HOMO and LUMO are formed by the contributions of the metal core as well as the molecular frame. **Figure 3.24** shows the PDOS of the frame and the metal centre near the Fermi level at **bridge**$_+$ adsorption site. The inset contains the same information when the molecules is in the gas phase. An interesting observation is the spread of the $\mathbf{d}_{z^2}$ metal orbital around the Fermi level. It proves the powerful interaction between the metal core and the substrate that was previously inferred by the molecular deformation after adsorption. As it was observed in other surfaces [150], the orbital hybridization with the substrate is due to the interaction of the benzene rings and the **d** orbitals of the metal. Thus, the charge transfer at the interface is conducted by this two channels, the aromatic π-system and the $\mathbf{d}_{z^2}$ metal orbital.

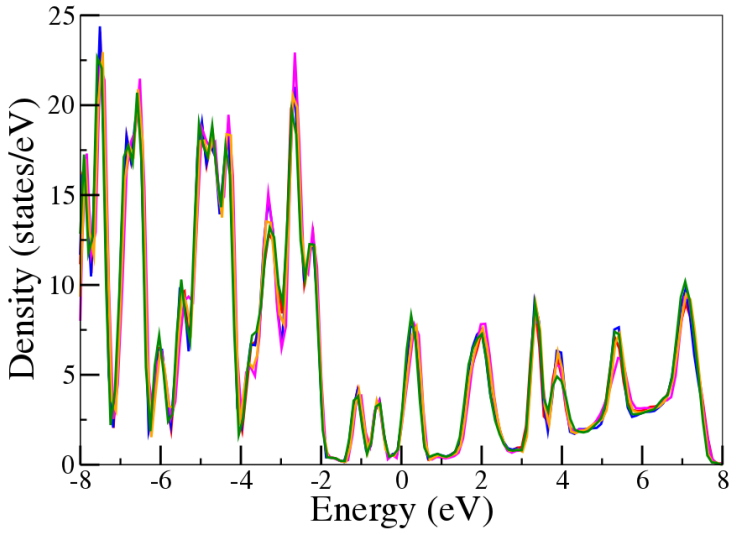

Fig. 3.20 M-DOS CuPc comparison between adsorption sites. CuPc adsorption on Ag[111] at fcc$_\times$ (red), top$_\times$ (blue), top$_+$ (magenta), bridge$_\times$ (orange) and bridge$_+$ (green) sites. Energies are referred to the Fermi level.

The addition of a chlorine atom has an important effect in the Mn metal core. When the Cl bonds to the metal there is a reduction of the charge transfer to the metal centre. This is expected, since Cl is a very electronegative species. Meanwhile the surface transfers a similar amount of charge to the molecule ($\sim$ 0.7 e) than in the MnPc case, which is explicitly showed in **Table 3.13**. Curiously, while this charge transfer from the substrate leads to a tiny increase of the Mn charge, that of Cl is slightly reduced up adsorption. The ligand produces an increment in the adsorption distance and, therefore, in the distance of the metal centre to the surface. This gives rise to a reduction in the interaction between molecule and substrate.

Table 3.13 Valence Bader charges for the manganese atom, chlorine atom and the Cl-MnPc molecule.

	Mn (e)	**Cl (e)**	**total charge (e)**
Cl-MnPc gas phase	5.237	7.620	198.000
Cl-MnPc fcc$_\times$	5.325	7.547	198.660
Cl-MnPc top$_\times$	5.301	7.556	198.614
Cl-MnPc top$_+$	5.278	7.551	198.654
Cl-MnPc bridge$_\times$	5.322	7.550	198.638
Cl-MnPc bridge$_+$	5.308	7.561	198.697

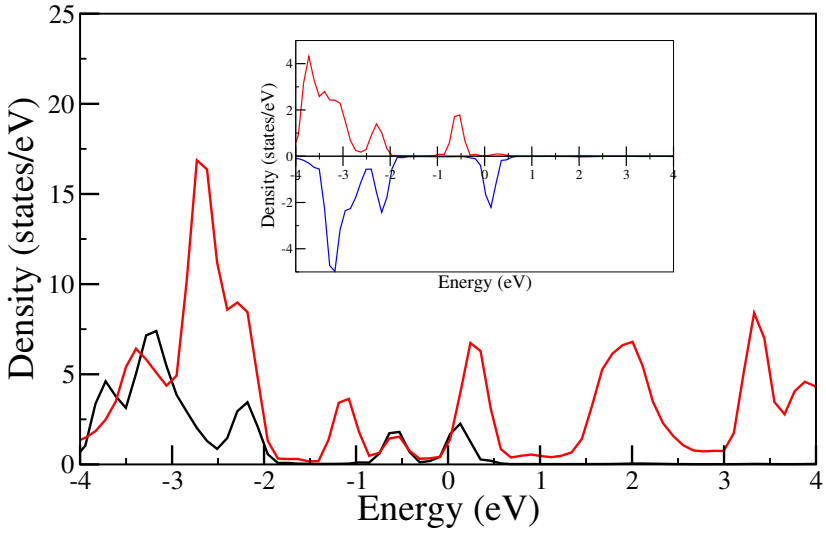

Fig. 3.21 PDOS projected onto the cooper atom (black) and the molecular backbone (red) at bridge$_+$ site. The inset shows the PDOS onto the Cu atom, α spin (red) and β spin (blue) contributions. Energies are referred to the Fermi level.

The M-DOS for the Cl-MnPc adsorbed on Ag[111] is plotted in **Figure 3.25** around the Fermi level. The increment in the adsorption distance is reflected in the M-DOS. Thus, if in the previous case (MnPc) we observed some slight dependence of the computed M-DOS on the adsorption site, it utterly disappears in this case. The electronic structure of the molecule does not present any variation related to the adsorption site. As for the MnPc molecule, the LUMO is almost fully charged. Cl-MnPc HOMO and LUMO are composed by the contributions of the molecular backbone and the manganese group. As depicted in **Figure 3.26**, near to the Fermi level, the HOMO is mainly formed by the metal core orbitals but also has contributions from the molecular frame. The inset contains the same information when the molecule is in the gas phase. The large interaction with the substrate is still visible in the huge width of the $\mathbf{d}_{z^2}$ contribution. However, it appears now at a higher energy, clearly above the Fermi level. We can find also some contribution from the $\mathbf{d}_{z^2}$ orbital below -2.0 eV. These two contributions clearly correspond to a bonding/antibonding splitting caused by the Cl-Mn interaction. The antibonding part, with larger Mn character lies now well above the Fermi level and gains a large width due to the interaction with the substrate. Thus, in the adsorbed Cl-MnPc molecule the Mn $\mathbf{d}_{z^2}$ has a larger contribution to the LUMO+1. As a result of this, the molecule loses the main d-channel charge transfer and the metal-substrate charge exchange is now mainly controlled by the aromatic molecular frame. This explains

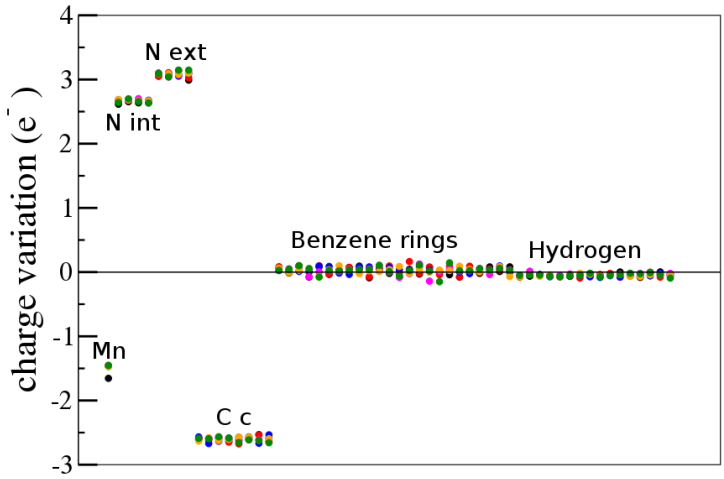

Fig. 3.22 Charge variation (Bader charge - atom valence charge) for all atoms in the MnPc molecule in the gas phase (black) and after adsorption on Ag[111] at $fcc_{\times}$ (red), $top_{\times}$ (blue), top_{+} (magenta), $bridge_{\times}$ (orange) and $bridge_{+}$ (green) sites.

the reduction in the interaction between the substrate and the molecule as well as the large molecular deformation.

3.3.2.d *Summary of Bader charges and density of states*

Thus, it was shown that the metal core controls the behaviour of the interaction between the MePc and the Ag[111] surface. Despite the different adsorption sites tested, the electronic structure of the molecule is very weakly affected by the selection of a particular adsorption configuration. The similarity of the M-DOS regardless of the adsorption site is a clear signature of the small chemical interaction between the molecule and the surface.

The transition metal determines the charge transfer and the molecular magnetization. Our results prove that the choice of metal core widely changes the electronic structure of the molecule close to the Fermi level. The TM controls the interaction with the substrate. In particular, frontier molecular orbitals from different MePc show a very different degree of hybridization with the substrate. The most common interaction path between the d-states of the metal center and the substrate is mediated by the aromatic π-system. However, the metal core can interact directly with the surface as happens in the case of the MnPc molecule. The molecular geometry is crucial for this. As we have shown, the titanium atom in TiOPc does not interact with the substrate and the adsorption is mediated by the organic part of the

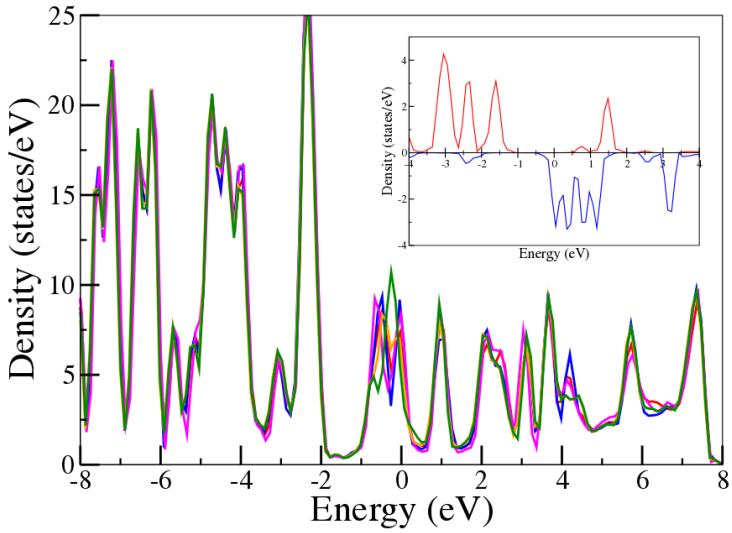

Fig. 3.23 M-DOS MnPc comparison between adsorption sites. MnPc adsorption on Ag[111] at $\text{fcc}_{\times}$ (red), $\text{top}_{\times}$ (blue), top_{+} (magenta), $\text{bridge}_{\times}$ (orange) and bridge_{+} (green) sites. The inset shows the PDOS projected onto the Mn atom, α spin (red) and β spin (blue) contributions in the gas phase. Energies are referred to the Fermi level.

molecule. CuPc has a weak interaction with the substrate, as expected for a noble metal, that is not large enough to annihilate the magnetization of CuPc on gas phase. Meanwhile when the Mn atom is acting as metal center, there is a large interaction with the substrate as clearly indicated by the large width (hybridization with the substrate) of the $\mathbf{d}_{z^2}$ level located close to the Fermi level. This creates a direct interaction and charge transfer route between the Mn atom and the surface. Nevertheless, the addition of a ligand modifies the molecular interaction. It produces an energy shift of the metal orbital, closing this direct charge transfer channel. It is clear then, that the interface properties depend crucially on the energetic positions of the metal orbitals and their occupations.

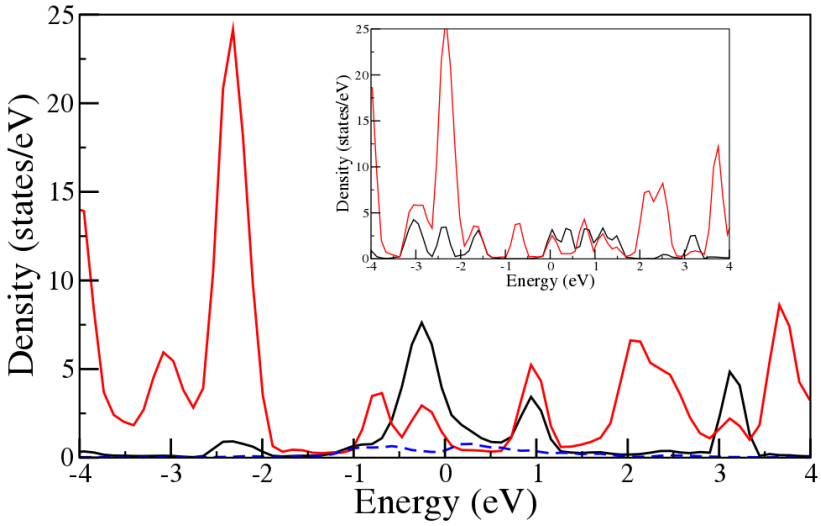

Fig. 3.24 PDOS MnPc projected onto the manganese atom (black)), $\mathbf{d}_{z^2}$ Mn orbital (blue dash line) and the molecular backbone (red) for the case of the bridge$_+$ site. The inset shows the PDOS projected onto the manganese atom (black)) and the molecular backbone (red) contributions in the gas phase. Energies are referred to the Fermi level.

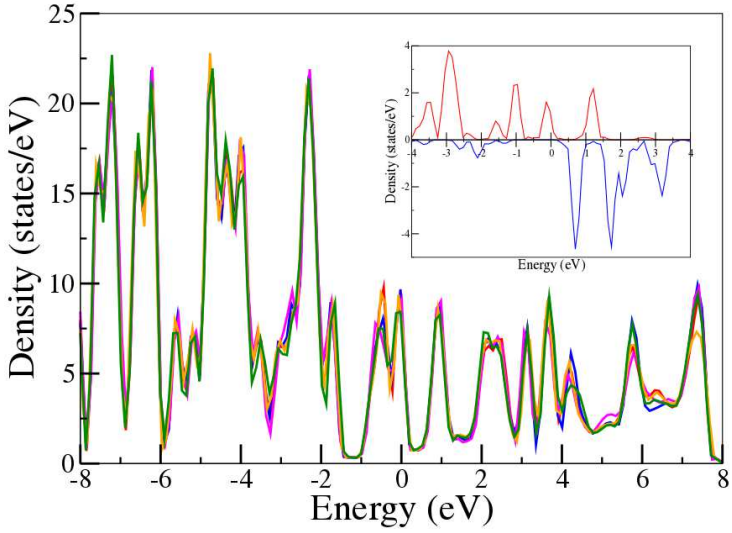

Fig. 3.25 M-DOS Cl-MnPc comparison between adsorption sites. Cl-MnPc adsorption on Ag[111] at fcc (red), top$_\times$ (blue), top$_+$ (magenta), bridge$_\times$ (orange) and bridge$_+$ (green) sites. The inset shows the PDOS projected onto the Mn atom, α spin (red) and β spin (blue) contributions in the gas phase. Energies are referred to the Fermi level.

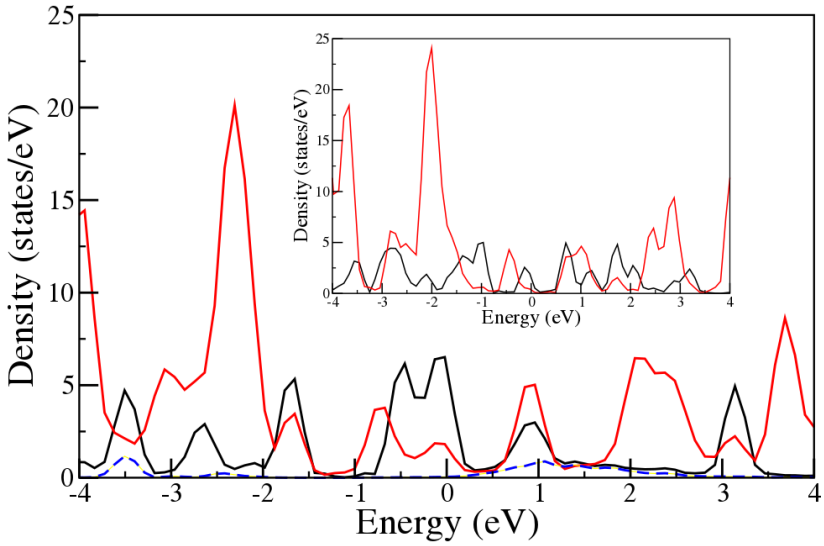

Fig. 3.26 PDOS Cl-MnPc projected onto the manganese group (black), $\mathbf{d}_{z^2}$ Mn orbital (blue dash line) and the molecular backbone (red) for the case of the bridge$_+$ site. The inset shows the PDOS projected onto the manganese group (black)) and the molecular backbone (red) contributions in the gas phase. Energies are referred to the Fermi level.

3.3.3 Induced electron density and dipole moment

We have calculated the induced electron density after adsorption for all the MePc molecules. Our results show the presence of an electron accumulation in the surface both below and around the molecule. The electron accumulation spills out from the region covered by the molecule, forming a rim of negative charge surrounding the molecule. This is a common observation when organic molecules are adsorbed on a metal substrate [160–163]. It is produced by the pushback of surface electrons into the substrate caused by the Pauli repulsion between them and the electrons of the molecule. The molecular electron cloud is usually harder to deform than that in the metallic substrate. Thus, when the molecule is close to the surface the MePc electron cloud pushes back the substrate electrons into the metal.

Similar to the case of the PDOS, there is not significant difference in the induced charge arrangement at different adsorption sites. In order to simplify the analysis, we have depicted 3D induced electron density figures at the **bridge**$_+$ site for all the MePc molecules. In addition, we have calculated the dipole moment for the molecules in the gas phase and after adsorption. However, the induced dipole moment and the total dipole moment for the adsorbed molecules can not be obtained along the directions parallel to the surface (x-axis in our plots along the $\langle\bar{1}10\rangle$ and y-axis along the $\langle\bar{1}\bar{1}2\rangle$ directions) because the density is not strictly confined along those directions, but rather corresponds to a continuous periodic distribution. Thus, we focus our attention on the out-of-plane dipole (along the $\langle 111\rangle$ direction). We have analysed the induced electron density Δn(z) averaged in the XY plane and plotted it along the z direction as well as the total dipole moment in this direction.

3.3.3.a *TiOPc/Ag[111]*

The TiOPc molecule was adsorbed on the Ag[111] surface, the interaction with the surface produces an electronic rearrangement on both, the molecule and the surface. This variation is plotted on **Figure 3.27**. The TiOPc (**O-up**) adsorption creates an apparent electron depletion on the π-system in the molecule. Despite the fact that there is no charge transfer between the substrate and the Ti atom, there is a charge accumulation beneath the metal core. These observations are consistent with the effects due to the Pauli pushback of the surface electrons. This is also reflected in the distribution of the planar-averaged induced density plotted in **Figure 3.28** along the surface normal. All the studied adsorption sites and configurations are plotted together, however, the variation of the curves is very small and they are fairly independent on the adsorption site. The chart shows the electron accumulation on the topmost layer in the substrate and the apparent depletion at the π-system in the molecule.

Using the calculated electron densities, we have obtained the dipole moments for the molecule on gas phase and after adsorption. The results are displayed in **Table 3.14**. TiOPc has a large dipole moment produced by the tytanil group (-0.60 eÅ) along the normal direction (here we assume the oxygen occupies a higher position along z, explaining the negative sign of the dipole). The geometrical changes of the molecule upon adsorption only produce a slight increment of the molecular dipole with respect to the gas phase. The total

Table 3.14 Dipole moment of TiOPc/Ag[111] along the surface normal direction $\langle 111 \rangle$. Label "ads. geom." refers to free-standing molecules for which the relaxed adsorbed geometry is used. For free-standing molecules, the reported dipole is computed along the normal to the molecular plane. The induced dipole is the dipole associated with the rearrangement of the electron density after adsorption.

configuration	**free (ads. geom.) (e Å)**	**induced (e Å)**	**total (e Å)**
gas phase	-0.594		-0.594
fcc$_\times$	-0.623	0.939	0.276
top$_\times$	-0.614	0.945	0.290
top$_+$	-0.622	0.888	0.225
bridge$_\times$	-0.616	0.958	0.300
bridge$_+$	-0.625	0.910	0.245

and induced dipoles obtained after adsorption present slight differences as a function of the adsorption site. The most noteworthy result is the inversion of the total dipole when the TiOPc molecule is adsorbed on the Ag[111] surface. While the molecular dipole initially was pointing downwards, once the effect of the adsorption is taken into account it points upwards. The absolute value of the dipole is also much smaller for the adsorbed species. We attribute this behaviour to the Pauli repulsion, which is responsible for creating a strong dipole opposed to the molecular one in this case. Mind that the induced dipole due to the pushback of the surface electrons is expected to be always positive and proportional to the area covered by the molecular frame.

For TiOPc adsorbed in an inverted (**O-down**) geometry the molecule-substrate interface changed completely. The dipole moments are described on **Table 3.15**. The surface presents the typical electron accumulation around the molecular edge (see **Figure 3.29**). The main ingredient to understand the induced charge in the **O-down** case is also the Pauli pushback of surface electrons. However, it is important to take into account that besides the electrons occupying the π molecular states, now we must take into account the interaction of the surface electrons with the oxygen atom of the titanyl group, which strongly overlaps with electron cloud from the surface. A combination of Pauli repulsion and pure electrostatic repulsion pushes the electrons away from the neighborhood of the oxygen. This explains

the small electron accumulation found around the Ti within the molecular plane, and around the oxygen atom below the molecular plane. At the same time, the electron occupying the π molecular orbitals in the molecular frame also push the surface electrons towards the surface that accumulate forming a rim around the molecule. As a consequence of this combined action, the dipole created by the pushback effect is slightly reduced in this case with respect to the **O-up** case. However, in this case both the molecular dipole and the induced dipole point in the same direction (both point towards vacuum) and, therefore, the magnitude of the total dipole is now much larger than in the **O-up** case.

Table 3.15 Dipole moment of TiOPc/Ag[111] (**O-down**) along the surface normal direction $\langle 111 \rangle$. Labelling scheme like in **Table 3.14**.

configuration	**free (ads. geom.) (e Å)**	**induced (e Å)**	**total (e Å)**
fcc$_\times$	0.591	0.804	1.356
top$_\times$	0.452	0.877	1.289
top$_+$	0.492	0.818	1.271
bridge$_\times$	0.477	0.857	1.294
bridge$_+$	0.512	0.798	1.268

3.3.3.b *CuPc/Ag[111]*

The molecular plane of CuPc adsorbs closer to the surface than for TiOPc. CuPc electron induced density is plotted on **Figure 3.31** for the **bridge**$_+$ adsorption. There is an electron accumulation beneath the metal core and it is also observed the electron depletion around the π-system in the molecule, which is a clear signature of the Pauli repulsion. The CuPc adsorption gives rise to a strong charge rearrangement at the interface.

The induced density plotted in **Figure 3.32** is clearly consistent with the Pauli pushback of surface electrons: large electron accumulation in the surface and electron depletion in the region occupied by the molecular frame. Although the CuPc does not have a dipole moment in the gas phase, a strong induced dipole moment appears after adsorption due to the electronic repulsion between the electron clouds. Thus, the CuPc adquires a total dipole moment in the normal direction after adsorption on the Ag[111] substrate. The values are presented in **Table 3.16**. The results show a much larger variation of the total dipole depending on the adsorption site as compared to the TiOPc molecule. We understand these variations as directly related to the adsorption height of the molecule over the surface. For **top**$_\times$ adsorption site the distance between the metal core and the surface is ~ 3.11 Å and its total dipole along the normal is 1.47 eÅ, whereas at the **top**$_+$ adsorption site the height increases until ~ 3.18 Å and the dipole is reduced to 1.28 eÅ.

Table 3.16 Dipole moment of CuPc/Ag[111] along the surface normal direction $\langle 111 \rangle$. Labelling scheme like in **Table 3.14**.

configuration	free (ads. geom.) (e Å)	induced (e Å)	total (e Å)
gas phase	-0.001		-0.001
fcc$_\times$	-0.046	1.503	1.421
top$_\times$	-0.019	1.530	1.475
top$_+$	-0.043	1.362	1.279
bridge$_\times$	-0.072	1.456	1.344
bridge$_+$	-0.032	1.499	1.431

3.3.3.c *MnPc/Ag[111] and Cl-MnPc/Ag[111]*

The MnPc induced electron density is shown on **Figure 3.33**. In contrast to the case of CuPc, for the MnPc we can find clear traces of electron accumulation around the Mn atom and in some regions of the molecular frame. This is due to an additional ingredient that has a stronger influence in the case of MnPc than in the previous cases: the charge transfer of electrons from substrate to the molecule. For MnPc 0.7 electrons are transferred and distributed within the molecular frame. As a result, after MnPc chemisorption the MnPc-surface interface changes completely. This reduces the adsorption-induced pushback effect of metal electrons and substantially reduces the induced dipole moment. The results are shown on **Table 3.17**. Despite the fact that the metal core is closer to the substrate, there is a reduction of the induced dipole moment with regard to CuPc. Thus, the electronic charge transfer mitigates the Pauli pushback but it is not strong enough to compensate all the effect. As for the other MePc explored, the dependence on the adsorption site is rather weak. The net result is a reduction in the total dipole moment in the $\langle 111 \rangle$ direction in comparison with the CuPc molecule, although the dipole is still pointing up as in the previous case.

Table 3.17 Dipole moment of MnPc/Ag[111] along the surface normal direction $\langle 111 \rangle$. Labelling scheme like in **Table 3.14**.

configuration	free (ads. geom.) (e Å)	induced (e Å)	total (e Å)
gas phase	0.000		0.000
fcc$_\times$	-0.031	0.558	0.490
top$_\times$	-0.002	0.627	0.587
top$_+$	-0.013	0.521	0.467
bridge$_\times$	-0.041	0.550	0.470
bridge$_+$	-0.021	0.503	0.525

The Cl-MnPc presents a different behaviour than without the ligand. The chlorine atom bonding the metal core in the phthalocyanine gives a strong dipole moment to the molecule.

The induced electron density is shown in **Figure 3.35**. There is an electron accumulation under the metal core, although we know that there is no charge transfer from the substrate to the Mn atom. Like in the previous case, we also observe the electron accumulation on the π orbitals from the organic framework. The planar average of the induced electron density along $\langle 111 \rangle$ direction plotted on **Figure 3.36** has a similar shape to that of MnPc at the interface, however, there is a clear reduction on the amount of charge rearranged. In the chart the Mn-Cl bond is clearly polarized due to the interaction with the surface.

Table 3.18 shows the dipole moments for Cl-MnPc. The chlorine atom bonded to the Mn causes the increase of the distance between the metal core and the surface, so the molecule is farther than the MnPc after adsorption. However, the charge transfer from the surface keeps the same, this charge is relocated on the π orbitals in the molecular framework. Similar to the case of MnPc, this cancels partially the effect of the Pauli repulsion leading to a reduction of the induced dipole at the interface. Moreover, the induced dipole moment is not large enough to compensate the molecular dipole moment. This situation results in a negative total dipole moment after adsorption on the normal direction. Thus, the total dipole in the system presents a comparable absolute value to that of MnPc, however, in the opposite direction.

Table 3.18 Dipole moment of Cl-MnPc/Ag[111] along the surface normal direction $\langle 111 \rangle$. Labelling scheme like in **Table 3.14**.

configuration	**free (ads. geom.) (e Å)**	**induced (e Å)**	**total (e Å)**
gas phase	-0.789		-0.789
fcc$_\times$	-0.636	0.150	-0.522
top$_\times$	-0.658	0.166	-0.529
top$_+$	-0.673	0.076	-0.629
bridge$_\times$	-0.634	0.214	-0.457
bridge$_+$	-0.566	0.131	-0.471

3.3.3.d *Summary of induced electron density and dipole moment*

The results obtained in this section showed that the MePc adsorption configuration has a small effect in the induced electron density and the dipole moment. A common observation was the electron accumulation in the topmost surface layer. This is caused by the Pauli repulsion between the molecular electron cloud and the electrons in the surface. The Pauli pushback causes a rearrangement of charges, creating a dipole moment along the normal to the surface.

TiOPc has an intrinsic molecular dipole moment that, however, is counteracted by a strong induced dipole upon adsorption The result is a dipole moment pointing towards

vacuum. In the TiOPc **O-down** adsorption on Ag[111] there is an additional electrostatic repulsion produced by the oxygen. It reduces the induced dipole, however, with both dipoles pointing in the same direction the total dipole increases. CuPc adsorbs closer to the surface that TiOPc. Therefore, the Pauli pushback effect increases and it was observed in the plots. This causes an increment in the induced dipole moment, and as a result, a strong total dipole moment in the normal direction to the Ag[111]. We also observed a subtle change in the total dipole moment with the adsorption site that was attributed to the distance with the surface. MnPc adsorption presents the smaller distance to the surface, nonetheless, the induced dipole moment is drastically reduced. The charge transfer from the substrate reduces the dipole produced by Pauli pusback effect. However, the charge transfer is not enough to completely cancel the effect of Pauli repulsion, and the total dipole still points towards vacuum. The addition of the chlorine atom bonding the metal core, as in the TiOPc case, gives a strong dipole moment to the molecule pointing towards the surface. When the Cl-MnPc is adsorbed the induced dipole is smaller than in the previous cases. The charge transfer cancels part of the induced dipole. Thus, contrary to the previous cases, the charge transfer together with the molecular dipole moment in the Cl-MnPc causes a total dipole moment that is pointing towards the surface after adsorption.

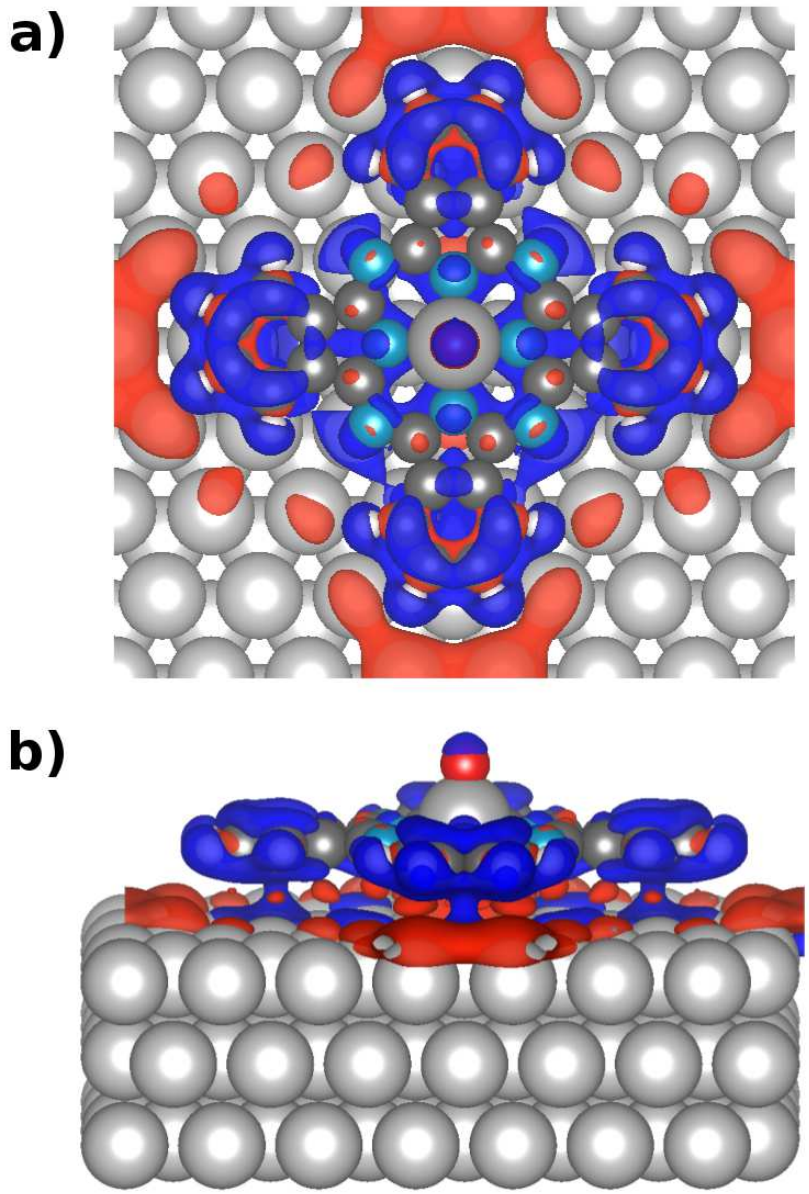

Fig. 3.27 Induced electron density for the TiOPc adsorbed at a bridge$_+$ site with the molecule aligned along the $\langle\bar{1}10\rangle$ symmetry direction of the Ag[111] surface. (a) Top and (b) side views of the isosurface (isovalue = $\pm$ 2 $_\times$ 10^{-4} e/Bohr^{-3}) of the induced electron charge. Red and blue surfaces indicate respectively electron accumulation and depletion.

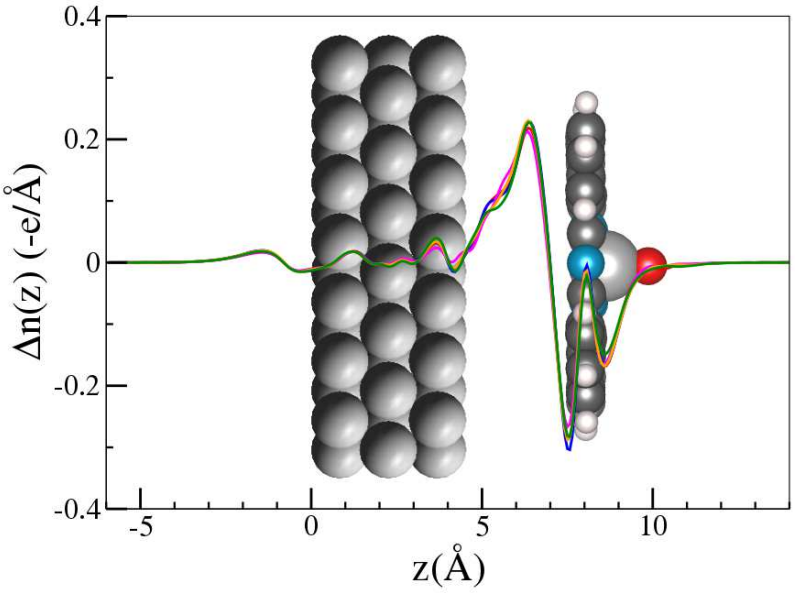

Fig. 3.28 Induced electron density Δn(z) averaged in the xy plane and plotted along z. TiOPc adsorption on Ag[111] at $fcc_{\times}$ (red), $top_{\times}$ (blue), top_{+} (magenta), $bridge_{\times}$ (orange) and $bridge_{+}$ (green) sites.

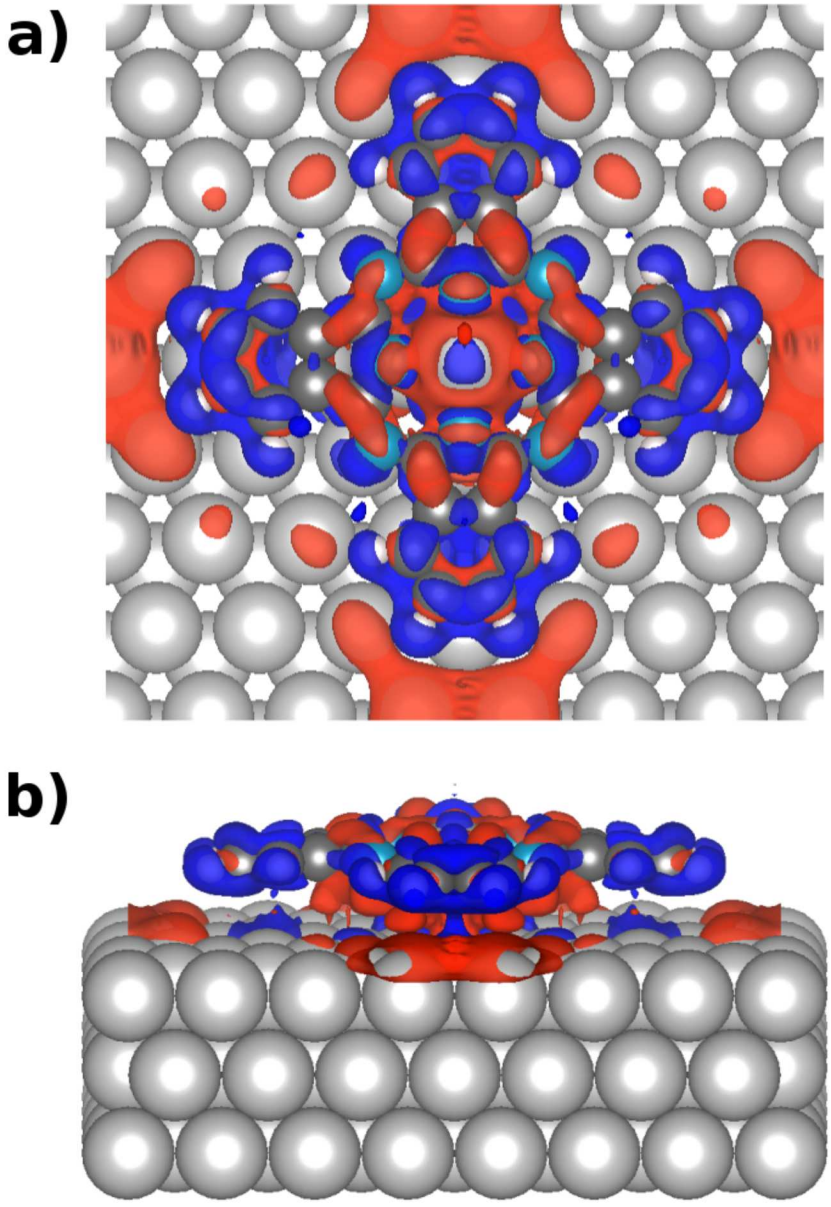

Fig. 3.29 Induced electron density for the TiOPc (O-down) adsorbed at a bridge$_+$ site with the molecule aligned along the $\langle \bar{1}10 \rangle$ symmetry direction of the Ag[111] surface. (a) Top and (b) side views of the isosurface (isovalue = $\pm$ 2 $\times$ 10^{-4} e/Bohr^{-3}) of the induced electron charge. Red and blue surfaces indicate respectively electron accumulation and depletion.

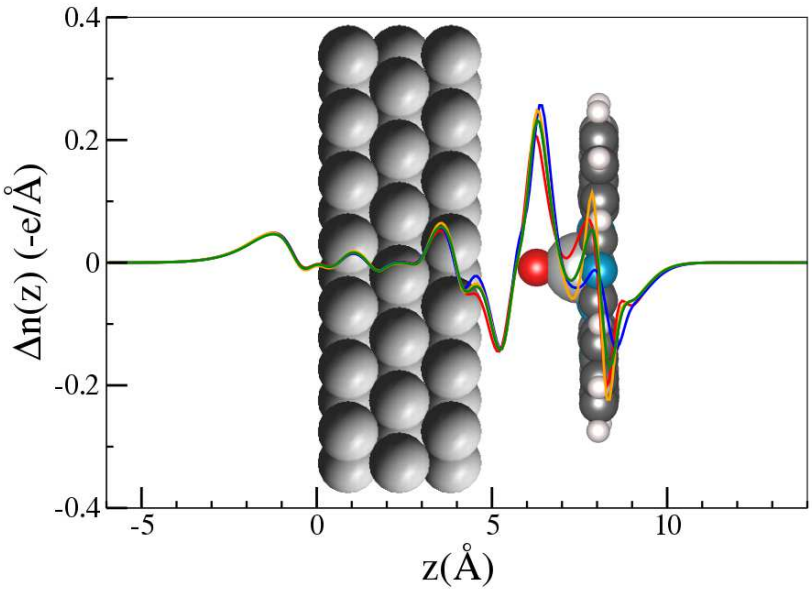

Fig. 3.30 Induced electron density Δn(z) averaged in the xy plane and plotted along z. TiOPc (O-down) adsorption on Ag[111] at $fcc_{\times}$ (red), $top_{\times}$ (blue), top_{+} (magenta), $bridge_{\times}$ (orange) and $bridge_{+}$ (green) sites.

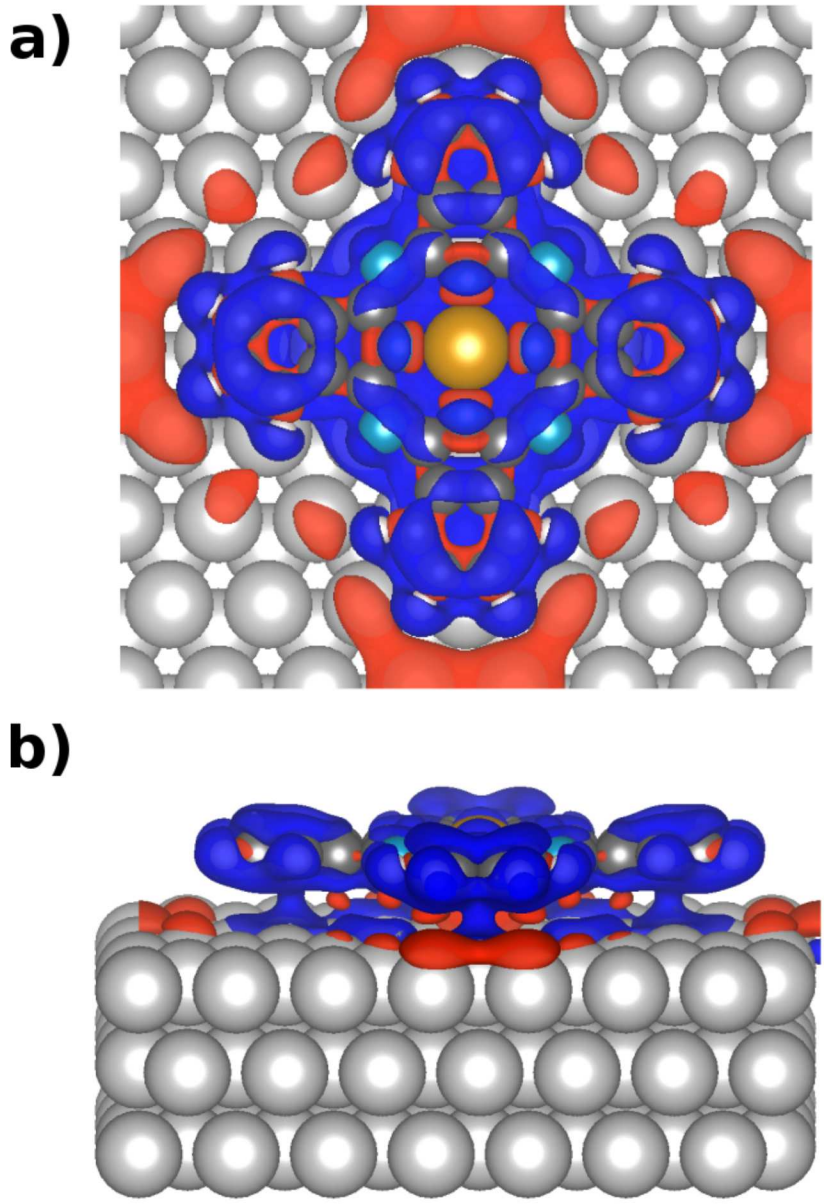

Fig. 3.31 Induced electron density for the CuPc adsorbed at a bridge$_+$ site with the molecule aligned along the $\langle\bar{1}10\rangle$ symmetry direction of the Ag[111] surface. (a) Top and (b) side views of the isosurface (isovalue = $\pm$ 2 $\times$ 10^{-4} e/Bohr^{-3}) of the induced electron charge. Red and blue surfaces indicate respectively electron accumulation and depletion.

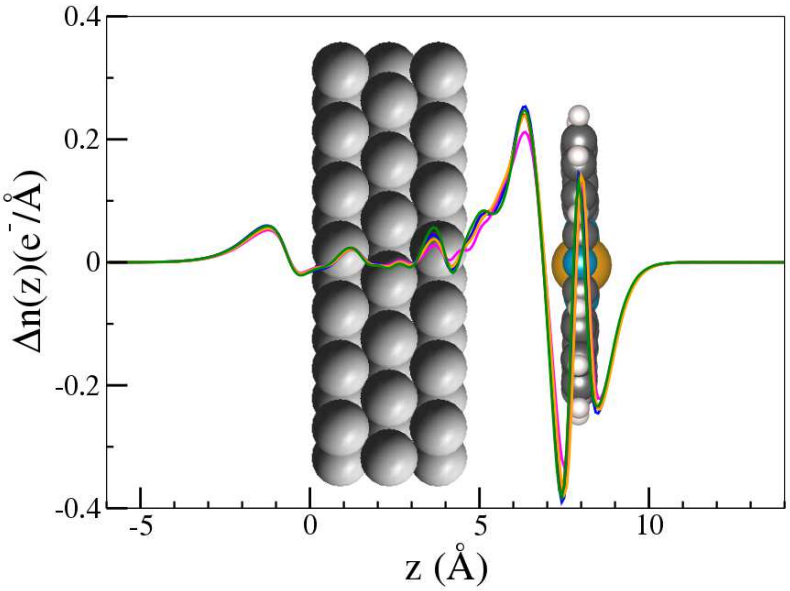

Fig. 3.32 Induced electron density Δn(z) averaged in the xy plane and plotted along z. CuPc adsorption on Ag[111] at $fcc_{\times}$ (red), $top_{\times}$ (blue), top_{+} (magenta), $bridge_{\times}$ (orange) and $bridge_{+}$ (green) sites.

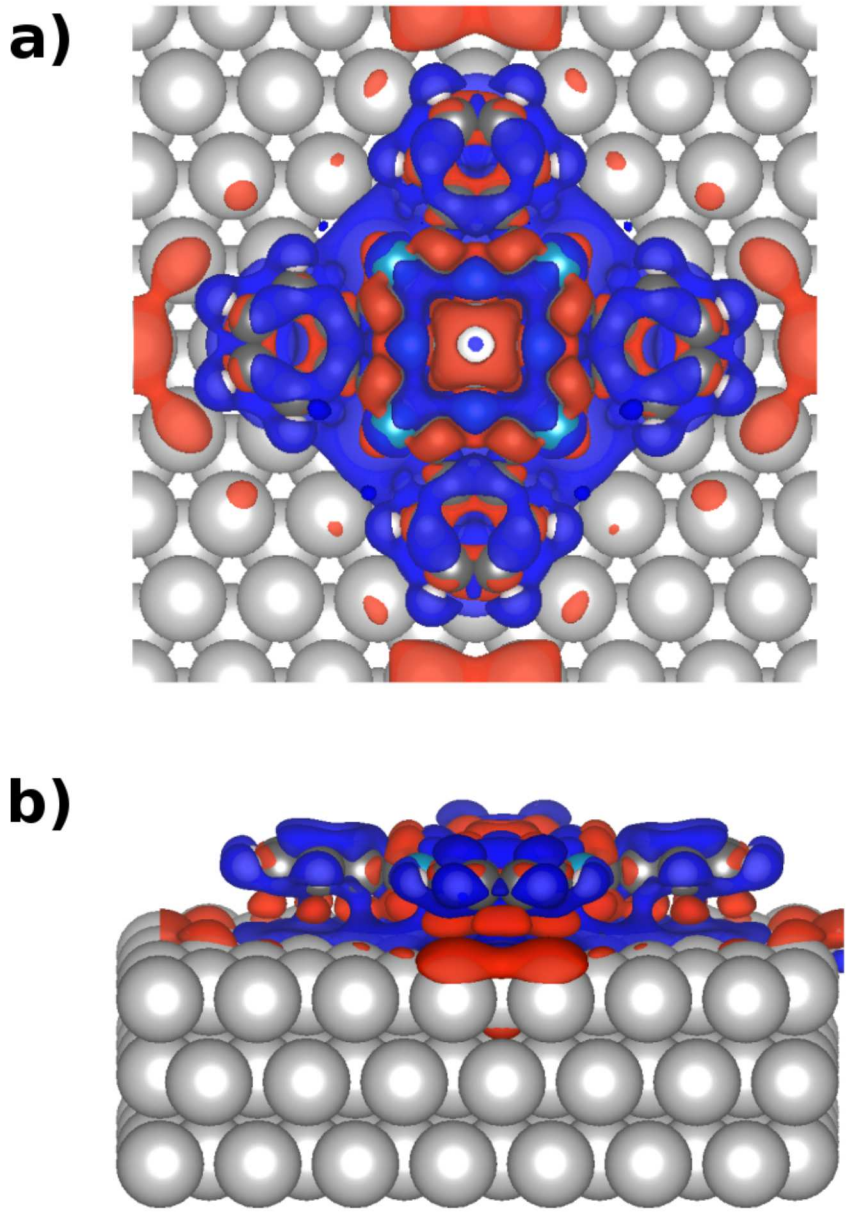

Fig. 3.33 Induced electron density for the MnPc adsorbed at a bridge$_+$ site with the molecule aligned along the $\langle \bar{1}10 \rangle$ symmetry direction of the Ag[111] surface. (a) Top and (b) side views of the isosurface (isovalue = $\pm$ 2 $\times$ 10^{-4} e/Bohr^{-3}) of the induced electron charge. Red and blue surfaces indicate respectively electron accumulation and depletion.

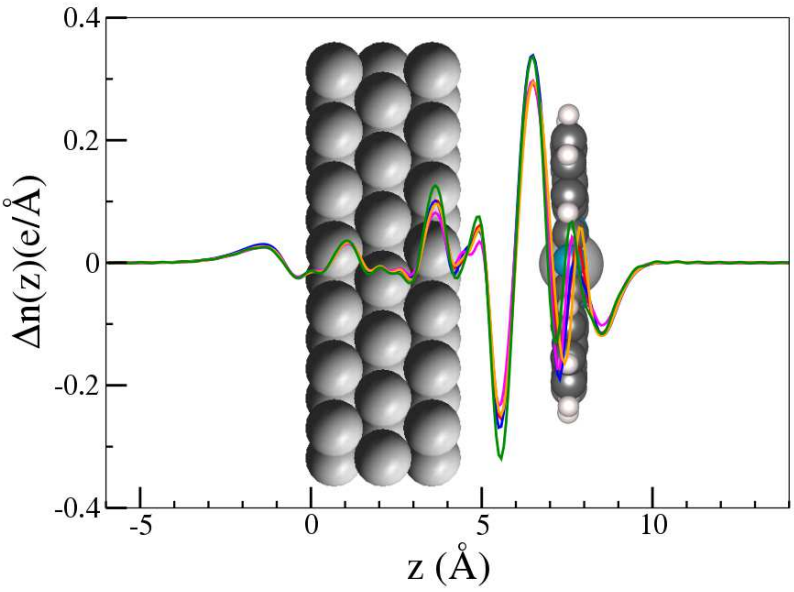

Fig. 3.34 Induced electron density Δn(z) averaged in the xy plane and plotted along z. MnPc adsorption on Ag[111] at $fcc_{\times}$ (red), $top_{\times}$ (blue), top_{+} (magenta), $bridge_{\times}$ (orange) and $bridge_{+}$ (green) sites.

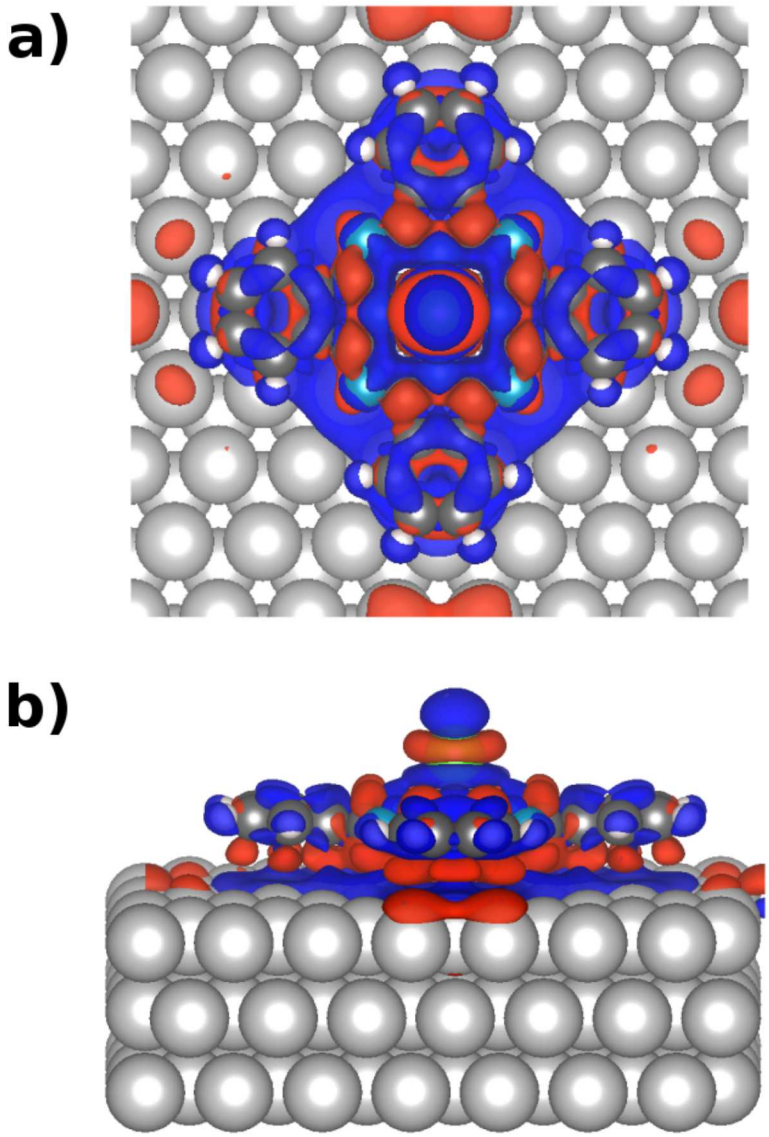

Fig. 3.35 Induced electron density for the Cl-MnPc adsorbed at a bridge$_+$ site with the molecule aligned along the $\langle \bar{1}10 \rangle$ symmetry direction of the Ag[111] surface. (a) Top and (b) side views of the isosurface (isovalue = $\pm$ 2 $_\times$ 10^{-4} e/Bohr^{-3}) of the induced electron charge. Red and blue surfaces indicate respectively electron accumulation and depletion.

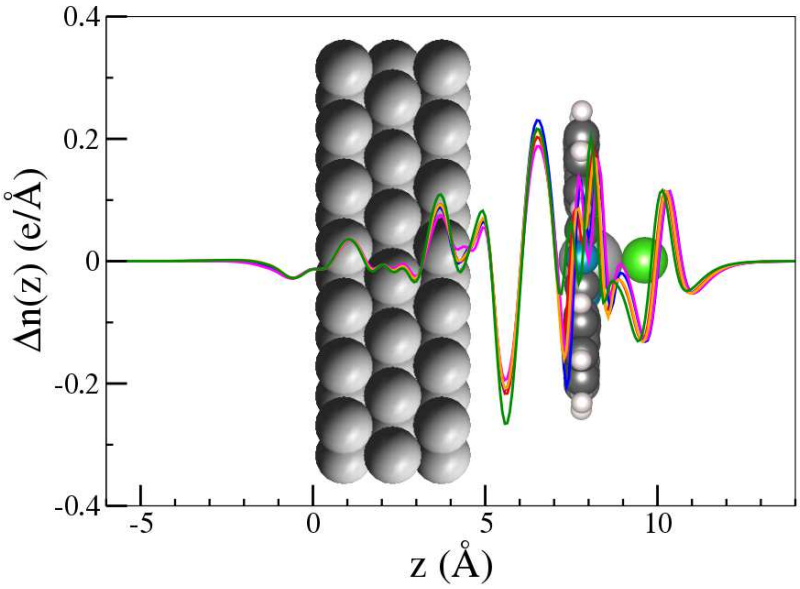

Fig. 3.36 Induced electron density Δn(z) averaged in the xy plane and plotted along z. Cl-MnPc adsorption on Ag[111] at $fcc_{\times}$ (red), $top_{\times}$ (blue), top_{+} (magenta), $bridge_{\times}$ (orange) and $bridge_{+}$ (green) sites.

3.4 General conclusions

We have thoroughly investigated the MePc (Me = Ti, Cu, Mn) adsorption on Ag[111]. In order to find the preferred adsorption site of the MePc interaction on the surface we have tested different possibilities. The adsorption configuration is defined by the metal core site and the azimuthal angle of the MePc on the substrate. Thus, molecules were adsorbed at **top**$_+$ and **bridge**$_+$ with two of the inner-ring N atoms are aligned along the $\langle\bar{1}10\rangle$ high symmetry direction of the Ag[111] surface or rotating 45° the molecule with respect to the $\langle\bar{1}10\rangle$ directions in the **fcc**$_\times$, **top**$_\times$ and **bridge**$_\times$ sites.

The main observation was the predilection of the MePc for the **bridge**$_+$ adsorption site in all cases. Thus, we have demonstrated that the adsorption site is dominated by the relative molecular disposition above the surface and not by the affinity of the metal core for a particular adsorption site. Our theoretical results highlight that the adsorption site is modulated by the stacking of the molecular frame with respect to the Ag[111] surface.

We have calculated the adsorption energies and molecular geometries. Regarding the adsorption energies, CuPc is the most stable and strongly attached to the surface. TiOPc is the second most stable adsorbate, with an adsorption energy 205 meV less stable. In this case the presence of an oxygen atom bonded to Ti reduces the interaction of the metal core with the surface, increasing the average height of the molecular plane over the topmost layer of the silver surface.

CuPc keeps part of its magnetic moment after adsorption whereas MnPc and Cl-MnPc completely lose their spin polarization when they are adsorbed on the surface. CuPc is more distant to the surface ($\sim$ 3.20 Å) than MnPc or Cl-MnPc, however, it is energetically more stable. Counterintuitively, the weak interaction between the Cu metal ion with the surface produces a small distortion of the molecular geometry leading to a more stable adsorption on the substrate. This seems to point to the importance of long-range dispersion forces to explain the computed adsorption energies. The interaction of the metal core with the surface and the charge transfer between the substrate and the molecule are other ingredients that must be taken into account. Additionally the energy cost associated with molecular deformation to favor direct chemical interactions between the metal core and the surface must be considered. The final result stems from a delicate interplay of all these ingredients and, thus, it is difficult to guess without a detailed calculation.

For example, in the case of MnPc, the addition of a ligand to the metal core in Cl-MnPc causes both a larger deformation of the molecule and pushes the Mn atom to a higher position, reducing the surface-metal core interaction. Both effects lower the stability of the system with respect to MnPc and, as a consequence Cl-MnPc has the smallest adsorption energy

among all the MePc considered here. Thus, ligands attached to the metal core are expected to weaken the interaction with the surface and give rise to lower adsorption energies.

We must mention the study developed for the TiOPc adsortion in the c-phase. In particular, our calculations for the adsorption energy dependence on the azimuthal angle were essential for the elucidation of the structural details of the self-assembled molecular layer formed at intermediate coverages on Ag[111] [16].

The electronic structure of the adsorbed molecules, M-DOS, supported the previous observations and clarified the MePc interaction with the substrate. A common observation was the electron charge transfer from the substrate to the molecule observed in the partially filled LUMO orbital. In addition, Bader charges together with the PDOS uncovered the metal core participation in the interaction and charge transfer process with Ag[111]. In the case of TiOPc, the LUMO that aligns with the Fermi level and gets partially populated does not have a large Ti character, but rather resides in the molecular frame. For CuPc the metal centre has only a minor contribution at Fermi level, explaining why the CuPc keeps the magnetic moment after adsorption. For MnPc and Cl-MnPc the LUMO has a large Mn **3d** content and receives 0.7 electrons. This, together with the very large hybridization with the surface, explains the complete disappearance of the spin polarization for these molecules. The Cl ligand produces an energy shift of the $\mathbf{d}_{z^2}$ orbital in the metal core, closing the σ-like electron channel for charge exchange between the metal centre and the surface. A general remark valid for all the studied MePc molecules is the very weak dependence of the M-DOS on the adsorption site. This is a clear proof of the rather weak electronic interaction between the MePc and the Ag[111] substrate.

Finally, we have obtained the induced electron density and calculated the dipole moments for the different MePc's. The total dipole of the system is related to the molecular distance to the surface as well as to metal ion electronic charge. The Pauli pushback of the surface metal electrons induced by the nearby molecule creates a rearrangement of charge and an induced dipole that points towards vacuum along the surface normal. This induced dipole may tend to cancel or to enhance the molecular dipole, depending on the molecular orientation. Thus, TiOPc (**O-up**) presents a total dipole that points in the opposite direction than the molecular one. The charge transfer reduces the Pauli repulsion and, as a consequence, the induced dipole as is the case for MnPc. For Cl-MnPc, this reduction of the induced dipole is such that it becomes smaller than the intrinsic molecular dipole. As a result, this is the only molecule among those studied here whose total dipole after adsorption points towards the surface.

In summary, our results prove that the adsorption configuration does not depend on the metal core and the interaction with the surface is weak. The main interaction with the surface is due to the aromatic π-system in the molecule and mediated by dispersion forces. Although

the metal core does not control the adsorption site, it defines the molecular magnetization. Additionally, the metal ion affects to the charge transfer, the adsorption height, the molecular distortion and has a strong influence on the rearrangement of charge at the molecule-substrate interface.

Chapter 4

CO_2 adsorption on TiOPc

If you don't like the answer, change the question.

Richard M. Martin

4.1 Introduction

In the previous chapter we have analyzed in detail the electronic, magnetic and structural properties of different phthalocyanine molecules adsorbed on Ag[111] and in the gas phase. Here we will consider the interaction of one of them, TiOPc, with carbon dioxide (CO_2) molecules in relation with experiments performed in the group of Prof. P. Jakob at Philipps-Universtät in Marburg (Germany).

Among other interesting technological applications, phthalocyanine molecules have been intensively used as active components for gas sensors [127, 128, 164, 165] and for their catalytic properties. For example, MePc show interesting catalytic and electroreduction properties. MePc (Me = Fe, Co) were theoretically studied using DFT as catalytic molecules [166]. When an oxygen molecule (O_2) is adsorbed on the metal core, up to four different stable configurations are found. In the case case of FePc, the Fe metal core transfers electronic charge to the O_2 molecule, leading to a weaker O-O bond, making possible an oxygen reduction reaction.

Magdesieva *et al.* [167] investigated the CO_2 electroreduction using porphyrins and MePc (Me = Co, Cu) molecules as catalyst adsorbed on activated carbon fiber nanoporous supports. They showed that MePc based complex are effective catalysts for CO_2 electroreduction. They also demonstrate that these kind of compounds are highly effective, yielding efficiencies up

to 70%. In their study they found that the specific metal core or macrocyclic ligands does not have an strong influence on the CO_2 electroreduction.

In this chapter we have studied CO_2 adsorption on TiOPc. The molecule has a Ti core bonded to an oxygen ligand. We have proposed different adsorption geometries for the CO_2 molecule on the TiOPc identifying the most probable configuration. Afterwards, we have increased the CO_2 coverage on the TiOPc. Our results shows that the adsorption of multiple CO_2 molecules on the TiOPc is energetically feasible. In addition, we have calculated the charge transfer between TiOPc and CO_2 and the induced electron density upon adsorption in order to explain the interaction between both molecules. We also computed the total dipole moment of the system and its change after molecular adsorption. Finally, we have obtained the vibrational density of states (VDOS) in an attempt to characterize how the CO_2 adsorption affects the Ti-O bond and to compared with the infrared spectroscopy data from Prof. Jakob's group.

4.2 Methodology

Our results were obtained using VASP (version 5.3.5) [12] and the PBE functional [55]. In order to take into account the vdW interactions we have included the D3 Grimme approximation [63] in the input. We have used a 400 eV plane-wave cutoff as well as the PAW method [99] to describe the atomic cores. The relaxation process is stopped when the forces acting on all the atoms were smaller than 0.03 eV/Å.

A large supercell (20.160 Å x 19.953 Å) was used with a view to avoiding the interaction between the TiOPc periodic images. In the same way, a large vacuum distance $\sim$ 20 Å was used to prevent the interaction along the normal to the molecular plane. A 3x3x1 k-point Monkhorst-Pack grid [91] and the Methfessel-Paxton occupation scheme [168] (σ = 0.2 eV) was used in the simulations.

In this system, we consider different adsorption configurations that will be described extensively below. CO_2 adsorption on TiOPc figures and the induced electronic density figures were created using VESTA [155]. The E_{ads} is calculated with **Eq. 2.1** and the population analysis was performed like in **Chapter 2**. Heights reported in this chapter were obtained using the TiOPc molecular plane as a reference.

The induced electronic density for the system was calculated using the Fermi occupation scheme [169] and σ = 0.02 eV. The Methfessel-Paxton occupation scheme is used in most of the reported calculations in this thesis due to its faster convergence for metallic systems. However, this method can provide (unphysical) negative occupations nearby the Fermi level, which could be an issue in the present case. The induced electron density was calculated

using **Eq. 3.1** and the dipole moments in the gas phase, the induced dipole moment and the total dipole moment were calculated following the same procedure than in **Chapter 3**.

The VDOS is obtained using the finite difference method around the relaxed geometry. The forces obtained from single point calculations for distorted geometries are used to computed the Hessian matrix (second derivative of the energy with respect to the atomic positions). From this matrix we can obtain the so-called dynamical matrix, whose eigenenergies and eigenvectors correspond to the vibrational frequencies and modes of the system. Here, the Hessian matrix was determined using a finite difference approach with a step size of 0.01 Å for the displacement of each atom in the system along each Cartesian coordinate.

4.3 Results

4.3.1 Adsorption energy and geometry

TiOPc is an organic macrocycle molecule with a titanium atom in the centre. As it was shown in **Chapter 3** in **Figure 3.1**, the molecule is composed by a organic frame (a ring formed by four pyrroles connected by Nitrogen atoms, plus four benzene rings) and a titanium metal core which is bonding an oxygen atom.

We have studied the CO_2 molecular adsorption on TiOPc. We have tested different adsorption geometries. The relaxed geometries are plotted on **Figure 4.1**. The studied configurations are: **a**) the CO_2 is adsorbed on top of the carbon atoms of the pyrroles, with the CO_2 axis parallel to the molecular plane, **b**) the carbon atom of the CO_2 molecule is on top of one of the external nitrogen atoms of the central ring, with the oxygen atoms pointing towards the carbon atoms of the neighbouring pyrrole groups, **c**) the CO_2 molecule interacts with the external nitrogen in the central ring via one of its oxygen atoms and **d**) CO_2 is adsorbed on the Ti metal core.

The adsorption energies are shown on **Table 4.1**. The preferred adsorption site is on the Ti metal core (**Figure 4.1 d**) that is 107 meV more stable than configuration **4.1 b** and 136 meV than **4.1 a**. The less stable adsorption site is **4.1 c**, where the CO_2 adsorption energy is $\sim$ 170 meV smaller than **4.1 d**.

Although the adsorption on the Ti metal centre is the preferred site, it is necessary to overcome a high energy barrier ($\sim$ 500 meV) in order for the CO_2 to adsorb on the metal core. This energy barrier was obtained mapping the energy as a function of the vertical position of a CO_2 molecule situated directly on top of the TiO group. We have fixed the z coordinate in the benzene rings and the carbon atom in the CO_2 preventing the main vertical positions of the molecules from moving during the relaxation and have run multiple calculations. Thus,

the energetic results of this sampling give us a good estimation for the energy barrier. This strong energy barrier rules out that **4.1 d** would be a reachable adsorption configuration under the relevant experimental conditions here (low temperature deposition of the CO_2). Based on the adsorption energy results, we have assumed that **4.1 b** is the most probable adsorption geometry.

Table 4.1 E_{ads} for the different adsorption geometries showed in **Figure 4.1**.

configuration	E_{ads} **(eV)**
a	0.221
b	0.250
c	0.186
d	0.357

In order to address the experimental observations from our colleagues we have increased the CO_2 coverage. We have adsorbed multiple CO_2 molecules simultaneously on the TiOPc molecule. Starting from the **4.1 b** adsorption configuration obtained previously we have increased the number of CO_2 molecules adsorbed on TiOPc. The possible adsorption geometries are plotted on **Figure 4.2**. We have adsorbed two CO_2 molecules on the TiOPc testing two different options. In case **a)** the CO_2 molecules were confronted (**parallel dimers**) while in case **b)** the CO_2 molecules were side by side (**perpendicular dimers**). Continuing with the increment of the coverage, in case **c)** 3 CO_2 (**trimer**) and in **d)** 4 CO_2 (**tetramer**) molecules were adsorbed on the TiOPc molecule respectively.

Adsorption energies, Ti-O bond distance, C-O bond length and the CO_2 bond angle are shown on **Table 4.2** for all coverages. As the number of CO_2 molecules increases on TiOPc there is a reduction of the adsorption energy per molecule. The adsorption energy is not directly proportional to the number of adsorbed molecules. However, even at the highest coverage (**tetramer**) the adsorption energy is much larger that the repulsion among the CO_2 molecules, leading only to a reduction of 40 meV with respect to the adsorption energy of a monomer. Therefore, despite small differences in the adsorption energies, configurations with multiple CO_2 adsorption on TiOPc should be expected as the CO_2 coverage is increased.

The interaction with the multiple CO_2 molecules tends to slightly increase the Ti-O bond length, although the effect is quite small. The molecular distortion of the TiOPc with the adsorbed CO_2 coverage is shown in **Figure 4.3**. In this chart it is observed that the CO_2 adsorption tends to slightly enlarge the Ti-O bond distance and increase the bending of the molecular plane. In addition, the increment of CO_2 molecules in the system also leads to larger distances between the CO_2 molecule and the TiOPc centre. We attribute this increment on the adsorption distance between the CO_2 and the oxygen atom of the TiOPc

to the electronic repulsion between neighboring CO_2 molecules as the coverage increases. Thus, at higher coverages CO_2 molecules keep larger distance to the TiOPc substrate and to each other. Despite the fact that CO_2 is a linear molecule on gas phase, the bond angle shows an interesting behaviour in these systems. During the adsorption on TiOPc, the CO_2 molecules presents a small bending that it is reduced as the number of molecules adsorbed on TiOPc increases.

Table 4.2 CO_2 adsorption energy per molecule on the TiOPc molecule for different CO_2 coverages. Ti-O bond length, CO_2 bond length (C-O) and CO_2 bond angle θ.

	E_{ads} **(eV)**	**Ti-O (Å)**	**C-O (Å)**	θ (°)
CO_2 gas phase			1.177	179.9
TiOPc gas phase		1.686		
monomer	0.250	1.688	1.177	177.6
parallel dimers	0.243	1.691	1.177	177.6
perpendicular dimers	0.240	1.690	1.177	178.1
trimer	0.230	1.692	1.177	178.4
tetramer	0.213	1.692	1.176	179.0

Table 4.3 Heights (Å) $\pm$ standard deviation of the TiOPc components (see **Figure 3.1** on **Chapter 3**) on gas phase and during the CO_2 adsorption at the lowest (**monomer**) and highest (**tetramer**) coverages. TiOPc molecular plane is used as a reference.

	TiOPc gas phase	**monomer**	**tetramer**
Ti	0.707 $\pm$ 0.010	0.726 $\pm$ 0.011	0.754 $\pm$ 0.014
N int	0.078 $\pm$ 0.035	0.105 $\pm$ 0.021	0.127 $\pm$ 0.022
N ext	0.015 $\pm$ 0.044	0.039 $\pm$ 0.035	0.056 $\pm$ 0.035
C c	0.029 $\pm$ 0.036	0.052 $\pm$ 0.028	0.067 $\pm$ 0.028
B1	-0.039 $\pm$ 0.024	-0.067 $\pm$ 0.052	-0.079 $\pm$ 0.067
B2	-0.009 $\pm$ 0.027	-0.052 $\pm$ 0.049	-0.065 $\pm$ 0.063
B3	-0.031 $\pm$ 0.036	-0.070 $\pm$ 0.044	-0.078 $\pm$ 0.064
B4	-0.042 $\pm$ 0.024	-0.007 $\pm$ 0.032	-0.027 $\pm$ 0.044
Oxygen	2.393 $\pm$ 0.010	2.414 $\pm$ 0.011	2.446 $\pm$ 0.014
central ring	0.041 $\pm$ 0.026	0.065 $\pm$ 0.021	0.083 $\pm$ 0.023
Benzene	-0.030 $\pm$ 0.019	-0.049 $\pm$ 0.028	-0.062 $\pm$ 0.037
Molecular plane	0.000 $\pm$ 0.018	0.000 $\pm$ 0.022	0.000 $\pm$ 0.028

Next, we compare in detail the CO_2 adsorption on TiOPc at low and high coverage in order to clarify the molecular interaction in the system.

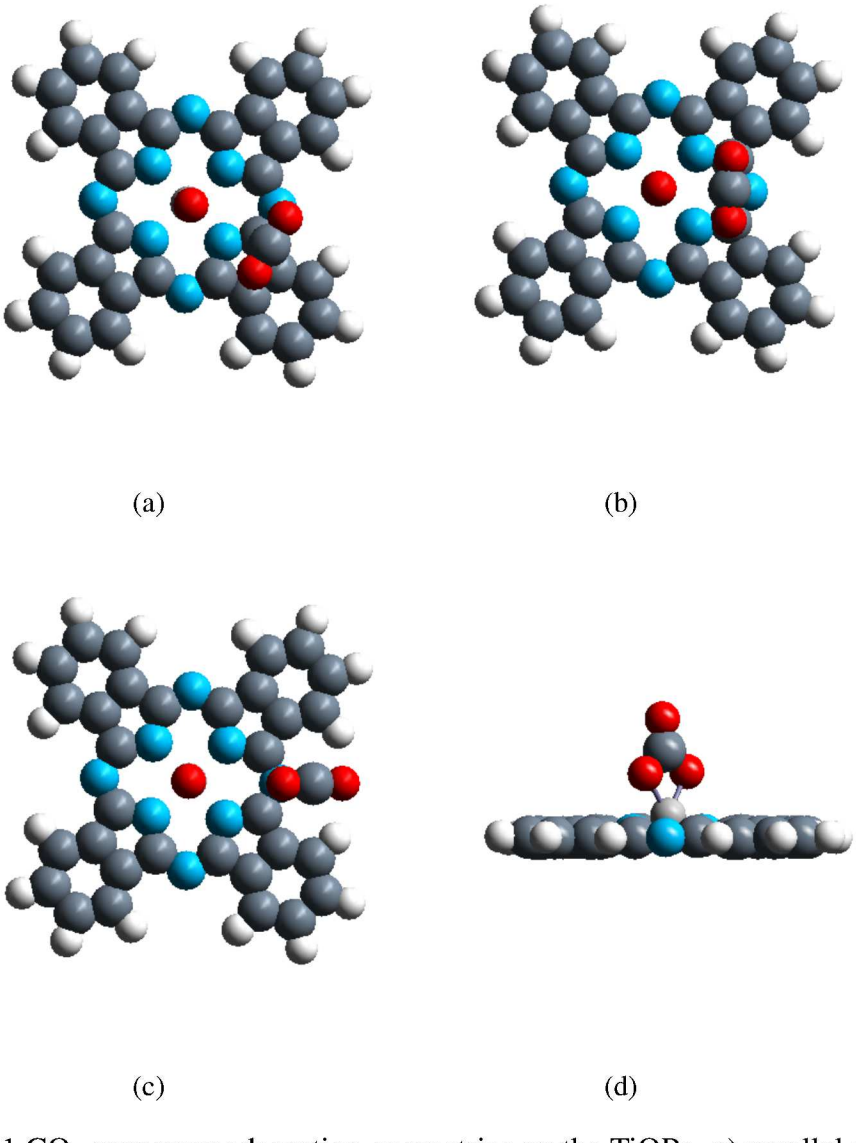

(a) (b)

(c) (d)

Fig. 4.1 CO_2 monomer adsorption geometries on the TiOPc. a) parallel adsorption on the pyrrole carbons, b) parallel CO_2 is adsorbed with the central carbon atom on top of one external nitrogen, c) CO_2 is adsorbed on the external nitrogen atom via one of its oxygen atoms and d) CO_2 is adsorbed on the Ti metal core.

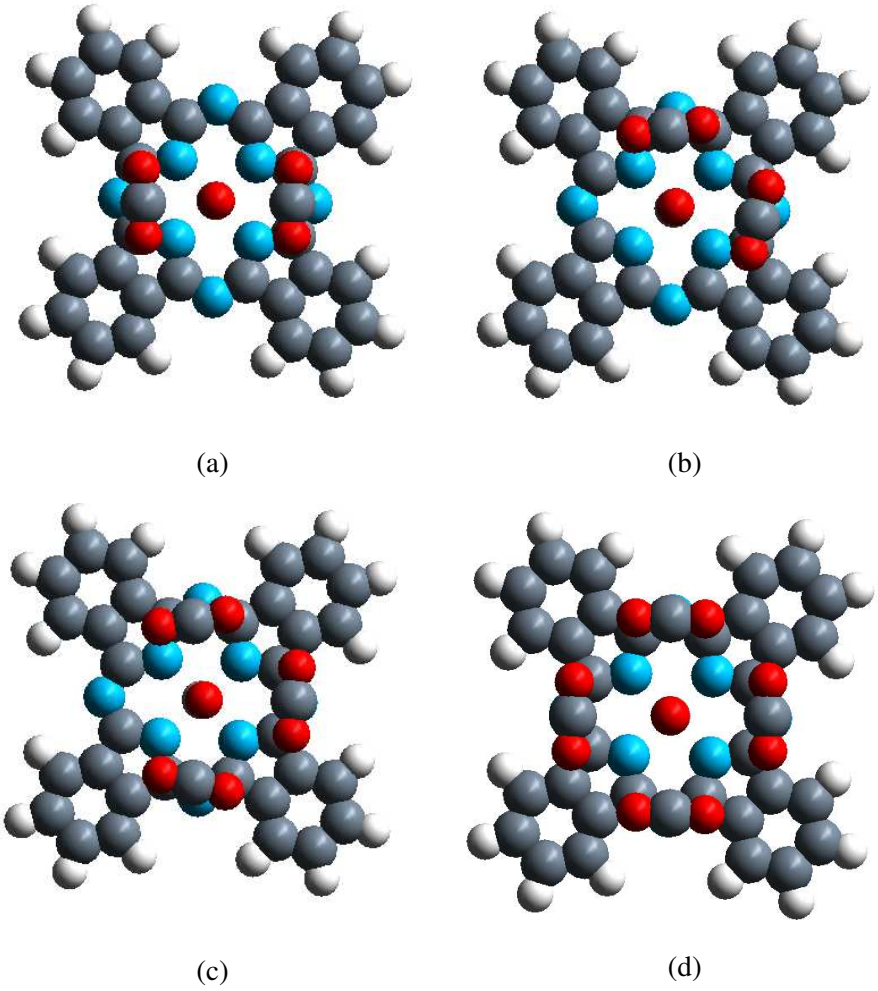

(a) (b)

(c) (d)

Fig. 4.2 Multiple CO_2 adsorbed on TiOPc. Using the **monomer** adsorption configuration **4.1 b**, the molecular coverage was increased. The following systems were studied: a) **parallel dimers** where the two CO_2 molecules are in opposite sites, b) **perpendicular dimers** with the two CO_2 molecules occupying contiguous sites, c) **trimer**, 3 CO_2 molecules are adsorbed and d) **tetramer**, 4 CO_2 molecules adsorbed on TiOPc.

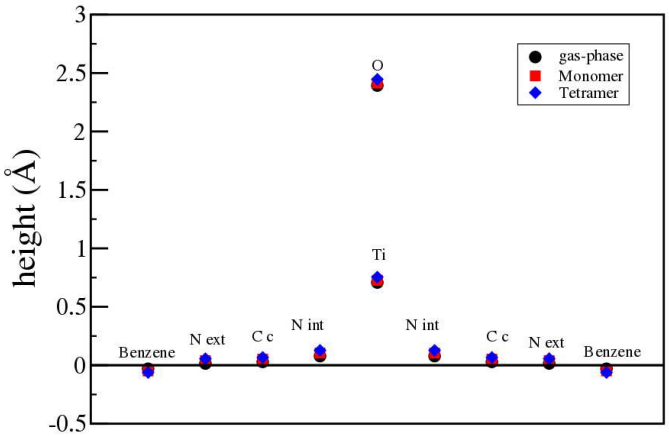

Fig. 4.3 Molecular height profile for the TiOPc on gas phase (black) and after the CO_2 molecular adsorption for low (**monomer**, red) and high (**tetramer**, blue) coverages. TiOPc molecular plane is used as reference.

4.3.2 CO_2 monomer versus CO_2 tretamer on TiOPc

CO_2 and TiOPc are weakly interacting. The adsorption energy and the minimal distortion of the TiOPc molecule support this idea. In order to identify and explain this interaction we have calculated the Bader charges and PDOS for the TiOPc in the gas phase and after the CO_2 adsorption. We have compared the most different coverages, *i.e*, when one CO_2 (**monomer**) and four CO_2 (**tetramer**) molecules are adsorbed on TiOPc.

The valence Bader charges were calculated for the TiOPc in the gas phase and when the CO_2 is adsorbed on TiOPc at both coverages. The charge transfer between the adsorbate molecules and adsorbent is negligible (< 0.02 e per CO_2 molecule) as expected, due to the large gap of CO_2. In addition, we have studied the valence Bader charges of all the atoms in the system. The charge variation (Bader charge - valence atomic charge) are plotted on **Figure 4.4** for the TiOPc central ring. The chart contains the charge variation for the TiOPc on gas phase and after the CO_2 adsorption at low (**monomer**) and high (**tetramer**) coverage. The **monomer** adsorption did not produce a noteworthy change in the TiOPc atomic charges. This beaviour did not vary with the coverage when the **tretramer** was adsorbed on TiOPc. The atomic charges in the TiOPc atoms were practically identical to the gas-phase molecule. Thus, the charge arrangement does not show any relevant variation at any coverage, proving again the weak interaction between the molecules.

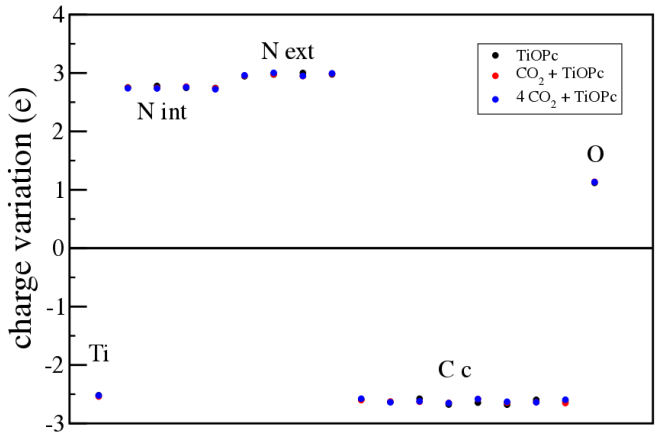

Fig. 4.4 Charge variation (Bader charge - atom valence charge) for Ti atom, central ring (N int, N ext, C c) and oxygen atom in the TiOPc molecule. TiOPc on gas phase (black), and during the CO_2 adsorption at low (**monomer**, red) and high (**tetramer**, blue) coverages.

Figure 4.5 contains the PDOS for the TiOPc molecule in the gas phase and after the CO_2 adsorption in the neighborhood of the Fermi level. There are not significant changes in the PDOS produced by the CO_2 adsorption. The main change comes from a slight downshift of the LUMO+1 orbital with the increment of CO_2 molecules adsorbed on TiOPc. However, similar to the isolated case, the main contribution to the LUMO+1 level comes from the $d_{x^2-y^2}$ orbital of the Ti metal core. Thus, the minimal distortion on the electronic structure of the TiOPc molecule together with the insignificant valence Bader charge variation proves that the CO_2 molecule is physisorbed on the TiOPc.

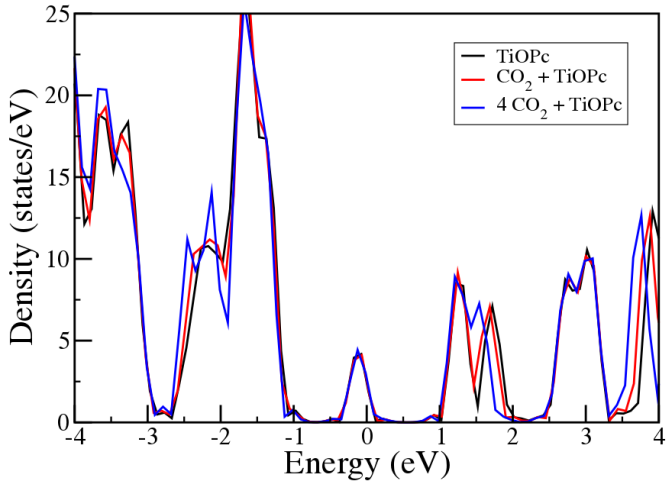

Fig. 4.5 PDOS comparison for the TiOPc molecule in the gas phase (black) and after the CO_2 adsorption at low (**monomer**, red) and high (**tetramer**, blue) coverages. Energies are referred to the Fermi level given by VASP, which aligns with tail of the HOMO level in this system.

In order to identify the CO_2 interaction on the TiOPc after the physisorption we have calculated the induced electron density. The charge rearrangement observed on **Figure 4.6** provides a clear hint that helps to understand the dominant interactions in the system.

When the **monomer** is physisorbed on the TiOPc, a redistribution of the electron charge is observed in both molecules. There is a polarization of the CO_2 molecule, but also in the oxygen atom from the TiOPc. The CO_2 π molecular orbitals present an electron depletion facing the oxygen atom from the TiOPc, whereas the oxygen atom of the titanyl group shows an electron accumulation, proving the polarization of the titanyl group in the TiOPc molecule. Furthermore, it is is also possible to find a smaller charge accumulation on the nitrogen atoms immediately below the CO_2 molecule. This charge rearrangements indicate that, in addition to the van der Waals interaction between the CO_2 molecule and the molecular frame,

electrostatic interactions between the negatively charged nitrogen and oxygen atoms of the TiOPc and the quadrupolar charge distribution of the CO2 molecule also play a crucial role in the adsorption. Moreover, the fields generated by the very polar out-of-plane TiO and in plane CN bonds create a polarization of the CO_2 that reinforces the interaction.

The same behaviour was observed for the tetrameric adsorption. Although, as it was already mentioned, the addition of CO_2 molecules to the system produces an electronic repulsion between the CO_2 molecules. The electrostatic CO_2-CO_2 repulsion moves the molecules away from the oxygen atom in the titanyl group, thus reducing slightly the attractive TiO-CO_2 interaction. Despite the CO_2 molecules being farther than in the **monomer** case, a similar polarization is observed (see **Figure 4.7**). In addition, the CO_2 molecules are now adsorbed directly over the N ext nitrogen atom from the TiOPc, so the electron accumulation on those N atoms is substantially increased.

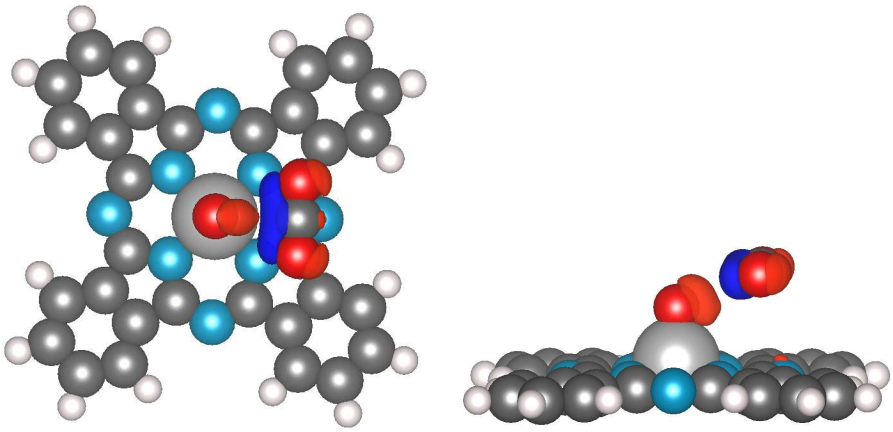

Fig. 4.6 Induced electron density after the CO_2 **monomer** adsorption on TiOPc. Top and side views of the isosurface (isovalue = $\pm$ 5 $\times$ 10^{-4} e/Bohr^{-3}) of the induced electron charge. Red and blue isosurfaces indicate electron accumulation and depletion respectively.

Following the same procedure than on **Chapter 3** for the TiOPc dipole, we have analyzed the changes in the dipole moment produced by the CO_2 adsorption on TiOPc. In **Figure 4.8** we plot the induced electron density along the z direction (Δn(z)) averaged in the XY plane. In both cases, **monomer** and **tetramer** adsorption, the electronic charge rearrangement is clearly visible in the titanyl group and on the CO_2 molecules. The addition of CO_2 molecules to the system increases the polarization of the titanyl group. These observations are also supported by the dipole moments obtained for these systems. **Table 4.4** shows the dipole moments for the TiOPc molecule along the normal to the molecular plane. TiOPc posses a strong dipole moment along the z direction (-0.640 eÅ) on gas phase. The adsorption of the CO_2 **monomer** produces a charge rearrangement on the molecules. Thus, the electronic

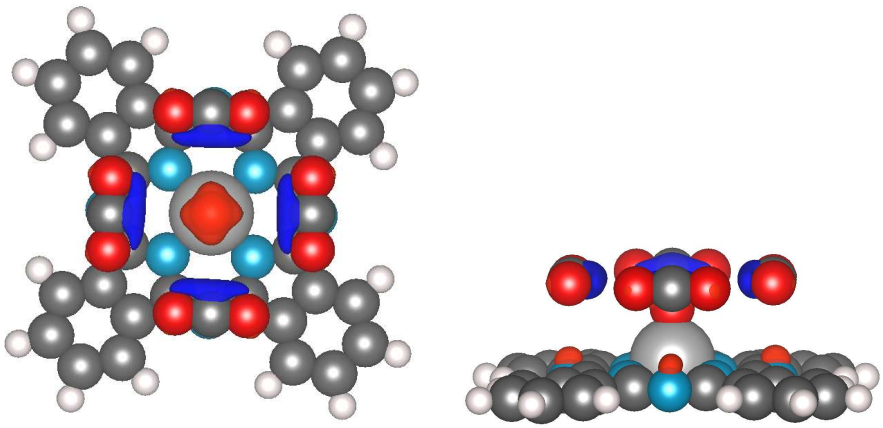

Fig. 4.7 Induced electron density during the CO_2 **tetramer** adsorption on TiOPc. Top and side views of the isosurface (isovalue = $\pm$ 5 $\times$ 10^{-4} e/Bohr^{-3}) of the induced electron charge. Red and blue isosurfaces indicate electron accumulation and depletion respectively.

interaction polarizes the Ti-O bond leading to an increment of the dipole moment along the z direction (-0.683 eÅ). Increasing the number of CO_2 molecules physisorbed on the TiOPc strengthens the polarization in the Ti-O group resulting in the increment of the TiOPc dipole moment perpendicular to the molecular plane (-0.748 eÅ) in the **tetramer** case.

Table 4.4 Dipole moment for the TiOPc on gas phase and after the CO_2 adsorption along the normal to the molecular plane. Label "ads. geom." refers to free-standing molecules for which the relaxed adsorbed geometry is used. The induced dipole is the dipole associated with the rearrangement of the electron density after adsorption.

configuration	**free (ads. geom.) (e Å)**	**induced (e Å))**	**total (e Å)**
TiOPc gas phase	-0.640		-0.640
Monomer	-0.635	-0.044	-0.683
tetramer	-0.674	-0.075	-0.748

IRAS measurements were performed by Dr. Laura Fernández in the laboratory of Prof. P. Jakob in Philipps-Universtät in Marburg after the adsorption of CO_2 molecules on an ultra-thin layer of TiOPc grown on the Ag[111] surface [16, 18]. The results showed a systematic modification in the characteristic vibrational signature of the Ti-O stretching mode (993.6 cm^{-1}) at low temperature. As the CO_2 dosage was increased new Ti-O stretching modes (987.7, 982.7, 978.0, 971.4 and 967.6 cm^{-1}) appeared on the vibrational spectrum.

Since electronic interaction takes place principally between the CO_2 and the oxygen atom in the TiOPc, we can expect that the Ti-O stretching mode will be affected after the adsorption of the CO_2 molecules. We have calculated the VDOS for the TiOPc on gas phase and after the CO_2 **monomer** and **tetramer** adsorption. **Figure 4.9** contains the Ti-O stretching modes

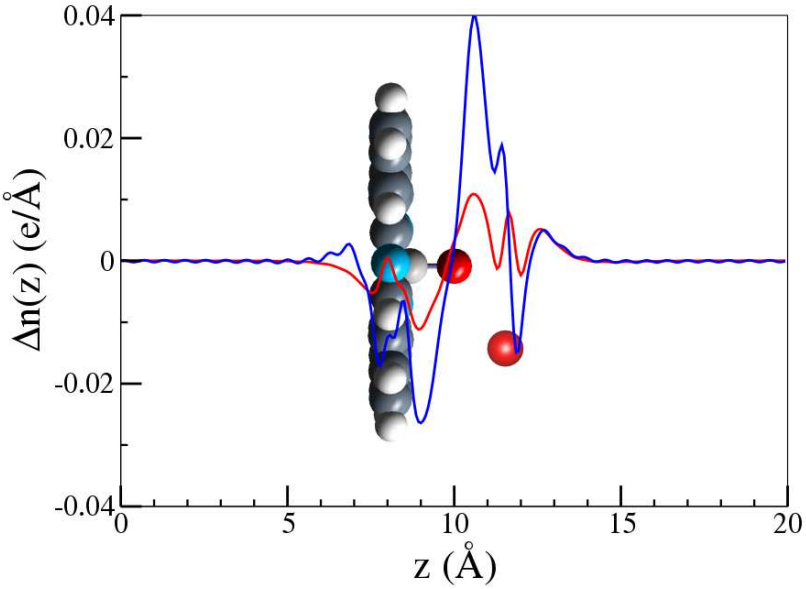

Fig. 4.8 Induced electron density Δn(z) averaged in the XY plane and plotted along z. CO_2 adsorption on TiOPc at low (**monomer**, red) and high (**tetramer**, blue) coverages.

in the different cases. The physisoprtion of a single CO_2 molecule causes a reduction on the Ti-O stretching mode (5.07 cm^{-1}). This reduction is amplified with the addition of more CO_2 molecules to the system. As shown in the **Figure 4.9**, after the **tetramer** adsorption, the energy reduction on the Ti-O vibrational mode is $\sim$ 14.53 cm^{-1}. Despite the weak interaction between the CO_2 molecules and the TiOPc, the molecular adsorption reduces significantly the Ti-O vibrational energy. We attribute this changes to the electrostatic interaction with the CO_2 molecules, which are responsible of the elongation of the Ti-O group and the variation on its dipole moment.

Thus, the reduction in the Ti-O stretching mode (987.7, 982.7, 978.0, 971.4 cm^{-1}) is related to the addition of CO_2 molecules adsorbed on the TiOPc. After a long CO_2 dosage ($>$ 90 s) only one frequency is detected (967.6 cm^{-1}). It is attributed to the formation of CO_2 clusters on the adsorption sites. According to this identification, the addition of each CO_2 molecule will reduce the Ti-O stretching by $\sim$ 5 cm^{-1} , in very good agreement with our calculations.

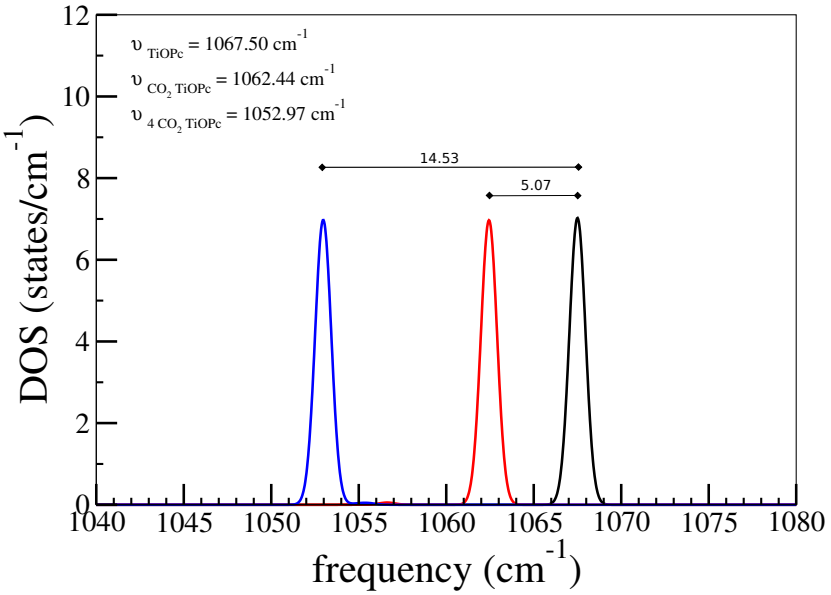

Fig. 4.9 VDOS comparison. Ti-O stretching mode on gas phase (black) and after the CO_2 adsorption at low (**monomer**, red) and high (**tetramer**, blue) coverages.

4.4 Conclusions

We have studied the CO_2 molecular adsorption on TiOPc molecule. Based on our total energy results the most probable adsorption site is with the CO_2 **monomer** parallel to the molecular plane where the CO_2 molecule is adsorbed close to the external nitrogen atoms in the molecular frame (**Figure 4.1 b**).

The CO_2 coverage on the TiOPc was increased using the proposed configuration. Several CO_2 molecules were adsorbed creating different configurations as, **dimers**, **trimers** and **tetramers**. Increasing the CO_2 coverage produces a slight increase of the distance between the CO_2 molecules and the tintanyl group. This is a consequence of the electrostatic repulsion between contiguous CO_2 molecules, causing a weakening of the interaction with the TiO group and, thus, a small reduction of the adsorption energy per CO_2. Still, our calculations prove that a single TiOPc molecule can host up to four CO_2 molecules with only a small energy penalty, *i.e.*, multiple CO_2 adsorption on TiOPc is perfectly possible.

In order to understand the interaction between molecules, we have studied and compared the **monomer** and **tetramer** systems. In both cases the electronic structure of TiOPc is minimally perturbed by the interaction with the CO_2 molecules and just the Ti-O bond distance is slightly affected. The charge transfer between the molecules was also negligible.

The Bader charges and the PDOS showed that the CO_2 molecules are physisorbed on the TiOPc.

In addition, the induced electron density was calculated. It shows a clear electronic polarization in the CO_2 molecule and the oxygen atom in the TiOPc. The electronic rearrangement in the CO_2 produces a small bending of the CO_2 molecule after adsorption. This bending is reduced when increasing the number of CO_2 molecules on the system. This shows that, besides van der Waals interaction with the molecular frame, the electrostatic interaction between the polar TiO group and the quadropolar charge distribution of the CO_2 molecules is crucial to understand the adsorption mechanism in this system. The polarization of CO_2 molecules contributes to increase the adsorption energy. These conclusions are further supported by the increment in the dipole moment along the z direction due to the polarization in the titanyl group as the CO_2 coverage increases.

Finally, the coverage increment produces the appearance of new Ti-O stretching modes detected in the experimental observations. The VPDOS calculations explain that the shift in the Ti-O stretching mode is directly dependent on the CO_2 coverage (~ 5 cm^{-1} per adsorbed CO_2 molecule) and consequence of the CO_2 electrostatic interaction with the TiOPc.

Chapter 5

Role of Strain on the Core-Level Energy Shift in [111] vicinal surfaces

God made solids, but surfaces were the work of the Devil.

Wolfgang Ernst Pauli

5.1 Introduction

The variation on the chemical environment causes physical effects on matter. The surface atoms have lost part of their neighbours, the change of the environment originates a variation in the electronic structure of surface atoms, which are different from the atoms in the crystalline bulk. This change is reflected, for example, in the electron binding energies. Thus, when an electron is emitted from an inner atomic shell, there is a variation in the binding energy measured for an atom in the bulk and other in the surface. The binding energies reflect the chemical environment of the atom from which the core electron is removed. The observed variation in the binding energy is known as core-level energy shift (CLS).

In the early 80's several measurements were done for the CLS of photoelectrons emitted from Pt crystals. Baetzold *et al.* investigated the CLS for Pt $4f_{7/2}$ electrons in Pt[111] surfaces [170]. Using Auger-electron spectroscopy (AES) and soft-x-ray photoelectron spectroscopy (SXPS) they were able to measure the CLS for the surface Pt $4f_{7/2}$ photoelecton with respect to bulk, fixing its value in approximately -400 $\pm$ 50 meV. Other experimental observations showed slight variations in the binding energies. For example, Apai *et al.* [171] measured the CLS for Pt $4f_{7/2}$ electrons on Pt[111] surface, fixing its value in -320 meV while Duckers *et al.* [172] result was -370 $\pm$ 50 meV.

Recent studies [79], based on XPS and DFT, have determined the CLS of the Pt $4f_{7/2}$ electrons to be $\sim$ -400 meV on the Pt[111] clean surface. This is also in very good agreement with the observations by Bianchettin *et al.*: -420 meV as determined experimentally versus -410 meV for theoretically estimated [173].

Similar investigations were done on Rhodium surfaces. Beutler *et al.* [174] measured the CLS of the Rh $3d_{2/5}$ photoelectron on the Rh[111] surface. Using low-energy electron diffraction (LEED) in order to characterise the system and high-resolution core-level spectroscopy (HRCLS) they obtained a CLS of $\sim$ -500 meV. A similar value was obtained by Birgersson *et al.* in their theoretical research using DFT [175]. Baraldi *et al.* using HRCLS technique and DFT obtained a value of -485 meV [176, 177]. The theoretical works show values in the range of -420 and -500 meV for the Rh $3d_{5/2}$ CLS [78, 80, 175, 178] that depend on the DFT approximation applied.

The variation in the binding energy is attributed to the reduced coordination of surface atoms with respect to bulk atoms. This produces a narrowing of the surface d-band, which is shifted in order to maintain the same chemical potential at the surface and in the bulk. As a result surface components move to lower (higher) binding energy when the d-band is more (less) than half filled [176, 179].

Many reactions can be triggered by surface defects like adatoms or steps. Stepped surfaces are created by cutting a crystal along a plane that is slightly misoriented with respect to a high symmetry direction (like the [111] plane). The step density and, thus, the terrace width depends on the miscut angle. Stepped surfaces are chemically relevant due to their catalytic properties [180–184]. An interesting observation was the variation observed in the CLS energy for stepped surfaces. Experimental results [171] showed different values for the CLS in Pt[331] and Pt[557] vicinal surfaces with respect to the flat Pt[111] surface. They measured a similar CLS value than in Pt[111] surface ($\sim$ 300 meV) but also a second energy ($\sim$ 600 meV). They attributed the first one as due to the terrace atoms in the step, while the other energy shift was assigned to the atoms in the step edge. Furthermore, they realized that the variation in the binding energies and, consequently, in the CLS was related to the step density. They explained this result assuming that the reduction of the CLS with the step size is due to a large effective coordination of the surface atoms for the shorter steps.

In vicinal Rh[111] surfaces the Rh 3d core-level binding energy was also measured using HRCLS [185]. It was demonstrated that it is possible to distinguish the different types of surface atoms in the step based on the Rh $3d_{5/2}$ photolectron energy shift. This result supported the idea that the CLS depends on the coordination number of the atoms. Along the same direction, Bianchettin *et al.* proved that the CLS is related to the number of nearest-neighbours [173, 186]. Their observations showed a relationship between the CLS

and the atom coordination. This tendency was found in vicinal Pt[111] and Rh[111] surfaces, both experimentally using HRCLS and confirmed by *ab initio* calculations. It was found that the core-level binding energies are sensitive to the local coordination number in different transition metal surfaces.

The variation of the atomic coordination has a strong influence on structural properties. Therefore, surfaces tend to have a different lattice constant as compared to that of bulk. This tendency produces a stress on the surface. The stress appears owing to the atoms in the surface usually trying to increase the surface density to increase their effective coordination.

Needs and Mansfield studied the surface stress tensor in various unreconstructed [111] surfaces (Ir, Pt, and Au). Their calculations, which were based on the plane-wave pseudopotential techniques, found that Pt presents the largest surface stress, closely followed by Ir, while Au surface has the smallest [187]. Similarly, they calculated the surface stress tensor for [111] and [110] Al surfaces. They obtained positive surface stresses for the topmost surface layer in contradiction to the intuitively expected behaviour [188]. These results were confirmed and improved a few years later by Needs and Godfrey [189]. They showed that in the case of high electron densities, such as Al, the surface stress tensor is due, mainly, to the kinetic energy term. Feibelman evaluated the strain derivative of the total energy using first-principles linear combination of atomic orbitals (LCAO) [190], computing the bulk and the surface contributions separately to the surface stress. His results are in agreement with Needs and Godfrey [189] previous investigation.

In the early nineties Fiorentini *et al.* investigated the role of strain in surface reconstruction [191]. Based on their *ab initio* calculations, they showed that the [001] surface reconstruction occurred at the end of 5d transition metals (Ir, Pt, Au) while it did not happen for the isovalent 4d metals (Rh, Pd, Ag), in agreement with the experimental observations. There is a competition between the energy gain due to the increment of the atomic density at the surface and the energy lost owing to the disruption or stretching of the bonds between the mismatched top and second layers. According to these authors, the key parameter is the tensile strain. The tensile strain is two times bigger for the last metals in the 5d group than in the corresponding 4d metals. This produces an increment in the surface density large enough to outweigh the mismatch energy loss, making the reconstruction favorable for the late 5d transition metals.

The effect of strain was extensively studied on different stepped surfaces by Prévot *et al.*. They studied the [1,1,19] copper stepped surface. Based on molecular dynamic calculations, using semi-empirical many-body potentials derived from tight-binding models, they found that atomic displacements are maximal for the step edge and the corner atoms in the step. Furthermore, they showed that the displacement field induced by steps is equivalent to that

created by a line of dipoles on a flat surface [192]. This dipolar pattern confirms one of the standard models used to account for steps at surfaces in continuum elasticity theory. Their calculations showed a good agreement, for the computed elastic displacements and interactions between steps, for Cu [001] and Pt[001] vicinal surfaces [193] in comparison with the results based on the Marchenko and Parshin approximation [194] . They also compared molecular dynamics calculations [195, 196] with atomic positions deduced from grazing incidence x-ray diffraction (GIXD) in different stepped surfaces, being able to precisely determine the strain field at the surface region, as well as the values of the equivalent elastic dipoles at the steps.

In this chapter we analyze theoretical calculations of the CLS of Pt 4f and Rh 3d photoelectrons in different flat and stepped surfaces. We have studied the variation of the binding energies in vicinal surfaces around the [111] crystal direction. These simulations, together with the inestimable collaboration from the NanoPhysics Lab group directed by Prof. J. E. Ortega at the Centro de Física de Materiales in Donostia-San Sebastián (CSIC-UPV/EHU), will be used to understand in depth the observed CLS in curved crystals. Measurements performed on Pt[111] curved crystals, which were provided by BihurCrystal company, using XPS, STM and LEED [19] and our theoretical results show a systematic variation of the CLS with the step size that can be traced back to the different strain accumulated at different vicinal surfaces.

It is known that the surface stress has a key role in determining both the physical and chemical properties of surfaces [197–201]. The presence of steps further influences this behaviour, since atoms at the steps suffer strong relaxations to try to increase their effective coordination (which is smaller than that of the atoms in a flat surface). It is also interesting to point out that the presence of steps also changes the mechanical boundary conditions of the topmost atomic layer at the surface, *i. e.* that containing the terrace atoms. This is likely to allow much larger relaxations of the terrace atoms than observed in a flat surface or for very long step terraces. Thus, larger strains are likely to appear in stepped surfaces. XPS measurements of the studied systems revealed that the CLS observed in the vicinal surfaces in the curved Pt[111] crystal is reduced with respect to the flat [111] surface. The hypothesis is that this smaller CLS is a signature of the larger strain of the vicinal surfaces, that increases with the miscut angle. This was demonstrated by our calculations [19] that obtained systematically higher binding energies for the Pt 4f electrons the larger the miscut angle. The increment of the surface strain causes an increment of the effective coordination of the terrace atoms in the stepped surface, reducing the CLS and the terrace atoms acquiring a larger bulk-like character.

We have calculated the CLS for different platinum stepped surfaces. Our results show that the displacement in the binding energies for the Pt 4f photoelectron in Pt[111] vicinal surfaces is due to the strain increment in the stepped surface and is consistent with the experimental observation. Furthermore, we were able to create an artificial strain in the Pt surfaces to model the behaviour of the CLS due to the step strain. Our Terrace Compression Model (TCM) supports the observed tendency in the CLS on the stepped surface offering a better approximation to the experimental results than the first-principles calculations in large supercells.

Finally, we have studied the CLS for Rh[111] vicinal surfaces, obtaining an even clearer relation between the CLS and the strain at the surface. Thus, our theoretical results give a reasonable account of the experimentally observed reduction in the CLS energy in the curved crystal surfaces.

5.2 Methodology

We have used first-principles calculations in order to simulate the different surfaces. The calculations have been performed with VASP [12]. We have used the PBE functional [55] and a plane-wave cutoff of 230.3 eV for the Pt surfaces and 229 eV for the Rh surfaces. The PAW method [99] has been used to describe the atomic cores.

The calculated lattice constant was 3.972 Å for Pt and 3.824 Å for Rh, in good agreement with the experimental values 3.924 Å [202] and 3.800 Å [203, 204], respectively. We employed a k-sampling of 25x25x25 Monkhorst-Pack grid [91] in the bulk calculation to sample the Brillouin zone. A first order Methfessel-Paxton occupation scheme [168] with a $\sigma = 0.2$ eV smearing width. The structures were relaxed until atomic forces were smaller than 0.03 eV/Å and the total energy tolerance was set to 10^{-4} eV. We have kept a large distance along the z direction ($\sim$ 30 Å) in order to avoid the interaction between the periodic replicas of the slab.

In this chapter the CLS was obtained applying the FS approximation. The electron binding energy of the core electron in atom i is obtained as the difference between two separate calculations like it was explained in **Chapter 1**. Therefore, the BE and CLS are obtained using **Eq. 1.52** and **Eq. 1.53** respectively. In the FS approximation the CLS is calculated as the energy difference between an unexcited ground-state calculation and a core-excited state calculation. In the excited simulation, one electron from a selected inner shell is removed and added to the valence. Thus, a core hole is introduced in the 4f shell in Pt or the 3d shell in Rh surfaces. The excited electron is removed from the core to the valence shell in order to keep the charge neutrality, filling the first unoccupied level in our

slab. This is not a problem since our systems are metallic and contain many atoms in the simulation cell. The electronic structure of these excited systems is allowed to relax and the core-hole is adequately screened by the valence electrons in the metallic system. Notice that in our calculations the ground-state is the same ($E_a(n_c, n_v) = E_b(n_c, n_v)$), where "a" and "b" now stand for a surface atom and the corresponding bulk reference. This procedure has been shown to provide accurate results to compute CLS's if sufficiently large cells and slabs are considered [78, 79, 85]. Additionally we have checked that similar results for the variation of the Pt 4f surface CLS with strain/miscut angle are found using the initial [78] and the transition state [83, 84] approximations.

In order to study the CLS structural relaxations were performed for the Pt[111] surface. We have used a slab containing five layers where the two upmost layers were relaxed. We have studied various vicinal surfaces, which are stepped surfaces around the [111] high-symmetry orientation. There are two possible kinds of vicinal surfaces on the Pt[111] substrate. The difference in the step type is related to the miscut angle direction. For the A-type stepped surfaces the terraces are (n + 2/3) atomic rows wide and have [100]-like steps, while the B-type terraces have a width of (n + 1/3) atomic rows and [111]-like step (see **Figure 5.1**). Thus, we have studied A-type Pt[557] and Pt[335], as well as the B-type Pt[332] and Pt[221] stepped surfaces. As in the flat surface, the stepped surface contains five layers where the two topmost layers were relaxed. In all cases the k-point sampling employed was consistent with a 15x15x1 sampling for the surface Brillouin zone of Pt[111]. The A-type surfaces Pt[557] and Pt [335] presented a terrace width (d) of 13.6 Å and 8.8 Å respectively. In the other case, B-type steps, the terrace sizes were 12.8 Å for Pt[332] and 8.0 Å for Pt[221].

Test calculations doubling the number of k-points for both flat and vicinal surfaces did not find significant changes. Tests using a surface containing six Pt layers were performed in several cases, finding always almost identical geometries and very similar values for the electronic binding energies. Furthermore, we have studied the influence of the supercell size in the CLS. The variation of the CLS of the 4f level of Pt atoms in the Pt[111] was ≤ 20 meV when using $2\times\sqrt{3}$, $2\times3\sqrt{3}$ and $4\times2\sqrt{3}$ supercells, as well as slabs containing 5 or 6 layers. This indicates that the CLS's in the present system shows a fast convergence with respect to the system size.

The CLS is sensitive to atom coordination and the details of the local structure. In the case of stepped surfaces, this introduces an extra-uncertainty since, in order to compare results obtained for different substrates (obtained using different supercell sizes), we compare the CLS of the Pt 4f level terrace and steps atoms with respect to a well defined reference, such as central bulk atoms. Thus, in each calculation we define the bulk atoms as those belonging to the central layer of the slab (we only compare results obtained with slabs of the same

thickness). For stepped surfaces we have several inequivalent atoms in such central layer. Therefore, we need to average over these different atoms, adding a $\sim$ 10 meV uncertainty to the bulk reference for each miscut angle.

Based on the same premises, the Rh[111] surface was studied using a $2\times\sqrt{3}$ supercell and a slab containing six layers, of which the two topmost were relaxed. All calculations were performed with a 33x33x1 k-sampling of the Brillouin zone in Rh[111], and consistently for all other surfaces. In the Rh[111] only A-step surfaces were investigated. We started from the critical case of steps containing a single row of atoms in the terrace, Rh[113], and increasing the number of terrace atoms until we reach the Rh[557] surface. The terrace widths are 3.9 Å for Rh[113] , 6.2 Å for Rh[112], 8.5 Å for Rh[335], 10.9 Å for Rh[223] and 13.2 Å for Rh[557].

5.3 Pt[111] vicinal surfaces

Cutting with the appropriate angle an polishing the Pt[111] surface it is possible to obtain a wide range of vicinal surfaces. The vicinal surfaces leads to, as it was explained before, two different stepped surfaces, namely A-type and B-type. Curved crystals are excellent samples to determine how the presence of steps and their density affect the mechanical and electronic properties of surfaces, as well as their chemical reactivity. Therefore, curved crystals provide the best way to systematically investigate how the CLS evolves with the terrace size. As it is shown in **Figure 5.1**, curved crystals expose surfaces with increasing step density as we move from the central position, allowing a continuous investigation as a function of the miscut angle.

We have recently participated in a join experimental and theoretical investigation of the variation of the CLS in platinum curved crystals [19]. Our first-principles calculations are in agreement with the experimental observations. **Figure 5.1** shows the schematic experimental crystal sample employed in this research. Using STM and XPS techniques our collaborators were able to measure accurately the terrace width and to study the dependency of the CLS with the step size.

The experimental XPS results are summarized in **Figure 5.2**. The plot is composed using individual XPS spectra and superimposing 15 different spectra systematically recorded across the curved surface [19]. We could identify the Pt $4f_{5/2}$ and Pt $4f_{7/2}$ spin-orbit-split lines contributions from the terrace (T) and bulk (B) atoms. The bulk binding energy showed a constant value along the curved crystal. However, the binding energy associated to the terrace atoms presents an energy shift increment in both Pt $4f_{5/2}$ and Pt $4f_{7/2}$ terrace peaks as the step density increases. The BE of the photoelectons ejected from the surface atoms

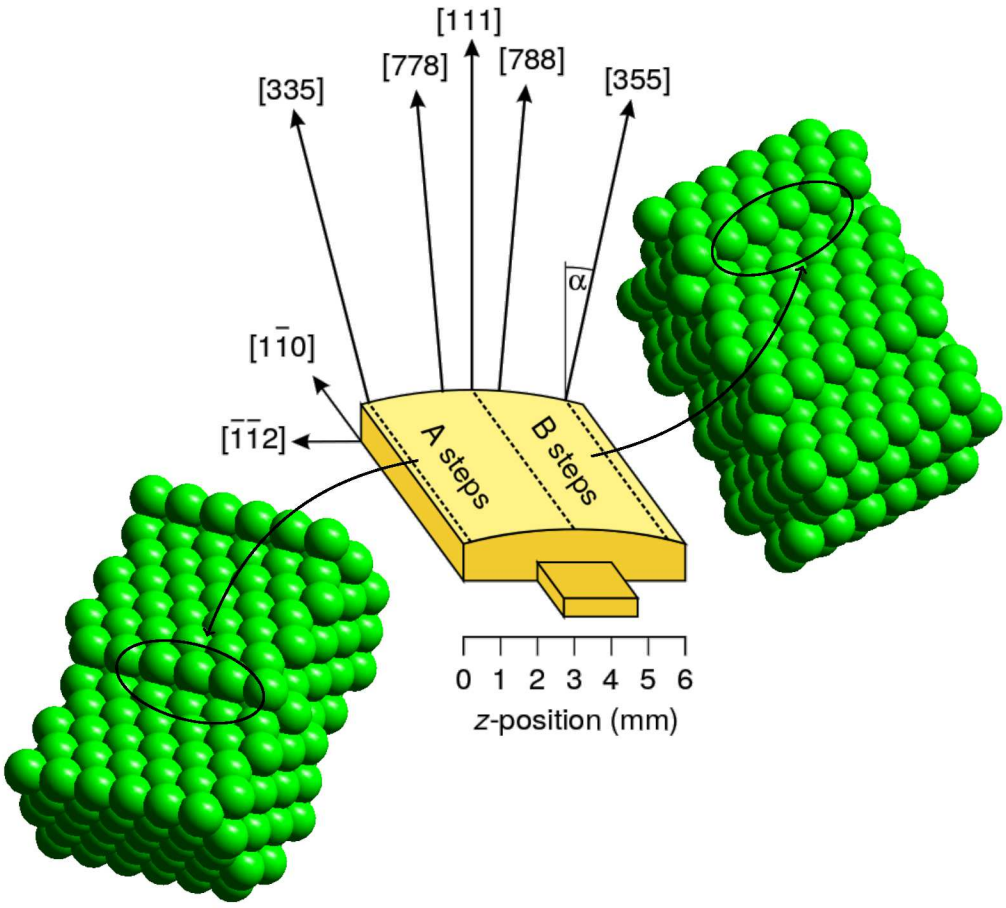

Fig. 5.1 Scheme of the Pt curved crystal discussed in the present chapter. It allows a smooth transition in photoemission experiments through the indicated miscut surfaces by moving the crystal along the bottom z-scale. α is the miscut angle.

suffers a systematic variation. The CLS is reduced as the miscut angle increases. Thus, the variation in the CLS is related to the reduction in the terrace width.

A possible way to understand this systematic variation of the CLS is to correlate it with the level of surface strain. As the terrace width is reduced there is an increment in the surface strain. A contraction of the surface layer (compressive surface strain) will produce that the terrace atoms get more bulk-like (*i. e.*, their effective coordination is increased). Therefore, the inner electrons move to higher binding energies.

From a theoretical point of view, besides the Pt[111] surface we have studied various vicinal surfaces: The [557] and [335] A-type and [221] and [332] B-type stepped surfaces. The calculations for the CLS in the different surfaces are compiled in **Table 5.1**. The CLS

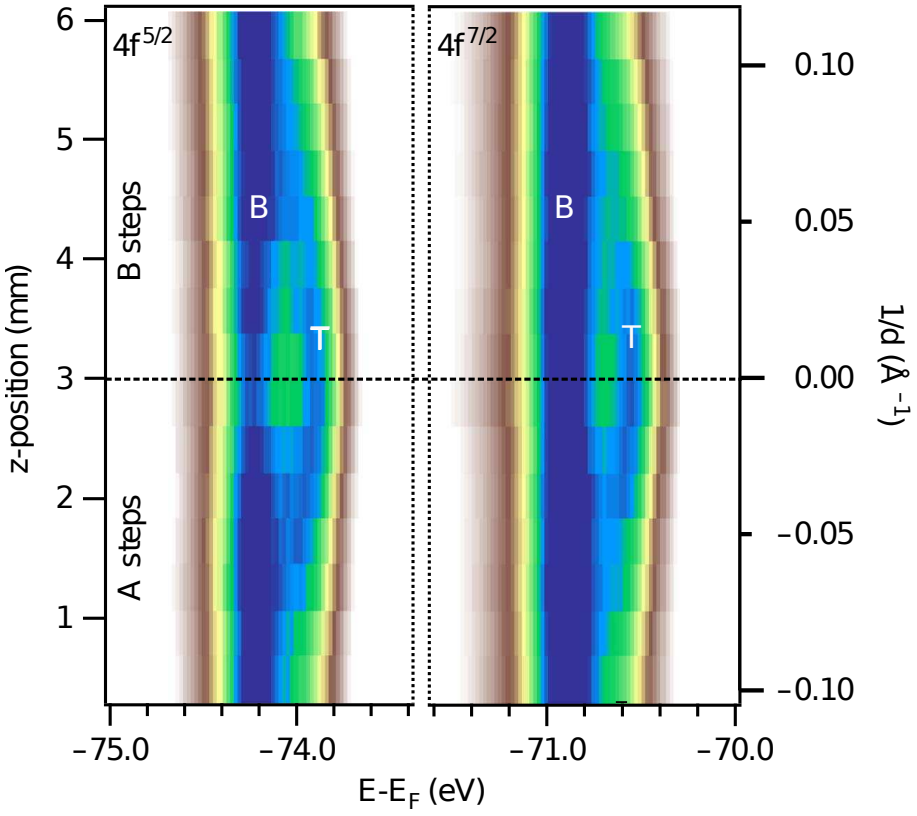

Fig. 5.2 Compilation of XPS spectra showing the evolution of the Pt 4f binding energy across the curved crystal [19]. A characteristic step-density-dependent shift is observed in the surface component (T). As explained in detail in text this reveal a 1/d-dependent accumulation of compressive strain at the surface plane. Notice that the bulk component (B) is completely independent on the miscut angle.

is sensitive to the atomic coordination (n) and a change of the binding energy is observed depending on the atom position in the step (see **Figure 5.3** for the labelling scheme). Atoms in the flat Pt[111] topmost layer have a coordination n = 9, the same that the terrace atomic rows (T_i) in stepped surfaces. The atoms in the step edge (S) have n = 7 and the corner atoms (C) present n = 10 in step A-type ([557] and [335]) and n = 11 for B-type ([332] and [221]) stepped surfaces.

We have plotted in **Figure 5.4** the CLS of the different atoms across the steps using the bulk atom as a common reference for the different vicinal surfaces. The S atom presents the maximal variation in the CLS referred to the bulk and it is quite independent on the miscut angle. This independence of the CLS can be explained in terms of the reduced constraints. The S atom is free to move and find its preferred distance to its neighbours and, as a result, vary its effective coordination. However, although the S atom CLS is independent of the terrace size it is not independent on the step type, which is discernible in the values obtained.

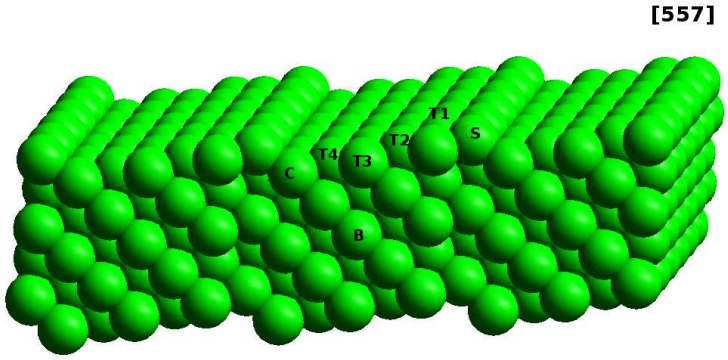

Fig. 5.3 Stepped surface on Pt[557] indicating the atoms with different coordination number (n). S = step atom (n = 7), T_i, i=1,4 terrace atoms (n = 9) numbered from the step edge to the corner, C = corner atom (n=10) and B = bulk atom (n=12).

Table 5.1 CLS (meV) obtained for the different atoms in the Pt[111] vicinal surfaces. Atom labels are specified in **Figure 5.3**.

surface	S	T1	T2	T3	T4	C
[335]	-501	-262	-274	——	——	-260
[557]	-516	-314	-306	-323	-358	-316
[111]	——	-425	——	——	——	——
[332]	-439	-325	-253	-281	-364	-143
[221]	-453	-248	-268	——	——	-67

The CLS is $\sim$ -500 meV for A-type and $\sim$ -450 meV for B-type. A similar behaviour is observed for the C atoms, where the B-type steps present the smaller CLS (-143 meV in Pt[332] and -67 meV in Pt[221]). This is not surprising due to the bigger coordination (n = 11) for the C atom in B-type steps, which increases its bulk-like character.

A distinct situation is observed for the terrace atoms. We have not found a clear dependence on the step orientation. Nevertheless, the CLS show a dependence on the miscut angle and the position of the atom within the step terrace. Thus, in **Figure 5.4** is straightforwardly visible the reduction in the CLS for the T atoms as the miscut angle is increased. In addition, the theoretical results for the core-level energies of the T atoms are notably lower than in the flat Pt[111] surface (-425 meV) in excellent agreement with the experiment. Our theoretical results reproduce the experimental behaviour where the CLS decreases when the surfaces present a larger miscut angle.

In the same figure, the inset shows the variation of the Pt 4f electron CLS versus the inverse of the terrace size (1/d) in each stepped surface. In this plot we have averaged the CLS of the Pt 4f level, relative to that of surface atoms in flat Pt[111], for the T_i atoms (black symbols) and the T_i plus S atoms (red symbols). We have done so because in the case of

experiments for the Pt stepped surfaces it is not possible to distinguish the Pt 4f CLS of the different atoms in the surface. The experimental measurement do not permit to obtain separate S and T contributions for the Pt 4f emission peaks [19]. The problem arises from the T line width, which is 170 meV, preventing from obtain the T and S CLS separately unlike in Rh or W surfaces [173, 185]. This very large width of the T contribution seems to correlate with the substantial dependence of the CLS of T atoms as a function of its position in the terrace (see **Figure 5.4**). Thus, we have plotted the average value of the T_i plus S atoms in the figure. As it was found in the experiment, the Pt 4f CLS decreases as function of the miscut angle.

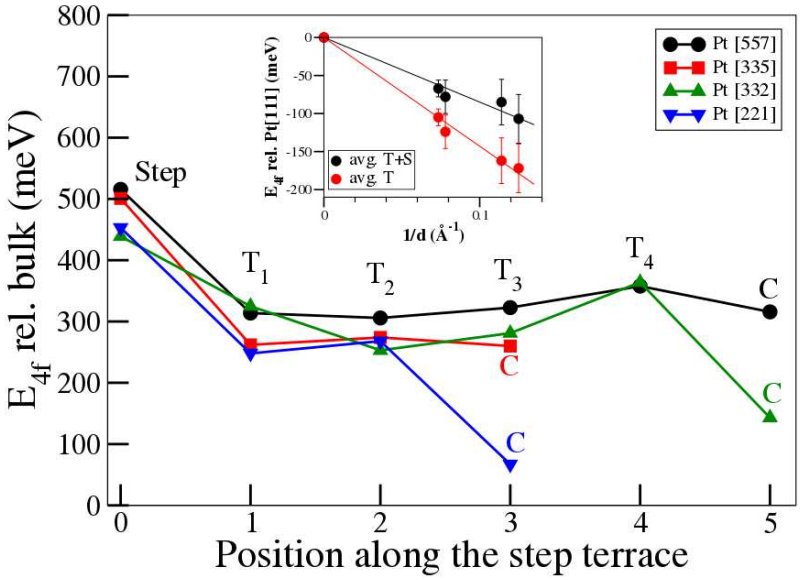

Fig. 5.4 Pt 4f core-level energy of S, T_i and C atoms with respect to the bulk reference calculated for different stepped surfaces. The inset shows the resulting CLS with respect to the flat Pt[111] surface, after averaging over all the atoms in a given terrace (T, red), or additionally considering step atoms (T+S, black), as a function of 1/d. The error bars show the uncertainty coming from the bulk reference atom and the uncertainties on the determination of the Pt[111] surface reference (mostly associated with the supercell size). The CLS diminishes as the miscut angle increases, similarly to the measured XPS data showed in **Figure 5.2**. Continuous lines in the inset are linear fits.

The variation of the CLS along the curved crystal is related to the terrace width. Based on the XPS measurements it is possible to calculate how the terrace size is affecting to the CLS. A Doniac-Sunjic fit is applied in the individual XPS spectral that permitted to determine the

energy shift ΔE_T(d) of the surface core-level [19]. The experimental values obtained are plotted in **Figure 5.5**.

In order to obtain the relationship between the CLS and the strain in the surface it is possible to use a simple model based on the effective coordination of the terrace atoms for each surface. Bianchettin *et al.* found the linear relation between the coordination number and the core-level energy [173, 186]. A detailed explanation is presented in **Appendix B**. In this model the dependence of the CLS with the coordination number (parametrized from the CLS of the surface atoms in Pt[111] with respect to bulk) is used to estimate the dependence of the CLS with the average distance to neighboring atoms (density). In this way, one can try to correlate the observed shifts in the surface CLS as a function of the miscut angle with the level of compressive strain for different stepped surfaces. The fit result is plotted in **Figure 5.5** as a black solid line. From the model there is an estimated average reduction of ~ 2 % in the nearest neighbour Pt-Pt distance for the surface layer of the highly stepped Pt[335] and Pt[355] surfaces. Here we assume a linear variation of the CLS with the atomic coordination between the bulk (n=12) and the surface (n=9) atoms. The fit shows a good agreement with the experimental values near to the high symmetry direction [111] (large d values). However, as the miscut angle increases the model seems to over estimate CLS reduction as compared to the measured results. One possible explanation might be related to the relative importance of the step atom, whose CLS does not depend on the miscut angle and whose contribution will become more important the shorter the terrace. This might be the cause why the experimental CLS cannot be properly associated to a given strain through the effective coordination model using n=9 [19].

We have also plotted in **Figure 5.5** the results of our first-principles simulations. In spite of the agreement with the experimentally observed trend, our calculations present an overestimation by more than a 50 % of the terrace size dependence. The reason for this large divergence is not clear and could be related to the limitations of the approximations utilized (e.g., use of semilocal density functionals or the lack of core relaxation in the current implementation of the final state approximation within VASP).

From the above discussion, one can conclude that it is sensible to interpret this energy shift as primarily due to the average compressive strain present in the terraces of the vicinal surfaces. With a view to obtaining the different contributions to the strain, we have analyzed our relaxed structures and differentiated between the out-of-plane strain (s_{out}), which is perpendicular to the terrace plane, and the in-plane strain (s_{in}) that is contained in the plane of the step terrace. The s_{out} is obtained as the variation of the distance between the topmost and the second layer using the Pt[111] surface as reference. To get s_{in}, the step width d is compared with the corresponding distance for the same number of atomic rows on the Pt[111]

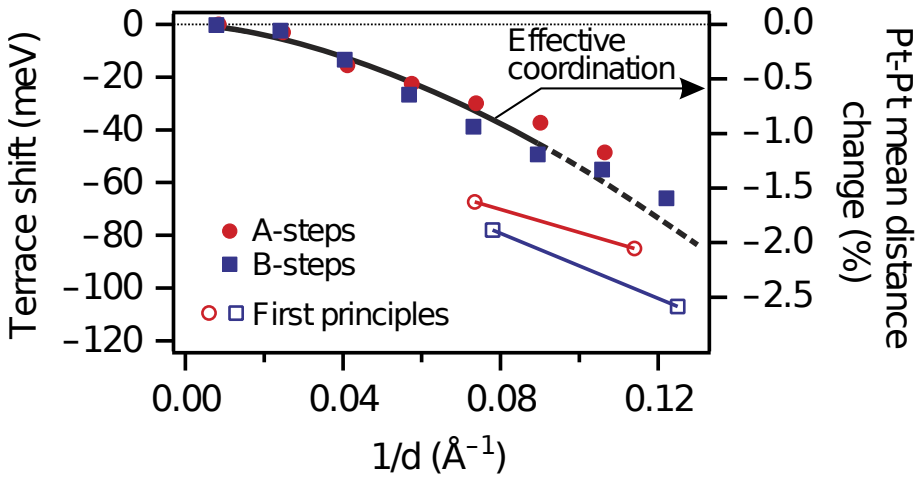

Fig. 5.5 Surface core-level energy variation across the curved crystal [19]. Red and blue symbols are the experimental values whereas the open symbols are core-level shifts determined from first-principles calculations for some stepped surfaces. The black solid line represents the lattice strain with respect to bulk Pt, as deduced from the core-level energy and the associated effective coordination change n_{eff}(d) using a simple model described in **Appendix B**.

surface. The total strain (s_t) is calculated using the average distance to all the first-neighbours of all the atoms in the topmost layer. The results of s_{out}, s_{in} and s_t are shown in **Table 5.2**.

Table 5.2 s_{out}, s_{in}, s_t and terrace witdth (d) for the studied Pt vicinal surfaces. Pt[111] is used as a reference to define zero strain (0 %).

	surface	% s_{out}	% s_{in}	% s_t	d (Å)
A-type	**[335]**	1.27	-3.97	-0.92	8.8
	[557]	0.78	-2.76	-0.68	13.6
	[111]	0	0	0	∞
B-type	**[332]**	1.14	-3.81	-0.90	12.8
	[221]	1.68	-4.97	-1.11	8.0

Thus, we have confirmed that there is a compressive strain acting on the surface of the stepped surfaces. Our results showed that when the stepped surface is relaxed it suffers a compression in the first layer. As the miscut angle increases there is a increment in the compressive strain in the stepped surface which causes a contraction of the width of the terraces.

The in-plane strain s_{in} is partially compensated by s_{out}. The stepped surfaces present a larger distance between the first and the second layer in order to compensate the increment of s_{in}, however, the global result is a compressive strain in first layer of the material. In addition,

we have calculated the local strain for all of the T_i atoms in the different stepped surfaces. We show s_{out}, s_{in} and s_t strains for the atoms in the terrace as well as their CLS in **Table 5.3**.

Table 5.3 s_{out}, s_{in} and s_t for the T_i terrace atoms (see **Figure 5.3**) in the different vicinal surfaces and their CLS (meV) . Pt[111] is used as a reference to define zero strain (0 %).

Surface	site	% s_{out}	% s_{in}	% s_t	CLS (meV)
[335]	T_1	1.43	-2.10	-0.92	-262
	T_2	1.11	-1.96	-0.93	-274
[557]	T_1	1.64	-1.82	-0.67	-314
	T_2	0.66	-1.31	-0.65	-305
	T_3	0.15	-0.93	-0.57	-323
	T_4	0.64	-1.17	-0.57	-358
[332]	T_1	2.15	-2.13	-0.70	-325
	T_2	0.76	-1.87	-0.99	-253
	T_3	0.67	-1.87	-1.02	-280
	T_4	0.96	-1.80	-0.88	-364
[221]	T_1	1.96	-2.71	-1.15	-247
	T_2	1.38	-2.51	-1.21	-268

A clear correlation between the Pt 4f energy shift and the strain at every T_i site is observed. The data also show an evident correlation between s_{out} and s_{in} changes. Despite the large uncertainties in the results obtained for the CLS's, our data show that CLS's are mostly influenced by the strain acting in the surface.

In summary given the numerical uncertainties in the CLS calculations and the small size of the shifts we are addressing, we believe that our first-principles calculations give a reasonable account of the experiments and confirm that the change of the strain of the surface layer as a function of the miscut angle is the main source of the observed effect.

5.4 Terrace Compression Model

We have shown with our explicit calculations that the strain is playing a key role in the variation of the binding energy observed in the experiment. With the aim to further understand how the compressive strain affects the CLS in stepped surfaces we have developed the so-called Terrace Compression Model. The aim of the TCM is to describe in a controlled way the relationship between the surface strain and the variation in the Pt 4f binding energy.

Prevot *et al.* obtained the relaxation of the terrace atoms decomposing it into two contributions. One comes from the relaxation of the terrace plane whereas the other part is the specific relaxation due to the presence of the step [195, 196, 205]. In a similar way we have decomposed the strain in two separated contributions.

We have studied the CLS variation due to the out-of-plane strain using a flat Pt[111] surface. The distance between the first and second layer in this surface, 2.308 Å, is used as a reference to define $s_{out} = 0\%$. As it is schematically shown in **Figure 5.6**, we can applied an artificial strain in the normal direction. Using the converged geometry where all atoms are fixed, we have moved the topmost layer atoms. Thus, the variation in the distance between the first and the second layer could be interpreted as applying a compressive or expansive strain in the normal direction to the surface.

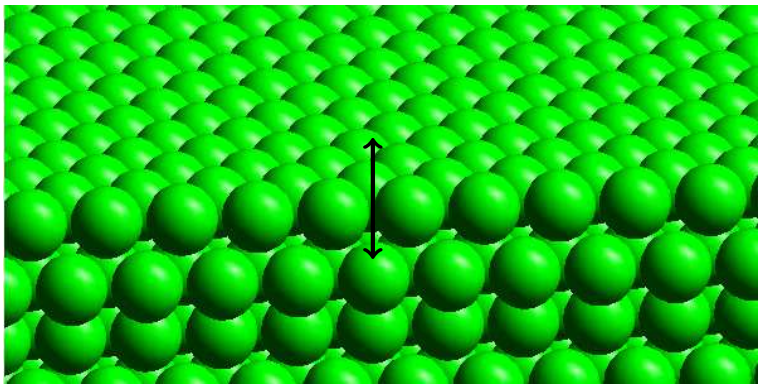

Fig. 5.6 s_{out} in the TCM. The topmost layer is artificially displaced to change s_{out} in a controlled, continuous way and calculate the associated variation of the CLS.

We have calculated the CLS for the T atoms referred to the B atom in the Pt[111] surface for different interplanar distances. This gives the Pt 4f level in the surface atoms in Pt[111] as a function of the distance between the topmost layer and the second one. The results for the CLS versus the out-of-plane strain percentage are plotted in **Figure 5.7**. It permits to estimate the derivative with respect to the s_{out}. The result shows $\frac{\partial E_{4f}}{\partial s_{out}} \sim 13$ meV, which is the variation of the CLS with regard to the % s_{out}.

On the other hand, the effect of the in-plane strain was investigated using the Pt[557] stepped surface. **Figure 5.8** contains the schematic diagram for the artificial strain applied along the $\langle \bar{1}\bar{1}2 \rangle$ direction. In order to apply a given value of s_{in} to the surface, and to be able to change this value continuously, we take the relaxed structure of the Pt[557] surface and apply a constant compression/expansion along the $\langle \bar{1}\bar{1}2 \rangle$ direction to the top layer of atoms forming the terrace. Taking the C atom as a reference, we calculated the distance to the other atoms in the first layer of the stepped surface. Afterwards, we applied a given strain and calculated the distance variation between the corner atom and the topmost layer atoms due to such strain. Finally, the T_i and S atoms were relocated in the new sites obtained with the addition of the distance change to the original coordinates. Therefore, we have only applied an artificial s_{in} on the topmost layer and moved the atoms in the step direction. The variation

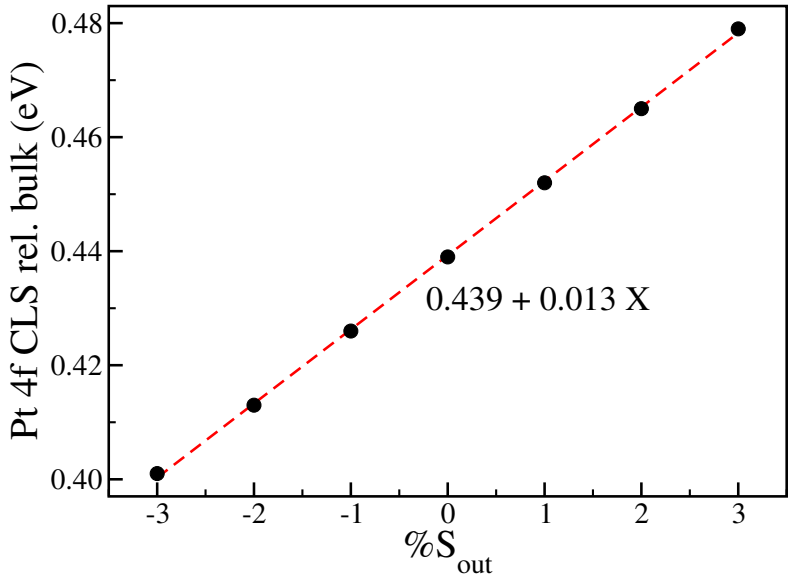

Fig. 5.7 Pt 4f CLS versus percentage strain out-of-plane strain ($\%s_{out}$) at the Pt[111] surface. CLS energies are referred to bulk. The red dashed line is a linear fit.

in the distance between the atoms in the first layer, results in a variation in the surfacce s_{in} without changing the size of the supercell.

We have calculated the position of the Pt 4f level of each T_i atoms in the terrace for different values of the applied s_{in}. The results are plotted in **Figure 5.9**. The variation of the CLS as a function of the applied strain is very similar for all the T_i atoms in the stepped surface, allowing to unambiguously define the derivative of the Pt 4f level energy with respect to the in-plane uniaxial strain $s_{in}^{<\overline{1}12>}$. Our results show that the variation observed is $\frac{\partial E_{4f}}{\partial s_{in}^{<\overline{1}12>}}$ $\sim$ 23 meV with respect to the percentage variation of s_{in}.

We have obtained an estimation for the Pt 4f level variation as a function of the strain applied on the surface. Based on the deduced relations, we can argue that the CLS would depend on the change of the strain. We have approximated the variation of the Pt 4f level in vicinal surfaces as:

$$\Delta E_{4f} = 13 \times s_{out} + 23 \times s_{in} \ (meV) \tag{5.1}$$

where the variation in the binding energy (meV) comes from the addition of the contributions of the percentage of strains, s_{out} and s_{in}.

Same argument could be applied to the variation of the average Pt-Pt distances for the atoms in the topmost layer with respect to Pt[111]. The average Pt-Pt distance change (Δr)

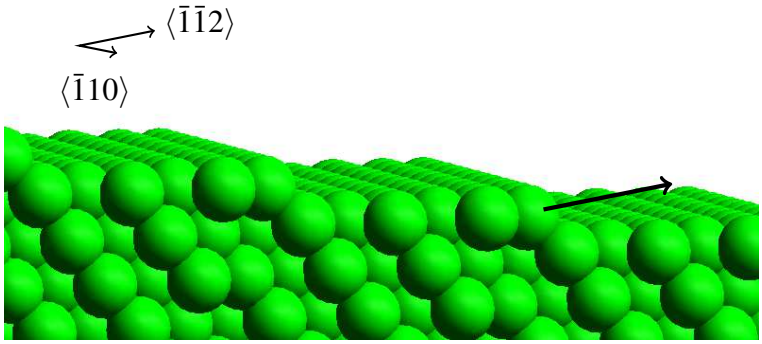

Fig. 5.8 s_{in} in the TCM. The T_i and S atoms are artificially displaced in order to change s_{in} in a continuous way, and calculate the associated variation of CLS.

in the first layer owing to the strain on the surface is obtained with the following relation:

$$\frac{\Delta r}{r} = \frac{2 \times s_{out} + 3 \times s_{in}}{9} \tag{5.2}$$

The complete deduction of the formula is in **Appendix B**.

With a view to reducing our model to a single parameter, it is necessary to establish a relationship between the two components of the strain. Analyzing the geometries of the different vicinal surfaces a good approximation was obtained for the four stepped surfaces. This relationship between the s_{out} and s_{in} for the different vicinal surfaces is:

$$s_{out} \sim -0.45 \times s_{in} \tag{5.3}$$

Thus, we could reduce the variation of the E_{4f} level to a single parameter. Assuming that this approximate relation between the s_{out} and s_{in} holds for terraces of all sizes, we can express the E_{4f} shift as a function of the average percentage change of the Pt-Pt distance in the terraces of Pt[111] vicinal surfaces as:

$$E_{4f} \sim 17.15 \times s_{in} \sim 73.5 \times \frac{\Delta r}{r} \tag{5.4}$$

The results are plotted in **Figure 5.10**. In the chart we can easily compare all the results obtained in this chapter. As it was shown, the effective coordination model (black solid line) was derived from the experimental data and gave a good approximation to the experimental measurements. However, it corresponds to an empirical fit and, therefore, it could not be used alone to justify the dominant role of strain. First-principles calculations (green solid line) describe the correct behaviour of the CLS with the strain, but they present an important overestimation with regard to the experimental values. Finally, the TCM (solid orange line)

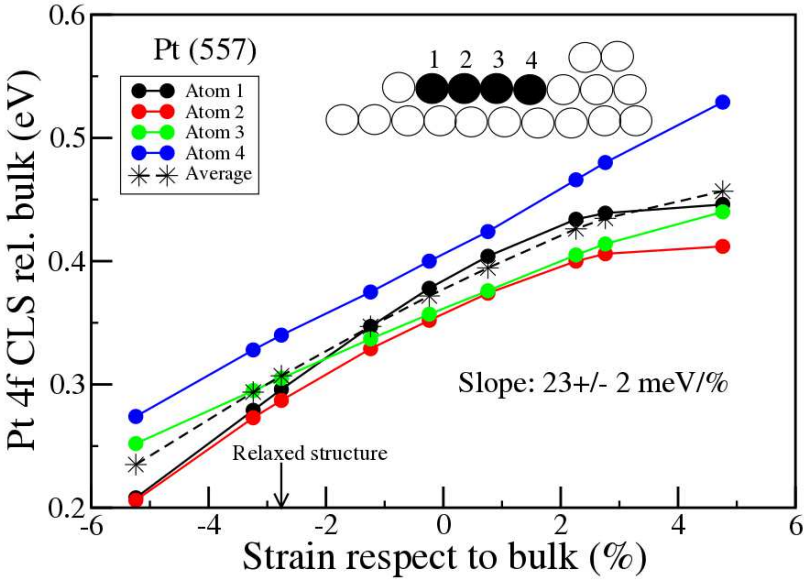

Fig. 5.9 Pt 4f CLS versus s_{in} calculated applying an homogeneous strain to Pt[557] terrace. CLS energies are referred to bulk.

produces a more accurate approximation to those deduced from the experiment using the empirical effective coordination model. It gives significantly smaller CLS values than those obtained from DFT calculations in the different stepped surfaces. Moreover, the TCM clearly demonstrates that the CLS changes are mainly produced by the increasing compressive strain that the stepped surfaces suffer as the miscut angle increases. This proves and provides the relation between the changes in the binding energies and the size of the terraces in the stepped surfaces.

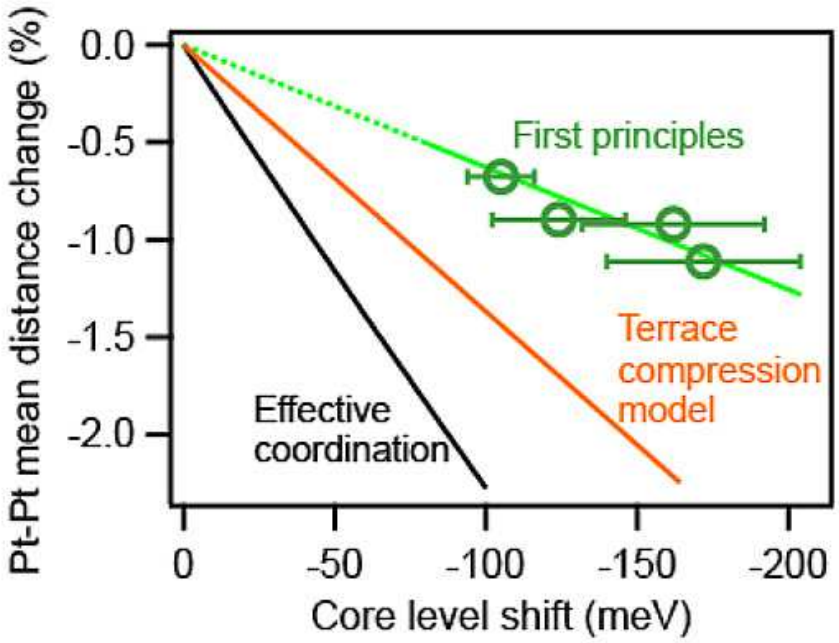

Fig. 5.10 Average nearest-neighbour distance change of T atoms as a function of the core-level energy shift (CLS) as deduced from different theoretical models [19]. Comparison between the results obtained from the effective coordination model (black line, it can be considered a fit of the experimental data), the Terrace Compression Model (orange line) and first-principles calculations (green points) in the different stepped surfaces. The green line is a guide to the eye for the latter. The error bars associated to the DFT results reflect the uncertainty associated with the bulk reference atom in the stepped surface plus the uncertainties due to different cell sizes for Pt[111].

5.5 Rh[111] vicinal surfaces

We have conducted the same research for the Rh[111] vicinal surfaces. In this case, we have only investigated A-type stepped surfaces. Bearing in mind that the terrace size affects to the CLS we have simulated five different stepped surfaces near the Rh[111] surface. Thus, apart from the flat surface we have studied the extreme Rh[113] which contains only one atom in the terrace, *i. e.*, only the step atom. Increasing the number of atoms in the terrace we have modelled the [112], [335], [223] and [557] vicinal surfaces.

The computed Rh 3d level shifts are presented in **Table 5.4**. Our calculation reveal that the CLS for the Rh[111] surface is $\sim$ -503 meV, which is consistent with the -500 meV obtained in previous DFT calculations [175] and experimental measurements [174, 175] and in good agreement with the -485 meV obtained in a recent work of Baraldi *et al.* [176, 177]. Our results show that the variation in the Rh 3d level between the S and T_i atoms is always bigger than 300 meV. Experimental measurements are able to distinguish between the different contributions to the spectra from B, T and S atoms [185]. The binding energy shifts observed in our theoretical simulations are consistent with the experimental results.

Table 5.4 CLS (meV) values for the different atoms on the Rh[111] vicinal surfaces. Atom labels' are explained in **Figure 5.3**.

surface	S	T1	T2	T3	T4	C
[111]	——	-503	——	——	——	——
[557]	-837	-452	-484	-529	-445	-362
[223]	-828	-441	-475	-477	——	-347
[335]	-822	-449	-424	——	——	-363
[112]	-830	-389	——	——	——	-334
[113]	-771	——	——	——	——	-291

The variation in the binding energies are plotted in **Figure 5.11**. This chart contains the CLS with respect to the bulk reference. The S atoms show the larger change in the CLS with respect to the Rh[111] surface atom, independently of the terrace size. Leaving aside the Rh[113], where the steps are composed by just one S atom, we observed a stable value of the CLS for the S atom ($\sim$ -829 meV) in our vicinal surfaces. This independence is not surprising taking into consideration that the S atom is free to move an arrange its bonding distance to the terrace leading to a constant CLS value. A similar result was also observed for Pt[111] vicinal surfaces.

Concerning the terrace atoms, the binding energies show a systematic variation along the terrace. Furthermore, there is a steady increment of the Rh 3d binding energy with the terrace size. Our results show that as the miscut angle increases there is a CLS reduction in the T atoms of the stepped surfaces. In the case of the C atom, the Rh 3d level do not present

large variations and, in average, the CLS is $\sim$ -340 meV. The energy variations are small in this case and do not show a clear relation to the miscut angle or the terrace size.

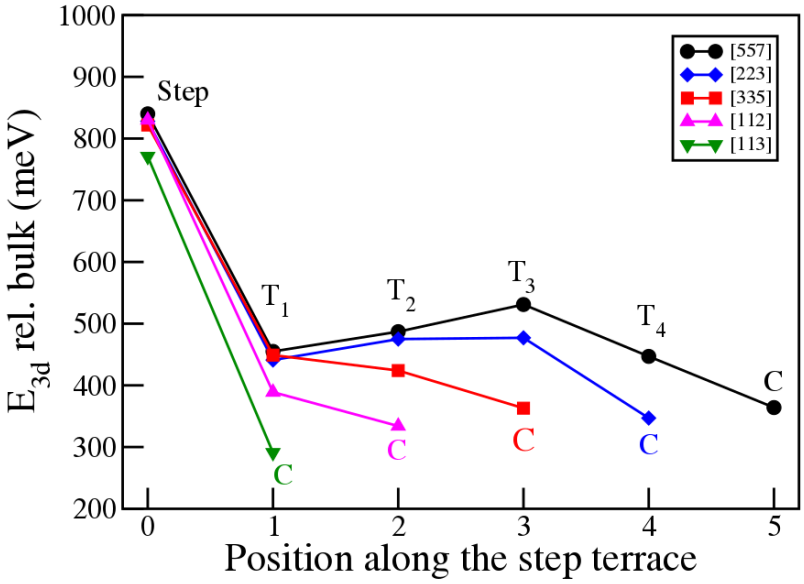

Fig. 5.11 Rh 3d core-level energy of S, T_i and C atoms with respect to bulk calculated for different stepped surfaces. Atom labels are explained in **Figure 5.3**.

We have calculated the average CLS for the T_i atoms in the different stepped surfaces. In **Figure 5.12** these results are presented as a function of the inverse of the terrace size. In our calculations we have considered the error coming from the supercell size ($\sim$ 3 meV) as well as the error from the bulk reference uncertainty, which is maximum for the [113] stepped surface (13 meV). These uncertainties in the CLS values are plotted in the chart. The red solid line is the linear fit obtained with the CLS average values of the T atoms in each case. The maximal difference between the adjustment and the value obtained is $\sim \pm$ 20 meV. Knowing that the uncertainty is less than 16 meV in the worst case scenario, our results reveal an accurate approximation to the linear fit. In this sense, we find a straightforward relationship between the Rh 3d level shift and the terrace size.

Comparing with the experimental measurements obtained by our collaborators at the Nanophysics Lab at CFM [206], our results predict accurately the CLS for large terrace sizes. However, there is a deviation between the first-principles calculations and the experiment when the miscut angle increases up to 13-15°. We could not figure out the cause that produces this diversion in the experiment. We are currently discussing with our colleagues the possible reasons for the weird behaviour encountered in the experiment. Nevertheless, our results are

in good agreement with the experimental measurements for small miscut angles. Proving that there is a relationship between the CLS observed and the size of the terraces.

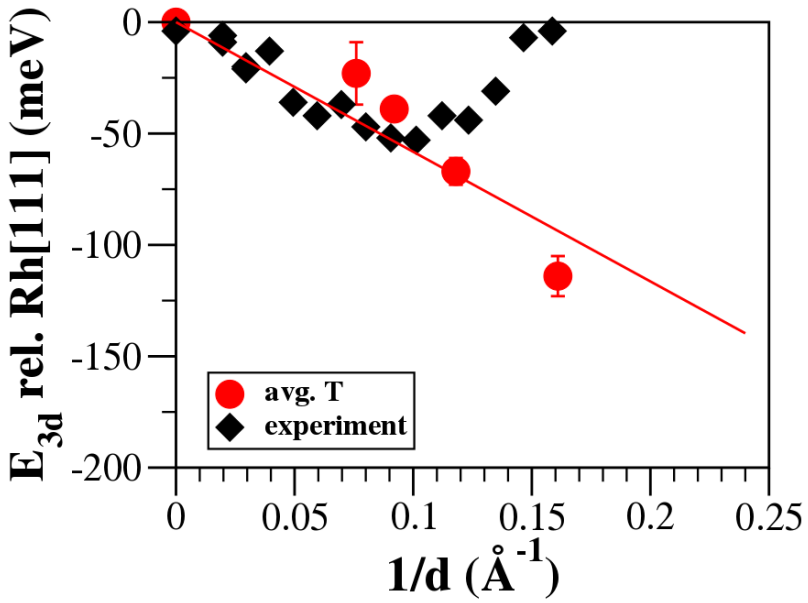

Fig. 5.12 CLS vs 1/d. CLS averaged over the terrace atoms with respect to the flat Rh[111] surface (red circles) and experimental results (black diamonds) [206]. The error bars show the uncertainty coming from the bulk reference atoms and the uncertainties owing to the supercell sizes for the Rh[111] ($\sim$ 3 meV). The continuous line is a linear fit.

We surmised that the CLS reduction when the miscut angle increases is related with the increment in the strain in the topmost layer. Using the formulas explained in **Section 5.3** and the relaxed structures we have calculated the different strains in the stepped surfaces. The results are contained in **Table 5.5**. In addition, we show the CLS average value for the T atoms in each surface. As expected, in the Rh[111] vicinal surfaces we observed that s_{in} increases with the miscut angle. As we reduce the size of the terrace and the s_{in} increases, concurrently, the s_{out} increases partially redressing the balance between the s_{in} and s_{out}. It is worth noting that for Rh surfaces s_{out} is much smaller than in the case of Pt[111] vicinals.

In the light of the results it is clear that in the topmost layer as the strain increases with the miscut angle there is a reduction in the CLS. This demonstrates that the strain in the surface is a key player in the variation of the binding energy. Further analysis, similar to that preformed for Pt[111] vicinal surfaces, should be necessary to understand the observed variation in depth. At the same time, we should study the B-type stepped surfaces in order to see if the variation is consistent in both substrates as one can expect. It would be also

interesting to test our TCM in the Rh surface in order to corroborate that indeed the strain is the main factor to explain the CLS changes.

Table 5.5 s_{out}, s_{in}, s_t and CLS for the Rh[111] vicinal surfaces. CLS (meV) are the averaged values for the T_i atoms in each case.

surface	**% s_{out}**	**% s_{in}**	**% s_t**	**CLS (meV)**
[111]	—	—	—	-503
[557]	-0.02	-1.11	-0.33	-480
[223]	0.00	-1.40	-0.41	-464
[335]	0.08	-1.67	-0.56	-436
[112]	0.10	-2.69	-0.82	-389
[113]	—	-4.10	-1.11	-291

5.6 Conclusions

Curved crystals are really interesting surfaces that permit systematic measurements for different stepped surfaces at same time. Therefore, studying systematically the properties of material surfaces using only a single sample. In this chapter we have investigated the CLS on different curved crystals, namely Pt and Rh substrates. Our calculations have been run in different vicinal surfaces around the high symmetry [111] direction . We have simulated a few stepped surfaces and obtained the binding energy variation for distinct atoms in the material.

In first case, we have carried out research into Pt[111] vicinal surfaces in depth. The experimental observations for the Pt 4f level energy shift have shown that the CLS is related to the terrace size. The CLS was observed in the two kinds of vicinal surfaces, A-type and B-type, presenting a reduction as the miscut angle increases. An empirical model used to interpret the experimental data for the variation of the binding energies showed a correlation between the effective coordination and the CLS.

Our first-principles calculations showed the same tendency as the experimental results, however, there is an overestimation of the CLS. Despite the overestimated values, the DFT results qualitatively agree with the experiment and proves that the additional strain, which appears in the first layer on the stepped surface, is the main factor affecting to the Pt 4f binding energy changes.

Based on *ab initio* calculations we provide a detailed model, the so-called TCM, of the relation between the surface strain and the CLS. The TCM gives a better approximation to the experimental values in comparison with the supercell first-principles results. Thus, we

have demonstrated that the strain in the surface plays the main role in the variation of the CLS. Furthermore, the TCM proves that as the strain increases in the surface the Pt 4f energy shift is reduced. This, together with the analysis of the relaxed structures for different vicinal surfaces, provides a clear link between the energy displacement and the step size.

Finally, we have studied the variation in the CLS in Rh[111] vicinal surfaces. The CLS present a stable value for the S atom. The energy difference between the electronic binding energies of S and T atoms is consistent with the experimental observation where they are able to distinguish between the two contributions to the spectra. We have found a clear correlation between the terrace size and the Rh 3d level shift for small miscut angles. Moreover, we have proved that the strain in the surface increases due to the reduction of the terrace size. It produces a progressive upshift in the Rh 3d level. Thus, the increment in the miscut angle leads to a reduction in the CLS. We expect that these results will help to interpret the experimental data. The preliminary experimental results show a very good agreement with the calculated results for small miscut angles, although strongly deviate at large miscut angles. The reason for this deviation is still unknown to us.

Chapter 6

CO adsorption on Pt[111] vicinal surfaces

Reserve your right to think, for even to think wrongly is better than not to think at all.

Hypatia of Alexandria

6.1 Introduction

The understanding of the structures, adsorption sites and molecular interactions is a fundamental issue for the study of catalytic reactions. The CO molecule is commonly used to test surfaces due to its simplicity and the well-known adsorption properties. CO adsorption on Pt surfaces is relevant due to heterogeneous catalytic reactions of industrial processes and environmental implications. Pt surfaces are renowned catalyst for CO adsorption and oxidation and have been used to lower CO emissions from combustion processes [207–209].

CO adsorption on Pt surfaces was extensively studied theoretically [210–216] and experimentally [217–223]. Experimental observations show that the CO molecule adsorbs at top sites on Pt[111] at low coverage. When the coverage increases the CO molecules start to occupy the bridge sites [217–220] on the substrate too. To mention just one work, Blackman *et al.* studied CO adsorption on Pt[111] [220]. Using LEED, HREELS and IRAS they were able to identify the CO adsorption on top sites at low coverage. In addition, they showed that as the coverage was increased the CO molecules were also adsorbed at bridge sites.

Defects like adatoms, steps or kinked steps frequently present a large catalytic activity. Stepped surfaces are regular arrangements of steps, in metal surfaces frequently monatomic

steps. It is possible to access to many different stepped surfaces by cutting a low miller index flat substrate producing a curved crystal. Thus, different surfaces near to a high symmetry direction can be obtained. These stepped surfaces are known as vicinal surfaces and its terrace size depends on the miscut angle. Stepped surfaces are really interesting due to their catalytic properties [180–184, 224, 225] and a more appropriate model in relation with real surfaces than monatomically flat surfaces.

Combining theoretical and experimental studies Brown *et al.* identified the CO adsorption preference on Pt[211] [226, 227]. Applying RAIRS, temperature programmed desorption (TPD) together with DFT calculations they showed that CO adsorbs first on the step edge and then on the terraces. Thus, the step edge adsorption presents a higher binding energy than the terrace. In both cases, the CO adsorption was found at top and bridge sites, however, the top step site was confirmed as the most stable. Based on these results, Orita *et al.* studied CO adsorption on different vicinal Pt[111] surfaces using first-principles calculations [228, 229]. In their results the CO molecule adsorbed at top step edge on Pt[211] and Pt[311] at low coverage. The second most stable adsorption site was found at bridge step site. Like in the experiment, CO adsorbed first at top and bridge sites on the step edge and, when the coverage was increased, also on the terraces.

Luo *et al.* observed CO adsorption on Pt[335] [230]. Using EELS and TPD they found that CO adsorption happens at top and bridge sites on the step edge before the terrace adsorption occurs. Xu *et al.* studied CO adsorption on the Pt[335] and Pt[112] vicinal surfaces [231]. Applying TPD and IRAS techniques they were able to distinguish four different adsorption sites. Similar to the previous case they found that the CO adsorbs at top and bridge sites. In addition, they showed that the CO molecule is more strongly bound at the step edge than on terraces.

The presence of steps in the surface produces changes in the crystal properties. We studied in **Chapter 5** how the step geometry, and the associated strain, affects to the surface CLS on vicinal Pt[111] surfaces. The BE is sensitive to the geometry and chemical environment [176, 232]. Thus, the variation in the CLS could be used to precisely determine the properties of CO adsorption on metal surfaces.

Different XPS experiments confirmed that CO adsorption on Pt[111] occurred at top and bridge sites [223, 232, 233]. The variation in the electron BE for the C 1s on the Pt[111] surface was measured, obtaining a CLS between both sites of 700 meV. Applying the same technique, C 1s measurements on the Pt[331] stepped surface confirmed that the step edge is the preferred CO adsorption site over the terrace at low coverage [171].

CO adsorption on Pt stepped surfaces was extensively investigated by Tränkenschuh *et al.* [234, 235]. Their XPS measurements showed a dependence of the CO adsorption on

the step direction. They used vicinal Pt[111] surfaces composed by five atomic rows wide steps that are separated by monatomic steps. They found that, in the type-A steps of the Pt[322] surface, the CO molecule was adsorbed on top and bridge sites on the step edge. However, in type-B steps in Pt[355] only the top step site was detected. Additionally, their observations revealed that the step edge site was preferred for the CO adsorption over the terrace. Only when the step edge was almost saturated the CO adsorption on the terrace was detected, corroborating previous experiments.

In this chapter we present a study of CO adsorption on Pt[111] using first-principles calculations. In addition, we investigated different Pt[111] vicinal surfaces with a view to unveiling the adsorption site on the different stepped substrates. CO adsorption was studied for four different Pt stepped surfaces: [557], [335], [332] and [221]. Thus, we could simulate CO molecular adsorption on the two kind of steps (type-A and type-B) and compared our results with XPS measurements performed by our colleagues from the NanoPhysics Lab directed by Prof. J. E. Ortega at the Centro de Física de Materiales in Donostia-San Sebastián (CSIC-UPV/EHU) using Pt[111] curved crystals [19].

We also investigated the limit of high CO coverage. We have increased the number of molecules adsorbed on the surfaces until 0.5 monolayers (ML). The theoretical results revealed a reduction of the adsorption energies with the increased coverage. However, the step edge adsorption site was still preferred over the terrace sites in all the cases. After CO adsorption was characterized, we calculated the C 1s BE for the different systems. Our results are in good agreement with previous theoretical [79, 85, 233] and experimental [234, 235] observations. Unfortunately for the C 1s level of the adsorbed CO, as opposed to the CLS in the Pt[111] vicinal surfaces, there is not a clear reference in order to calculate the variation of the BE. Thus, it is not obvious how to compare theoretical results obtained for different supercell sizes. This is a problem, since the experimental results seem to indicate a systematic shift of C 1s level of the CO molecules adsorbed on the terraces as a function of the miscut angle and we would like to analyze this possibility from a theoretical point of view. In **Chapter 5** we observed a similar effect for the 4f level of the Pt atoms in the terraces of vicinal Pt[111] surfaces. It was possible to conclude that this shift was mostly related to the different surface strain in different stepped surfaces. Therefore, here we will also investigate the strain of the surface layer as the main ingredient characterizing the different surfaces, and study the position of the C 1s level of a CO molecule as a function of the strain of the surface below. Our approach to this problem will be based on the previous explained TCM (**Section 5.4**). This will permit to study theoretically the variation of the C 1s CLS with the miscut angle on a Pt curved crystal.

6.2 Methodology

The calculations were performed with VASP [12] using the PBE functional [55]. The PAW method [99] was applied to describe the electron-ion interactions with a plane-wave cutoff of 400 eV for the kinetic energy. A Monkhorst-Pack mesh [91] of 25x25x25 was employed to sample the Brillouin zone in the bulk calculation. First-order Methfessel-Paxton scheme [168] with smearing width of σ = 0.2 eV was used with the electronic convergence set to 10^{-4} eV. The structures were optimized until the atomic forces acting in the system were less than 0.03 eV/Å.

CO adsorption on Pt[111] was studied in a $2\times\sqrt{3}$ supercell using a 15x15x1 k-mesh for the Brillouin zone. The Pt[111] slap contains five layers where the two upmost layers were allowed to relax. A large distance (30 Å) was kept with a view to avoiding the interaction between the periodic slab replicas.

Two kind of stepped surfaces were investigated after CO adsorption. The main difference between the stepped surfaces comes from the type of step edge. In type-A surfaces the step is [100]-like meanwhile the type-B surfaces has [111]-like step atoms. Like in the flat surface, we used a five layer slab where two superficial layers were relaxed. The distance in the vertical direction was large enough ($\sim$ 30 Å) to ensure that there was no interaction between the periodic slab in the normal direction. We took advantage of the previous calculated stepped surfaces in **Chapter 5**. CO adsorption on the Pt[111] vicinal surfaces was studied for the Pt[557], Pt[335] (type-A) and Pt[332], Pt[221] (type-B) surfaces. In all cases the number of k-points was consistent with the sampling for the Brillouin zone in the Pt[111] surface. The adsorption energy for a single molecule is obtained with **Eq. 2.1**. When the coverage was increased until 0.5 ML, which is the saturation coverage measured for the stepped surfaces [19], the adsorption energy of the *i* molecule E^i_{ads} was obtained as:

$$E^i_{ads} = E_{adsorbate} + E_{system-i} - E_{system} \tag{6.1}$$

where $E_{adsorbate}$ is the energy for CO molecule in the gas-phase, $E_{system-i}$ is the total energy of the saturated system without the CO molecule adsorbed in the *i* site and E_{system} is the total energy of the system with the CO adsorbed at 0.5 ML coverage.

The next step in our research was the study of the BE in the C 1s electron after the adsorption on the Pt substrates. We calculated the BE using the FS approximation. Thus, the C 1s electron is excited, removing it from the inner shell and relocated in the valence band. The BE of C 1s level is obtained using **Eq. 1.52**. The CLS is obtained as the variation in the electronic BE for two different measurements. It is usually measured against some well-defined energy reference, as it is a bulk atom. Nevertheless, in the case of the CO

adsorption it is not possible to define a reference value for our calculations. We have used the top adsorption site on the step edge as a reference assuming that this site, and the attachment of the CO molecule to it, would be very similar in all the vicinal surfaces. This expectation seems to be confirmed by the experimental evidence (see **Figure 6.7**). This permits to compare the variation of the CLS as a function of the adsorption site for each of the studied surfaces and with our experimental results [19]. However, the fact that there was not a clear reference for the C 1s CLS and the subtle variation observed with the miscut angle [19] creates difficulties in our research. Moreover, due to the limited range of miscut angles that can be explored with first-principles methods, the experimentally observed variation is comparable to the uncertainties that we have in our CLS calculations. Thus, we have considered the TCM approximation as a better way to deal with the issue. Applying the TCM it is possible the analysis of the CLS as a continuous function of the strain, that we associated with the size of the terrace following our finding from **Chapter 5**.

6.3 Results

First we studied CO adsorption on the flat Pt[111] surface. The CO molecule was adsorbed on the Pt[111] surface in different sites. **Figure 6.1** shows the adsorption sites that we explored, which were at top (**T**), bridge (**B**), fcc hollow (**F**) and hcp hollow (**H**) sites with the carbon atom pointing towards the Pt[111] substrate.

The energy results are shown on **Table 6.1**. They predict that the CO preferred adsorption site is at hollow sites (**F** and **H**), followed by the **B** site and the less favoured was the **T** site. However, the experimental observations show that at low coverage the adsorption takes place at top site and when the coverage increases the CO molecules are detected at bridge site [217–220] as well. Therefore, DFT calculations fail to describe the CO/Pt[111] system. They predict CO adsorption on hollow sites as energetically favoured over low coordinated sites on Pt[111] [236]. Local and semilocal density functionals do not correctly describe the most stable CO adsorption site on Pt surfaces. Kresse *et al.* studied such error. According to these authors the problem arises from the overestimation of the interaction of the CO LUMO with the metal substrate, overestimating its occupation [237, 238]. Nevertheless, the incorrect order of the adsorption site does not imply a complete failure in describing the chemical interaction. This fact is supported by the CO bonding distance. After the CO adsorption the predicted C-Pt bond distance totally agrees with the experimentally measured of 1.86 ± 0.02 Å at top site and 2.02 ± 0.04 Å at bridge site [223] as it is show in **Table 6.1**.

We are interested in the CO adsorption on vicinal Pt[111] surfaces. Therefore, we have created different stepped surfaces and adsorbed the CO molecule on the step edge and on the

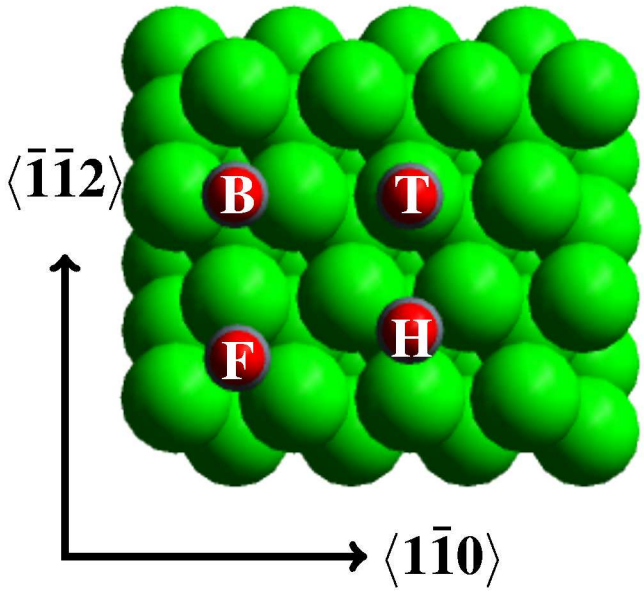

Fig. 6.1 CO adsorption on Pt[111]. The CO molecule was adsorbed at top (T), bridge (B), hcp hollow (H) and fcc hollow (F) sites.

terrace. We studied the following possible adsorption sites. The CO molecule adsorbed on the step edge at top (**ST**) and bridge (**SB**) sites or in the middle of the terrace at top (**TT**) and bridge (**TB**) sites.

The adsorption energies for type-A steps are displayed in **Table 6.2**. In both stepped surfaces, Pt[335] and Pt[557], the step edge was preferred over the terrace atoms. The adsorption energy still favoured the bridge adsorption site over the top site in both cases, step and terrace. We compared the energy results of the terrace with those on the step edge. They show an energy stabilization of ~ 450 meV for the adsorption on the step edge with respect to the terrace sites. **Figure 6.2** shows clearly this behaviour on the Pt[557] substrate. The CO molecule prefers the step edge adsorption over the terrace sites. In addition, the energy stabilization at the step is similar for both top and bridge adsorption sites.

When the CO molecule was studied for type-B steps a different results was observed. **Table 6.3** presents the adsorption energies for the Pt[332] and Pt[221] stepped surfaces.

Table 6.1 E_{ads} and the C-Pt bond length (l) after the CO adsorption on the Pt[111] surface.

site	**E_{ads} (eV)**	**l (Å)**
T	2.238	1.84
B	2.308	2.02
H	2.330	2.11
F	2.365	2.11

Table 6.2 CO adsorption energy on type-A stepped surfaces. A top view of the supercell used in the calculations can be found in **Fig. 6.2**.

Surface	**site**	**E_{ads} (eV)**
[557]	**TT**	1.970
	TB	2.034
	ST	2.399
	SB	2.476
[335]	**TT**	1.813
	TB	1.922
	ST	2.269
	SB	2.351

Also in this case the CO molecule is more strongly attached to the step edge than to the terrace atoms. Although in the terrace the **TB** is favoured over the on-top geometry the situation changed when the molecule was adsorbed on the step atoms. The **ST** adsorption was preferred over the **SB** adsorption site. As it is shown in **Figure 6.3** the energy stabilization at the step is twice bigger in the top sites than for the bridge case. The obtained stabilization energies are in agreement with the theoretical work of Busó-Rogero *et al.* [224]. Their results showed an energy difference for the CO adsorption between step edge site and terrace site around 0.3-0.4 eV on different vicinal Pt surfaces.

Table 6.3 CO adsorption energy on type-B stepped surfaces. A top view of the supercell used in the calculations can be found in **Fig. 6.3**.

Surface	**site**	**E_{ads} (eV)**
[332]	**TT**	1.935
	TB	2.019
	ST	2.319
	SB	2.204
[221]	**TT**	1.794
	TB	1.924
	ST	2.247
	SB	2.158

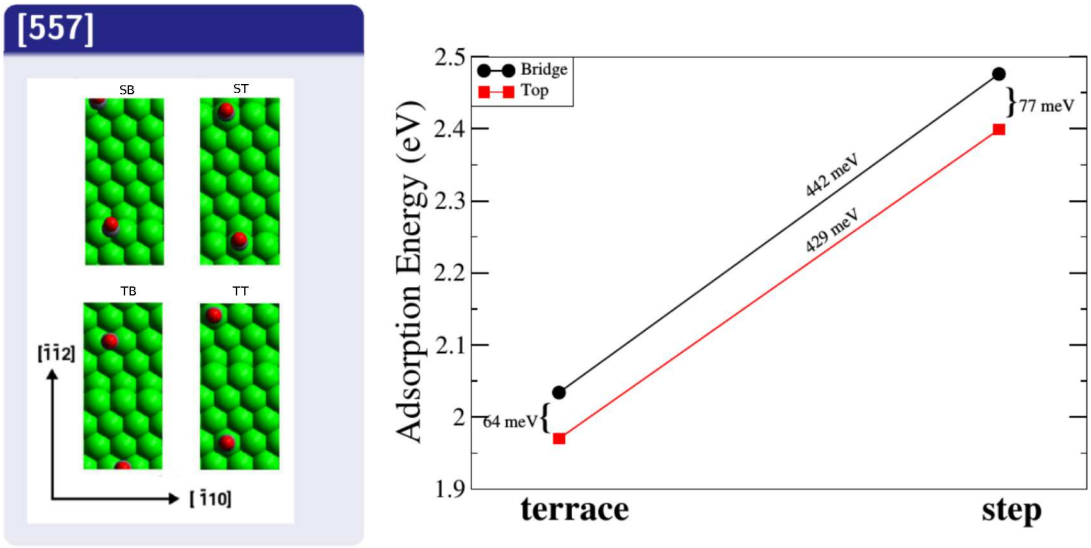

Fig. 6.2 CO adsorption on Pt[557] stepped surface.

Thus, our theoretical results are in agreement with the experimental observations [19, 234, 235, 239]. Supported by the energy stabilization obtained in our calculations we can conclude that the CO molecule adsorbs at **ST** and **SB** sites in type-A Pt crystals. However, only the **ST** adsorption site was detected on type-B Pt surfaces at low coverage, in accordance with the computed energetics.

High CO coverage was also contemplated in our research. The observations by our experimental collaborators showed that Pt[111] vicinal surfaces were saturated at 0.5 ML [19]. Therefore, we have simulated CO adsorption on Pt stepped surfaces at such maximum coverage. **Figure 6.4** depicts a side view of the considered structure to simulate CO adsorption on the Pt[557] surface at 0.5 ML. CO is adsorbed on the step atom **S** and on the different terrace atomic rows ($\mathbf{T}_i$). We have considered the two possible **T** and **B** adsorption sites in the type-A stepped surfaces. The energy results are presented in **Table 6.4**. We found evidence of a long-range repulsion among molecules with a clear reduction of the adsorption energies in all sites. Still, in spite of the global reduction of the adsorption energies, the step edge continues to provide the preferred adsorption sites.

As it was already mentioned, XPS is an important experimental technique in order to study molecular adsorption, in particular to determine the relative occupation of different adsorption sites since they frequently produce distinct spectroscopic features and changes in the BE of inner atomic shells. For this reason, we have calculated the BE for the C 1s photoelectron at different adsorption sites in the Pt[111] surface. The CLS between the **T** and **B** adsorption sites is 688 meV, in excellent agreement compared to the 700 meV observed in

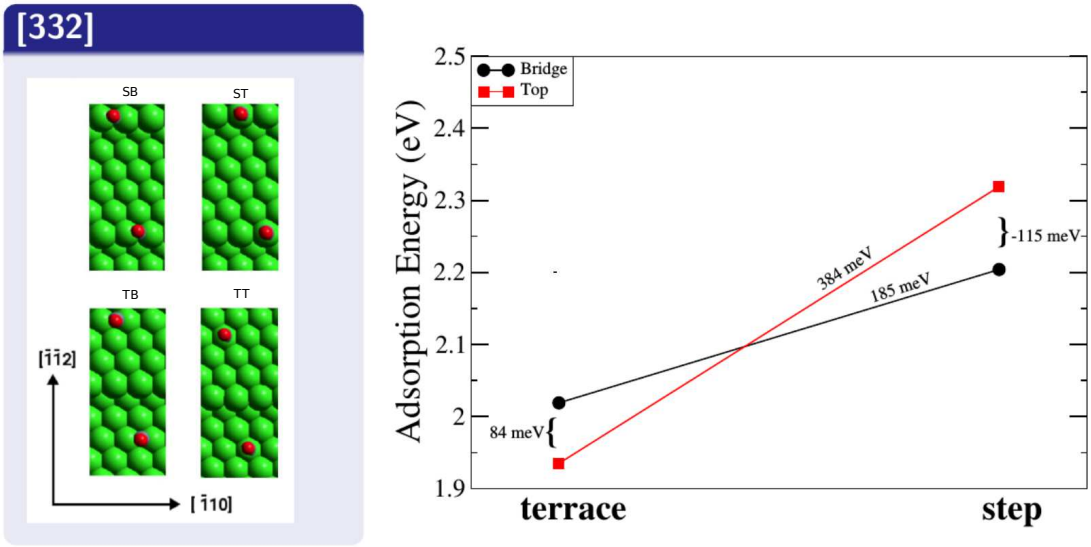

Fig. 6.3 CO adsorption on Pt[332] stepped surface.

the experiments [223, 232, 233]. We have also studied the CLS for each adsorption site in the vicinal Pt[111] surfaces. Due to the lack of a well-defined reference for different surfaces, we have used the **ST** adsorption site as a reference for each surface. Assuming that the CO adsorption at this site is only weakly dependent on the miscut angle, this permits to compare the C 1s core-level as a function of the adsorption site. The results are plotted in **Figure 6.5**. The CLS obtained between the **TT** and **ST** is $\sim$ 450 meV and 475 meV for the type-A and type-B stepped surfaces respectively. The C 1s CLS between the **TT** and **SB** adsorption sites is about 1000 meV in both Pt[557] and Pt[335] substrates. Our results are consistent with the previous theoretical studies [85, 79]. Furthermore, taking into consideration that the experimental accuracy is $\pm$ 200 meV, our results are in good agreement with the experimental observations of $\sim$ 280 meV and $\sim$ 900 meV obtained for the CLS of the **SB** and **ST** referred to the **TT** adsorption site [19, 234, 235].

The use of curved crystals by our experimental colleagues allows, besides identifying different adsorption sites, to monitor how their occupation changes as a function of the miscut angle. **Figure 6.6** shows the intensity (indicated by color) of the experimental XPS signal as a function of the C 1s BE and the miscut angles (represented by the z-position along the curved crystal sample) or the inverse of the terrace width. Superimposed with this 3-D plot we can find individual spectra for selected miscut angles ([335],[111] and [553]). The coverage is 0.25 ML. They straightforwardly prove that CO adsorption on Pt[111] vicinal surfaces occurs at **T** site on Pt[111] and the **ST** on the stepped surfaces at low coverage.

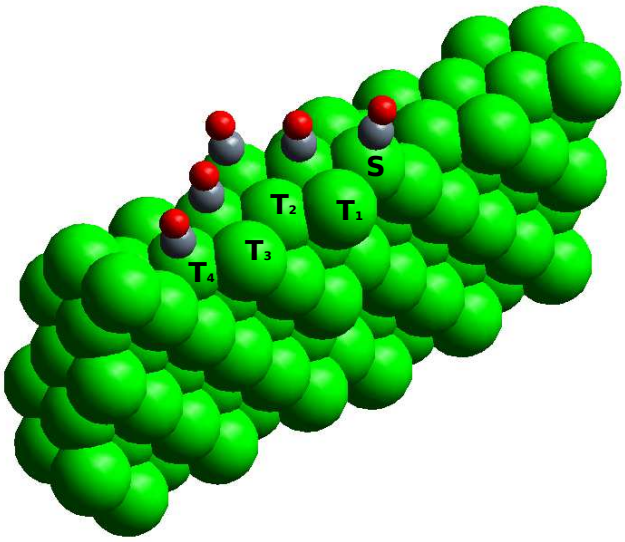

Fig. 6.4 CO adsorption on Pt[557] stepped surface at high coverage. The CO molecules were adsorbed at step edge (S) and terrace atomic rows (T_i) on the topmost layer.

Moreover, a second peak was observed for Pt[335] that is associated with adsorption at **SB** sites at low coverages, as can be inferred from our calculations for type-A stepped surfaces.

Table 6.4 CO adsorption energy at different positions in the different atoms at 0.5 ML coverage for the type-A stepped surface Pt[557] and Pt[335].

Surface	**site**	**E_{ads} (eV)**
[557]		
	ST	1.966
	TT_1	1.459
Top adsorption	**TT_2**	1.260
	TT_3	1.268
	TT_4	1.384
	SB	1.925
	TB_1	1.593
Bridge adsorption	**TB_2**	1.456
	TB_3	1.582
	TB_4	1.536
[335]		
	ST	1.989
Top adsorption	**TT_1**	1.448
	TT_2	1.454
	SB	2.008
Bridge adsorption	**TB_1**	1.643
	TB_2	1.509

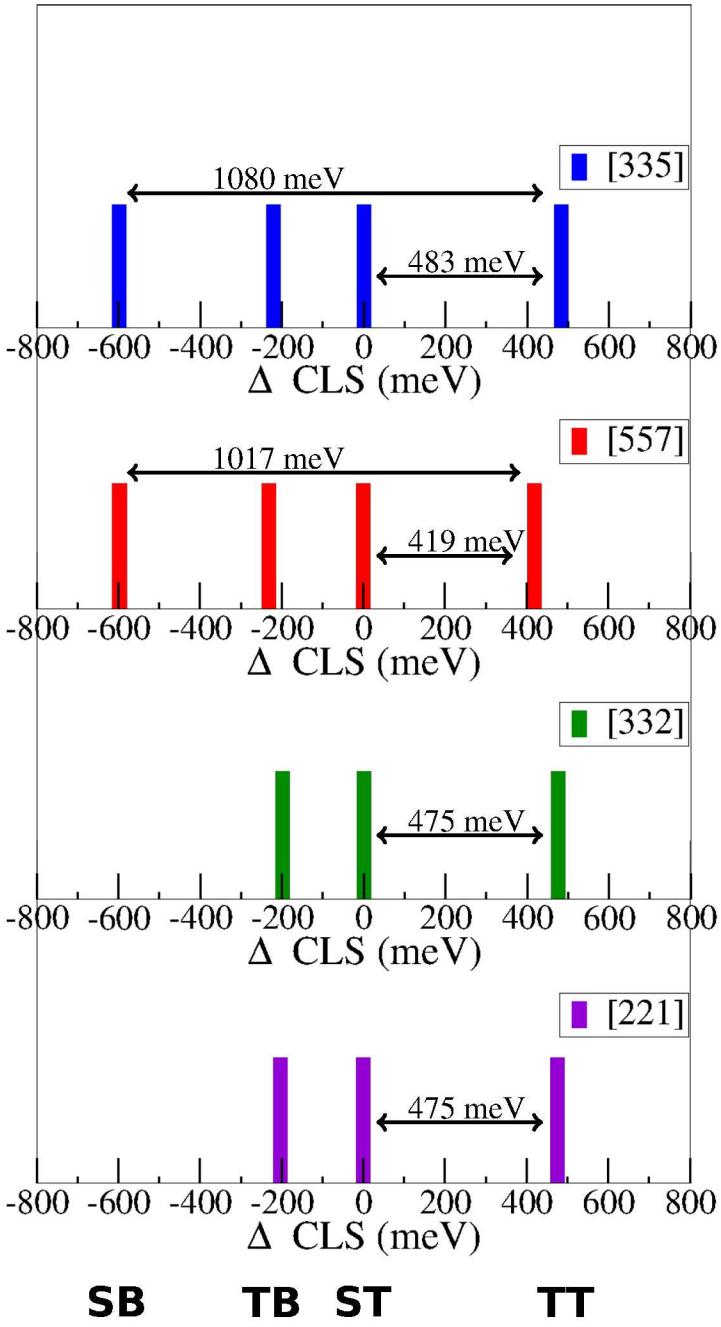

Fig. 6.5 Computed C 1s CLS in different stepped surfaces as a function of the adsorption site. CO molecule was adsorbed at top (**ST**) and bridge (**SB**) sites on the step edge and on the terrace at top (**TT**) and bridge (**TB**) sites. The **ST** adsorption site is used as a reference in all cases.

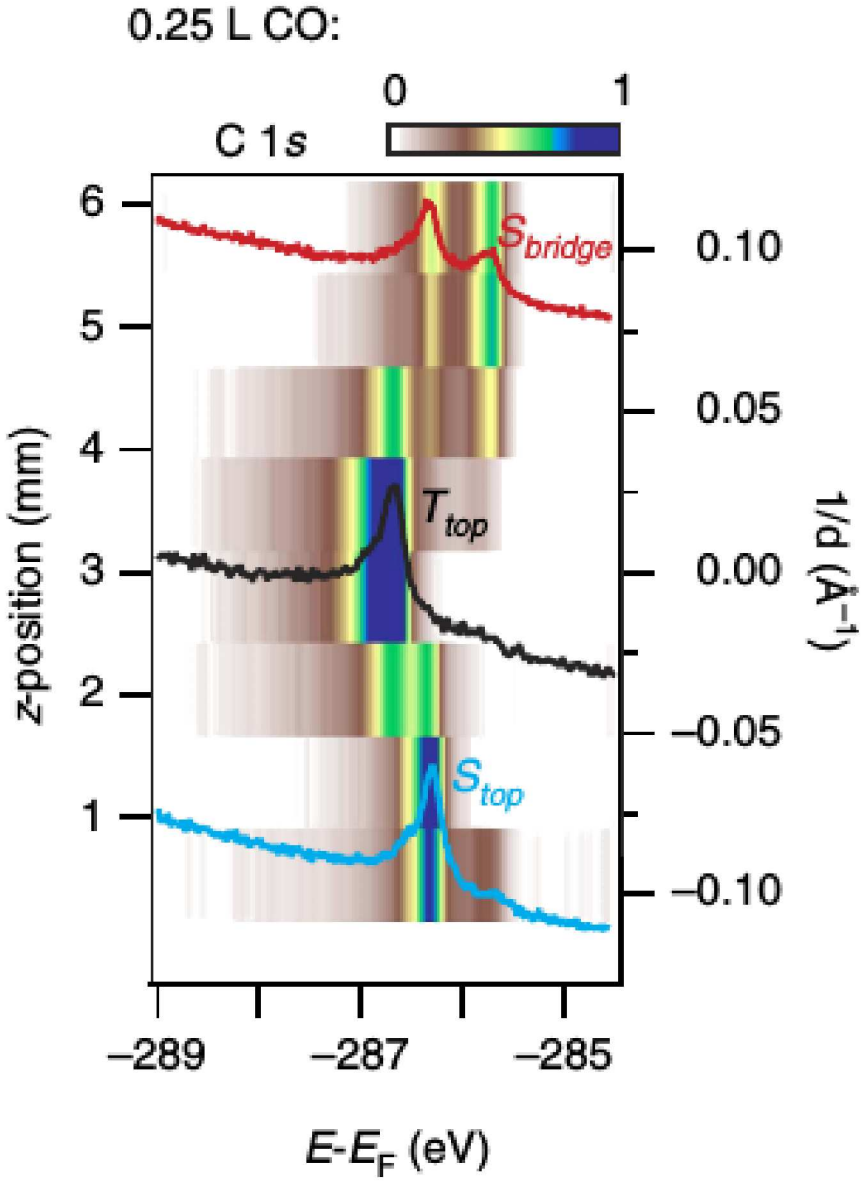

Fig. 6.6 C 1s BE on the Pt[111] curved crystal at low coverage [19]. The profiles superimposed in the plot are for the [335] (red), [111] (black) and [553] (blue) stepped surfaces respectively.

6.4 Terrace Compression Model applied to CO adsorption

Figure 6.7 presents a summary of the experimental binding energy of the C 1s for all adsorption sites as a function of the miscut angle in the high coverage limit (10 ML). It is particularly surprising the behaviour of the **TT** component, that shows a clear systematic variation with the terrace width. The direct comparison of this experimental variation with our calculations faces a fundamental difficulty. In the case of the CO adsorption we lack a common reference that allows comparing the results obtained for different supercell (such as bulk atoms provided in **Chapter 5**). In addition, we are trying to disentangle a minimal energy variation which is comparable with the error associated to the methodological procedure. Therefore, the TCM was applied in order to study the CLS for the C 1s photoelectron as a function of the terrace size. The CLS would be obtained as the contribution of the strain out-of-plane (s_{out}) and the strain in-plane (s_{in}) both depending on the miscut angle as obtained in **Chapter 5**.

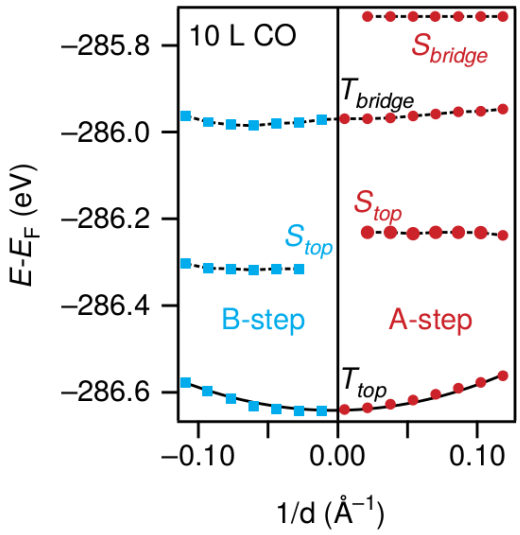

Fig. 6.7 BE variation across the curved surface for all the C 1s adsorption sites as a function of the miscut angle at high coverage (10 ML) [19].

The effect of s_{out} was simulated in a $2x\sqrt{3}$ Pt [111] supercell. The CO molecule was adsorbed on a **T** site on the surface. We varied the distance between the topmost and the second Pt layer, changing s_{out} while keeping fixed the in-plane atomic coordinates (see **Figure 6.8**). However, the CO adsorption height of the molecule over the terrace was always allowed to relax, so the Pt-C distances are optimized for each out-of-plane strain.

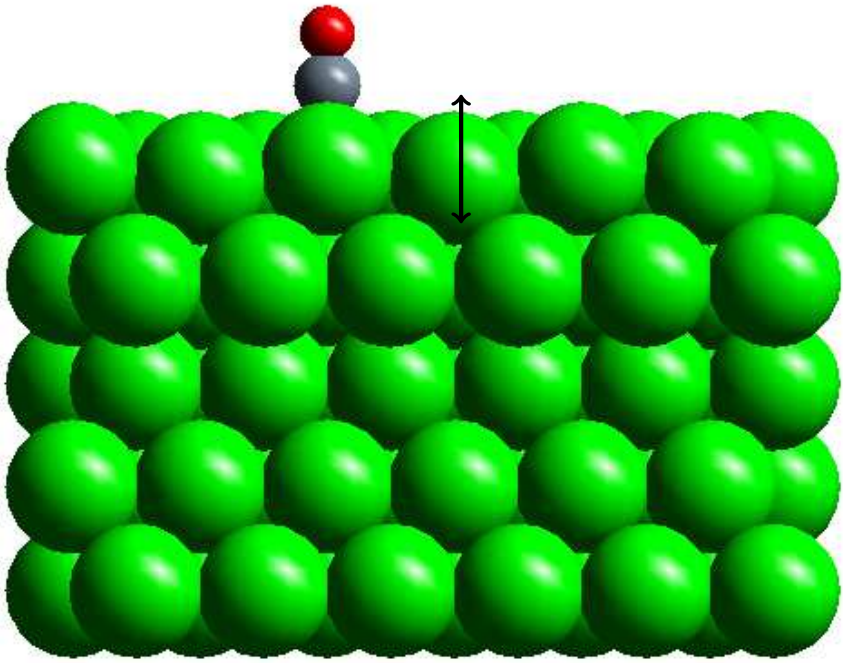

Fig. 6.8 CO adsorption on Pt[111]. The topmost layer is artificially displaced with a view to changing s_{out} and obtain the C 1s BE as a function of the layer distance.

Figure 6.9 exhibits the variation of the C 1s BE versus the distance between the first and second layers in the slab. We have used the BE value obtained for the relaxed geometry as reference. When the distance between layers was increased a linear increment of the BE is observed. The loss of coordination in the topmost layer is also reflected in the increment of the CO adsorption energy and a reduction in the adsorption Pt-C bond distance. From these data it is possible to obtain the C 1s CLS produced by the application of a given amount of s_{out}. These results show that $\frac{\partial E_{1s}}{\partial s_{out}} \sim 1.1$ eV where s_{out} is the strain along the normal.

To investigate the effect of the s_{in} on the BE, the Pt[557] vicinal surface was used. The CO molecule was adsorbed in the middle of the terrace (T_3 position) on a top site. We applied a rigid compression/expansion of the terrace in order to explore the effect of different values of the s_{in} on the C 1s level position. Thus, we have artificially displaced the Pt atoms in the first layer and avoided further optimizations on the positions allowing us to control the strain percentage applied on the topmost layer. As in the previous case, the CO adsorption height was relaxed but the adsorption site on the plane was kept fix. The schematic procedure is shown in **Figure 6.10**. The variation of the C 1s BE are shown in **Figure 6.11**. We have used the relaxed adsorption geometry as a reference for the variation of the BE with the s_{in} percentage. The data show a reduction of the C 1s BE with the increment of the s_{in} in the

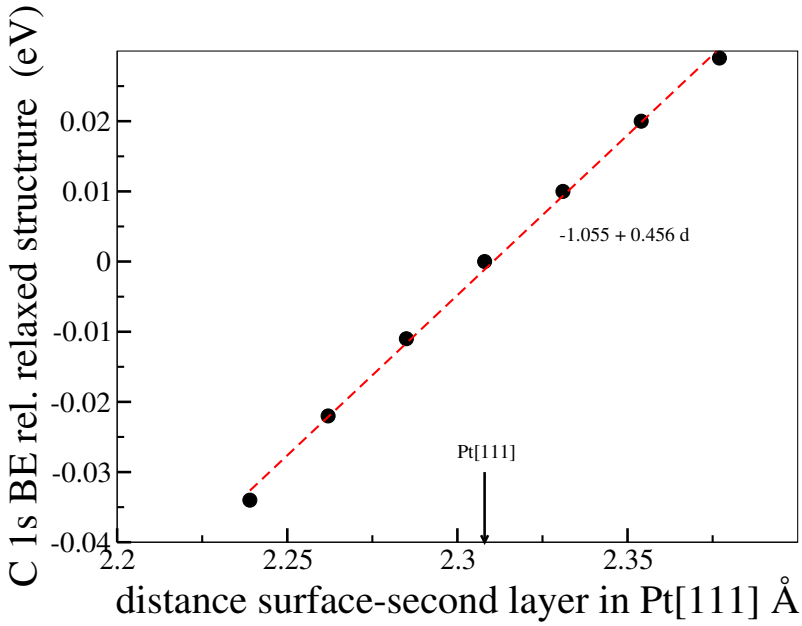

Fig. 6.9 C 1s BE versus distance between the topmost and the second layer at Pt[111] surface. C 1s BEs are referred to the relaxed adsorption structure.

surface. The result for the derivative with respect to the in-plane uniaxial strain is $\frac{\partial E_{1s}}{\partial \varepsilon_{<\bar{1}\bar{1}2>}} \sim$ -0.83 eV.

We can now insert the data computed previously for the average strain in terrace of the different vicinal surfaces. If we do so we arrive to the conclusion that the C 1s level for the CO molecule adsorbed on **T** sites moves to lower energies (higher binding energies) as we increase the miscut angle. This is in contradiction with the experimental result [19], suggesting that either the calculation method or the central assumption that the strain of the terrace is the main factor determining the shift of the C 1s BE are faulty. Nevertheless, we should be a bit more careful in the previous analysis. We have assumed that the average strain in the terraces is not affected by the adsorption of as much as $\sim$ 0.5 ML of CO. This is against well-known experimental evidence [240] and theoretical results [241, 242], which indicate that the tensile stress of Pt[111] is largely relieved by adsorption and, which is somewhat more surprising, quite independently on the donor or acceptor character of the adsorbed species. Under these conditions, we can expect that the compression of the terrace will be smaller once it is covered with CO. This behaviour was indeed observed in our calculations. Thus, the average in plane strain s_{in}, which was estimated in **Chapter 5** from the width of the relaxed terraces to be -2.8% and -4% respectively for Pt[557] and Pt[335], is substantially reduced upon CO adsorption. The values of s_{in} are -0.8% and

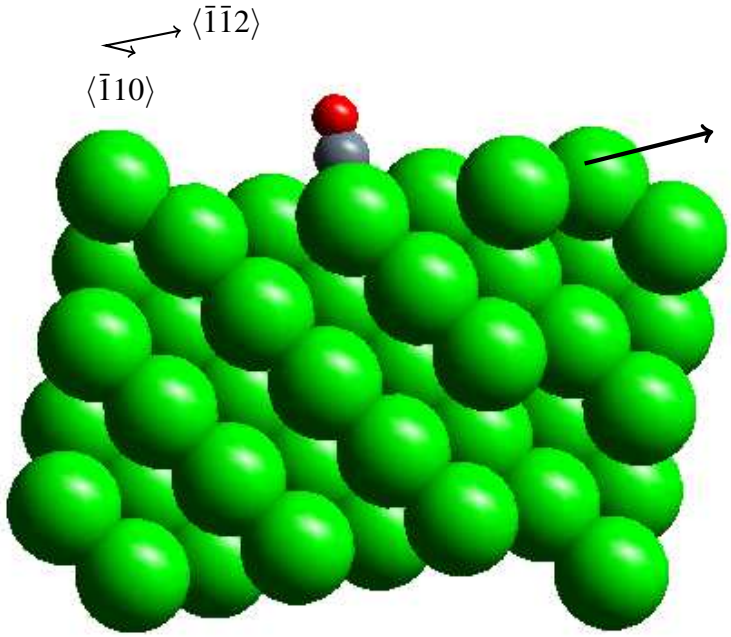

Fig. 6.10 TCM applied to the CO adsorption on Pt[557]. The T_i and S atoms in the topmost layer were artificially displaced with a view to to changing the in-plane strain s_{in} in the step terrace. This permits to estimate the effect of s_{in} on the C 1s level in each case.

-0.9% respectively for CO/Pt[557] and CO/Pt[335] at 0.5 ML coverage from the analysis of the computed relaxed geometries. Indeed, the average compression of the 'in-plane' Pt-Pt bond lengths in the covered terraces is even smaller, -0.2% and -0.4%, but translates into a somewhat larger reduction of the terrace size due to the buckling of the surface layer. Furthermore, the out-of-plane expansion that was observed before in response to the lateral compression, it is now larger with the response to the CO adsorption. The average height of the surface layer over the second layer in clean Pt[557] and Pt[335] is, respectively, 1.2% and 1.9% larger than in the case of the clean Pt[111]. This increment goes up to 1.6% and 2.2% for the CO covered surfaces when the main position of the surface plane is considered. There is also a strong buckling ($\sim$0.24 Å) of the surface layer, with the Pt atoms attached to CO molecules at higher positions. Notice that the size of the buckling is considerably larger than the changes in the average height of the surface layer, which complicates the analysis in terms of our simple model. Finally, the average change in Pt-Pt nearest neighbour distances

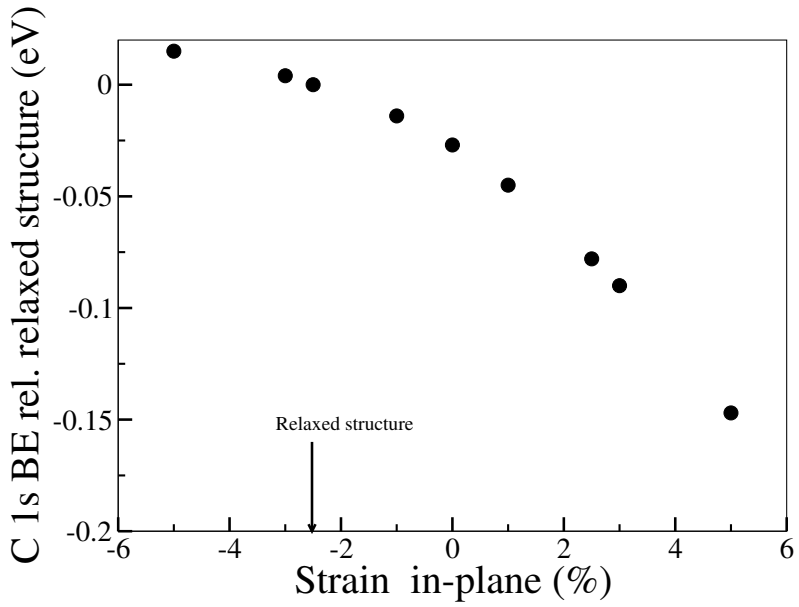

Fig. 6.11 C 1s BE versus s_{in} calculated applying an homogeneous strain to the Pt[557] terrace. BE energies are referred to C 1s on the relaxed structure.

for the T_i atoms with respect to Pt[111] becomes 0.28% and 0.33% for the CO/Pt[557] and CO/Pt[335] respectively, i. e., it has changed its sign with respect to the clean case.

Thus, after the adsorption of CO at the saturation coverage we find that: i) the average lateral compression of the terraces is much smaller and shows a weak dependence on the miscut angle, ii) the average height of the Pt atoms in the surface increases and the terrace becomes buckled and finally, in contrast to the case of the clean vicinal surfaces, iii) we find a small increase of the average nearest-neighbour distance for the atoms in the terrace as a function of the vicinal angle.

We can now revisit the issue of the C 1s level shift bearing in mind the opposite behaviour of the average Pt-Pt distances as compared to the case of the clean vicinal surfaces. This can help to reconcile the data of our simple TCM with the experimental observation for **T** adsorption [19] on the Pt vicinal surfaces. Unfortunately a detailed comparison is involved, since the structural changes are more complex for the CO covered than for the clean surface, and will not be attempted here. However, from the analysis presented above, it is tempting to interpret the shift of C 1s level that we observe experimentally as an indication that the relief of the compressive stress induced by CO adsorption is larger for smaller terraces, i. e., for larger miscut angles.

6.5 Conclusions

We have studied CO adsorption on Pt[111] vicinal surfaces. It is well-known that DFT fails in describing the most stable adsorption site for CO on Pt surfaces [236], which is identified as a hollow site rather than top site. Despite the difference in the adsorption hierarchy with regard to the experimental observation, DFT is able to correctly describe the main features of the Pt-CO bonding and the C 1s core level shifts of the molecule on the different adsorption sites that is one of the main focus of our work. In agreement with experiment, the step edge sites are predicted to be more stable than those in the terrace for all the considered vicinal surfaces [19]. Thus, the CO molecule adsorbs at **ST** and **SB** sites in type-A steps, while only **ST** adsorption is observed for type-B Pt steps at low coverage.

When the coverage was increased at the saturation level (0.5 ML) observed experimentally [19] we obtained a global reduction of the computed adsorption energies (E_{ads}). Such reduction can be attributed to the electronic repulsion between the CO molecules adsorbed on the stepped surfaces. However, the step edge adsorption sites are still preferred over the terrace sites in each of the different Pt surface considered here.

We have calculated the BE for the C 1s level when the CO molecule is adsorbed on the Pt surfaces. On the Pt[111] the computed CLS between the **T** and **B** adsorption sites showed a similar value to the experimental measurement. For the stepped surfaces we also get values of the C 1s CLS between molecules adsorbed on the terraces and at the step edge in good agreement with our experimental observations and previous experimental and theoretical reports. In our case, thanks to the use of a curved crystal by our experimental colleagues we could identify a characteristic dependence of the C 1s BE of the CO molecules on top sites in the terraces as function of the miscut angle. The lack of a well-defined reference for different surfaces for the C 1s level, as well as the small values of the BE changes as a function of the miscut angle, refrained us from trying to compare directly this experimental observation to our calculations on different vicinal surfaces. We rather preferred to use a variant of the Terrace Compression Model presented in **Chapter 5** in order to disentangle the effect of the strain in the surface on the observed C 1s CLS. The scope of TCM model is somewhat limited, since it mostly focuses on the strain of the surface layer as the main ingredient characterizing the reactive and electronic properties of terraces of different widths. Thus, the result of our analysis is rather speculative, although quite interesting if confirmed: it seems to indicate that the observed systematic decrease of the C1s BE as a function of the miscut angle might be an indication that the relief of compressive stress in the surface layer induced by CO adsorption is larger for smaller terraces.

Summary and Outlook

To see a World in a Grain of Sand
And a Heaven in a Wild Flower,
Hold Infinity in the palm of your hand
And Eternity in an hour.

William Blake, Auguries of Innocence

The aim of this Thesis was the theoretical study of molecular adsorption on different surfaces. This aim has been pursued using *ab initio* density functional theory calculations. DFT foundations as well as the approximations used were explained in **Chapter 1**. Despite the fact that the conclusions were presented in each chapter, an overview of the main conclusions will be presented here to help the reader to get a global perspective of the achievements of this Thesis work.

NO adsorption on Cu surfaces was investigated in **Chapter 2**. NO was adsorbed on Cu[110] and O(2x1)/Cu[110] on different adsorption sites. Our results showed that NO adsorption at bridge site with the N atom bonding the surface was preferred on Cu[110]. The molecule loses its magnetization due to the interaction with the substrate. In addition, our results predicted the dimer formation along the $\langle 1\bar{1}0 \rangle$ surface direction in a tilted geometry. However, the row formation is not expected on this substrate. In O(2x1)/Cu[110] the NO bonds two of the Cu atoms on the Cu-O rows, causing a large disruption on the geometry of the Cu-O-Cu rows on the substrate. The vertical adsorption is marginally preferred over a tilted geometry. The lower adsorption energy in comparison with the previous case and the survival of the magnetization after adsorption indicates a lower interaction with the substrate in comparison to clean Cu[110]. The dimers were found very unstable compared with the monomer. Thus, the formation of dimers and also rows is not expected for NO on O(2x1)/Cu[110]. This in contrast to the case of CO on O(2x1)/Cu[110], which has been reported to form well-separated and straight single-molecule rows on this substrate. The exploration of this possibility for NO was one the main motivations to study this system.

Chapter 3 was devoted to an in-depth study of MePc adsorption on Ag[111]. MePc molecules were adsorbed in different configurations on the surface, taking in consideration the adsorption site and the azimuthal angle on the substrate. In all the cases, the most stable adsorption site was on bridge$_+$, revealing that the stacking of the molecular frame with respect to the substrate is the key factor determining the adsorption configuration. Thus, the adsorption is primarily mediated by the organic part of the molecule. However, the metal ion has a strong influence in the properties of the molecule. For example, in spite of having the largest adsorption energy among the cases studied here, CuPc keeps its magnetic moment almost intact after adsorption due to the small interaction between the metal ion and the surface. This interaction only causes a small deformation of the molecule. On the other hand, MnPc loses its spin polarization due to the charge transfer from the surface and the participation of the d metal orbitals in the LUMO. This produces large changes in the molecular geometry after adsorption and reduces the adsorption energy in spite of being closer to the topmost surface layer. The addition of a ligand (chlorine atom) to the manganese atom in the MnPc moves the metal centre farther away from the substrate. This reduces the surface-metal core interaction and produces the most unfavourable adsorption energy. TiOPc shows the largest adsorption distance among the cases we studied and there is not a significant interaction between Ti-O group and the surface. As a general remark, we find that for the adsorption of MePc molecules on Ag[111] there is a competition between the interaction of the metal core and the deformation of the organic frame. Too little interaction of the metal centre gives rise to small adsorption energies. This can be controlled by the addition of ligands, that tend to push the metal atom away from the surface, reducing the interaction. However, a very strong substrate-metal core interaction can end up being detrimental for the adsorption stability. This is the case of MnPc, where the strong Mn-Ag[111] interaction creates a large deformation of the molecule that reduces its adsorption energy. For the molecules that we studied CuPc seems to present the best compromise between these two effects. A common observation for all MePc molecules was the electron accumulation on the substrate due to the Pauli repulsion of the surface electrons away from the position of the molecular frame. This so-called Pauli pushback phenomenon has a strong influence in the total dipole of the molecule. For example, for TiOPc the total dipole of the adsorbed molecule points in the opposite direction than the dipole determined by Ti-O group.

Following our research on MePc, in **Chapter 4** a careful study was developed for the CO_2 adsorption on TiOPc. Several adsorption geometries were tested and we concluded that the monomer is adsorbed parallel to the molecular plane over the central carbon atoms in the inner ring. Furthermore, we investigated the possibility of multiple molecules adsorbed on TiOPc. Our calculations show that the adsorption energy diminishes as the coverage

increases. However, the small energy difference demonstrates that it is possible for multiple molecules to adsorb simultaneously (dimers, trimers and tetramers). The induced electron density shows the charge polarization on the molecules, revealing that the interaction is due to electrostatic forces. Furthermore, a shift of the Ti-O stretching mode was observed in the vibrational spectra with the increment of CO_2 exposition at low temperature. We were able to simulate the shift of the Ti-O stretching mode with our calculations. Moreover, we demonstrated that this shift is caused by the adsorption of CO_2 and proportional to the number of molecules adsorbed on the TiOPc.

We did not just focus on molecular adsorption, we also devoted our efforts to other fascinating properties of surfaces. A large part of the work behind this dissertation was devoted to the study and characterization of [111] vicinal surfaces of several transition metals. This is motivated by experimental results obtained at the NanoPhysics Lab at CFM using curved crystals to explore XPS as a function of the miscut angle. In **Chapter 5** we present a joint theoretical and experimental study of the dependence of the surface core-level energy shift on the miscut angle of Pt[111] vicinals. Our theoretical results allow establishing unambiguously a relation between the experimentally observed CLS and the average surface strain in the terraces of the different stepped surfaces. We calculated the CLS on different stepped surfaces around the high symmetry $\langle 111 \rangle$ direction. The *ab initio* calculations showed the same behaviour observed experimentally, a decrease of the surface CLS of the Pt 4f as the miscut angle is increased. We speculated that the change of the strain with the terrace size is the main ingredient explaining the variation of the Pt 4f BE. In order to demonstrate this we performed calculations of highly idealized situations that allow disentangling the relation between the CLS and the strain at the surface from other effects. This is the so-called TCM model. Using this model we could get a better approximation to the empirical observations and confirm that the main factor behind the observed BE differences is the surface strain. In the other metallic substrate studied in this chapter the same tendency was found. Rh[111] vicinal surfaces showed that the CLS increment in the Rh 3d level is correlated with the miscut angle. The first-principles calculations are in very good agreement for small miscut angles.

The last part connects the study of the properties of the stepped surface with that of molecular adsorption. **Chapter 6** was devoted to CO adsorption on Pt[111] vicinal surfaces. We simulated the adsorption of CO on different stepped surfaces, finding a good agreement with experiment regarding the relative stability of adsorption in the terraces and at the steps. CO is adsorbed at step top and step bridge sites on type-A ((n + 2/3) atomic rows wide and have [100]-like steps) and just in the step top site in type-B ((n + 1/3) atomic rows and [111]-like step) stepped surfaces at low coverage. The increment of CO molecules adsorbed

on the surface (0.5 ML) causes a reduction on the adsorption energy due to the electrostatic repulsion between molecules. Nonetheless, the step site adsorption was still preferred over the terrace sites. Next, we computed the CLS of the C 1s level for different adsorbed species in an attempt to compare to the experimental evidence that indicates a systematic shift with the miscut angle. Experiments were performed by our colleagues in the NanoPhysics Lab at CFM. In absence of a clear reference for the C 1s photoelectron, we decided to use the C 1s level of the molecules adsorbed on step top sites to compare the results from different stepped surfaces. The hypothesis, consistent with experimental data, is that this should have a negligible dependence on the terrace size. The results obtained for the BE at different adsorption sites are in good agreement with experiment. Moreover, we applied our TCM to estimate the variation of the C 1s level as a function of the miscut angle. When the considered strain corresponds to that of the clean stepped surface, the predicted movement of the C 1s BE for the molecules adsorbed in the terrace is opposite to the experimental observation. However, it is important to take into account that CO adsorption produces a stress-release that compensates the compressive strain in the surface. The net result, once this effect is taken into account, is an increase of the effective Pt-Pt distances in the surface layer as the miscut angle decreases (*i. e.*, exactly the opposite trend observed for the bare vicinal Pt[111] surface). Therefore, this translates to a movement of the C 1s peak to lower BE in agreement with experiment. Interestingly, this seems to indicate that the experimental observation is an indication that the relief of compressive strain induced by CO adsorption is larger for smaller terraces.

Thus, in this Thesis we have performed an in-depth study of the adsorption of several molecular species. We have also investigated the interaction between molecules as in the case of NO adsorption on Cu surfaces or the CO adsorption on TiOPc. In addition, we studied the correlation between structural (surface strain as a function of the miscut angle) and electronic properties in stepped surfaces. We were able to answer several questions raised by experimental results obtained in the laboratory. Therefore, the cooperation between experimental groups and theoreticians demonstrated to be a valuable tool in the study and explanation of the observed phenomena. In spite of finding some answers other issues are still open. We would like to be able to respond those questions in our future work.

Appendix A

Supplementary information Chapter 3

In this appendix are included some tables and figures which were skipped in the **Chapter 3** discussion. They were avoided in the main text because of they do not contribute with crucial information.

Table A.1 Distance between adjacent CuPc molecules (C-C) along the symmetry crystal directions.

	$\langle\bar{1}10\rangle$ (Å)	$\langle\bar{1}\bar{1}2\rangle$ (Å)
CuPc fcc	9.893	9.680
CuPc top$_X$	9.876	9.678
CuPc top$_+$	7.036	6.820
CuPc bridge$_X$	9.894	9.686
CuPc bridge$_+$	7.030	6.821

Table A.2 Distance between adjacent MnPc molecules (C-C) along the symmetry crystal directions.

	$\langle\bar{1}10\rangle$ (Å)	$\langle\bar{1}\bar{1}2\rangle$ (Å)
MnPc fcc	9.920	9.710
MnPc top$_X$	9.906	9.713
MnPc top$_+$	7.076	6.869
MnPc bridge$_X$	9.913	10.896
MnPc bridge$_+$	7.063	6.859

Table A.3 Distance between adjacent Cl-MnPc molecules (C-C) along the symmetry crystal directions.

	$\langle\bar{1}10\rangle$ (Å)	$\langle\bar{1}\bar{1}2\rangle$ (Å)
Cl-MnPc fcc	9.913	9.698
Cl-MnPc top$_X$	9.901	9.697
Cl-MnPc top$_+$	7.056	6.843
Cl-MnPc bridge$_X$	9.904	9.701
Cl-MnPc bridge$_+$	7.055	6.854

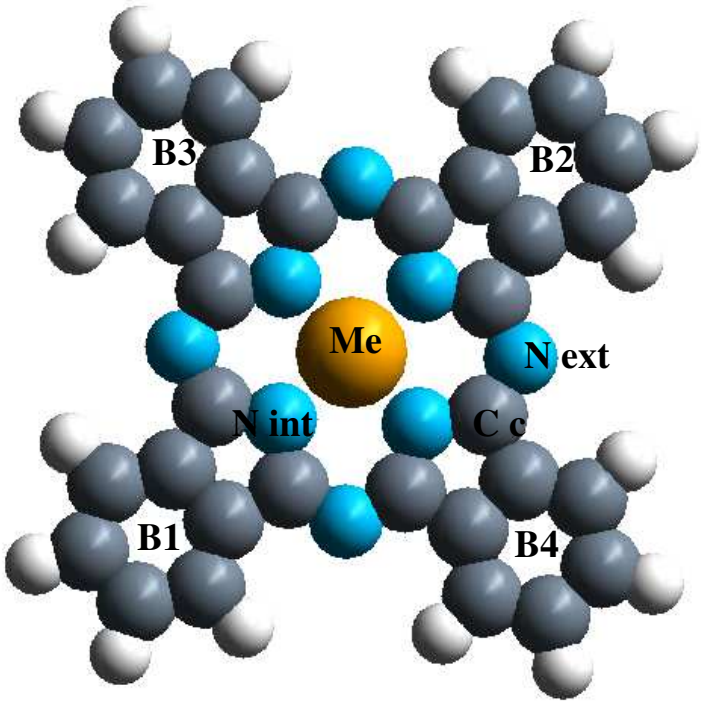

Fig. A.1 Name references for **Table A.4**, **A.5** and **A.6**. N int are nitrogen atoms bonding the metal atom (Me), N ext correspond to exterior nitrogen atoms in the central ring. C c are carbon atoms in the central frame and B1, B2, B3, B4 the different benzene rings.

Table A.4 Heights ± standard deviation in (Å) for the CuPc on gas phase and after the adsorption on Ag[111]. The CuPc molecular plane is used as reference.

	gas phase	**fcc$_X$**	**top$_X$**	**top$_+$**	**bridge$_X$**	**bridge$_+$**
Ag[111] (h2)		-3.224 ± 0.029	-3.218 ± 0.021	-3.304 ± 0.015	-3.287 ± 0.024	-3.200 ± 0.018
Cu (h1)	0.000 ± 0.000	-0.161 ± 0.014	-0.105 ± 0.004	-0.120 ± 0.002	-0.076 ± 0.010	-0.160 ± 0.003
N int	0.000 ± 0.000	-0.036 ± 0.056	-0.018 ± 0.005	-0.027 ± 0.005	0.030 ± 0.024	-0.040 ± 0.007
N ext	0.000 ± 0.000	-0.018 ± 0.070	-0.019 ± 0.013	-0.011 ± 0.005	0.019 ± 0.034	-0.021 ± 0.006
C c	0.000 ± 0.000	-0.014 ± 0.056	-0.011 ± 0.011	-0.008 ± 0.009	0.028 ± 0.027	-0.016 ± 0.006
B1	0.000 ± 0.000	0.003 ± 0.039	0.015 ± 0.019	0.002 ± 0.004	-0.024 ± 0.038	0.008 ± 0.006
B2	0.000 ± 0.000	0.046 ± 0.032	0.016 ± 0.020	0.005 ± 0.003	-0.002 ± 0.042	0.013 ± 0.006
B3	0.000 ± 0.000	0.018 ± 0.042	0.007 ± 0.018	0.020 ± 0.009	-0.019 ± 0.050	0.027 ± 0.017
B4	0.000 ± 0.000	0.001 ± 0.035	0.010 ± 0.019	0.018 ± 0.008	-0.032 ± 0.038	0.029 ± 0.016
central ring	0.000 ± 0.000	-0.023 ± 0.041	-0.016 ± 0.008	-0.015 ± 0.005	0.026 ± 0.021	-0.026 ± 0.005
Benzene	0.000 ± 0.000	0.017 ± 0.025	0.012 ± 0.012	0.011 ± 0.004	-0.019 ± 0.026	0.019 ± 0.008
Molecular plane	0.000 ± 0.000	0.000 ± 0.027	0.000 ± 0.009	0.000 ± 0.004	0.000 ± 0.021	0.000 ± 0.006

Table A.5 Heights ± standard deviation in (Å) for the MnPc on gas phase and after the adsorption on Ag[111]. The MnPc molecular plane is used as reference.

	gas phase	**fcc$_X$**	**top$_X$**	**top$_+$**	**bridge$_X$**	**bridge$_+$**
Ag[111] (h2)		-3.130 ± 0.036	-3.132 ± 0.036	-3.200 ± 0.038	-3.150 ± 0.023	-3.084 ± 0.032
Mn (h1)	0.000 ± 0.000	-0.304 ± 0.017	-0.306 ± 0.016	-0.363 ± 0.019	-0.251 ± 0.007	-0.344 ± 0.015
N int	0.000 ± 0.000	-0.132 ± 0.022	-0.134 ± 0.022	-0.168 ± 0.028	-0.079 ± 0.011	-0.145 ± 0.028
N ext	0.000 ± 0.000	-0.062 ± 0.040	-0.064 ± 0.040	-0.077 ± 0.030	-0.026 ± 0.030	-0.062 ± 0.022
C c	0.000 ± 0.000	-0.070 ± 0.033	-0.072 ± 0.033	-0.091 ± 0.037	-0.028 ± 0.020	-0.068 ± 0.022
B1	0.000 ± 0.000	0.068 ± 0.077	0.066 ± 0.076	0.064 ± 0.096	0.027 ± 0.024	0.062 ± 0.063
B2	0.000 ± 0.000	0.069 ± 0.077	0.068 ± 0.077	0.067 ± 0.093	0.044 ± 0.028	0.066 ± 0.065
B3	0.000 ± 0.000	0.063 ± 0.069	0.061 ± 0.068	0.095 ± 0.076	0.031 ± 0.025	0.067 ± 0.073
B4	0.000 ± 0.000	0.076 ± 0.064	0.074 ± 0.063	0.109 ± 0.073	0.030 ± 0.024	0.080 ± 0.066
central ring	0.000 ± 0.000	-0.088 ± 0.027	-0.090 ± 0.026	-0.112 ± 0.027	-0.044 ± 0.016	-0.092 ± 0.021
Benzene	0.000 ± 0.000	0.069 ± 0.045	0.067 ± 0.044	0.084 ± 0.052	0.033 ± 0.016	0.069 ± 0.041
Molecular plane	0.000 ± 0.000	0.002 ± 0.033	0.000 ± 0.032	0.000 ± 0.038	0.000 ± 0.013	0.000 ± 0.030

Table A.6 Heights ± standard deviation in (Å) for the Cl-MnPc on gas phase and after the adsorption on Ag[111]. The Cl-MnPc molecular plane is used as reference.

	gas phase	**fcc$_X$**	**top$_X$**	**top$_+$**	**bridge$_X$**	**bridge$_+$**
Ag[111] (h2)		-3.156 ± 0.028	-3.166 ± 0.017	-3.176 ± 0.021	-3.143 ± 0.024	-3.122 ± 0.035
Mn (h1)	0.349 ± 0.009	-0.004 ± 0.014	0.101 ± 0.003	0.088 ± 0.003	0.039 ± 0.007	-0.072 ± 0.019
N int	0.049 ± 0.031	-0.060 ± 0.045	0.003 ± 0.006	-0.006 ± 0.011	-0.027 ± 0.009	-0.115 ± 0.029
N ext	0.024 ± 0.042	-0.022 ± 0.068	-0.001 ± 0.011	-0.002 ± 0.009	-0.012 ± 0.036	-0.067 ± 0.022
C c	0.026 ± 0.034	-0.027 ± 0.052	0.005 ± 0.010	0.002 ± 0.013	-0.009 ± 0.023	-0.069 ± 0.027
B1	-0.033 ± 0.026	0.010 ± 0.051	-0.002 ± 0.009	-0.002 ± 0.009	0.009 ± 0.025	0.048 ± 0.084
B2	-0.003 ± 0.032	0.055 ± 0.034	0.007 ± 0.011	0.007 ± 0.011	0.016 ± 0.026	0.051 ± 0.086
B3	-0.025 ± 0.041	0.029 ± 0.043	-0.005 ± 0.009	0.003 ± 0.013	0.011 ± 0.026	0.068 ± 0.090
B4	-0.038 ± 0.026	0.014 ± 0.044	-0.007 ± 0.013	-0.002 ± 0.015	0.012 ± 0.026	0.083 ± 0.084
Cl	2.645 ± 0.009	2.226 ± 0.014	2.324 ± 0.003	2.307 ± 0.003	2.262 ± 0.007	2.166 ± 0.019
central ring	0.033 ± 0.025	-0.036 ± 0.038	0.002 ± 0.006	-0.002 ± 0.008	-0.016 ± 0.018	-0.083 ± 0.023
Benzene	-0.025 ± 0.021	0.027 ± 0.029	-0.002 ± 0.007	0.002 ± 0.008	0.012 ± 0.016	0.063 ± 0.053
Molecular plane	0.000 ± 0.019	0.000 ± 0.027	0.000 ± 0.005	0.000 ± 0.006	0.000 ± 0.014	0.000 ± 0.038

Bader charge variation for the MePc adsorption on the Ag[111] surface.

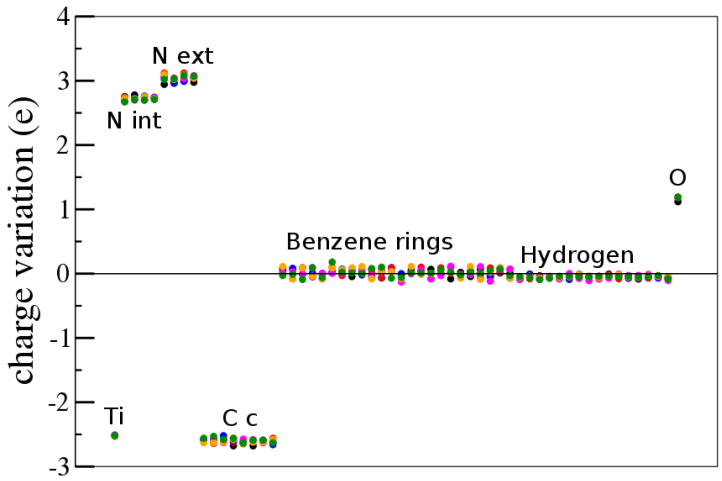

Fig. A.2 Charge variation (Bader charge - atom valence charge) for all atoms in the TiOPc molecule on gas phase (black) and during the (**O-down**) adsorption on Ag[111] at fcc_X (red), top_X (blue), top_+ (magenta), $bridge_X$ (orange) and $bridge_+$ (green) sites.

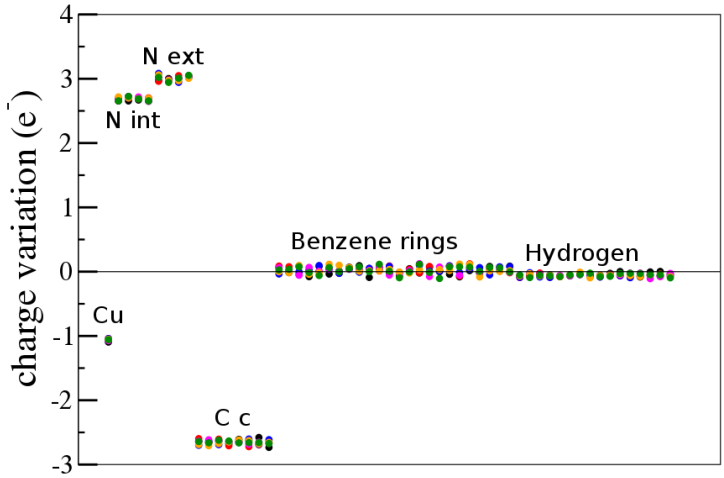

Fig. A.3 Charge variation (Bader charge - atom valence charge) for all atoms in the CuPc molecule on gas phase (black) and during the adsorption on Ag[111] at fcc_X (red), top_X (blue), top_+ (magenta), $bridge_X$ (orange) and $bridge_+$ (green) sites.

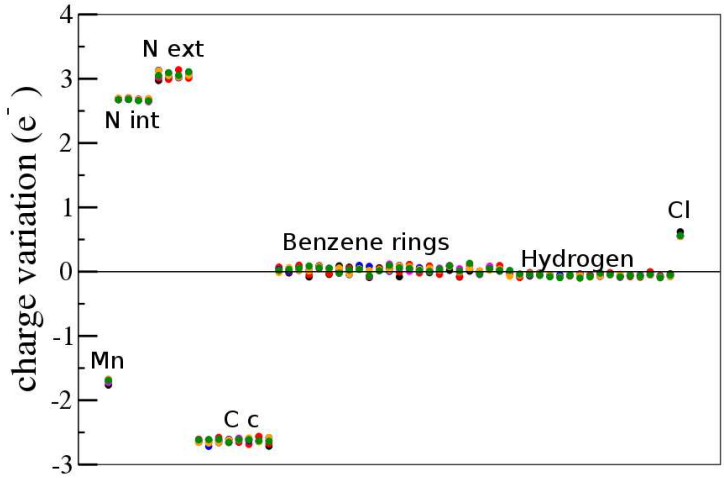

Fig. A.4 Charge variation (Bader charge - atom valence charge) for all atoms in the Cl-MnPc molecule on gas phase (black) and during the adsorption on Ag[111] at fcc_X (red), top_X (blue), top_+ (magenta), $bridge_X$ (orange) and $bridge_+$ (green) sites.

Appendix B

Supplementary information Chapter 5

Stress is an ignorant state. It believes that everything is an emergency.

Natalie Goldberg

Effective coordination model

Using the experimental values it is possible to devise a simple model to evaluate the average distance to nearest neighbours of the surface atoms. This provides a relationship between the CLS and the strain in the surface.

Bianchettin *et al* [173, 186] defined an effective coordination number (n_{eff}), by weighting the actual length of each individual Pt atom bond R_j as :

$$n_{eff} = \sum_j e^{b(R_{bulk} - R_j)} \tag{B.1}$$

where the sum runs for all j nearest neighbours, b is a decay constant calculated for the charge density of an isolated Pt atom, which in the range of the interactomic distances (R_{bulk}=2.77 Å) may be taken as b= 1.27 $Å^{-1}$ [243].

The strain is defined as the variation of the interatomic distances using the bulk as reference $\Delta R = \frac{R_{bulk} - R_{surface}}{R_{bulk}}$. This permits to describe the effective coordination at the surfaces as a function of of the strain as:

$$n_{eff} = 9 \times e^{1.27 \times 2.77 \times \Delta R(d)} \tag{B.2}$$

The experimental results for the 4f CLS photoelectron in the Pt[111] surface is $\Delta E_T = E_{9 \to 12}$ = -400 meV. If it is assumed a linear variation of the CLS as a function of the atomic

coordination between the surface (n = 9) and bulk (n = 12) atoms as :

$$\Delta E_T(d) = -400\frac{(n_{eff}-9)}{3} \tag{B.3}$$

Substituting in **Eq. B.2**, we can obtain the relationship between the strain and the measured core level $\Delta E_T(d)$.

$$\Delta R(d) = -\frac{1}{3.52} \times \ln\left[\frac{\Delta E_T(d)}{1.2} + 1\right] \tag{B.4}$$

With this equation it is possible to describe the experimental values $\Delta E_T(d)$ as function of the strain $\Delta R(d)$. This is the empirical relation used to deduce the strain data as a function of the terrace width as plotted in **Figure 5.5**.

Relationship Pt-Pt distance and strain

The square of the distance between the atoms (r) in the surface is defined as :

$$r^2 = r_x^2 + r_y^2 + r_z^2 \tag{B.5}$$

where r_i (i= x,y,z) are the projections on the arbitrary x,y,z directions.

Considering that the strain is produced along one direction, *e. g.*, x, while the others remained constant we have:

$$2r\Delta r = 2r_x\Delta r_x \tag{B.6}$$

and can be easily obtained that

$$\frac{\Delta r}{r} = \left(\frac{r_x}{r}\right)^2 \frac{\Delta r_x}{r_x} \tag{B.7}$$

Thus, it is possible to define the variation of the interatomic distance as a function of the strain in the direction out-of-plane (s_{out}) or in-plane (s_{in}) as :

$$\begin{aligned} \frac{\Delta r}{r} &= \left(\frac{r_{out-of-plane}}{r}\right)^2 s_{out} \\ \frac{\Delta r}{r} &= \left(\frac{r_{in-plane}}{r}\right)^2 s_{in} \end{aligned} \tag{B.8}$$

For the case in the normal direction, the distance between the layers is defined as :

$$r_{out-of-plane} = \sqrt{\frac{2}{3}}r \tag{B.9}$$

Therefore, the variation with s_{out} is :

$$\frac{\Delta r}{r} = \frac{2}{3} s_{out} \tag{B.10}$$

In the case of the s_{in} only four of the six bonding atoms are changing the distances with the variation produce in the step direction $\langle \bar{1}\bar{1}2 \rangle$ (see **Figure B.1**).

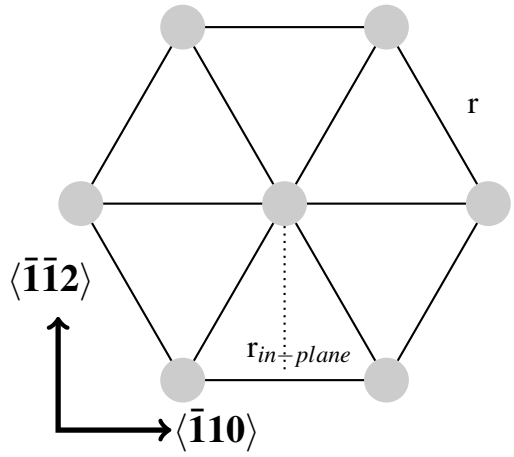

Fig. B.1 $r_{in-plane}$ is the distance between atomic rows along the step direction $\langle \bar{1}\bar{1}2 \rangle$ (dotted line).

$$r_{in-plane} = \frac{\sqrt{3}}{2} r \tag{B.11}$$

Then, substituing in **Eq. B.8**:

$$\frac{\Delta r}{r} = \frac{3}{4} s_{in} \tag{B.12}$$

As the topmost atom is bonding 9 nearest-neighbours, 6 in the surface layer and 3 in the underlayer, therefore:

$$\frac{\Delta r}{r} = \frac{1}{9} \left(3 \times \frac{2}{3} s_{out} + 4 \times \frac{3}{4} s_{in} \right) \tag{B.13}$$

Finally we obtain the relationship between the average variation of the nearest neighbours distance in the surface layer and the surface strain as:

$$\frac{\Delta r}{r} = \frac{1}{9} \left(2 \times s_{out} + 3 \times s_{in} \right) \tag{B.14}$$

Resumen en español

La interacción entre moléculas y materia tiene importantes implicaciones a nivel tecnológico e industrial lo que convierte a este área en un interesante campo de estudio [1–6]. La adsorción molecular es una cuestión fundamental debido a las implicaciones prácticas que conlleva, por ejemplo, en reacciones catalíticas [7–9].

El objetivo de esta tesis es el estudio de la adsorción molecular en distintas superficies. La adsorción de una molécula sobre una superficie puede modificar su estructura electrónica. La molécula puede estar químicamente ligada a la superficie, la carga eléctrica puede ser desplazada o transferida del adsorbato al adsorbente o viceversa y la hibridación con los estados electrónicos de la superficie puede modificar la densidad de estados molecular. Cada uno de estos cambios modificará las propiedades del sistema. Además, la interacción entre moléculas vecinas y la modificación de la densidad de estados electrónicos en la superficie puede afectar al proceso de autoensamblaje. El proceso de adsorción también puede estar influido por otros factores, como fuerzas de larga distancia (van der Waals), interacciones iónicas o electrostáticas y factores geométricos. La molécula adsorbida sobre la superficie puede ser fuertemente modificada durante el proceso, produciendo grandes cambios en sus propiedades electrónicas y creando un enlace químico fuerte con la superficie (quimisorción), por el contrario, el proceso de adsorción puede tener una influencia mínima en la molécula y no producir cambios de consideración sobre esta (fisisorción).

Desde el punto de vista teórico la descripción de un sistema de muchos cuerpos puede ser realizada utilizando la ecuación de Schrödinger. Sin embargo, el principal problema reside en la complejidad del sistema. Para un sistema que esté constituido por más de unas pocas partículas esta ecuación se hace irresoluble en la práctica. Dado un sistema que contiene N electrones, cada uno dependiente de 3 coordenadas espaciales y una coordenada de espín, y siendo N desde unas pocas decenas hasta 10^{23} electrones, la ecuación de Schrödinger no puede ser resuelta de forma exacta. Es por ello que será necesario realizar aproximaciones para poder obtener las soluciones al sistema.

Una alternativa para este problema fue desarrollada en los años sesenta, esta se basa en los teoremas de Hohenberg-Kohn [10] y la ecuaciones de Kohn-Sham [11]. La idea básica

consiste en suponer que podemos describir el estado fundamental de un sistema atómico utilizando unicamente la densidad electrónica del sistema en lugar de la función de onda de muchos electrones. Este es el principio básico de la teoría del funcional de la densidad (density functional theory (DFT) en inglés). La densidad electrónica del estado fundamental del sistema se calcula, y sus propiedades física se derivan a partir de esta. Los cálculos DFT han sido utilizados desde los años setenta, sin embargo, no fue hasta principios de los años noventa cuando los recursos computacionales junto con la mejora en los métodos de cálculo convirtieron al DFT en una herramienta versátil para el estudio de la materia condensada. El incremento en la precisión permitió la correcta descripción de los sistemas físicos y ello convirtió al DFT en una metodología popular a la hora de estudiar los sistemas físicos que, conjuntamente con las observaciones experimentales, ha dado excelentes resultados.

Basandonos en cálculos DFT y usando el programa de cálculo Vienna *ab initio* simulation package (VASP) desarrollado por Kresse *et al.* [12] hemos estudiado la adsorción molecular en distintas superficies metálicas. También hemos analizado las propiedades electrónicas y estructurales de distintas superficies escalonadas. Por ello hemos dividido la presentación de nuestra investigación en varios capítulos.

En el **capítulo 1** hemos descrito los fundamentos teóricos de la metodología utilizada en esta tesis. A partir de la ecuación de Schrödinger la aproximación de Born-Oppenheimer es introducida. En la siguiente sección se presenta la teoría básica de DFT. En ella se exponen las principales características de esta teoría. En esta parte se ha incluido una breve reseña de las aproximaciones que hemos utilizado para describir el funcional de intercambio y correlación, las fuerzas de van der Waals y el corrimiento de la energía de enlace de los electrones internos (core-level energy shift (CLS)). Finalmente se hace una descripción de la estructura cristalina de la materia y las principales aproximaciones para describir las soluciones de la ecuación de Schrödinger en dichos sistemas periodicos.

Nuestro grupo había investigado la adsorción del monóxido de carbono (CO) sobre una superficie de O(2x1)/Cu[110] en un trabajo previo [13, 14]. En dicho estudio se había observado la formación de filas perfectamente alineadas sobre dicha superficie y descrito el proceso de autoensamblaje de las moléculas. Es por ello que en el **capítulo 2** hemos realizado un estudio teórico similar para la adsorción del monóxido de nitrógeno (NO) sobre distintas superficies [15]. El NO se adsorbió sobre la superficie limpia Cu[110] y sobre O(2x1)/Cu[110] en los posibles sitios de adsorción. Para la primera superficie estudiada, Cu[110], el NO se adsorbe entre dos atómos de Cu con el N enlazando a la superficie. La hibridación entre los orbitales moleculares y la superficie produce la perdida de la magetización del NO. También se simuló la adsorción de múltiples moléculas sobre la superficie creando dimeros y filas en ella. Nuestros resultados predicen la formación de

dímeros a lo largo de la dirección $\langle 1\bar{1}0\rangle$ sobre la superficie. Por otra parte, la formación de filas en el substrato no resulta favorable en ningún caso. En la superficie O(2x1)/Cu[110] el NO enlaza dos átomos de cobre entre dos filas de Cu-O, produciendo una fuerte deformación en el substrato. Sin embargo, la menor energía de adsorción obtenida en comparación con el Cu[110] y la persistencia del momento magnético de la molécula después de ser adsorbida indican una menor interacción con esta superficie. La formación de dímeros es mucho más inestable en comparación con el monómero. Es por ello que tanto la formación de dímeros como la de filas no se espera en esta superficie. Este hecho contrasta con el caso del CO adsorbido sobre O(2x1)/Cu[110], en donde la molécula forma filas perfectamente separadas y bien definidas sobre la superficie. La posibilidad de que el NO presentase ese mismo comportamiento en esta superficie fue la principal motivación para el estudio de dicho sistema.

Una parte considerable de esta tesis es el resultado de la colaboración con distintos grupos experimentales. De esta forma nuestras investigaciones han ayudado a la correcta interpretación de los resultados obtenidos por nuestros colaboradores. A lo largo de estos años hemos desarrollado fructíferas colaboraciones con el grupo del Profesor P. Jakob de la Philipps-Universtät en Marburg (Alemania) [16] y el grupo del Profesor José Ignacio Pascual en el nanoGUNE en Donostia-San Sebastián (España) [17] en distintos temas relacionados con la adsorción de ftalocianinas en la superficie Ag[111]. La mayor parte de los resultados se presentan en el **capítulo 3** donde hemos desarrollado una profunda investigación sobre la adsorción de ftalocianinas metálicas (MePc, con Me = Cu, Ti-O, Mn y Mn-Cl) sobre Ag[111] [16, 17]. Las moléculas de MePc fueron adsorbidas en distinta configuraciones sobre la superfice, teniendo en cuenta el sitio de adsorción y el ángulo azimutal sobre el substrato. En todos los casos la adsorción más estable fue encontrada para la configuración "bridge$_+$", donde el centro metálico se sitúa entre dos átomos de la superficie y dos de los átomos de nitrógeno del anillo central se alinean con la dirección superficial $\langle\bar{1}10\rangle$. Así, queda patente que el principal factor para la adsorción de la molécula sobre esta superficie es la disposición de los átomos sobre el substrato y demostramos que la adsorción molecular está mediada por la parte orgánica de la molécula. Sin embargo, el centro metálico tiene una fuerte influencia en las propiedades moleculares. Por ejemplo, el CuPc a pesar de presentar la mayor energía de adsorción de todos los casos estudiados, mantiene su momento magnético prácticamente intacto después de la adsorción. Ello se debe a la mínima interacción entre el ion metálico y la superficie, y la pequeña deformación de la geometría de esta. Por otro lado, el MnPc pierde su magnetización debido a la transferencia de carga desde la superficie metálica y a la participación de los orbitales d del metal en el orbital molecular no ocupado de más baja energía (LUMO) de la molécula. Esto produce grandes cambios en la geometría molecular

después de la adsorción y reduce su energía de adsorción a pesar de ser la molécula que más cerca se adsorbe sobre la superficie. La adición de un ligando (un átomo de cloro) al centro de manganeso en la MnPc desplaza al centro metálico más lejos del substrato, esto reduce la interacción metal-substrato y reduce la energía de adsorción. El TiOPc presenta la mayor distancia de adsorción de todas las moléculas investigadas y no presenta una interacción importante entre el grupo Ti-O y la superficie. Resulta interesante reseñar aquí que nuestro estudio del TiOPc, en partícular el de la dependencia de la energía de adsorción con la orientación del plano molecular sobre la superficie, fue de gran ayuda para determinar la estructura de la fase conmensurada de las capas autoensambladas que dicha molécula forma sobre Ag[111] a recumbrimientos intermedios [16].

En general hemos observado que en la adsorción de MePc sobre Ag[111] hay una competición entre la interacción del centro metálico con la superficie y la deformación en el marco orgánico de la molécula. La baja interacción del centro metálico da lugar a bajas energías de adsorción. Esto puede ser controlado por la adición de ligandos que tienden a desplazar al ion metálico lejos de la superficie, reduciendo por tanto la interacción con la superficie. Sin embargo, una fuerte interacción metal-substrato puede ser contraproducente para la estabilidad energética del sistema. Este es el caso del MnPc en donde la fuerte interacción Mn-Ag[111] provoca grandes deformaciones en la geometría molecular y reduce la energía de adsorción de forma sustancial. De entre todas las moleculas estudiadas en este capítulo, CuPc presenta el mejor equilibrio entre dichos efectos. Una observación común para las MePc fue la acumulación de electrones en el substrato debido a la repulsión de Pauli. Los electrones de la superficie son repelidos por la nube electrónica molecular y tratarán de apartarse de la zona ocupada por la mólecula, bien sea acercandose lo más posible a superficie en la zona cubierta por la molécula, o bien acumulandose alrededor del marco molecular. Este fenómeno llamado "Pauli pushback" tiene una importante influencia en el dipolo total del sistema. Por ejemplo, en el caso del TiOPc el dipolo total después de la adsorción tiene la dirección contraria al definido por el grupo Ti-O de la molécula.

Continuando con nuestra investigación y con la vista puesta en la comparación de nuestros resultados con las medidas experimentales [18], hemos estudiado la adsorción del CO_2 sobre TiOPc. Estos resultados se presentan en el **capítulo 4**. Distintas geometrías de adsorción fueron investigadas y concluimos que el monómero se adsorbe paralelo al plano molecular sobre los carbonos centrales en el anillo interior del TiOPc. La posibilidad de tener varias moléculas adsorbidas sobre el TiOPc también fue estudiada. Nuestros cálculos muestran una disminución en la energía de adsorción a medida que aumenta el recubrimiento. Sin embargo, de las pequeñas variaciones en la energía se deduce que es posible la adsorción de múltiples CO_2 sobre el TiOPc. La densidad electrónica inducida indica una polarización

en las moléculas, revelando la naturaleza electrostática de la interacción. Adicionalmente, en el experimento se observó un corrimiento en el modo de "stretching" del Ti-O en el espectro vibracional de la molécula a medida que se incrementaba la exposición al CO_2 a baja temperatura. Fuimos capaces de simular dicho corrimiento y demostramos que se debe a la adsorción del CO_2 y es proporcional al número de moléculas adsorbidas sobre el TiOPc.

No sólo nos hemos centrado en la adsorción molecular, también hemos dedicado nuestro esfuerzo a otras fascinantes propiedades de las superficies. Una gran parte de esta disertación se centra en el estudio y caracterización de las superficies escalonadas vecinas a la dirección $\langle 111 \rangle$ en distintos metales de transición (Pt y Rh). Nuestro estudio está motivado por los resultados experimentales obtenidos por el grupo dirigido por el Profesor Enrique Ortega en el NanoPhysics Lab en el centro de Física de Materiales (CFM) del CSIC-UPV/EHU (Donostia-San Sebastián), que usando cristales curvados, investigan la variación de la señal XPS en función del ángulo de corte. La empresa BihurCrystal fabrica dichos cristales curvados. Los resultados experimentales muestran una variación sistemática de las energías de enlace de los electrones internos (CLS) para los niveles del Pt 4f y Rh 3d en cristales curvados que se relaciona con el tamaño de las terrazas. Intentando dilucidar este comportamiento hemos realizado cálculos *ab initio* para diferentes superficies escalonadas de Pt y Rh. En el **capítulo 5** presentamos un trabajo conjunto entre teoría y experimento sobre la dependencia del CLS con el ángulo de corte en las superficies vecinas de Pt[111] y Rh[111]. Nuestros resultados teóricos permiten establecer inequivocamente la relación entre el CLS observado experimentalmente y el porcentage de deformación promedio en las terrazas de las distintas superficies escalonadas.

Así, de los resultados obtenidos se deduce que el CLS para las distintas superficies escalonadas cerca de la dirección de alta simetría Pt[111] presenta la misma tendencia que las observaciones experimentales, hay una reducción en el CLS superficial de la capa Pt 4f a medida que aumenta el ángulo de corte. Nuestra hipótesis para entender estos resultados está relacionada con el cambio de la tensión superficial con el tamaño de la terraza del escalón y que este es el factor principal en la variación de las energías de enlace de la capa Pt 4f. Con la intención de demostrarlo hemos realizado una serie de cálculos en situaciones simplificadas que nos permitiesen corroborar la relación directa entre el CLS y la deformación en la superficie sobre otros posibles efectos. A esta aproximación utilizando situaciones simplificadas la hemos llamado "Terrace Compression Model" (TCM). Usando este modelo podemos obtener unos resultados más aproximados a las observaciones empíricas y confirmar que el factor principal detrás del corrimiento de las energías de enlace se debe al cambio en la deformación de la superficie. Las otras superficies metálicas estudiadas, las vecinas a Rh[111], mostraron claramente la relación en el incremento del CLS para los niveles Rh 3d

con el tamaño de la terraza, en muy buen acuerdo con los resultados experimentales para ángulos de corte pequeños.

La parte final de nuestra disertación conecta las propiedades de las superficies escalonadas con la adsorción molecular. El **capítulo 6** está centrado en al adsorción de CO sobre las superficies vecinas a Pt[111]. Hemos simulado la adsorción del CO en distintas superficies escalonadas hallando una buena relación con los resultados experimentales relativos a la adsorción en terrazas y escalones. El CO tiende a adsorberse sobre un átomo del escalón (top) o entre dos de estos (bridge) para los escalones tipo-A (formados por terrazas de (n+2/3) filas de átomos y un escalón tipo [110]) y sólo adsorbido en posición top para los escalones tipo-B (formados por terrazas de (n+1/3) filas de átomos y un escalón tipo [111]) a bajo recubrimiento. El incremento del número de móleculas de CO adsorbidas sobre la superficie (0.5 ML) provoca la reducción de la energía de adsorción debido a la repulsión electrostática entre las moléculas. A pesar de ello, la adsorción en los átomos del escalón sigue siendo preferida en detrimento de los átomos de la terraza. También hemos calculado la energía de enlace para los niveles C 1s en las distintas posiciones de adsorción en un intento por comparar nuestros resultados teóricos con la evidencia experimental que indica un corrimiento sistemático con el ángulo de corte del substrato. Los experimentos fueron llevados a cabo por nuestros colegas del NanoPhysics Lab en el CFM. A falta de una clara referencia para el nivel C 1s, en nuestras simulaciones decidimos usar el nivel C 1s para la molécula adsorbida en el escalón en posición top para comparar los resultados de las distintas superficies y de los distintos sitios de adsorción. La hipótesis, consistente con los resultados del laboratorio, es que la dependencia con el tamaño de la terraza debería ser mínima para el caso de la adsorción sobre el escalón. Los resultados obtenidos para las energías de enlace de la capa C 1s en los distintos sitios de adsorción estan de acuerdo con los observados experimentalmente. Además, también se ha aplicado el TCM para obtener una estimación de la variación del nivel C 1s en función del ángulo de corte. Cuando hemos considerado la deformación correspondiente a la superficie limpia, el movimiento de la energía de enlace predicho para el nivel C 1s de la molécula adsorbida en la terraza es contrario a la observación experimental. Sin embargo, debemos tener en cuenta que la adsorción del CO sobre el escalón produce una disminución de la tensión superficial que tiende a compensar la que da lugar a la deformación compresiva de la superficie limpia. El resultado neto, una vez tenidos en cuenta estos efectos, es un incremento de la distancia efectiva Pt-Pt en el plano de la superficie a medida que el ángulo de corte crece (*i. e.*, la tendencia contraria a la observada en la superficies limpias vecinas a la Pt[111]). Por lo tanto, ello se traduce en un movimiento del nivel C 1s hacia energías de enlace más bajas, en concordancia con la observación experimental.

List of Publications

Look at your children
See their faces in golden rays
Don't kid yourself they belong to you
They're the start of a coming race

David Bowie

- Andrew L. Walter, Frederik Schiller, Martina Corso, Lindsay R. Merte, Florian Bertram, Jorge Lobo-Checa, Mikhail Shipilin, Johan Gustafson, Edvin Lundgren, Antón X. Bríon-Ríos, Pepa Cabrera-Sanfelix, Daniel Sánchez-Portal, and J. Enrique Ortega. X-ray photoemission analysis of clean and carbon monoxide-chemisorbed platinum(111) stepped surfaces using a curved crystal. *Nature Communications*, 6:8903, 2015

- Antón X. Bríon-Ríos, Daniel Sánchez-Portal, and Pepa Cabrera-Sanfelix. NO adsorption on Cu(110) and O(2×1)/Cu(110) surfaces from density functional theory calculations. *Physical Chemistry Chemical Physics*, 18:9476–9483, 2016

- Laura Fernández, Sebastian Thussing, Alexander Mänz, Gregor Witte, Antón X. Bríon-Ríos, Pepa Cabrera-Sanfelix, Daniel Sánchez-Portal, and Peter Jakob. Structural and Vibrational Properties of the TiOPc Monolayer on Ag(111). *The Journal of Physical Chemistry C*, 121:1608–1617, 2017

- Eduard Carbonell-Sanromà, Martina Corso, Jingcheng Li, Antón X. Bríon-Ríos, Daniel Sánchez-Portal, and Jose Ignacio Pascual. Atomic-scale forces induced by a hydrogen molecule trapped in a tunneling junction. *Surface Science*, Accepted, 2018

List of Acronyms

AES	Auger-Electron Spectroscopy
ARPES	Angle-Resolved Photoemission Spectroscopy
BE	Binding Energy
B86b	Becke 86
BO	Born-Oppenheimer
Cl-MnPc	Chlorinated Manganese Phthalocyanine
CLS	Core-Level energy Shift
CO	Carbon Monoxide
CO_2	Carbon Dioxide
c-phase	commensurate phase
CuPc	Copper Phthalocyanine
DFT	Density Functional Theory
DOS	Density Of States
E_{ads}	Adsorption Energy
EELS	Electron Energy Loss Spectroscopy
FBZ	First Brillouin Zone
FS	Final State
GGA	Generalized Gradient Approximations
GIXD	Grazing Incidence X-ray Diffraction
HK	Hohenberg-Kohn
HOMO	Highest Occupied Molecular Orbital
HRCLS	High-Resolution Core-Level Spectroscopy
HREELS	High Resolution Electron Energy Loss Spectroscopy
IBZ	Irreducible Brillouin Zone
IRAS	Infrared Absorption Spectroscopy
IS	Initial State
KS	Kohn-Sham

LCAO	Linear Combination of Atomic Orbitals
LDA	Local Density Approximation
LDOS	Local Density Of States
LEED	Low Energy Electron Diffraction
LSDA	Local Spin Density Approximation
LUMO	Lowest Unoccupied Molecular Orbital
M-DOS	Molecular Projected Density Of States
MePc	Metal Phthalocyanine
MnPc	Manganese Phthalocyanine
MOs	Molecular Orbitals
NIXSW	Normal Incidence X-ray Standing Wave
NO	Nitrogen Monoxide
OptB86b-vdW	Optimized Becke 86
PAW	Projected Augmented Wave
PBE	Perdew-Burke-Erzenhof
PDOS	Projected Density Of States
POL	Point-On-Line
RAIRS	Reflection Absorption Infra-Red Spectroscopy
ResPES	X-ray Resonant Photoemission Spectroscopy
SPA-LEED	Spot Profile Analysis Low-Energy Electron Diffraction
STM	Scanning Tunnelling Microscopy
STS	Scanning Tunneling Spectroscopy
SXPS	Soft X-ray Photoelectron Spectroscopy
TCM	Terrace Compression Model
TD-DFT	Time-Dependent Density Functional Theory
TiOPc	Titanyl Phthalocyanine
TM	Transition Metal
TPD	Temperature Programmed Desorption
TS	Transition State
UPS	Ultra-violet Photoelectron Spectroscopy
VASP	Vienna *ab initio* Simulation Package
VDOS	Vibrational Density Of States
vdW	van der Waals
XAS	X-ray Absorption Spectroscopy
XC	Exchange-Correlation
XPS	X-ray Photoelectron Spectroscopy
XSW	X-ray Standing Wave

Bibliography

Pois logo dádelle ó César o que é do César e a Deus o que é de Deus.

Mateo 22:21

[1] R. Holm, D. Holtkamp, R. Kleinstück, H. J. Rother, and S. Storp. Surface analysis methods in the investigation of corrosion inhibitor performance. *Fresenius' Zeitschrift for Analytische Chemie*, 333:546–554, 1989.

[2] F. Bournel, C. Laffon, Ph. Parent, and G. Tourillon. Adsorption study of ethylene derivatives on Pt(111) at 95 K as probed by NEXAFS. *Physica B: Condensed Matter*, 208-209:436–438, 1995.

[3] Wendy K. Walter, David E. Manolopoulos, and Robert G. Jones. Chlorine adsorption and diffusion on Cu(111). *Surface Science*, 348:115–132, 1996.

[4] Terry A. Land, Tracie L. Martin, Sergey Potapenko, G. Tayhas Palmore, and James J. De Yoreo. Recovery of surfaces from impurity poisoning during crystal growth . *Nature*, 399:442–445, 1999.

[5] Michael Bowker. Automotive catalysis studied by surface science. *Chemical Society Reviews*, 37:2204, 2008.

[6] Shiran Zhang, Luan Nguyen, Jin-Xia Liang, Junjun Shan, Jingyue Liu, Anatoly I. Frenkel, Anitha Patlolla, Weixin Huang, Jun Li, and Franklin Tao. Catalysis on singly dispersed bimetallic sites. *Nature Communications*, 6:7938, 2015.

[7] R.M. Lambert and C.M. Comrie. The oxidation of CO by no on Pt(111) and Pt(110). *Surface Science*, 46:61–80, 1974.

[8] Václav Nehasil, Iva Stará, and Vladimír Matolín. Size effect study of carbon monoxide oxidation by Rh surfaces. *Surface Science*, 352-354:305–309, 1996.

[9] Francisco Zaera and Chinnakonda S. Gopinath. Role of adsorbed nitrogen in the catalytic reduction of NO on rhodium surfaces. *The Journal of Chemical Physics*, 111:8088–8097, 1999.

[10] Pierre Hohenberg and Walter Kohn. Inhomogeneous electron gas. *Physical review*, 136:864–871, 1964.

[11] W. Kohn and L. J. Sham. Self-Consistent Equations Including Exchange and Correlation Effects. *Phys. Rev.*, 140:A1133–A1138, 1965.

[12] G. Kresse and J. Furthmüller. Efficient iterative schemes for ab initio total-energy calculations using a plane-wave basis set. *Phys. Rev. B*, 54:11169–11186, 1996.

[13] M. Feng, P. Cabrera-Sanfelix, C. Lin, A. Arnau, D. Sánchez-Portal, J. Zhao, P. M. Echenique, and H. Petek. Orthogonal Interactions of CO Molecules on a One-Dimensional Substrate . *ACSnano*, 5:8877–8883, 2011.

[14] C. Lin, M. Feng, J. Zhao, P. Cabrera-Sanfelix, A. Arnau, D. Sánchez-Portal, and H. Petek. Theory of orthogonal interactions of CO molecules on a one-dimensional substrate. *Physical Review B*, 85:125426, 2012.

[15] Antón X. Brión-Ríos, Daniel Sánchez-Portal, and Pepa Cabrera-Sanfelix. NO adsorption on Cu(110) and O(2 × 1)/Cu(110) surfaces from density functional theory calculations. *Physical Chemistry Chemical Physics*, 18:9476–9483, 2016.

[16] Laura Fernández, Sebastian Thussing, Alexander Mänz, Gregor Witte, Antón X. Brión-Ríos, Pepa Cabrera-Sanfelix, Daniel Sánchez-Portal, and Peter Jakob. Structural and Vibrational Properties of the TiOPc Monolayer on Ag(111). *The Journal of Physical Chemistry C*, 121:1608–1617, 2017.

[17] Eduard Carbonell-Sanromà, Martina Corso, Jingcheng Li, Antón X. Brión-Ríos, Daniel Sánchez-Portal, and Jose Ignacio Pascual. Atomic-scale forces induced by a hydrogen molecule trapped in a tunneling junction. *Surface Science*, Accepted, 2018.

[18] L. Férnandez, A. X. Brión-Ríos, and *et al*. Detection of a discrete adsorption of CO_2 molecules on Tytanilphthalocianine. *In preparation*.

[19] Andrew L. Walter, Frederik Schiller, Martina Corso, Lindsay R. Merte, Florian Bertram, Jorge Lobo-Checa, Mikhail Shipilin, Johan Gustafson, Edvin Lundgren, Antón X. Brión-Ríos, Pepa Cabrera-Sanfelix, Daniel Sánchez-Portal, and J. Enrique Ortega. X-ray photoemission analysis of clean and carbon monoxide-chemisorbed platinum(111) stepped surfaces using a curved crystal. *Nature Communications*, 6:8903, 2015.

[20] E. Schrödinger. Quantisierung als Eigenwertproblem. *Annalen der Physik*, 384:361–376, January 1926.

[21] Max Born and Robert Oppenheimer. Zur quantentheorie der molekeln. *Annalen der Physik*, 389:457–484, 1927.

[22] A. Szabo and N. S. Ostlund. *Modern Quantum Chemistry*. Dover, 1996.

[23] Robert G. Parr and Weitao Yang. *Density-functional theory of atoms and molecules*. Oxford University Press, New York, 1994.

[24] J. A. Bort and J. Bertran, editors. *Theoretical and computational chemistry: foundations, methods and techniques*. Universitat Jaume I, Castelló de la Plana, 2007.

[25] Richard M. Martin. *Electronic structure: basic theory and practical methods*. Cambridge University Press, Cambridge, UK ; New York, 2004.

[26] Jorge Kohanoff. *Electronic Structure Calculations for Solids and Molecules: Theory and Computational Methods*. Cambridge University Press, 2006.

[27] W. Kohn. Nobel lecture: Electronic structure of matter-wave functions and density functionals. *Rev. Mod. Phys.*, 71:1253–1266, 1999.

[28] Ion Errea. *Pressure induced complexity in simple elements and alloys from first-principles calculations*. PhD thesis, ZTF-FCT, UPV/EHU and DIPC, 2011.

[29] Julian Arndt Hirschfeld. *Ab initio investigation of ground-states and ionic motion in particular in zirconia-based solid-oxide electrolytes*. PhD thesis, Forschungszentrum Jülich GmbH and Peter Grünberg Institute, 2013.

[30] L. H. Thomas. The calculation of atomic fields. *Proc. Cambridge Phil. Roy. Soc.*, 23:542–548, 1927.

[31] Fermi, E. Un metodo statistico per la determinzione di alcune prioriea dell'atome. *Rend. Accad. Naz. Lincei*, 6:602–607, 1927.

[32] Dirac, P. A. M. Note on exchange phenomena in the Thomas-Fermi atom. *Proc. Cambridge Phil. Roy. Soc.*, 26:376–385, 1930.

[33] Elliott H Lieb and Barry Simon. The Thomas-Fermi theory of atoms, molecules and solids. *Advances in Mathematics*, 23:22–116, 1977.

[34] Elliott H. Lieb. Thomas-Fermi and related theories of atoms and molecules. *Reviews of Modern Physics*, 53:603, 1981.

[35] Edward Teller. On the stability of molecules in the Thomas-Fermi theory. *Reviews of Modern Physics*, 34:627, 1962.

[36] Mel Levy. Universal variational functionals of electron densities, first-order density matrices, and natural spin-orbitals and solution of the v-representability problem. *Proceedings of the National Academy of Sciences*, 76:6062–6065, 1979.

[37] E. H. Lieb. *Density functionals for Coulomb systems. In physics as Natural Philosophy, Essays in Honor of Laszlo Tisza on his 75th birthday*. Cambridge: MIT press, 1982.

[38] P. A. M. Dirac. Note on Exchange Phenomena in the Thomas Atom. *Mathematical Proceedings of the Cambridge Philosophical Society*, 26:376–385, 1930.

[39] F. Bloch. Bemerkung zur Elektronentheorie des Ferromagnetismus und der elektrischen Leitfähigkeit. *Zeitschrift für Physik*, 57:545–555, 1929.

[40] E. Wigner and J. Bardeen. Theory of the Work Functions of Monovalent Metals. *Phys. Rev.*, 48:84–87, 1935.

[41] E. Wigner. Effects of the electron interaction on the energy levels of electrons in metals. *Trans. Faraday Soc.*, 34:678–685, 1938.

[42] D. Ceperley. Ground state of the fermion one-component plasma: A Monte Carlo study in two and three dimensions. *Phys. Rev. B*, 18:3126–3138, 1978.

[43] D. M. Ceperley and B. J. Alder. Ground state of the electron gas by a stochastic method. *Phys. Rev. Lett.*, 45:566–569, 1980.

[44] J. P. Perdew and A. Zunger. Self-interaction correction to density-functional approximations for many-electron systems. *Phys. Rev. B*, 23:5048–5079, 1981.

[45] S. H. Vosko, L. Wilk, and M. Nusair. Accurate spin-dependent electron liquid correlation energies for local spin density calculations: a critical analysis. *Canadian Journal of physics*, 58:1200–1211, 1980.

[46] A. D. Becke. Completely numerical calculations on diatomic molecules in the local-density approximation. *Phys. Rev. A*, 33:2786–2788, 1986.

[47] W. Koch and M. C. Holthausen. *A Chemist's Guide to Density Functional Theory*. VCH Verlag GmbH, 2001.

[48] Frank Herman, John P. Van Dyke, and Irene B. Ortenburger. Improved Statistical Exchange Approximation for Inhomogeneous Many-Electron Systems. *Phys. Rev. Lett.*, 22:807–811, 1969.

[49] Shang-Keng M. and K. A. Brueckner. Correlation Energy of an Electron Gas with a Slowly Varying High Density. *Phys. Rev.*, 165:18–31, 1968.

[50] Carlos Fiolhais, Fernando Nogueira, and Miguel A. L. Marques, editors. *A Primer in Density Functional Theory*. Springer Berlin Heidelberg, 2003.

[51] A. D. Becke. On the large-gradient behavior of the density functional exchange energy. *J. Chem. Phys.*, 85(12):7184–7187, 1986.

[52] A. D. Becke. Density-functional exchange-energy approximation with correct asymptotic behavior. *Phys. Rev. A*, 38:3098–3100, 1988.

[53] John P. Perdew, J. A. Chevary, S. H. Vosko, Koblar A. Jackson, Mark R. Pederson, D. J. Singh, and Carlos Fiolhais. Atoms, molecules, solids, and surfaces: Applications of the generalized gradient approximation for exchange and correlation. *Phys. Rev. B*, 46:6671–6687, 1992.

[54] Chengteh Lee, Weitao Yang, and Robert G. Parr. Development of the Colle-Salvetti correlation-energy formula into a functional of the electron density. *Phys. Rev. B*, 37:785–789, 1988.

[55] J. P. Perdew, K. Burke, and Ernzerhof M. Generalized Gradient Approximation Made Simple. *Phys. Rev. Lett.*, 77:3865–3868, 1996.

[56] Jacob N. Israelachvili. *Intermolecular and Surface Forces* . Elsevier BV, 2011.

[57] Neil W. Ashcroft and N. David Mermin. *Solid state physics*. Holt, Rinehart and Winston, New York, 1976.

[58] M. Dion, H. Rydber, E. Schröder, D. C. Langreth, and B. I. Lundqvist. Van derWaals Density Functional for General Geometries. *Phys. Rev. Lett.*, 92:246401, 2004.

[59] Guillermo Román-Pérez and José M. Soler. Efficient Implementation of a van der Waals Density Functional: Application to Double-Wall Carbon Nanotubes. *Physical Review Letters*, 103, 2009.

[60] J. Klimeš, D. R. Bowler, and A. Michaelides. Chemical accuracy for the van der Waals density functional. *Journal of Physics: Condensed Matter*, 22:022201, 2010.

[61] J. Klimeš, D. R. Bowler, and A. Michaelides. Van derWaals density functionals applied to solids . *Phys. Rev. B*, 83:195131, 2011.

[62] Oleg A. Vydrov and Troy Van Voorhis. Nonlocal van der Waals Density Functional Made Simple. *Phys. Rev. Lett.*, 103:063004, 2009.

[63] Stefan Grimme, Jens Antony, Stephan Ehrlich, and Helge Krieg. A consistent and accurate ab initio parametrization of density functional dispersion correction (DFT-D) for the 94 elements H-Pu. *The Journal of Chemical Physics*, 132:154104, 2010.

[64] Stefan Grimme, Stephan Ehrlich, and Lars Goerigk. Effect of the damping function in dispersion corrected density functional theory. *Journal of Computational Chemistry*, 32:1456–1465, 2011.

[65] E. Sokolowski, C. Nordling, and K. Siegbahn. Chemical Shift Effect in Inner Electronic Levels of Cu due to Oxidation. *Physical Review*, 110:776–776, 1958.

[66] Axel Knop-Gericke and et al. ChemInform Abstract: X-Ray Photoelectron Spectroscopy for Investigation of Heterogeneous Catalytic Processes. *ChemInform*, 40, 2009.

[67] Anna Maria Venezia. X-ray photoelectron spectroscopy (XPS) for catalysts characterization. *Catalysis Today*, 77:359–370, 2003.

[68] Daniel Spanjaard, Claude Guillot, Marie-Catherine Desjonquères, Guy Tréglia, and Jean Lecante. Surface core level spectroscopy of transition metals: A new tool for the determination of their surface structure. *Surface Science Reports*, 5:1–85, 1985.

[69] Stefan Hüfner. *Photoelectron Spectroscopy*. Springer Berlin Heidelberg, 2003.

[70] A. Baraldi, G. Comelli, S. Lizzit, M. Kiskinova, and G. Paolucci. Real-time X-ray photoelectron spectroscopy of surface reactions. *Surface Science Reports*, 49:169–224, 2003.

[71] Alessandro Baraldi. Structure and chemical reactivity of transition metal surfaces as probed by synchrotron radiation core level photoelectron spectroscopy. *Journal of Physics: Condensed Matter*, 20:093001, 2008.

[72] D. Teschner, E. Vass, M. Hävecker, S. Zafeiratos, P. Schnörch, H. Sauer, A. Knop-Gericke, R. Schlögl, M. Chamam, A. Wootsch, A. S. Canning, J. J. Gamman, S. D. Jackson, J. McGregor, and L. F. Gladden. Alkyne hydrogenation over Pd catalysts: A new paradigm. *Journal of Catalysis*, 242:26–37, 2006.

[73] D. Teschner, J. Borsodi, A. Wootsch, Z. Revay, M. Havecker, A. Knop-Gericke, S. D. Jackson, and R. Schlogl. The Roles of Subsurface Carbon and Hydrogen in Palladium-Catalyzed Alkyne Hydrogenation. *Science*, 320:86–89, 2008.

[74] C. Göransson, W. Olovsson, and I. A. Abrikosov. Numerical investigation of the validity of the Slater-Janak transition-state model in metallic systems. *Physical Review B*, 72:134203, 2005.

[75] W. Olovsson, C. Göransson, L. V. Pourovskii, B. Johansson, and I. A. Abrikosov. Core-level shifts in fcc random alloys: A first-principles approach. *Physical Review B*, 72:064203, 2005.

[76] Weine Olovsson, Christian Göransson, Tobias Marten, and Igor A. Abrikosov. Core-level shifts in complex metallic systems from first principle. *physica status solidi (b)*, 243:2447–2464, 2006.

[77] Weine Olovsson, Tobias Marten, Erik Holmström, Börje Johansson, and Igor A. Abrikosov. First principle calculations of core-level binding energy and Auger kinetic energy shifts in metallic solids. *Journal of Electron Spectroscopy and Related Phenomena*, 178-179:88–99, 2010.

[78] Lukas Köhler and Georg Kresse. Density functional study of CO on Rh(111). *Physical Review B*, 70:165405, 2004.

[79] ZhenHua Zeng, XiuFang Ma, WuChen Ding, and WeiXue Li. First-principles calculation of core-level binding energy shift in surface chemical processes. *Science China Chemistry*, 53:402–410, 2010.

[80] M. V. Ganduglia-Pirovano, M. Scheffler, A. Baraldi, S. Lizzit, G. Comelli, G. Paolucci, and R. Rosei. Oxygen-induced Rh3d5/2surface core-level shifts on Rh(111). *Physical Review B*, 63:205415, 2001.

[81] S. Lizzit, A. Baraldi, A. Groso, K. Reuter, M. V. Ganduglia-Pirovano, C. Stampfl, M. Scheffler, M. Stichler, C. Keller, W. Wurth, and D. Menzel. Surface core-level shifts of clean and oxygen-covered Ru(0001). *Physical Review B*, 63:205419, 2001.

[82] T. Marten, W. Olovsson, S. I. Simak, and I. A. Abrikosov. Ab initio study of disorder broadening of core photoemission spectra in random Cu-Pd and Ag-Pd alloys. *Physical Review B*, 72:054210, 2005.

[83] J. C. Slater and James C. Phillips. Quantum Theory of Molecules and Solids Vol. 4: The Self-Consistent Field for Molecules and Solids. *Physics Today*, 27:49–50, 1974.

[84] J. F. Janak. Proof that $\partial E/\partial n_i=\varepsilon_i$ in density-functional theory. *Physical Review B*, 18:7165–7168, 1978.

[85] Quang Thang Trinh, Kong Fei Tan, Armando Borgna, and Mark Saeys. Evaluating the Structure of Catalysts Using Core-Level Binding Energies Calculated from First Principles. *The Journal of Physical Chemistry C*, 117:1684–1691, 2013.

[86] A. Stierle, C. Tieg, H. Dosch, V. Formoso, E. Lundgren, J.N. Andersen, L. Köhler, and G. Kresse. Surface core level shift observed on NiAl(1 1 0). *Surface Science*, 529:L263–L268, 2003.

[87] G. Kresse and J. Hafner. *Ab initio* molecular dynamics for liquid metals. *Physical Review B*, 47:558–561, 1993.

[88] G. Kresse and J. Hafner. *Ab initio* molecular-dynamics simulation of the liquid-metal–amorphous-semiconductor transition in germanium. *Physical Review B*, 49:14251–14269, 1994.

[89] G. Kresse and J. Furthmüller. Efficiency of ab-initio total energy calculations for metals and semiconductors using a plane-wave basis set. *Computational Materials Science*, 6:15–50, 1996.

[90] M. C. Payne, M. P. Teter, D. C. Allan, T. A. Arias, and J. D. Joannopoulos. Iterative minimization techniques for *ab initio* total-energy calculations: molecular dynamics and conjugate gradients. *Rev. Mod. Phys.*, 64:1045–1097, 1992.

[91] Hendrik J. Monkhorst and James D. Pack. Special points for Brillouin-zone integrations. *Phys. Rev. B*, 13:5188–5192, 1976.

[92] Hafner, Jürgen. Ab-initio simulations of materials using vasp: Density-functional theory and beyond. *Journal of Computational Chemistry*, 29:2044–2078, 2008.

[93] D. R. Hamann, M. Schlüter, and C. Chiang. Norm-Conserving Pseudopotentials. *Physical Review Letters*, 43:1494–1497, 1979.

[94] G P Kerker. Non-singular atomic pseudopotentials for solid state applications. *Journal of Physics C: Solid State Physics*, 13:L189–L194, 1980.

[95] Leonard Kleinman and D. M. Bylander. Efficacious Form for Model Pseudopotentials. *Physical Review Letters*, 48:1425–1428, 1982.

[96] Andrew M. Rappe, Karin M. Rabe, Efthimios Kaxiras, and J. D. Joannopoulos. Optimized pseudopotentials. *Physical Review B*, 41:1227–1230, 1990.

[97] N. Troullier and José Luriaas Martins. Efficient pseudopotentials for plane-wave calculations. *Physical Review B*, 43:1993–2006, 1991.

[98] P. E. Blöchl. Projector augmented-wave method. *Physical Review B*, 50(24):17953–17979, 1994.

[99] G. Kresse and D. Joubert. From ultrasoft pseudopotentials to the projector augmented-wave method. *Phys. Rev. B*, 59:1758–1775, 1999.

[100] N. A. W. Holzwarth, G. E. Matthews, R. B. Dunning, A. R. Tackett, and Y. Zeng. Comparison of the projector augmented-wave, pseudopotential, and linearized augmented-plane-wave formalisms for density-functional calculations of solids. *Physical Review B*, 55:2005–2017, 1997.

[101] U. von Barth and C. D. Gelatt. Validity of the frozen-core approximation and pseudopotential theory for cohesive energy calculations. *Phys. Rev. B*, 21:2222–2228, 1980.

[102] J. F. Wendelken. A study of Nitric Oxide adsorption on copper (100) and (110) . *Appl. Surf. Sci*, 11:172–185, 1982.

[103] W. A. Brown, R. K. Sharma, D. A. King, and S. Haq. Adsorption and Reactivity of NO and N_2O on Cu110: Combined RAIRS and Molecular Beam Studies. *J. Phys. Chem.*, 100(30):12559–12568, 1996.

[104] M. Gajdoš, H. Jügen, and A. Eichler. Ab initio density-functional study of NO on close-packed transition and noble metal surfaces: I. Molecular adsorption . *J. Phys. Condens. Matter*, 18:13–41, 2006.

[105] M. Gajdoš, H. Jügen, and A. Eichler. Ab initio density-functional study of NO adsorption on close-packed transition and noble metal surfaces: II. Dissociative adsorption . *J. Phys. Condens. Matter*, 18:41–54, 2006.

[106] N. García Rey and H. Arnolds. Hot hole-induced dissociation of NO dimers on a copper surface . *J. Chem. Phys*, 135:224708, 2011.

[107] A. Shiotari, Y. Kitaguchi, H. Okuyama, S. Hatta, and T. Aruga. Imaging Covalent Bonding between Two NO Molecules on Cu(110). *Phys. Rev. Lett.*, 106:156104, 2011.

[108] H. Dürr, R. Schneider, and Th. Fauster. Added-row growth of the (2 X 1)O-Cu(110) reconstruction . *Phys. Rev. B*, 43:1802–1804, 1991.

[109] H. Dürr, Th. Fauster, and R. Schneider. Surface structure determination of the (2x1)O-Cu(110) reconstruction by low-energy ion scattering . *Surf. Sci.*, 244:237–246, 1991.

[110] X. Duan, O. Warschkow, A. Soon, B. Delley, and C. Stampfl. Density functional study of oxygen on Cu(100) and Cu(110) surfaces. *Phys. Rev. B*, 81:075430, 2010.

[111] P. Cabrera-Sanfelix, C. Lin, A. Arnau, and D. Sánchez-Portal. Hybridization between Cu-O chain and Cu(110) surface in the O(2x1)/Cu(110) surface from first principles. *J. Phys.:Condens. Matter*, 25:135003, 2013.

[112] K. Lee, E. D. Murray, L. Kong, B. I. Lundqvist, and D. C. Langreth. Higher-accuracy van der Waals density functional. *Phys. Rev. B*, 82:081101, 2010.

[113] R.F.W. Bader. *Atoms in Molecules - A quantum theory*. Oxford University Press, New York, 1990.

[114] W. Tang, E. Sanville, and G. Henkelman. A grid-based Bader analysis algorithm without lattice bias. *J. Phys. Condens. Matter*, 21:084204, 2009.

[115] E. Sanville, S. D. Kenny, R. Smith, and G. Henkelman. An improved grid-based algorithm for Bader charge allocation. *J. Comp. Chem.*, 28:899–908, 2007.

[116] G. Henkelman, A. Arnaldsson, and H. Jónsson. A fast and robust algorithm for Bader decomposition of charge density. *Comput. Mater. Sci.*, 36:354–360, 2006.

[117] J. Tersoff and D. R. Hamann. Theory and application for the scanning tunneling microscope. *Physical Review Letters*, 50:1998–2001, 1983.

[118] J. Tersoff and D. R. Hamann. Theory of the scanning tunneling microscope. *Physical Review B*, 31:805–813, 1985.

[119] M. Gajdoš, A. Eichler, and J. Hafner. CO adsorption on close-packed tansition and noble metal surfaces: trends from *ab initio* calculations. *J. Phys.: Condens. Matter*, 16:1141–1164, 2004.

[120] N. A. Besley. Theoretical study of the electronic of CO adsorbed on Pt(111). *J. Chem. Phys.*, 122:184706, 2005.

[121] J. L. Valmoria Moreno, A. A. Bustria Padama, and H. Kasai. A density functional theory-based study on the dissociation of NO on a CuO(110) surface. *CrystEngComm*, 16:2260–2265, 2014.

[122] I. Horcas, R. Fernández, J. Gómez-Rodríguez, J. Colchero, J. Gómez-Herrero, and A. M. Baro. WSXM: A software for scanning probe microscopy and a tool for nanotecnology. *Rev. Sci. Instrum.*, 78:013705, 2007.

[123] Zhenan Bao, Andrew J. Lovinger, and Ananth Dodabalapur. Organic field-effect transistors with high mobility based on copper phthalocyanine. *Applied Physics Letters*, 69:3066–3068, 1996.

[124] S. A. Van Slyke, C. H. Chen, and C. W. Tang. Organic electroluminescent devices with improved stability. *Applied Physics Letters*, 69(15):2160–2162, 1996.

[125] G. Parthasarathy, P. E. Burrows, V. Khalfin, V. G. Kozlov, and S. R. Forrest. A metal-free cathode for organic semiconductor devices. *Applied Physics Letters*, 72:2138–2140, 1998.

[126] M. Pfeiffer, K. Leo, X. Zhou, J. S. Huang, M. Hofmann, A. Werner, and J. Blochwitz-Nimoth. Doped organic semiconductors: Physics and application in light emitting diodes. *Organic Electronics*, 4:89–103, 2003.

[127] Jeffrey T. Mabeck and George G. Malliaras. Chemical and biological sensors based on organic thin-film transistors. *Analytical and Bioanalytical Chemistry*, 384:343–353, 2005.

[128] Marcel Bouvet. Phthalocyanine-based field-effect transistors as gas sensors. *Analytical and Bioanalytical Chemistry*, 384:366–373, 2005.

[129] M. Victoria Martínez-Díaz, Gema de la Torre, and Tomás Torres. Lighting porphyrins and phthalocyanines for molecular photovoltaics. *Chemical Communications*, 46:7090–7108, 2010.

[130] Diogenes Placencia, Weining Wang, R. Clayton Shallcross, Kenneth W. Nebesny, Michael Brumbach, and Neal R. Armstrong. Organic Photovoltaic Cells Based On Solvent-Annealed, Textured Titanyl Phthalocyanine/C60 Heterojunctions. *Advanced Functional Materials*, 19:1913–1921, 2009.

[131] S. W. Wu, G. V. Nazin, X. Chen, X. H. Qiu, and W. Ho. Control of Relative Tunneling Rates in Single Molecule Bipolar Electron Transport. *Phys. Rev. Lett.*, 93:236802, 2004.

[132] Jianzhuang Jiang. *Functional Phthalocyanine Molecular Materials*. Springer Berlin Heidelberg, 2010.

[133] Mirko Cinchetti, Kathrin Heimer, Jan-Peter Wüstenberg, Oleksiy Andreyev, Michael Bauer, Stefan Lach, Christiane Ziegler, Yongli Gao, and Martin Aeschlimann. Determination of spin injection and transport in a ferromagnet/organic semiconductor heterojunction by two-photon photoemission. *Nature Materials*, 8:115–119, 2008.

[134] S. Heutz, C. Mitra, W. Wu, A. J. Fisher, A. Kerridge, M. Stoneham, A. H. Harker, J. Gardener, H.-H. Tseng, T. S. Jones, C. Renner, and G. Aeppli. Molecular Thin Films: A New Type of Magnetic Switch. *Advanced Materials*, 19:3618–3622, 2007.

[135] Jeroen van den Brink and Alberto F. Morpurgo. Materials science: Magnetic blue. *Nature*, 450:177–178, 2007.

[136] H. Yamane, A. Gerlach, S. Duhm, Y. Tanaka, T. Hosokai, Y. Y. Mi, J. Zegenhagen, N. Koch, K. Seki, and F. Schreiber. Site-Specific Geometric and Electronic Relaxations at Organic-Metal Interfaces. *Physical Review Letters*, 105:046103, 2010.

[137] Jun Ren, Sheng Meng, Yi-Lin Wang, Xu-Cun Ma, Qi-Kun Xue, and Efthimios Kaxiras. Properties of copper (fluoro-)phthalocyanine layers deposited on epitaxial graphene. *The Journal of Chemical Physics*, 134:194706, 2011.

[138] Meng-Sheng Liao and Steve Scheiner. Electronic structure and bonding in metal phthalocyanines, Metal=Fe, Co, Ni, Cu, Zn, Mg. *The Journal of Chemical Physics*, 114:9780, 2001.

[139] Yandong Ma, Ying Dai, Zhenkui Zhang, Lin Yu, and Baibiao Huang. Magnetic properties of phthalocyanine-based organometallic nanowire. *Applied Physics Letters*, 101:062405, 2012.

[140] X. Sun, B. Wang, and Y. Yamauchi. Electronic Structure and Spin Polarization of Metal (Mn, Fe, Cu) Phthalocyanines on an Fe(100) Surface by First-Principles Calculations. *The Journal of Physical Chemistry C*, 116:18752–18758, 2012.

[141] Zhenpeng Hu, Bin Li, Aidi Zhao, Jinlong Yang, and J. G. Hou. Electronic and Magnetic Properties of Metal Phthalocyanines on Au(111) Surface: A First-Principles Study. *The Journal of Physical Chemistry C*, 112:13650–13655, 2008.

[142] M. Grobosch, C. Schmidt, R. Kraus, and M. Knupfer. Electronic properties of transition metal phthalocyanines: The impact of the central metal atom (d5–d10). *Organic Electronics*, 11:1483–1488, 2010.

[143] T. Bathon, P. Sessi, K. A. Kokh, O. E. Tereshchenko, and M. Bode. Systematics of Molecular Self-Assembled Networks at Topological Insulators Surfaces. *Nano Letters*, 15:2442–2447, 2015.

[144] E. Goiri, M. Matena, A. El-Sayed, J. Lobo-Checa, P. Borghetti, C. Rogero, B. Detlefs, J. Duvernay, J. E. Ortega, and D. G. de Oteyza. Self-Assembly of Bicomponent Molecular Monolayers: Adsorption Height Changes and Their Consequences. *Physical Review Letters*, 112:117602, 2014.

[145] Benjamin Stadtmüller, Daniel Lüftner, Martin Willenbockel, Eva M. Reinisch, Tomoki Sueyoshi, Georg Koller, Serguei Soubatch, Michael G. Ramsey, Peter Puschnig, F. Stefan Tautz, and Christian Kumpf. Unexpected interplay of bonding height and energy level alignment at heteromolecular hybrid interfaces. *Nature Communications*, 5:3685, 2014.

[146] Cornelius Krull, Roberto Robles, Aitor Mugarza, and Pietro Gambardella. Site- and orbital-dependent charge donation and spin manipulation in electron-doped metal phthalocyanines. *Nature Materials*, 12:337–343, 2013.

[147] Aitor Mugarza, Cornelius Krull, Roberto Robles, Sebastian Stepanow, Gustavo Ceballos, and Pietro Gambardella. Spin coupling and relaxation inside molecule–metal contacts. *Nature Communications*, 2:490, 2011.

[148] A. Mugarza, R. Robles, C. Krull, R. Korytár, N. Lorente, and P. Gambardella. Electronic and magnetic properties of molecule-metal interfaces: Transition-metal phthalocyanines adsorbed on Ag(100). *Physical Review B*, 85:155437, 2012.

[149] F. Petraki, H. Peisert, U. Aygül, F. Latteyer, J. Uihlein, A. Vollmer, and T. Chassé. Electronic Structure of FePc and Interface Properties on Ag(111) and Au(100). *The Journal of Physical Chemistry C*, 116:11110–11116, 2012.

[150] F. Petraki, H. Peisert, P. Hoffmann, J. Uihlein, M. Knupfer, and T. Chassé. Modification of the 3d-Electronic Configuration of Manganese Phthalocyanine at the Interface to Gold. *The Journal of Physical Chemistry C*, 116:5121–5127, 2012.

[151] F. Petraki, H. Peisert, F. Latteyer, U. Aygül, A. Vollmer, and T. Chassé. Impact of the 3d Electronic States of Cobalt and Manganese Phthalocyanines on the Electronic Structure at the Interface to Ag(111). *The Journal of Physical Chemistry C*, 115:21334–21340, 2011.

[152] Yu Huang, Elisabeth Wruss, David Egger, Satoshi Kera, Nobuo Ueno, Wissam Saidi, Tomas Bucko, Andrew Wee, and Egbert Zojer. Understanding the Adsorption of CuPc and ZnPc on Noble Metal Surfaces by Combining Quantum-Mechanical Modelling and Photoelectron Spectroscopy. *Molecules*, 19:2969–2992, 2014.

[153] Ingo Kröger, Benjamin Stadtmüller, Christoph Stadler, Johannes Ziroff, Mario Kochler, Andreas Stahl, Florian Pollinger, Tien-Lin Lee, Jörg Zegenhagen, Friedrich Reinert, and Christian Kumpf. Submonolayer growth of copper-phthalocyanine on Ag(111). *New Journal of Physics*, 12:083038, 2010.

[154] Ingo Kröger, Benjamin Stadtmüller, and Christian Kumpf. Submonolayer and multilayer growth of titaniumoxide-phthalocyanine on Ag(111). *New Journal of Physics*, 18:113022, 2016.

[155] K. Momma and F. Izumi. *VESTA3* for three-dimensional visualization of crystal, volumetric and morphology data. *Journal of Applied Crystallography*, 44:1272–1276, 2011.

[156] Wei-Xue Li, Catherine Stampfl, and Matthias Scheffler. Oxygen adsorption on Ag(111): A density-functional theory investigation. *Physical Review B*, 65, 2002.

[157] Lingling Jia, Yun Wang, and Kangnian Fan. Theoretical Study of Atomic Oxygen Adsorption on the Chlorine-Modified Ag(111) Surface. *The Journal of Physical Chemistry B*, 107:3813–3819, 2003.

[158] H. Schubert, U. Tegtmeyer, D. Herein, X. Bao, M. Muhler, and R. Schlögl. On the relation between catalytic performance and microstructure of polycrystalline silver in the partial oxidation of methanol. *Catalysis Letters*, 33:305–319, 1995.

[159] F. Schiller. *Private communication*, 2017.

[160] N. D. Lang. Interaction between Closed-Shell Systems and Metal Surfaces. *Phys. Rev. Lett.*, 46:842–845, 1981.

[161] Paul S. Bagus, Volker Staemmler, and Christof Wöll. Exchangelike Effects for Closed-Shell Adsorbates: Interface Dipole and Work Function. *Phys. Rev. Lett.*, 89:096104, 2002.

[162] Gregor Witte, Simon Lukas, Paul S. Bagus, and Christof Wöll. Vacuum level alignment at organic/metal junctions: "Cushion" effect and the interface dipole. *Applied Physics Letters*, 87:263502, 2005.

[163] Paul C. Rusu, Gianluca Giovannetti, Christ Weijtens, Reinder Coehoorn, and Geert Brocks. First-principles study of the dipole layer formation at metal-organic interfaces. *Physical Review B*, 81, 2010.

[164] Ahmet Altındal, Özgür Kurt, Abdurrahman Şengül, and Özer Bekaroğlu. Kinetics of CO2 adsorption on ball-type dicopper phthalocyanine thin film. *Sensors and Actuators B: Chemical*, 202:373–381, 2014.

[165] J. Spadavecchia, G. Ciccarella, and R. Rella. Optical characterization and analysis of the gas/surface adsorption phenomena on phthalocyanines thin films for gas sensing application. *Sensors and Actuators B: Chemical*, 106:212–220, 2005.

[166] Guofeng Wang, Nitia Ramesh, Andrew Hsu, Deryn Chu, and Rongrong Chen. Density functional theory study of the adsorption of oxygen molecule on iron phthalocyanine and cobalt phthalocyanine. *Molecular Simulation*, 34:1051–1056, 2008.

[167] T. V. Magdesieva, T. Yamamoto, D. A. Tryk, and A. Fujishima. Electrochemical Reduction of CO_2 with Transition Metal Phthalocyanine and Porphyrin Complexes Supported on Activated Carbon Fibers. *Journal of The Electrochemical Society*, 149:D89–D95, 2002.

[168] M. Methfessel and A. T. Paxton. High-precision sampling for Brillouin-zone integration in metals. *Physical Review B*, 40:3616–3621, 1989.

[169] N. David Mermin. Thermal Properties of the Inhomogeneous Electron Gas. *Physical Review*, 137:A1441–A1443, 1965.

[170] R. C. Baetzold, G. Apai, E. Shustorovich, and R. Jaeger. Surface core-level shifts for Pt single-crystal surfaces. *Physical Review B*, 26:4022–4027, 1982.

[171] G. Apai, R.C. Baetzold, P.J. Jupiter, A.J. Viescas, and I. Lindau. Influence of acceptor and donor adsorbates (CO, K, NH_3) on Pt surface core-level shifts. *Surface Science*, 134:122–134, 1983.

[172] K. Duckers, H.P. Bonzel, and D.A. Wesner. Surface core level shifts of Pt(111) measured with Y Mζ radiation (132.3 eV). *Surface Science*, 166:141–158, 1986.

[173] Laura Bianchettin, Alessandro Baraldi, Stefano de Gironcoli, Erik Vesselli, Silvano Lizzit, Luca Petaccia, Giovanni Comelli, and Renzo Rosei. Core level shifts of undercoordinated Pt atoms. *The Journal of Chemical Physics*, 128:114706, 2008.

[174] A. Beutler, E. Lundgren, R. Nyholm, J.N. Andersen, B.J. Setlik, and D. Heskett. Coverage- and temperature-dependent site occupancy of carbon monoxide on Rh(111) studied by high-resolution core-level photoemission. *Surface Science*, 396:117–136, 1998.

[175] M. Birgersson, C.-O. Almbladh, M. Borg, and J. N. Andersen. Density-functional theory applied to Rh(111) and CO/Rh(111) systems: Geometries, energies, and chemical shifts. *Physical Review B*, 67:045402, 2003.

[176] Alessandro Baraldi. High-Energy Resolution Core Level Photoelectron Spectroscopy and Diffraction: Powerful Tools to Probe Physical and Chemical Properties of Solid Surfaces. In *Synchrotron Radiation*, pages 519–538. Springer Berlin Heidelberg, 2014.

[177] Alessandro Baraldi, Silvano Lizzit, Alberto Novello, Giovanni Comelli, and Renzo Rosei. Second-layer surface core-level shift on Rh(111). *Physical Review B*, 67:205404, 2003.

[178] J. N. Andersen, D. Hennig, E. Lundgren, M. Methfessel, R. Nyholm, and M. Scheffler. Surface core-level shifts of some 4d-metal single-crystal surfaces: Experiments and *ab initio* calculations. *Physical Review B*, 50:17525–17533, 1994.

[179] A. Schlapka, M. Lischka, A. Groß, U. Käsberger, and P. Jakob. Surface Strain versus Substrate Interaction in Heteroepitaxial Metal Layers: Pt on Ru(0001). *Physical Review Letters*, 91:016101, 2003.

[180] H. Hopster. Catalytic oxidation of carbon monoxide on stepped platinum(111) surfaces. *Journal of Catalysis*, 46:37–48, 1977.

[181] Bas L. M. Hendriksen, Marcelo D. Ackermann, Richard van Rijn, Dunja Stoltz, Ioana Popa, Olivier Balmes, Andrea Resta, Didier Wermeille, Roberto Felici, Salvador Ferrer, and Joost W. M. Frenken. The role of steps in surface catalysis and reaction oscillations. *Nature Chemistry*, 2:730–734, 2010.

[182] Yongsheng Zhang, Jutta Rogal, and Karsten Reuter. Density-functional theory investigation of oxygen adsorption at Pd(11N) vicinal surfaces (N=3,5,7): Influence of neighboring steps. *Physical Review B*, 74:125414, 2006.

[183] B. Hammer, O.H. Nielsen, and J.K. Nrskov. Structure sensitivity in adsorption: CO interaction with stepped and reconstructed Pt surfaces. *Catalysis Letters*, 46:31–35, 1997.

[184] A. Stroppa, F. Mittendorfer, J. N. Andersen, G. Parteder, F. Allegretti, S. Surnev, and F. P. Netzer. Adsorption and Dissociation of CO on Bare and Ni-Decorated Stepped Rh(553) Surfaces. *The Journal of Physical Chemistry C*, 113:942–949, 2009.

[185] J. Gustafson, M. Borg, A. Mikkelsen, S. Gorovikov, E. Lundgren, and J. N. Andersen. Identification of Step Atoms by High Resolution Core Level Spectroscopy. *Physical Review Letters*, 91:056102, 2003.

[186] A Baraldi, L Bianchettin, E Vesselli, S de Gironcoli, S Lizzit, L Petaccia, G Zampieri, G Comelli, and R Rosei. Highly under-coordinated atoms at Rh surfaces: interplay of strain and coordination effects on core level shift. *New Journal of Physics*, 9:143–143, 2007.

[187] R. J. Needs and M. Mansfield. Calculations of the surface stress tensor and surface energy of the (111) surfaces of iridium, platinum and gold. *Journal of Physics: Condensed Matter*, 1:7555–7563, 1989.

[188] Richard J. Needs. Calculations of the Surface Stress Tensor at Aluminum (111) and (110) Surfaces. *Physical Review Letters*, 58:53–56, 1987.

[189] R. J. Needs and M. J. Godfrey. Surface stress of aluminum and jellium. *Physical Review B*, 42:10933–10939, 1990.

[190] Peter J. Feibelman. Calculation of surface stress in a linear combination of atomic orbitals representation. *Physical Review B*, 50:1908–1911, 1994.

[191] Vincenzo Fiorentini, Michael Methfessel, and Matthias Scheffler. Reconstruction mechanism of fcc transition metal (001) surfaces. *Physical Review Letters*, 71:1051–1054, 1993.

[192] G. Prévot, C. Cohen, D. Schmaus, P. Hecquet, and B. Salanon. Temperature dependence of the atomic relaxations and vibrations on a stepped surface: a molecular dynamics study of Cu(1,1,19). *Surface Science*, 506:272–286, 2002.

[193] G. Prévot and B. Croset. Revisiting Elastic Interactions between Steps on Vicinal Surfaces: The Buried Dipole Model. *Physical Review Letters*, 92:256104, 2004.

[194] V. I. Marchenko and A. Ya Parshin. Elastic properties of crystal surfaces. *Sov Phys JETP*, 52:129, 1980.

[195] G. Prévot, A. Coati, and Y. Garreau. Grazing-incidence x-ray diffraction measurement of the relaxations and elastic step interactions on Cu(211) and Cu(322). *Physical Review B*, 70:205406, 2004.

[196] G. Prévot, P. Steadman, and S. Ferrer. Determination of the elastic dipole at the atomic steps of Pt(977) from surface x-ray diffraction. *Physical Review B*, 67:245409, 2003.

[197] Elisabeth Kampshoff, Elmar Hahn, and Klaus Kern. Correlation between surface stress and the vibrational shift of CO chemisorbed on Cu surfaces. *Physical Review Letters*, 73:704–707, 1994.

[198] M. Mavrikakis, B. Hammer, and J. K. Nørskov. Effect of Strain on the Reactivity of Metal Surfaces. *Physical Review Letters*, 81:2819–2822, 1998.

[199] Sebastian Schnur and Axel Groß. Strain and coordination effects in the adsorption properties of early transition metals: A density-functional theory study. *Physical Review B*, 81:033402, 2010.

[200] M. Gsell, P. Jakob, and D. Menzel. Effect of Substrate Strain on Adsorption. *Science*, 280:717–720, 1998.

[201] M. F. Francis and W. A. Curtin. Mechanical work makes important contributions to surface chemistry at steps. *Nature Communications*, 6:6261, 2015.

[202] C. J. Zhang, R. J. Baxter, P. Hu, A. Alavi, and M.-H. Lee. A density functional theory study of carbon monoxide oxidation on the $Cu_3Pt(111)$ alloy surface: Comparison with the reactions on Pt(111) and Cu(111). *The Journal of Chemical Physics*, 115:5272–5277, 2001.

[203] G. Krenn, I. Bako, and R. Schennach. CO adsorption and CO and O coadsorption on Rh(111) studied by reflection absorption infrared spectroscopy and density functional theory. *The Journal of Chemical Physics*, 124:144703, 2006.

[204] Viktor N. Staroverov, Gustavo E. Scuseria, Jianmin Tao, and John P. Perdew. Tests of a ladder of density functionals for bulk solids and surfaces. *Physical Review B*, 69:075102, 2004.

[205] G. Prévot and B. Croset. Elastic relaxations and interactions on metallic vicinal surfaces: Testing the dipole model. *Physical Review B*, 74:235410, 2006.

[206] F. Schiller and J. E. Ortega. *Private communication*, 2018.

[207] Kathleen C. Taylor. *Automobile Catalytic Converters*. Springer Berlin Heidelberg, 1984.

[208] Bernard E. Nieuwenhuys. The Surface Science Approach Toward Understanding Automotive Exhaust Conversion Catalysis at the Atomic Level. In *Advances in Catalysis*, pages 259–328. Elsevier, 1999.

[209] G. A. Somorjai. *Introduction to Surface Chemistry and Catalysis* . Wiley, New York, 1994.

[210] B. N. J. Persson, M. Tüshaus, and A. M. Bradshaw. On the nature of dense CO adlayers. *The Journal of Chemical Physics*, 92:5034–5046, 1990.

[211] Sergei G. Podkolzin, Jianyi Shen, Juan J. de Pablo, and James A. Dumesic. Equilibrated Adsorption of CO on Silica-Supported Pt Catalysts. *The Journal of Physical Chemistry B*, 104:4169–4180, 2000.

[212] S. Kandoi, A.A. Gokhale, L.C. Grabow, J.A. Dumesic, and M. Mavrikakis. Why Au and Cu Are More Selective Than Pt for Preferential Oxidation of CO at Low Temperature. *Catalysis Letters*, 93:93–100, 2004.

[213] M. Gajdoš, A. Eichler, and J. Hafner. CO adsorption on close-packed transition and noble metal surfaces: trends from ab initio calculations. *Journal of Physics: Condensed Matter*, 16:1141–1164, 2004.

[214] N. A. Besley. Theoretical study of the electronic spectroscopy of CO adsorbed on Pt(111). *The Journal of Chemical Physics*, 122:184706, 2005.

[215] K. Doll. CO adsorption on the Pt(111) surface: a comparison of a gradient corrected functional and a hybrid functional. *Surface Science*, 573:464–473, 2004.

[216] A. Stroppa, K. Termentzidis, J. Paier, G. Kresse, and J. Hafner. CO adsorption on metal surfaces: A hybrid functional study with plane-wave basis set. *Physical Review B*, 76:195440, 2007.

[217] H. Hopster and H. Ibach. Adsorption of CO on Pt(111) and Pt 6(111) × (111) studied by high resolution electron energy loss spectroscopy and thermal desorption spectroscopy. *Surface Science*, 77:109–117, 1978.

[218] H. Steininger, S. Lehwald, and H. Ibach. On the adsorption of CO on Pt(111). *Surface Science*, 123:264–282, 1982.

[219] D.F. Ogletree, M.A. Van Hove, and G.A. Somorjai. LEED intensity analysis of the structures of clean Pt(111) and of CO adsorbed on Pt(111) in the c(4 × 2) arrangement. *Surface Science*, 173:351–365, 1986.

[220] G. S. Blackman, M. L. Xu, D. F. Ogletree, M. A. Van Hove, and G. A. Somorjai. Mix of Molecular Adsorption Sites Detected for Disordered CO on Pt(111) by Diffuse Low-Energy Electron Diffraction. *Physical Review Letters*, 61:2352–2355, 1988.

[221] Y. Y. Yeo, L. Vattuone, and D. A. King. Calorimetric heats for CO and oxygen adsorption and for the catalytic CO oxidation reaction on Pt{111}. *The Journal of Chemical Physics*, 106:392–401, 1997.

[222] K.Y. Kung, P. Chen, F. Wei, Y.R. Shen, and G.A. Somorjai. Sum-frequency generation spectroscopic study of CO adsorption and dissociation on Pt(111) at high pressure and temperature. *Surface Science*, 463:L627–L633, 2000.

[223] G. Nisbet, C.L.A. Lamont, M. Polcik, R. Terborg, D.I. Sayago, J.T. Hoeft, M. Kittel, R.L. Toomes, and D.P. Woodruff. Structural analysis of Pt(111)c($\sqrt{3}$×5)rect.–CO using photoelectron diffraction. *Surface Science*, 601:1296–1303, 2007.

[224] C. Busó-Rogero, E. Herrero, J. Bandlow, A. Comas-Vives, and Timo Jacob. CO oxidation on stepped-Pt(111) under electrochemical conditions: insights from theory and experiment. *Physical Chemistry Chemical Physics*, 15:18671, 2013.

[225] O. Balmes, G. Prevot, X. Torrelles, E. Lundgren, and S. Ferrer. Generation of surface steps on Pt(977) induced by the catalytic oxidation of CO. *Journal of Catalysis*, 309:33–37, 2014.

[226] R.J Mukerji, A.S Bolina, and W.A Brown. A RAIRS and TPD investigation of the adsorption of CO on Pt{211}. *Surface Science*, 527:198–208, 2003.

[227] S.C. Creighan, A.S. Mukerji, R.J. Bolina, D.W. Lewis, and W.A. Brown. The adsorption of CO on the stepped Pt{211} surface: a comparison of theory and experiment. *Catalysis Letters*, 88:39–45, 2003.

[228] Hideo Orita, Naotsugu Itoh, and Yasuji Inada. A comparison of CO adsorption on Pt(211), Ni(211), and Pd(211) surfaces using density functional theory. *Surface Science*, 571:161–172, 2004.

[229] Hideo Orita and Yasuji Inada. DFT Investigation of CO Adsorption on Pt(211) and Pt(311) Surfaces from Low to High Coverage. *The Journal of Physical Chemistry B*, 109:22469–22475, 2005.

[230] J.S. Luo, R.G. Tobin, David K. Lambert, Galen B. Fisher, and Craig L. DiMaggio. CO adsorption site occupation on Pt(335): a quantitative investigation using TPD and EELS. *Surface Science*, 274:53–62, 1992.

[231] Jiazhan Xu and John T. Yates. Terrace width effect on adsorbate vibrations: a comparison of Pt(335) and Pt(112) for chemisorption of CO. *Surface Science*, 327:193–201, 1995.

[232] J. G. Wang, W. X. Li, M. Borg, J. Gustafson, A. Mikkelsen, T. M. Pedersen, E. Lundgren, J. Weissenrieder, J. Klikovits, M. Schmid, B. Hammer, and J. N. Andersen. One-Dimensional PtO_2 at Pt Steps: Formation and Reaction with CO. *Physical Review Letters*, 95:256102, 2005.

[233] Ryo Toyoshima, Masaaki Yoshida, Yuji Monya, Kazuma Suzuki, Kenta Amemiya, Kazuhiko Mase, Bongjin Simon Mun, and Hiroshi Kondoh. A high-pressure-induced dense CO overlayer on a Pt(111) surface: a chemical analysis using in situ near ambient pressure XPS. *Phys. Chem. Chem. Phys.*, 16:23564–23567, 2014.

[234] B. Tränkenschuh, N. Fritsche, T. Fuhrmann, C. Papp, J. F. Zhu, R. Denecke, and H.-P. Steinrück. A site-selective in situ study of CO adsorption and desorption on Pt(355). *The Journal of Chemical Physics*, 124:074712, 2006.

[235] B. Tärnkenschuh, C. Papp, T. Fuhrmann, R. Denecke, and H.-P. Steinrück. The dissimilar twins – a comparative, site-selective in situ study of CO adsorption and desorption on Pt(322) and Pt(355). *Surface Science*, 601:1108–1117, 2007.

[236] Peter J. Feibelman, B. Hammer, J. K. Nørskov, F. Wagner, M. Scheffler, R. Stumpf, R. Watwe, and J. Dumesic. The CO/Pt(111) Puzzle. *The Journal of Physical Chemistry B*, 105:4018–4025, 2001.

[237] G. Kresse, A. Gil, and P. Sautet. Significance of single-electron energies for the description of CO on Pt(111). *Physical Review B*, 68:073401, 2003.

[238] A Gil. Site preference of CO chemisorbed on Pt(111) from density functional calculations. *Surface Science*, 530:71–87, 2003.

[239] Manuel J. S. Farias, Enrique Herrero, and Juan M. Feliu. Site Selectivity for CO Adsorption and Stripping on Stepped and Kinked Platinum Surfaces in Alkaline Medium. *The Journal of Physical Chemistry C*, 117:2903–2913, 2013.

[240] H. Ibach. The role of surface stress in reconstruction, epitaxial growth and stabilization of mesoscopic structures. *Surface Science Reports*, 29:195–263, 1997.

[241] P. J. Feibelman. First-principles calculations of stress induced by gas adsorption on Pt(111). *Physical Review B*, 56:2175–2182, 1997.

[242] Z. Tian, D. Sander, N. N. Negulyaev, V. S. Stepanyuk, and J. Kirschner. H- and O-induced compressive surface stress on Pt(111): Experiments and density functional theory calculations. *Physical Review B*, 81:113407, 2010.

[243] S. M. Foiles, M. I. Baskes, and M. S. Daw. Embedded-atom-method functions for the fcc metals Cu, Ag, Au, Ni, Pd, Pt, and their alloys. *Physical Review B*, 33:7983–7991, 1986.